

DNA origami scaffolds to control lipid membrane shape



Alena Khmelinskaja

München 2018

DNA origami scaffolds to control lipid membrane shape



Dissertation
an der Fakultät für Physik
der Ludwig-Maximilians-Universität München

vorgelegt von
Alena Khmelinskaia
aus Novosibirsk, Russland

München, den 01. August 2018

Dissertation eingereicht am: 01. August 2018

1. Gutachter: Prof. Dr. Petra Schwille

2. Gutachter: Prof. Dr. Ralf Jungmann

Mündliche Prüfung am: 13. September 2018

"And I wonder"

— FF, Everlong

KURZFASSUNG

Gerüstproteine, beispielweise Proteine der Bin/Amphiphysin/Rvs (BAR) Domänen Familie, vermitteln und regulieren durch ihre Membranbindung und Selbstorganisation die Verformungen von Zellmembranen. Die quantitative Charakterisierung der Interaktionen von synthetischen Gerüst-Molekülen mit Lipidmembranen unter kontrollierten Bedingungen kann fundamental zu unserem Verständnis der physikalischen Prinzipien beitragen, die diesen Membranverformungsphänomenen zugrunde liegen. In dieser Arbeit wurde daher die DNA-Origami-Technologie verwendet, um Funktionselemente zu schaffen, die die physikalischen Eigenschaften von Gerüstproteinen aufweisen und Lipidmembranen kontrolliert deformieren können.

Zunächst wurden die Voraussetzungen bestimmt, unter denen stark negativ geladene DNA Nanostrukturen effizient an Membranen binden. Ich zeige, dass Cholesterin-Anker, die nahe an den sperrigen DNA Nanostrukturen positioniert sind, lokal an der Membranbindung gehindert sind, und dass das Vorhandensein mehrere Cholesterin-Anker oder das Einführen von DNA-„Abstandshaltern“ die Membranbindung verstärkt. Fluoreszenz-Korrelations-Spektroskopie (FCS) Daten zeigen, dass sowohl die Anzahl als auch die Art der DNA-„Abstandshalter“ die Interaktionen der DNA-Nanostrukturen mit Lipiddoppelmembranen bestimmen. Zusätzlich zu Experimenten mit Doppelmembranen haben wir auch die experimentellen Bedingungen für FCS Experimente etabliert, die die Interaktionen von Makromolekülen und Lipidfilmen untersuchen.

Untersuchungen der Selbstorganisation von DNA-Origami-Nanostrukturen auf Lipidmembranen mittels Hochgeschwindigkeits-Atomkraftmikroskopie (HSAFM) haben aufgedeckt, dass per se rein repulsive DNA Nanostrukturen auf Lipidmembranen sowohl Spitze-an-Spitze als auch Seite-an-Seite Kontakte ausbilden, und sich damit anisotropische Domänen bilden. Die bevorzugte Art der Interaktion hängt von der Oberflächendichte der Teilchen und damit der Membranspannung ab. Ich zeige auch, dass man DNA-Nanostrukturen nutzen kann, um 2D Phasenübergänge (iso- zu anisotrop) von Teilchen verschiedener Aspektverhältnisse zu untersuchen.

Zuletzt verwenden wir DNA-Nanostrukturen, um Lipidmembrane zu verformen und dabei die Funktionen von Gerüstproteinen nachzuempfinden. Wir zeigen, dass Lipidmembra-

nen von gekrümmte DNA-Gerüsten Tubus-förmig geformt werden, die damit nicht nur die Form, sondern auch die Wirkung von BAR Proteinen nachstellen können. Die Verformung der Lipidmembran korrelierte mit der Krümmung der DNA-Gerüste und deren Dichte auf der Membran. Um Membranen dynamisch und kontrolliert verformen zu können, habe ich eine DNA-Origamistruktur entworfen, die drei Zustände hat, und die von ihrer passiven in ihre Membran-verformende Konformation geschaltet werden kann. Um das Design zu optimieren wurde ein komplementärer Ansatz in Form von oxDNA Molekül-Dynamik-Simulationen (MD Simulationen) und Transmissionselektronen-mikroskopie (TEM) verwendet.

ABSTRACT

Membrane-binding and self-organization of scaffolding proteins, e.g. Bin/Amphiphysin/Rvs (BAR) domain family, mediates and regulates the shape transformations of cell membranes. The quantitative characterization of the interaction of synthetic scaffolds with lipid membranes in defined conditions will greatly add to our understanding of the fundamental physical principles driving membrane-shaping phenomena. In this work, DNA origami technology was used to create elements that bear physical features of scaffolding proteins and controllably shape lipid membranes.

First, I determined the requirements for efficient membrane-binding of highly negatively charged DNA nanostructures. I show that cholesteryl-anchors positioned close to the bulky DNA nanostructures are locally hindered, and that multiple cholesteryl-anchors or DNA spacers can enhance membrane binding. Fluorescence correlation spectroscopy (FCS) data demonstrates that both the number and type of DNA spacer determine the interaction of DNA nanostructures with lipid bilayers. In addition to bilayers, we established conditions for FCS experiments investigating macromolecule-lipid monolayer interactions.

Studies of the self-organization of DNA origami nanostructures on lipid membranes using high speed atomic force microscopy (HSAFM) revealed that both tip-to-tip and side-by-side interactions, and the resulting anisotropic domains, are observed on lipid membranes for *per se* purely repulsive DNA nanostructures. The preferred type of interaction depends on the particle surface density and thus membrane tension. I also demonstrate the use of DNA nanostructures for the study of isotropic-anisotropic phase transition of particles of different aspect-ratios in 2D.

Last, we employ DNA nanostructures to shape lipid membranes, mimicking the function of scaffolding proteins. We show that curved DNA scaffolds tubulate lipid membranes, resembling not only the shape but also the action of BAR proteins. Lipid membrane deformation was correlated to the DNA scaffolds' curvature and membrane density. To dynamically control membrane shaping, I present the design of a three-state DNA origami structure that can be switched from its passive to its active membrane-shaping conformation. A complementary approach of oxDNA molecular dynamic simulations (MD simulations) and transmission electron microscopy (TEM) imaging was used to optimize the design.

Contents

Kurzfassung	vii
Abstract	ix
List of Abbreviations	xix
I Introduction and outline	1
II Basic concepts	3
II.1 Lipid membranes	3
II.1.1 Cellular membranes	3
II.1.2 Principle of membrane formation and organization	4
II.1.3 Membrane shaping	5
II.1.3.1 Scaffolding proteins	6
II.1.3.2 Energetics of membrane shaping	7
II.1.4 Lipid systems for <i>in vitro</i> studies	8
II.1.4.1 Supported lipid bilayers	9
II.1.4.2 Lipid monolayers	9
II.1.4.3 Giant unilamellar vesicles	10
II.2 Deoxyribonucleic acid (DNA)	10
II.2.1 DNA in a biological context	10
II.2.2 DNA in a physics context	11
II.2.3 DNA origami nanotechnology	12
II.2.4 DNA nanostructures on lipid membranes	13
II.3 Diffusion and Binding	15
II.3.1 Diffusion models	15
II.3.1.1 Brownian motion	15
II.3.1.2 Diffusion of membrane inclusions	16
	xi

II.3.2	Binding kinetics	18
II.4	Methods	19
II.4.1	Fluorescence microscopy	19
II.4.1.1	Fluorescence as a biophysical tool	19
II.4.1.2	Confocal microscopy	20
II.4.2	Fluorescence Correlation Spectroscopy (FCS)	20
II.4.2.1	Principle of FCS	20
II.4.2.2	Confocal single-point FCS	21
II.4.2.3	Confocal FCS on lipid membranes and membrane-bound DNA nanostructures	22
II.4.3	Atomic Force Microscopy (AFM)	23
II.4.4	Transmission electron microscopy (TEM)	25
III	Binding and Diffusion of membrane-bound DNA nanostructures	27
III.1	Effect of anchor positioning on binding and diffusion of elongated 3D DNA nanostructures on lipid membranes	29
III.2	Control of membrane binding and diffusion of cholesteryl-modified DNA origami nanostructures by DNA spacers	41
III.3	FCS analysis of protein mobility on lipid monolayers	81
IV	Self-organization of membrane-bound DNA nanostructures	93
IV.1	Introduction	93
IV.2	Results and Discussion	94
IV.2.1	Density-dependent organization of rodlike DNA nanostructures on mica	95
IV.2.2	Self-organization of rodlike DNA nanostructures on supported lipid bilayers (SLBs)	96
IV.2.3	Dependence of the anisotropic phase formation on the aspect ratio of DNA nanostructures	100
IV.3	Conclusions	102
V	DNA-based scaffolds for shaping lipid membranes	103
V.1	Membrane sculpting by curved DNA origami scaffolds	104
V.2	Integration of a conformational switch into DNA origami scaffolds	115
V.2.1	Introduction	115

CONTENTS

V.2.2	Results and Discussion	117
V.2.2.1	Modular design and characterization of a DNA origami nanostructure with an integrated conformational switch	117
V.2.2.2	DNA nanostructure fine-tuning towards a three-state struc- ture	121
V.2.2.3	Bent DNA nanostructures bind and deform lipid membranes	124
V.2.3	Conclusions	126
VI	Conclusions and outlook	127
	Bibliography	131
A	Appendix to II.1.4.2	157
B	Appendix to III.1	175
C	Appendix to III.2	185
D	Appendix to III.3	197
E	Appendix to IV	213
E	Materials and Methods	213
E.1	DNA origami folding and purification	213
E.2	TEM	213
E.3	Agarose gel electrophoresis	214
E.4	SLB preparation	214
E.5	HSAFM	214
F	Appendix to V.1	219
G	Appendix to V.2	265
G	Materials and Methods	265
G.1	DNA origami folding and purification	265
G.2	oxDNA simulations	266
G.3	TEM	267
G.4	Agarose gel electrophoresis	267

G.5	Giant unilamellar vesicle (GUV) preparation and confocal microscopy imaging	268
	Publications and Manuscripts	275
	Acknowledgements	277

List of Figures

II.1	Structural characteristics of lipid molecules.	5
II.2	Lamellar phases of lipid bilayers.	6
II.3	Deoxyribonucleic acid (DNA) double helix.	11
II.4	Principles of atomic force microscopy (AFM).	24
IV.1	DNA nanostructures of different aspect ratios.	95
IV.2	DNA nanostructures show purely repulsive interactions on a rigid surface.	97
IV.3	DNA nanostructures show tip-to-tip and side-by-side attraction on SLBs.	99
IV.4	Anisotropic phases formed by DNA nanostructures at high surface densities.	101
V.1	Design principles for a DNA origami nanostructure with an integrated conformational switch.	118
V.2	Structural characterization of individual DNA origami modules.	120
V.3	DNA origami nanostructures switch their conformation upon strand displacement.	121
V.4	oxDNA modelling reveals that small modifications in design result in major structural changes.	122
V.5	Three-state DNA origami nanostructure achieved by combination of modules N, S and L.	123
V.6	Binding of the "open" conformation of module L by the negatively curved surface causes large scale deformations on GUVs.	125
E.1	Cadnano design and oligonucleotide sequences of the DNA origami structure AR1.	215
E.2	Cadnano design and oligonucleotide sequences of the DNA origami structure AR7.	216
E.3	Cadnano design and oligonucleotide sequences of the DNA origami structure AR22.	217

G.1	Cadnano design and oligonucleotide sequences of the core DNA origami structure.	269
G.2	Predicted hairpin folding in the "closed" conformation of module L. . . .	270
G.3	Schematic representation of the vectors taken into account for bending angle determination.	271

List of Tables

G.1	List of nucleotide sequences for assembly of each module.	272
G.2	List of nucleotide sequences for assembly of each module – continuation. . .	273

List of Abbreviations

A	adenine
aa	amino acid
ADE model	Area-difference elasticity model
AFM	atomic force microscopy
APD	avalanche photodiode
BAR	Bin/Amphiphysin/Rvs
bp	base-pair
C	cytosine
Chol	cholesterol
chol-TEG	cholesterol modified with a tetra-ethylene glycol linker
cpp	counts per particle
DNA	deoxyribonucleic acid
DOPC	1,2-dioleoyl- <i>sn</i> -glycero-3-phosphocholine
DOPE	1,2-dioleoyl- <i>sn</i> -glycero-3-phosphoethanolamine
DSPC	1,2-distearoyl- <i>sn</i> -glycero-3-phosphocholine
FCS	fluorescence correlation spectroscopy
FJC model	freely-jointed chain model
FRET	Förster resonance energy transfer
G	guanine
GTP	guanosine triphosphate
GUV	giant unilamellar vesicle
HPW model	Hughes-Pailthorpe-White model

HSAFM	high speed atomic force microscopy
IN transition	isotropic-nematic transition
l_p	persistence length
LSM	laser scanning microscope
LUV	large unilamellar vesicle
MD simulations	molecular dynamic simulations
mFJC model	modified freely-jointed chain model
MSD	mean squared displacement
NA	numerical aperture
nt	nucleotide
PH	plekstrin-homology
QCMD	quartz crystal microbalance with dissipation monitoring
SC model	spontaneous-curvature model
SD model	Saffman-Delbrück model
SLB	supported lipid bilayer
SPM	scanning probe microscopy
SPR	surface plasmon resonance
SUV	small unilamellar vesicle
T	thymine
T_m	phase transition temperature
TEM	transmission electron microscopy
WLC model	worm-like chain model

List of Abbreviations

I

INTRODUCTION AND OUTLINE

Biological membranes are fundamental cellular entities whose curvature varies from predominantly flat in the plasma membrane to highly curved in the endoplasmic reticulum or the Golgi apparatus. Shaping of membranes into structures with different curvatures takes place in the most fundamental processes in living cells, e.g. cell division, organelle formation, endocytosis. Previously, several force sources that act on biological membranes inducing curvature have been identified [Baumgart et al., 2011, McMahon and Gallop, 2005, Prinz and Hinshaw, 2009] (see section II.1.3). Although scaffolding elements are one common feature to most curvature-generating processes, the fundamental physical principles underlying membrane bending phenomena are not yet fully understood.

A classic example of such scaffolds that imprint their shape on lipid membranes are the banana-shaped dimers of proteins from the Bin/Amphiphysin/Rvs (BAR) domain superfamily [Qualmann et al., 2011]. Recent studies that used the BAR family as a model protein system, emphasized the relevance of physical-chemical foundations for membrane bending [Simunovic et al., 2015, Traub, 2015]. Taking this into account, it is tempting to take a synthetic biology approach [Schwille and Diez, 2009, Schwille, 2011] to engineer a minimal nanotechnological element that bears the physical features of membrane-scaffolding proteins. Through such an approach, one can identify the minimal set of requirements necessary to shape lipid membranes and extend the current knowledge of highly complex biological processes.

The aim of this thesis was to design a DNA-based synthetic scaffold that can mimic the unique and inherent properties displayed by natural membrane-shaping scaffolds, and thus can induce local membrane curvature. The DNA origami technique (see section II.2.3) appeared to be the perfect tool for such task. Based on the arrangement of thousands of nucleotides with subnanometer-precision, DNA origami was used to produce structures of defined shapes [Rothemund, 2006, Douglas et al., 2009a, Dietz et al., 2009]. DNA nanostructures were further modified in order to regulate their hydrophobicity as well as their conformational changes [Czogalla et al., 2016]. Focusing on

understanding the physical basis of scaffold action in membrane-shaping, these constructs were quantitatively characterized in lipid membrane model systems (see section II.1.4) to address the following key questions:

1. Can one control the membrane binding and diffusion of DNA origami nanostructures? (Chapter III)

In recent years, DNA origami has been used to design amphipathic nanostructures with rather complex functions (see section II.2.4) [Czogalla et al., 2016, Göpfrich et al., 2018]. Nonetheless, the specific requirements for membrane binding have not been previously systematically assessed. In this thesis, I extensively studied the effects of the number, positioning and type of anchors based on cholesterol modified with a tetra-ethylene glycol linker (chol-TEG), one of the most popular hydrophobic modifications, on membrane binding and diffusion of DNA origami nanostructures.

2. How do DNA origami nanostructures organize on lipid membranes? (Chapter IV)

It has been proposed that scaffold-dependent shaping of lipid membranes is initiated by membrane-assisted self-organization of membrane-bound proteins into anisotropic phases [Ramakrishnan et al., 2013, Simunovic et al., 2013a, Cui et al., 2013, Lipowsky, 2013]. The resulting protein "domains" enhance the effect of individual proteins in generating local curvature. However, no direct evidence for this initial self-organization has been found so far. In this thesis, I proposed to study in real-time the organization of purely repulsive rodlike DNA nanostructure on lipid bilayers using high speed atomic force microscopy (HS-AFM), as a first approximation to this problem.

3. Can DNA-based scaffolds mimic BAR proteins' function and shape lipid membranes? (Chapter V)

Here, we designed DNA origami nanostructures with shapes mimicking those of scaffolding proteins. First, we studied the effect of curved shapes, resembling those of proteins of the BAR domain family [Qualmann et al., 2011], on lipid membranes (Subchapter V.1). Second, we designed a DNA nanostructure that can actively change its conformation, similarly to what is described for dynamin [Doherty and McMahon, 2009, Schmid and Frolov, 2011], in order to dynamically control and manipulate lipid membrane shaping (Subchapter V.2).

II

BASIC CONCEPTS

II.1 Lipid membranes

II.1.1 Cellular membranes

Lipids are a class of molecules essential for life, whose function is nowadays recognized to exceed the simple formation of membranes, as physical barriers that enclose cellular compartments [Gennis, 2013]. More specifically, cellular membranes are rather sophisticated organelles themselves, which directly or indirectly participate in a variety of cellular processes, such as protein and lipid synthesis, metabolite transport and signal transduction [Mouritsen and Bagatolli, 2015].

Since the acknowledgement of the complexity of biological membranes and their interplay with proteins by Singer and Nicolson, with the proposal of the fluid mosaic model [Singer and Nicolson, 1972], several models have been brought forward to describe at least fractions of membrane function [Nicolson, 2014, Kusumi et al., 2012, Lingwood and Simons, 2010]. Such models take into account the structural diversity, asymmetric lipid distribution between leaflets and lateral heterogeneity of lipid bilayers [de Almeida and Loura, 2004].

Generally, it is widely accepted that the cell membrane is composed of a lipid bilayer (two antiparallel lipid leaflets) [Gorter and Grendel, 1925] that contains almost 50 % w/w of proteins in its lipid core [Singer and Nicolson, 1972]. Furthermore, lipids and proteins show transient structural and functional heterogeneity at the nanometer scale, as firstly proposed by the so called ‘lipid-raft model’ [Simons and Ikonen, 1997].

II.1.2 Principle of membrane formation and organization

The naturally occurring fats, waxes, sterols, vitamins, mono-, di- and triglycerides and phospholipids are all part of the group of amphipathic molecules that we call lipids. The composition of lipid membranes is highly variable, not only between species but also between tissues in the same organism. Furthermore, even within the same lipid bilayer, lipids are asymmetrically distributed across both leaflets. Nonetheless, generally the major components of lipid membranes are phospholipids and sterols (Figure II.1A). [Harayama and Riezman, 2018]

Membranes are the result of the spontaneous self-organization of lipid molecules. Amphipathic in their nature, lipids have one polar group, which coordinates preferentially with the water (hydrophilic) and one non-polar group, which is buried in the hydrophobic core of the bilayer. Additionally, the shape of the lipid molecules plays an important role in membrane assembly. The shape of lipids is theoretically characterized by the "shape factor" S [de Almeida and Loura, 2004]:

$$S = \frac{V}{A_0 L_C} \quad (\text{II.1})$$

where V is the volume of the molecule, A_0 is the "optimal" area of the lipid headgroup taking into account its dimensions and protonation state, while L_C is the length of the straight acyl chain. Depending on S , lipids will spontaneously form different structures (Figure II.1B): inverted micelles (also called H_{II} phase) for $S > 1$ (conical shape); for $S = 1$ (cylindrical shape), lamellar structures; and micelles for $S < 1$ (inverted conical shape). In nature, however, membranes are formed by a wide variety of lipid species of different S and thus it is possible to form lamellar structures.

Temperature influences the properties of the lamellar phase formed by lipids. In result, different lipid phases can be distinguished (Figure II.2): fluid or liquid disordered (l_d), gel phase or ordered solid (gel) and liquid ordered phase (l_o). Under physiological conditions, the lipid bilayer is in the l_d phase and lipid molecules show high lateral mobility. As lipid chains are mostly in the gauche conformation or have *cis*-double bonds, lipids in the bilayer are loosely packed [de Almeida and Loura, 2004]. Below the phase transition temperature (T_m), lipids become tightly packed and their lateral diffusion is almost completely arrested, marking the gel phase. Due to the difference in lipid packing, the gel phase appears to

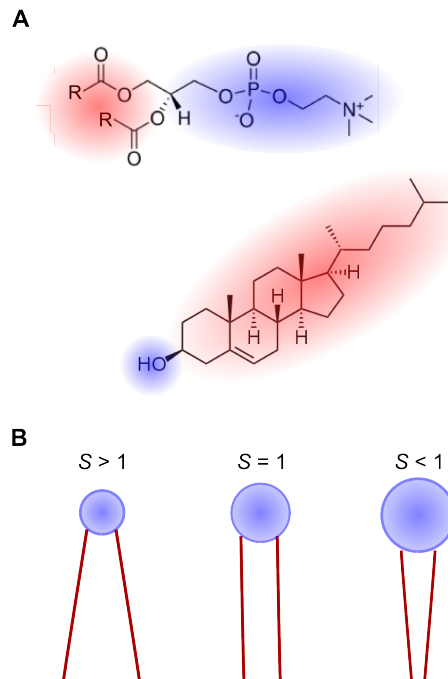


Figure II.1: Structural characteristics of lipid molecules. A) Structure of representative molecules of common lipid groups: top - general structure of phosphatidylcholines and bottom - cholesterol. The amphipathic nature of lipids is highlighted: in red, hydrophobic regions and in blue, polar areas. B) Schematic representation of lipids with different shape factor S : cone shape, cylindrical shape and inverted cone shape for $S > 1$ (left), $S = 1$ (center) and $S < 1$ (right), respectively.

be thicker in comparison to the l_d phase. Importantly, this phase transition is accompanied by changes in other physical properties of the lipid bilayer, such as the membrane Young's modulus [Jadidi et al., 2014] and bending rigidity κ [Dimova et al., 2000, Mecke et al., 2003, Dimova, 2014]. Notably, in lipid mixtures different phases can coexist due to the distinct thermotropic properties of individual lipid species. The special case of the intermediate l_o phase is characterized by a high lipid order in which lipid diffusion is retained [Chiantia et al., 2006]. While gel and l_d phases are found for all pure lipids, the l_o phase is characteristic of mixed bilayers containing sterols.

II.1.3 Membrane shaping

Cellular membranes are dynamic and heterogeneous in their shape [McMahon and Gallop, 2005]. For example, many important cellular processes such as cell division and organelle

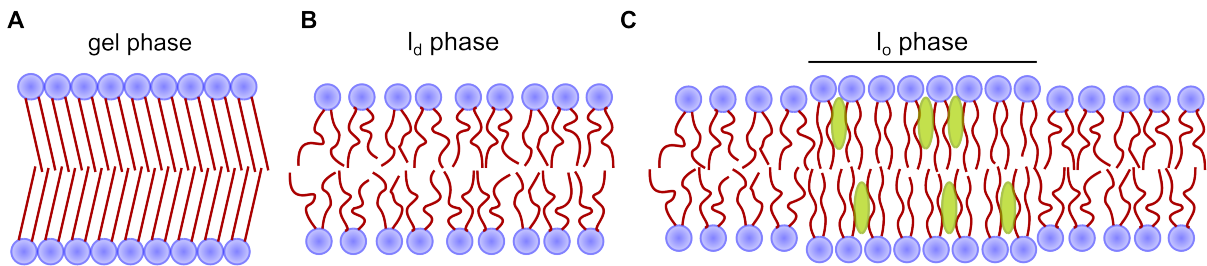


Figure II.2: Lamellar phases of lipid bilayers. Schematic representation of different lipid bilayer phases: A) gel phase or ordered solid (gel), B) liquid-disordered (l_d) and C) liquid-ordered phase (l_o). Green ovals represent cholesterol molecules.

formation, viral budding, cellular trafficking and specific types of signalling are dependent on the capacity of lipid membranes to be sculpted. The induction and stabilization of membrane curvature depends on the interplay between lipids and proteins and may involve: changes in lipid composition, structural rearrangements of integral membrane proteins, activity of cytoskeletal and motor proteins, scaffolding by peripheral membrane proteins and/or active helix insertion into membranes. Generally, the deformation of membranes starts with the anchoring or insertion of specific proteins into the lipid bilayer. Locally, defects and curvature are generated, due to the resulting destabilization of the preformed membrane tension. Subsequently, organization of proteins near the perturbed membrane region will promote the formation of special shapes, such as buds or tubes [Prinz and Hinshaw, 2009, Baumgart et al., 2011].

II.1.3.1 Scaffolding proteins

A common feature involved in most membrane curvature generating proteins are scaffolding elements [Prinz and Hinshaw, 2009, Baumgart et al., 2011]. One such example of scaffolding are the proteins from the Bin/Amphiphysin/Rvs (BAR) domain family [Qualmann et al., 2011, Zimmerberg and McLaughlin, 2004, Frost et al., 2008]. BAR proteins dimerize to form characteristic banana-shaped scaffolds that presumably sense and stabilize local membrane curvature [Frost et al., 2008, Qualmann et al., 2011, Bhatia et al., 2010, Madsen et al., 2010]. BAR proteins bind lipid membranes through electrostatic or hydrophobic interactions [Qualmann et al., 2011]. Furthermore, they were shown to tubulate membranes *in vitro* [Baumgart et al., 2011, Drin and Antonny, 2010]. Importantly, different families of BAR modules adopt shapes with different degrees of curvature ($C \approx 10 - 100 \mu\text{m}^{-1}$) [Qual-

mann et al., 2011, Frost et al., 2008]. Thus, BAR proteins are believed to rely on their curved shape for their function.

Another classical example of membrane-scaffolding is the clathrin-dependent endocytosis. Through interaction with several adaptor proteins, clathrin forms an exoskeleton able to bend and invaginate membranes from the inside of cells [Doherty and McMahon, 2009]. This process is also dependent on several other scaffolding proteins, such as BAR domain proteins and the guanosine triphosphate (GTP)ase dynamin. This protein binds to phosphatidylinositol phospholipids through plekstrin-homology (PH) domains, polymerizes into a helical coat and constricts the neck of growing endocytic pits, leading to membrane fission [Pawlowski, 2010, Schmid and Frolov, 2011, Ferguson and De Camilli, 2012]. Several models were suggested in which concerted GTP hydrolysis and conformational changes in the dynamin oligomer, including constriction, extension, torsion, twisting or other movements, will lead to the physical cleavage of the enclosed lipid tube and to its final vesiculation [Roux et al., 2010, Pawlowski, 2010, Schmid and Frolov, 2011, Ferguson and De Camilli, 2012].

II.1.3.2 Energetics of membrane shaping

Shaping of lipid membranes has been theoretically described by the Helfrich-Canham-Evans elastic membrane model (or spontaneous-curvature model (SC model)) [Helfrich, 1973]:

$$E = \frac{\kappa}{2} \int dA (C_1 + C_2 - C_0)^2. \quad (\text{II.2})$$

Here, E is the energy necessary to bend a membrane segment of area A , such that the principal curvatures of the membrane surface are C_1 and C_2 . For a membrane tube, $C_1 = 1/R$ and $C_2 = 0$, where R is the radius of the tubule, while for a spherical surface $C_1 = C_2 = 1/R$, where R is the radius of the sphere. E further depends on the spontaneous curvature C_0 , which reflects the asymmetry of the lipid bilayer (for homogeneous symmetric bilayers $C_0 = 0$), and the membrane bending rigidity κ . For 1,2-dioleoyl-*sn*-glycero-3-phosphocholine (DOPC) membranes, as the ones used in this thesis, κ at room temperature was assumed to be $23.1k_B T$ [Fa et al., 2007].

Notably, in the SC model the membrane is considered to be infinitely thin in comparison to the overall membrane surface (in our case, correlated to the vesicle size). Practically, the

lipid bilayer has a finite thickness, which results in the compression of the negatively curved leaflet, while the positively curved leaflet is expanded. Consequently, an energetic penalty arises from the area difference between leaflets. Thus, the Area-difference elasticity model (ADE model) [Miao et al., 1994] was introduced to refine the SC model by a respective term for the area mismatch of both leaflets:

$$E = \kappa \left(\frac{1}{2} \int dA (C_1 + C_2 - C_0)^2 + \frac{\alpha}{2} \frac{\pi}{AD^2} (\Delta A - \Delta A_0) \right). \quad (\text{II.3})$$

Here, in the second term ΔA is the differential monolayer area, determined by the difference in the number of molecules between the leaflets, and ΔA_0 its value at equilibrium. D is the membrane thickness and $\alpha = \bar{\kappa}/\kappa$, with $\bar{\kappa}$ being the non-local bending rigidity modulus. Generally, α is estimated to be in the order of unity and the approximation $\alpha = 3/\pi$ [Seifert and Lipowsky, 1995] was used in this thesis.

II.1.4 Lipid systems for *in vitro* studies

Protein-lipid interactions are the result of a highly complex interplay of a manifold of parameters. For example, electrostatics, membrane curvature and steric hindrances, to name only a few, can affect the binding of a protein to a membrane. Studies of proteins themselves, protein-protein and protein-membrane interactions in the cellular environment are thus rather difficult to perform and interpret. Moreover, *in vivo* systems are intrinsically highly variable.

In the last few decades, a number of *in vitro* methods have been developed, aiming to reduce the complexity of the studied systems to their essentials. The study of membrane-associated processes under defined and controlled conditions is enabled by several membrane model systems [Lagny and Bassereau, 2015]. The choice of the used membrane model system is dependent on the biological question of interest, as each of them bears advantages and disadvantages related to their structure (lipid mono- or bilayer, uni- or multilamellar), curvature or used membrane support.

In this thesis, three different model systems have been used: supported lipid bilayers (SLBs) (section II.1.4.1), lipid monolayers (section II.1.4.2) and giant unilamellar vesicles (GUVs) (section II.1.4.3).

II.1.4.1 Supported lipid bilayers

SLBs are planar membranes with an ideal thickness of a single bilayer. In this thesis, SLBs are formed by fusion and rupture of small unilamellar vesicles (SUVs) on a flat surface (such as mica or glass), typically in the presence of divalent cations. Alternatively, SLBs can be deposited by Langmuir-Blodgett transfer [Castellana and Cremer, 2006] or spin coating [Thormann et al., 2007] on a hydrophilic surface. Although SLBs are a perfect membrane model system for surface or contact methods, such as quartz crystal microbalance with dissipation monitoring (QCMD), surface plasmon resonance (SPR) or atomic force microscopy (AFM) (II.4.3), additional interactions with the support may influence the studies [Dertinger et al., 2006, Macháň and Hof, 2010].

II.1.4.2 Lipid monolayers

Langmuir lipid monolayers are formed by deposition of lipids on the air-water interface or over an available surface. Due to their amphiphathic nature, the lipid molecules re-organize themselves into a single lipid layer such that, on an air-water interface, the more hydrophilic part of the molecule coordinates with the water subphase whereas the hydrophobic part sticks out towards the air. Although the system lacks essential features of a biological membrane, it enables the fine tuning of lipid packing, a parameter of great relevance for lipid-protein interactions that is hardly accessible in bilayer assays.

In classical Langmuir lipid monolayers, the lipid packing is controlled by mechanical compression of the lipid monolayer. The change in lipid packing can be monitored by the change in surface pressure π , measured through a Wilhelmy plate (thin plate of platinum or ash-free filter paper) or a dyne probe attached to a micro-balance and immersed in the aqueous subphase.

Typically, the Langmuir-Blodgett troughs used in lipid monolayer experiments require large sample volumes (of order of tens of mL per sample). Since the introduction of miniaturized chambers [Chwastek and Schwille, 2013], lipid monolayers are of easy handling and require considerably smaller volumes (hundreds of μL), making monolayers compatible with protein systems purified on lab scale. In this setup, the lipid packing is no longer controlled by mechanical compression, but rather by controlling the amount of lipids deposited on

the air-water interface.

Importantly, complex biological networks have been successfully reconstituted using this model system [Vogel et al., 2013, Zieske et al., 2016]. For example, in this thesis (see Appendix A [Vogel et al., 2017]) lipid monolayers have been used to study the action of a minimal actin-myosin network on the organization of lipid domains. We showed that the addition of myosin to the system induces shape change, fusion and fission of lipid domains.

II.1.4.3 Giant unilamellar vesicles

GUVs are one of the most popular models of free-standing lipid bilayers. This class of liposomes has sizes ranging from 5 to 100 μm . Thus, in the opposition of smaller liposomes (SUVs and large unilamellar vesicles (LUVs)), GUVs are quasi-planar at the length scale of a number of biological molecules and processes. Generally, GUVs can be produced by electroformation [Angelova and Dimitrov, 1986] at high yields under several salt conditions and are stable over long periods of time [Jørgensen et al., 2017].

II.2 Deoxyribonucleic acid (DNA)

II.2.1 DNA in a biological context

In living organisms, deoxyribonucleic acid (DNA) has a critical function as the information storage and the functional code that enables cells to generate all other necessary macromolecules and replicate themselves [Lehninger et al., 2005]. DNA molecules are long polymers of four repeating nucleotides: adenine (A), thymine (T), guanine (G) and cytosine (C) (Figure II.3). In these long molecules, genes encode for proteins, with each combination of three nucleotides coding for one of the 20 amino acids that constitute proteins. Due to its length, in cells DNA is usually packed in higher order structures, called chromosomes.

DNA exists mainly as a right-handed double helix of antiparallel long polynucleotides, held together by hydrogen bonds between base pairs (Figure II.3). This base pairing is specific, such that A pairs with T, while G pairs with C. Base-stacking interactions among aromatic

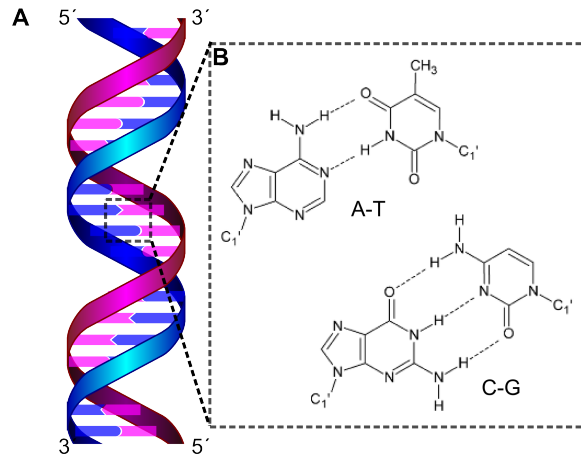


Figure II.3: DNA double helix. A) Schematic representation of the antiparallel DNA double helix. B) The chemical structure of all four nucleotides (A, T, C and G) is shown. Dotted lines represent the hydrogen bonds established in base-pairing and stabilizing the DNA double helix. Adapted from [Szabat et al., 2015] (a reprint permission has been granted by the publisher).

bases and consequent minimization of the solvation shell contributes for the molecules stabilization. Although usually present in its double-stranded form, the two DNA strands can come apart to form two single-stranded DNA molecules. This DNA melting is temperature dependent and strongly depends on the GC/AT content of the specific DNA duplex.

II.2.2 DNA in a physics context

DNA in its single- and double-stranded form can be treated as any other polymer [Phillips et al., 2012]. The worm-like chain model (WLC model) describes polymers in function of their persistence length (l_p), which quantifies the stiffness of a polymer, i.e. it's the measure of the length scale over which a polymer is roughly straight. For single- and double-stranded DNA the l_p is 2.2 nm and 50 nm respectively [Smith et al., 1996, Bloomfield et al., 2000, Chi et al., 2013, Tinland et al., 1997, Murphy et al., 2004]. The mean-square end-to-end distance of a polymer $\langle R^2 \rangle$ is defined by:

$$\langle R^2 \rangle = 2l_p^2 \left(\frac{L}{l_p} - 1 + e^{L/l_p} \right). \quad (\text{II.4})$$

In the limiting case of a stiff rod ($L \ll l_p$) $\langle R^2 \rangle = L^2$, while for a flexible polymer ($L \gg l_p$) $\langle R^2 \rangle = 2Ll_p$.

Other models have further been developed to describe the properties of polymers [Phillips et al., 2012]. In the freely-jointed chain model (FJC model), a flexible polymer can be described as a chain of Kuhn segments with length b , connected by flexible links that permit the adjacent segments to point in various directions. Taking this into account, the contour length (L) of a polymer is given by $L = Nb$ and the mean-square end-to-end distance of a polymer can be calculated through $\langle R^2 \rangle = Nb^2$, where N is the number of segments. From the comparison with the WLC model, comes that $b = 2l_p$.

In this thesis, for short single- and double-stranded DNA (when L/l_p is small), the WLC model is considered to estimate $\langle R^2 \rangle$ (chapter III.2). However, for the thermodynamic description of long single stranded DNA ($L \gg l_p$), the modified freely-jointed chain model (mFJC model) is used. In this model, the force F necessary to stretch the DNA molecule to an end-to-end distance x can be calculated from:

$$x = L \left(\coth\left(\frac{Fb}{k_B T}\right) - \frac{k_B T}{Fb} \right) \left(1 + \frac{F}{S} \right) \quad (\text{II.5})$$

where $b = 1.5$ nm and S is the stretch modulus of single stranded DNA (800 pN) [Smith et al., 1996]. This approximation was used to determine the force released by toehold-mediated strand displacement mechanism in the chapter V.2.

II.2.3 DNA origami nanotechnology

In the early 1980s, Nadrian Seeman laid the conceptual foundations for DNA nanotechnology [Seeman, 1982]. The exceptional properties of DNA, including high specificity of molecular recognition, defined secondary structure and high stability, led to its natural choice as a building material for the construction of synthetic nanostructures.

The DNA origami methodology led to a major breakthrough in the field of nanotechnology. This technique is based on the arrangement of long single-stranded nucleic acid molecules into 2D and 3D nanostructures with sub-nanometer precision by hybridization with hundreds of short oligonucleotides, called "staples" [Rothemund, 2006, Douglas et al., 2009a, Dietz et al., 2009]. Importantly, DNA origami structures can be modified with

functional moieties, e.g. small biomolecules, fluorescent dyes, metallic nanoparticles, peptides, proteins or hydrophobic moieties [Czogalla et al., 2016, Simmel, 2012, Hong et al., 2017, Nummelin et al., 2018].

Notably, other DNA nanostructure design methodologies have been developed, such as the tile-design [Jiang et al., 2017] and the wireframe design [Orponen, 2018]. However, the comparison of these methodologies overcomes the scope of this thesis.

II.2.4 DNA nanostructures on lipid membranes

DNA nanostructure modification with hydrophobic moieties enables the investigation of biophysical processes in biologically relevant environments, such as lipid membranes, resorting to minimal lipid model systems or directly addressing cells [Czogalla et al., 2016, Göpfrich et al., 2018]. Even though the first targetting of DNA nanostructures to lipid membranes was implemented only five years ago [Czogalla et al., 2013], the field has been rapidly expanding in several directions.

Studies have shown that cholesterol modified with a tetra-ethylene glycol linker (chol-TEG) modified DNA nanostructures can be designed to achieve switching behaviors in terms of: binding to lipid membranes by exposure of the cholesteryl-moieties [List et al., 2014]; Mg^{2+} dependent preferential partitioning in phase-separated lipid bilayers [Czogalla et al., 2013, Sato et al., 2018, Dohno et al., 2017, Avakyan et al., 2017]; light-mediated reversible assembly and disassembly of dimers [Suzuki et al., 2014].

Due to the sequence specificity, DNA nanostructures can be used as platforms to organize different functional moieties on lipid membranes, such as dyes, membrane anchors or oligomerizing strands that allow the formation of larger scale assemblies [Johnson-Buck et al., 2014]. Indeed, DNA nanostructures can organize themselves in 2D arrays [Suzuki et al., 2015, Sato et al., 2018, Dohno et al., 2017, Avakyan et al., 2017]. Moreover, membrane-assisted oligomerization of DNA origami nanostructures has been shown to deform and even disrupt lipid vesicles, in similarity to scaffolding proteins (see section II.1.3) [Kocabey et al., 2015, Czogalla et al., 2015a]. Interestingly, curved DNA origami nanostructures can shape lipid membranes even without further polymerization [Franquelim et al., 2018, Grome et al., 2018] (see chapter V.1).

Other complex biological functions have also been reproduced using DNA origami nanostructures. For example, a four-helix DNA bundle has been shown to insert into the lipid bilayer and act as a scramblase, enhancing the mixing of lipids between the two lipid leaflets [Ohmann et al., 2018]. Furthermore, DNA-based channels that not only insert into the lipid bilayer, but also conduct ion current, even in a voltage dependent manner, have been successfully produced in different sizes and with different anchoring moieties [Langecker et al., 2012, Burns et al., 2013a, Burns et al., 2013b, Seifert et al., 2015, Göpfrich et al., 2015, Göpfrich et al., 2016a, Göpfrich et al., 2016b]. Additionally, such structures have been shown to have a cytotoxic effect *in vivo* [Burns et al., 2014]. The future possibility of selectively targeting such pore-forming structures to specific cell types opens exciting possibilities for biomedical applications.

Hybrid DNA nanostructures have also been explored as a delivery vehicle for biomedical processes [Perrault and Shih, 2014]. Moreover, amphipathic DNA nanostructures have been shown to be useful tools to form vesicles of narrow size distribution [Yang et al., 2016] or programmed shape [Zhang et al., 2017], to characterize isotropic-anisotropic phase transition by monitoring their rotational and translational diffusion [Czogalla et al., 2015b], to study different protein complexes *in vitro* as well as *in vivo* [Xu et al., 2016, Fisher et al., 2018, Henning-Knechtel et al., 2017, Kurokawa et al., 2018], and even to program cellular function [Akbari et al., 2017]. Notably, although the binding of DNA nanostructures to lipid membranes can be easily accomplished using divalent cations such as Mg^{2+} , which establish an electrostatic interaction between the negatively charged DNA backbone and the phosphate group of lipid phospholipid (e.g. [Gromelski and Brezesinski, 2006, Czogalla et al., 2013, Suzuki et al., 2015]), only the site-specific modification of DNA nanostructures with amphipathic molecules allows one to control their binding orientation. In this thesis, Mg^{2+} -mediated membrane binding is explored in chapter IV, while chol-TEG anchors are used in chapters III and V.

II.3 Diffusion and Binding

II.3.1 Diffusion models

II.3.1.1 Brownian motion

The thermally driven random motion of microscopic particles in a solvent is termed Brownian motion [Brown, 1828]. This movement is caused by the collision of particles with the surrounding solvent molecules, which at a temperature $T > 0$ are constantly moving. Notably, this motion is random and memoryless, when observed at sufficiently long time scales.

Quantitatively, the process of Brownian motion is described by Fick's second law (or diffusion equation) [Fick, 1855, Sutherland, 1905, Einstein, 1905, von Smoluchowski, 1906]:

$$\frac{\partial}{\partial t}\rho(\vec{r}, t) = D\nabla^2\rho(\vec{r}, t) \quad (\text{II.6})$$

where D is the diffusion coefficient, considered to be an isotropic quantity in the context of this work. The solution of equation II.6 is the probability ρ to find a diffusing particle at time t at the location \vec{r} , provided it was located at \vec{r}_0 at $t_0 = 0$. Taking into account the normalization $\int \rho(\vec{r}, t) d^3\vec{r} = 1$, the solution for 3D diffusion reads:

$$\rho(\vec{r}, t) = (4\pi Dt)^{-\frac{3}{2}} e^{-\frac{\vec{r}^2}{4Dt}}. \quad (\text{II.7})$$

This is the description of a Gaussian distribution centred in $\vec{r}_0 = 0$, with standard deviation $\sqrt{6Dt}$ that widens with time. Consequently, the mean displacement is $\langle \vec{r} \rangle = 0$. On the other hand, the mean squared displacement (MSD) reads:

$$\langle \vec{r}^2 \rangle = \int \vec{r}^2 \rho(\vec{r}, t) d^3\vec{r} = 6Dt. \quad (\text{II.8})$$

This linear relation between MSD and time implies that the measurement of the displacement of particles at different time points gives access to their diffusion coefficient.

Furthermore, as Brownian motion is a quasi-ergodic process, the ensemble average is equivalent to the time average over a single particle trajectory. This becomes specially relevant

when considering the calculation of the autocorrelation function in fluorescence correlation spectroscopy (FCS) (see section II.4.2).

The diffusion coefficient D depends on the temperature T and the friction constant ζ of the considered particles [Sutherland, 1905, Einstein, 1905, von Smoluchowski, 1906]:

$$D = \frac{k_B T}{\zeta}. \quad (\text{II.9})$$

For simplicity, diffusing particles are often approximated to be spherical, with a characteristic hydrodynamic radius a . The friction constant is then given by the Stokes relation $\zeta = 6\pi\eta a$, where η is the bulk viscosity of the medium. The combination of the Stokes relation with equation II.9 is typically termed Stokes-Einstein-Smoluchowski or Stokes-Einstein relation and is often used to estimate the physical size of the diffusing particles.

II.3.1.2 Diffusion of membrane inclusions

In this thesis, mainly the diffusion of lipids and macromolecules in lipid membranes is considered (chapters III.2 and III.3). The most commonly used model to describe the Brownian motion of particles embedded in quasi two-dimensional systems is the Saffman-Delbrück model (SD model) [Saffman and Delbrück, 1975, Saffman, 1976]. In the SD model, a cylindrical inclusion with radius a diffuses in a flat layer of thickness h and surface viscosity η_s . Here, $\eta_s = \eta h$, where η is the membrane viscosity. The membrane is surrounded above and below by media with bulk viscosities η_1 and η_2 , which both influence the diffusion of membrane inclusions. This is translated into the characteristic length scale of the system, so-called Saffman-Delbrück length: $l_{\text{SD}} = \eta_s / (\eta_1 + \eta_2)$. Moreover, similar to many other diffusion models, the SD model assumes that the inclusion is much larger than the surrounding lipid molecules. Thus, the SD model derives the diffusion coefficient D of a membrane inclusion as:

$$D = \frac{k_B T}{4\pi\eta_s} \Delta_{\text{SD}} \quad (\text{II.10})$$

where Δ_{SD} is referred to as the reduced mobility and is defined as $\Delta_{\text{SD}} = \ln(2l_{\text{SD}}/a) - \gamma$. Here, γ is the Euler constant.

The SD model assumes at all times that the membrane inclusion a is much larger than

the lipids and $a \ll l_{\text{SD}}$. In the regime $a \ll l_{\text{SD}}$ the diffusion coefficient is predicted to have only a weak dependence on the inclusion size. Indeed, several experimental and simulation studies [Peters and Cherry, 1982, Ramadurai et al., 2009, Weiß et al., 2013, Guigas and Weiss, 2006] confirmed the applicability of the SD model to a number of proteins. However, the SD model fails to describe the diffusion of large membrane domains [Cicutta et al., 2007, Petrov et al., 2012], where the inclusion size a is in the order of l_{SD} .

Hughes, Pailthorpe, and White derived a more general model that covers arbitrary cylindrical inclusion sizes, assuming that the lipids are much smaller [Hughes et al., 1981]. To circumvent the difficult numerical calculations of D according to the original publication of the Hughes-Pailthorpe-White model (HPW model), Petrov and Schwille derived a high-accuracy analytical approximation for the reduced mobility Δ_{HPW} [Petrov and Schwille, 2008b]:

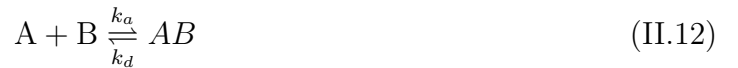
$$\begin{aligned} \Delta_{\text{HPW}} = & \left(\ln \left(\frac{2l_{\text{SD}}}{a} \right) - \gamma + \frac{4a}{\pi l_{\text{SD}}} - \frac{a^2}{2l_{\text{SD}}^2} \ln \left(\frac{2l_{\text{SD}}}{a} \right) \right) \\ & \times \left(1 - \frac{a^3}{\pi l_{\text{SD}}^3} \ln \left(\frac{2l_{\text{SD}}}{a} \right) + \frac{c_1 \frac{a^{b_1}}{l_{\text{SD}}^{b_1}}}{1 + c_2 \frac{a^{b_2}}{l_{\text{SD}}^{b_2}}} \right)^{-1}. \end{aligned} \quad (\text{II.11})$$

With $c_1 = 0.73761$, $b_1 = 2.74819$, $a_2 = 0.52119$, and $b_2 = 0.51465$, equation II.11 was found to accurately describe the numerical results of the HPW model and match the asymptotic expressions from the analytical theory. In the regime $a/l_{\text{SD}} \ll 1$, Δ_{HPW} has only a weak dependence on the inclusion size and reproduces the SD model. For very large membrane inclusions, a much stronger inverse proportionality of Δ_{HPW} with the ratio a/l_{SD} is observed and, at the limit $a \gg l_{\text{SD}}$ the diffusion coefficient becomes independent of the membrane viscosity [Hughes et al., 1981].

In this thesis, the HPW model is used to estimate the effective insertion size of macromolecules in lipid monolayers and bilayers, as well as estimate the viscosity of lipid monolayers at different lipid densities (chapters III.2 and III.3).

II.3.2 Binding kinetics

Protein-lipid interactions are essential for a number of cellular processes, such as membrane shaping (section II.1.3). Although membrane shaping involves the interplay of a number of protein and lipid molecules, let us first focus in the simplest case of a bimolecular interaction. In such scenario, two binding partners A and B transiently form the product AB with association rate k_a (in $\text{M}^{-1} \text{s}^{-1}$) and dissociation rate k_d (in s^{-1}).



In equilibrium, the rate of production and decay of AB become equivalent and thus:

$$\frac{d}{dt}[AB] = k_a[A][B] - k_d[AB] = 0 \quad (\text{II.13})$$

Considering the law of mass action, the corresponding dissociation constant K_D is given by:

$$K_D = \frac{[A][B]}{[AB]} = \frac{k_d}{k_a} \quad (\text{II.14})$$

In this thesis, the K_D of several origami nanostructures to lipid membranes is determined through titration experiments (chapter V.1). Generally, in such experiments the total concentration of one of the binding partners is kept constant (for A, one gets $[A] + [AB] = \text{const}$) and the concentration of the complex (AB) is measured depending on the concentration of the second binding partner (B).

$$[AB] = \frac{[A] + [AB]}{K_D + [B]}. \quad (\text{II.15})$$

Practically, for macromolecules binding GUVs, the membrane surface area is kept constant and the concentration of the macromolecule of interest is titrated. To determine the concentration of bound macromolecules, the fluorescence intensity at the membrane surface is monitored. The obtained titration curve is then fitted with a Langmuir isotherm model, an adapted form of equation II.15. Alternatively, direct measurement of k_a and k_d , which also apply out of equilibrium, can be used to determine K_D . From the determined K_D , it is further possible to determine the apparent free energy of membrane binding $\Delta G = RT \ln K_D$, where R is the ideal gas constant.

II.4 Methods

II.4.1 Fluorescence microscopy

II.4.1.1 Fluorescence as a biophysical tool

Luminescence is the process of photon emission by previously excited substrates. In fluorescence, a type of luminescence, the emission of a photon occurs in the nanosecond regime and is the result of the relaxation from a singlet excited state back to the ground state S_0 (reviewed in [Valeur and Berberan-Santos, 2012, Lakowicz, 2006]). The process of fluorescence is accompanied by energy dissipation, resulting in a red-shift of the emission fluorescence spectrum with respect to the excitation spectrum, known as Stokes' shift.

Over the past century, the phenomenon of fluorescence has been vastly explored and applied to the study of biological systems by means of fluorescence microscopy and spectroscopy. Due to the inherent Stokes' shift, the excitation and the fluorescence emission light can be easily separated by appropriate dichroic mirrors. Importantly, fluorescence experiments can be performed in the visible wavelength range, compatible with biological samples and high-performance optical components, while avoiding the absorption by water molecules. A variety of fluorescent probes (chemical or naturally occurring) can be specifically attached to biological molecules, both *in vitro* and *in vivo*. As excitation typically takes femtoseconds, and the fluorescence lifetime is on the order of nanoseconds, with high excitation rates sufficiently high signals are generated for detection. Indeed, with the current state-of-the-art equipment it is possible to routinely perform measurements on a single-molecule scale.

However, fluorescent labels have a few disadvantages. Non-native fluorescent labels can alter the system under study and controls should be performed to ensure that the observed effects are independent of the fluorescent tag (e.g. [Swulius and Jensen, 2012, Margolin, 2012]). Typical examples, are the possibility of occurring nonspecific interactions with the substrate or dimerization of fluorophores (e.g. [Costantini et al., 2012]). On the other side, photo-induced damage can arise due to energy deposition in the system or the generation of reactive (and thus, toxic) singlet oxygen, associated to the triplet state of fluorophores [Davidson, 1979, Wilkinson et al., 1994, Eggeling et al., 1999].

II.4.1.2 Confocal microscopy

In chapters III and V a confocal microscope [Minsky, 1957] is used, both for imaging and FCS [Rigler et al., 1993, Eigen and Rigler, 1994]. The main advantage over widefield microscopy comes from the elimination of out-of-focus light by the introduction of a pinhole in the image plane of the detection pathway. Moreover, the focal volume is reduced by coinciding narrowly focused excitation and detection profiles. Using a high-numerical aperture (NA) objective (typically $NA \simeq 1.2$), the observation volume is typically on the order of femtoliters.

II.4.2 Fluorescence Correlation Spectroscopy (FCS)

II.4.2.1 Principle of FCS

In the 1970's, Magde, Elson and Webb introduced the principle of FCS [Magde et al., 1972, Elson and Magde, 1974, Magde et al., 1974]. In FCS, the fluorescence signal collected from an observation volume is analyzed with respect to its fluctuations, which appear from stochastic deviations from thermal equilibrium. To be sensitive to fluctuations of the fluorescence signal, the number of particles that contribute to it should be low. Two decades later, FCS was demonstrated in combination with confocal microscopy [Rigler et al., 1993, Eigen and Rigler, 1994], which enabled single-molecule sensitivity at biologically relevant concentrations by reducing the size of the detection volume.

Typically, fluorescence fluctuations arise from brightness fluctuations of the fluorescent particles or from their diffusion in and out of the detection volume [Petrov and Schwille, 2008a]. The timescale of these fluctuations is related to the underlying process, thus properties of the sample can be recovered from the analysis of the time scale of the fluctuations. For this purpose, the signal is autocorrelated in time and the resulting autocorrelation curves are typically fitted by an appropriate model. FCS can be thus used to investigate e.g. diffusion [Elson and Magde, 1974, Magde et al., 1974], active transport [Magde et al., 1978], reversible binding [Michelman-Ribeiro et al., 2009], or blinking dynamics of the fluorophore (e.g. [Widengren et al., 1995, Haupts et al., 1998, Widengren et al., 1999, Widengren and Schwille, 2000, Torres and Levitus, 2007]).

II.4.2.2 Confocal single-point FCS

Generally, the fluorescence signal trace $F(t)$ can be described by the fluctuation $\delta F(t)$ around its temporal mean $\langle F \rangle$:

$$F(t) = \langle F \rangle + \delta F(t). \quad (\text{II.16})$$

The autocorrelation of the later over time translates the temporal similarity of the signal into its characteristic decay.

$$G(\tau) = \frac{\langle \delta F(t) \delta F(t + \tau) \rangle}{\langle F \rangle^2} \quad (\text{II.17})$$

In the case of fluorophores undergoing Brownian motion, the characteristic decay of the temporal autocorrelation function is determined by the diffusion coefficient of the particles and the size of the detection volume. In its simplest form, in confocal FCS the detection volume (or effective volume, V_{eff}) is approximated by a 3D Gaussian, with the lateral $1/e^2$ -width w_{xy} and axial length $w_z = S w_{xy}$. Here, the structure parameter S is a measure of the elongation of the detection volume.

$$V_{eff} = \pi^{\frac{3}{2}} w_{xy}^2 w_z \quad (\text{II.18})$$

Thus, the autocorrelation function for 3D diffusion in a confocal volume takes the form:

$$G(\tau) = N^{-1} \left(1 + \frac{\tau}{\tau_D}\right)^{-1} \left(1 + \frac{\tau}{S^2 \tau_D}\right)^{-1/2} \quad (\text{II.19})$$

where N is the average number of particles in the confocal volume and τ_D is the characteristic diffusion time of the fluorescent species. The amplitude of the autocorrelation function at $\tau \rightarrow 0$ corresponds to the inverse mean number of particles N^{-1} in the effective volume and can be translated into the respective concentration once the size of the detection volume is known. To determine w_{xy} , a calibration measurement using a freely diffusing fluorophores of known diffusion coefficient D is performed taking into account:

$$\tau_D = \frac{w_{xy}^2}{4D} \quad (\text{II.20})$$

The diffusion coefficients of the calibration fluorophores used in this study are: $D_{Alexa488} = 414 \pm 10 \mu\text{m}^2/\text{s}$ [Petrov et al., 2006] and $D_{ATTO655} = 426 \pm 8 \mu\text{m}^2/\text{s}$ [Dertinger et al., 2007], at 25 °C. Once w_{xy} is known, the diffusion coefficient of the biomolecules of interest can be determined from subsequent FCS experiments.

In many confocal FCS measurements, the autocorrelation curve is not exclusively governed by diffusion processes and additional terms are added to the model [Krichevsky and Bonnet, 2002]. In this thesis, when Alexa488 or ATTO488 dyes are used, the inherent fluorophore blinking due to triplet state is considered by introducing the factor $g_T = 1 + (T/(1 - T)) e^{-\tau/\tau_T}$, where T is the triplet fraction and τ_T is the triplet decay time. Importantly, when the triplet contribution to the autocorrelation function is not taken into account, the particle number N and diffusion time τ_D can be underestimated.

II.4.2.3 Confocal FCS on lipid membranes and membrane-bound DNA nanostructures

In this thesis, FCS has been used to study the diffusion of lipid and membrane bound DNA origami nanostructures (chapters III and V). Such measurements are typically performed on planar membranes by positioning the confocal volume such that the counts per particle (cpp) are maximized [Schwille et al., 1999]. The diffusion in the membrane is restricted to two dimensions and thus the autocorrelation function takes the form:

$$G_{2D}(\tau) = N^{-1} \left(1 + \frac{\tau}{\tau_D} \right)^{-1}. \quad (\text{II.21})$$

Additionally, the contribution of avalanche photodiode (APD) afterpulsing in confocal FCS is eliminated by a pseudo-crosscorrelation approach [Burstyn and Sengers, 1983]. In brief, the fluorescence signal is split by a 50:50 beamsplitter and directed onto two independent APDs.

The autocorrelation function II.21 decays slower than for 3D diffusion, due to its lower dimensionality and due to the higher membrane viscosity, when compared to aqueous media. Importantly, the positioning of the confocal volume is crucial when measuring confocal FCS on planar membranes, as defocusing results in larger membrane cross-sections, larger τ_D and N , as well as lower cpp [Przybylo et al., 2006].

When studying the diffusion of elongated DNA origami nanostructures on lipid membranes, one needs to take into account the individual contributions of translational and rotational diffusion. In order to eliminate potential complications in data interpretation, in this study the contribution from rotational diffusion was eliminated by placing the fluorophores close to the centre of the DNA structures [Czogalla et al., 2013, Czogalla et al., 2015b]. Additionally, the diffusion coefficient is expected to reduce upon crowding. Thus, all measurement in this thesis have been performed in the regime $\rho < 0.5$ in which the effect of crowding on the translational diffusion is expected to be below 10% [Czogalla et al., 2015b]. Here, the reduced surface density ρ is defined by $\rho = \sigma L^2$, where σ is the surface density of membrane-bound DNA nanostructures per μm^2 and L is the DNA nanostructure length.

II.4.3 Atomic Force Microscopy (AFM)

Atomic force microscopy AFM is a type of scanning probe microscopy (SPM) [Bhushan, 2017]. In SPMs, images describing the topography and/or mechanical, electrostatic, magnetic or optical properties of the sample are obtained by scanning the sample with a probe that interacts with the surface [Eaton and West, 2010]. The resolution of such methods is thus not limited by diffraction, like in conventional optical microscopy.

In AFM, the attractive and repulsive forces between the tip at the edge of a flexible cantilever and the sample surface are measured [Braga and Ricci, 2004, Eaton and West, 2010]. A small laser is focused on the back of the cantilever and is reflected onto a split photodiode detector (Figure II.4A). The position of the laser on the photodiode detector encodes the deflection of the cantilever when the tip interacts with the sample. This mechanism detects forces in the range between 10^{-7} to 10^{-12} N (e.g. [Müller and Anderson, 2002]).

AFM imaging can be performed under contact or tapping modes (Figure II.4B) [Bhushan, 2017, Braga and Ricci, 2004, Eaton and West, 2010]. In contact mode the interaction force is fixed to a certain set-point and maintained by a feedback loop. As a result, the tip-sample distance is constant. In tapping (or AC) mode, the cantilever oscillates and, instead of the deflection, the oscillation of the cantilever is measured. This oscillation is acoustically-driven close to the resonance frequency and the scanning forces can be much

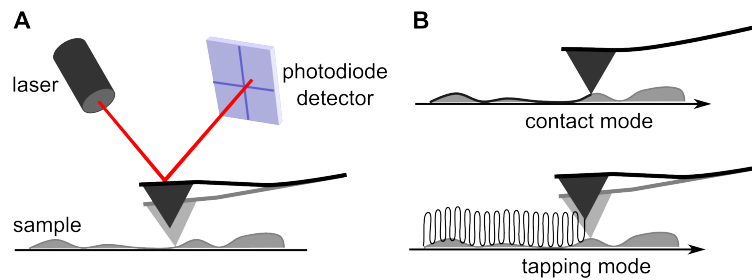


Figure II.4: Principles of AFM. A) A tip at the edge of a flexible cantilever scans the surface of the sample. A laser beam focused on the back of the cantilever, is reflected on a split photodiode. As a result, the deflection of the cantilever due to interactions with the surface is amplified and detected. B) Commonly used AFM operating modes: contact and tapping modes.

lower than in contact mode, since the proportion of the time where the tip and the sample are in contact is low [Santos and Castanho, 2004, Eaton and West, 2010].

In the last two decades, the temporal resolution of AFM has been greatly improved by several technological developments, such as improvement of the feedback loop, higher frequency of the z -scanner and significantly shorter and smaller cantilevers, with high resonant frequency and small force constant (κ_c) [Ando et al., 2001, Bozec et al., 2007, Viani et al., 2000]. Additionally, short cantilevers contributed to an increased detection sensitivity and reduced sample invasiveness [Ando et al., 2014, Stamov et al., 2015]. Indeed, with high speed atomic force microscopy (HSAFM), a range of dynamic processes in the second and even millisecond scale, previously inaccessible with traditional systems, can now be studied. In this thesis, HSAFM is used in tapping mode to study the self-organization of DNA origami nanostructures on SLBs (chapter IV).

Additionally to imaging, AFM also has a force spectroscopy mode, in which force curves between the tip and the sample can be acquired [Noy, 2007, Hinterdorfer and Dufrene, 2006, Puchner and Gaub, 2009]. Force curves are recorded by approaching and retracting the tip in a chosen location up to a full field of view, yielding in the latest case spatially-resolved maps of physical properties or molecular interactions.

II.4.4 Transmission electron microscopy (TEM)

Transmission electron microscopy (TEM) was developed in the 1930's with the intent to overcome the diffraction limited resolution of light microscopy [Williams and Carter, 1996, Gauvin, 1997]. In this method, a high energy electron beam is transmitted through a thin specimen slice to form an image. From the interaction of the electrons with the specimen, one can extract structural, phase, crystallographic and compositional information of materials, up to atomic scale. In this thesis, TEM has been used mainly as a characterization method to confirm the design and folding quality of the target DNA nanostructures, specially in the context of chapter V.2.

III

BINDING AND DIFFUSION OF MEMBRANE-BOUND DNA NANOSTRUCTURES

Binding of scaffolding proteins to cellular membranes is essential to their function of shaping lipid membranes. Particularly, proteins from the Bin/Amphiphysin/Rvs (BAR) domain family (see section II.1.3) bind to lipid membranes through hydrophobic and electrostatic interactions [Bhatia et al., 2010, Madsen et al., 2010, Qualmann et al., 2011]. In order to design a BAR-mimicking DNA-based scaffold for shaping lipid membranes, firstly we studied how to effectively bind bulky DNA origami nanostructures to lipid membranes. Targeting of DNA nanostructures to lipid membranes using anchors based on cholesterol modified with a tetra-ethylene glycol linker (chol-TEG) has been particularly popular as such modified oligonucleotides are commercially available and have been extensively characterized [Banchelli et al., 2008, Bunge et al., 2009, Banchelli et al., 2010]. Thus, in recent years amphipathic DNA origami nanostructures have been used to study several biophysical processes on lipid membranes, such as oligomerization or pore formation (see section II.2.4). However, to date a systematic approach to membrane binding of DNA origami nanostructures has been lacking, in terms of number and length of the chol-TEG anchors.

I approached this question with a series of two studies aiming to understand how the total hydrophobicity, steric hindrance and charge influence the binding and diffusion of cholesteryl-modified DNA nanostructures. For this purpose, I designed an elongated DNA origami structure with 15 addressable locations for modification with chol-TEG anchors. Their membrane binding and dynamics on giant unilamellar vesicles (GUVs) were studied by fluorescence microscopy and fluorescence correlation spectroscopy (FCS). Firstly, I unraveled the minimal steric requirements for binding of DNA nanostructures to lipid membranes (chapter III.1). I produced DNA nanostructures with directly incorporated single or multiple cholesteryl-modified oligonucleotides. My results show that the accessibility of the anchoring moieties within the bulky DNA origami plays a crucial role for its binding behaviour to membranes. Additionally, I confirmed that the use of multiple cholesteryl-anchors improves the membrane binding of the elongated DNA nanostructure

and slows down membrane diffusion. In the following study (chapter III.2), I demonstrated how the rational choice of the strategy for attachment of chol-TEG anchors can be used to control the binding and mobility of DNA nanostructures on membranes. Here, I explored single- and double-stranded DNA spacers between the chol-TEG anchors and the bulk DNA nanostructure to overcome local steric hindrances and thus, improve membrane binding. Moreover, my results show that the type of used DNA spacers has a pronounced effect on the diffusion of elongated DNA nanostructures on membranes and their response to charges in the environment.

Lastly, in the chapter III.3 we extended the study of membrane-bound macromolecules with FCS to lipid monolayers (II.1.4.2), a lipid model system with unique access to the quantitative variation of lipid packing. Although the application of FCS to study lipid diffusion on monolayers has been previously accomplished by others [Gudmand et al., 2009, Chwastek and Schwille, 2013], the extension to studying membrane proteins has so far been lacking. Here, we provided an attractive and useful solution for technical challenges of applying FCS to lipid monolayers, and demonstrated how this method can be used to quantitatively study various peripheral macromolecules on monolayers. We further determined the monolayer viscosity at different lipid densities and found that the monolayer assay is more distinctive with regard to differentiating the size of the diffusing particles than free-standing lipid membranes as GUV.

III.1 Effect of anchor positioning on binding and diffusion of elongated 3D DNA nanostructures on lipid membranes

The results discussed in this section have been published as:

*Khmelinskaia, A., Franquelim[§], H. G., Petrov, E. P., Schwille, P[§]. (2016) Effect of anchor positioning on binding and diffusion of elongated 3D DNA nanostructures on lipid membranes. *J. Phys. D Appl. Phys.*, 49: 194001. doi:10.1088/0022-3727/49/19/194001.*

[§] denotes co-corresponding authors. A reprint permission has been granted by the publisher.

The supplementary information can be found in Appendix B.

Effect of anchor positioning on binding and diffusion of elongated 3D DNA nanostructures on lipid membranes

Alena Khmelinskaia^{1,2}, Henri G Franquelim¹, Eugene P Petrov¹ and Petra Schwille¹

¹ Max Planck Institute of Biochemistry, Department of Cellular and Molecular Biophysics, Am Klopferspitz 18, 82152 Martinsried, Germany

² Graduate School of Quantitative Biosciences, Ludwig-Maximilians-University, Feodor-Lynen-Str. 25, 81337 Munich, Germany

E-mail: hgfranq@biochem.mpg.de and schwille@biochem.mpg.de

Received 8 January 2016, revised 4 March 2016

Accepted for publication 14 March 2016

Published 13 April 2016



Abstract

DNA origami is a state-of-the-art technology that enables the fabrication of nano-objects with defined shapes, to which functional moieties, such as lipophilic anchors, can be attached with a nanometre scale precision. Although binding of DNA origami to lipid membranes has been extensively demonstrated, the specific requirements necessary for membrane attachment are greatly overlooked. Here, we designed a set of amphipathic rectangular-shaped DNA origami structures with varying placement and number of chol-TEG anchors used for membrane attachment. Single- and multiple-cholesterol-modified origami nanostructures were produced and studied in terms of their membrane localization, density and dynamics. We show that the positioning of at least two chol-TEG moieties near the corners is essential to ensure efficient membrane binding of large DNA nanostructures. Quantitative fluorescence correlation spectroscopy data further confirm that increasing the number of corner-positioned chol-TEG anchors lowers the dynamics of flat DNA origami structures on freestanding membranes. Taken together, our approach provides the first evidence of the importance of the location in addition to the number of hydrophobic moieties when rationally designing minimal DNA nanostructures with controlled membrane binding.

Keywords: DNA origami, cholesterol-TEG anchor, lipid bilayers, membrane binding, translational diffusion

 Online supplementary data available from stacks.iop.org/JPhysD/49/194001/mmedia

(Some figures may appear in colour only in the online journal)

1. Introduction

The invention of the DNA origami methodology [1], which consists in the arrangement of long single-stranded nucleic acid molecules into nanometre-scale objects, led to a major breakthrough in the field of nanotechnology [2]. The establishment of DNA as building material for the construction of synthetic nanostructures with specific shape and function was a natural result of its exceptional properties: on the one hand, DNA helix hybridization is not only highly specific but also

directional, resulting in a well-defined and relatively stable secondary structure; on the other hand, the AGTC code is simpler when compared to the protein code, resulting in facilitated rational design procedures. In the DNA origami approach, a large number of short oligonucleotides (the so-called 'staples') bind to defined segments of a long single-stranded DNA 'scaffold' molecule in a sequence-specific manner [3]. Individual staple strands can hybridize with several scaffold-strand segments, constraining the latter to double-helical structures in 2D or 3D arrays [1, 2]. Importantly, individual staple strands with

III.1 Effect of anchor positioning on binding and diffusion of elongated 3D DNA nanostructures on lipid membranes

unique sequence and position in the DNA origami structure can be further chemically functionalized, allowing for positioning of a wide variety of functional moieties with a nanometre-scale precision within the DNA array [4]. DNA origami structures have been successfully functionalized to be used as an organizing material for metallic nanoparticles [5], as a template for protein assembly [6], as a calibration tool for super-resolution fluorescence microscopy [7], or as a platform for studies of chemical reactions at the single molecule level [8], to mention only a few. In principle, by modifying DNA nanostructures with site-specific functions, it is even conceivable to mimic complex bio-functionalities so far attributed to proteins [9].

DNA-based nanomaterials can be further used in biologically-relevant environments like lipid membranes [10] and such studies can be performed under controlled conditions using minimal lipid model systems [11, 12]. For this purpose, lipophilic moieties, such as alkyl chains [13], cholesterol [14–16], tocopherol [17], and porphyrins [18] have been previously covalently attached through a flexible linker to DNA molecules. Oligonucleotides bearing cholesterol anchors with a tetra-ethylene glycol linker (chol-TEG) have been particularly well characterized in terms of incorporation and influence on lipid membranes [15, 16, 19]; as a result, this moiety became the most popular anchor when coming to the specific targeting of DNA origami nanostructures to lipid membranes.

The first DNA origami nanostructures described to decorate membranes of various lipid compositions were simple stiff 3D nanorods in the form of six-helix bundles (6HB), functionalized with chol-TEG anchors on one facet and fluorescent labels on the opposite side [20]. These nanostructures showed a switchable liquid-ordered/liquid-disordered partitioning on phase-separated membranes, controlled by the presence of divalent ions. Furthermore, selective fluorescent labelling allowed one to study membrane dynamics of 6HB on freestanding lipid membranes by means of fluorescence correlation spectroscopy (FCS) and even to distinguish between translational and rotational diffusion. An extension of this study not only demonstrated a decrease in the mobility of membrane-bound 6HB with increasing the number of chol-TEG anchors, but also clearly indicated the onset of the isotropic-nematic transition upon an increase in the surface density of nanoneedles on the membrane, which results in the progressive 2D ordering of initially randomly oriented nanoparticles [21].

Alternative strategies have been developed recently to ensure controllable binding of cholesterol-modified DNA nanostructures to lipid membranes [22, 23], as well as to induce different degrees of membrane-assisted oligomerization of amphipathic DNA origami structures of different shapes [22, 24, 25]. For instance, it has been shown that the oligomerization of DNA origami nanostructures on the membrane can mimic the behaviour of membrane-sculpting proteins, inducing shape deformation and disruption of small vesicles [25] and even large-scale deformation of giant unilamellar vesicles (GUVs) [26]. DNA origami has also been used to extend the design of synthetic membrane nanochannels capable of conducting ion currents through lipid bilayers. In this context, the use of different numbers of chol-TEG

anchors has been shown to promote efficient membrane insertion of several types of DNA-based nanochannels, ranging from large hemolysin-inspired channels consisting of 54 parallel DNA helices [27] to small subnanometre-sized channels made of DNA tiles [28].

Although in all previously mentioned studies efficient membrane anchoring of DNA nanostructures has been achieved and important physical properties unravelled, to our knowledge, an extensive and systematic characterization of the membrane binding properties of cholesterol-anchored DNA nanostructures has not been carried out. By examining the binding of different origami structures with similar membrane contact area as described in the literature, we find that membrane attachment has been accomplished through various numbers of chol-TEG anchors, such as 4, 9 or even 47 (see references [22, 25, 26]). Such a simple comparison between origami structures highlights the lack of precise understanding of the minimal steric requirements for membrane attachment for such DNA-based nanostructures. To close this gap in understanding, we aimed to elucidate the effects of the number and positioning of cholesterol anchors in the attachment of a rectangular-shaped 3D DNA origami object to freestanding membranes. More precisely, we designed a 20-helix bundle DNA origami with three Atto488 dyes at the centre of the upper facet for fluorescence labelling and 15 distinct positions at the opposite facet for the attachment of chol-TEG anchors, which allowed us to vary the precise positions and numbers of membrane anchors (figures 1 and S1) (stacks.iop.org/JPhysD/49/194001/mmedia). Thus, single- and multiple-cholesterol-modified origami nanostructures have been produced, and their localization, membrane density and dynamics have been studied by fluorescence microscopy and FCS on GUVs. Our results show that the accessibility of the anchoring moieties within the bulky DNA origami plays a crucial role for its binding behaviour to membranes. Additionally, the influence of the number of cholesterol anchors on effective membrane binding of the elongated DNA nanostructure and its membrane diffusion is confirmed. We hereby propose a minimal set of factors to take into account when rationally designing membrane binding DNA origami nanostructures, more specifically in terms of the total DNA nanostructure hydrophobicity, as well as local steric hindrances and membrane accessibility of lipophilic moieties used for membrane anchoring.

2. Materials and methods

2.1. Design, folding and purification of the elongated DNA origami structures

The elongated DNA origami structure, consisting of a 20-helix bundle (figure 1) with hexagonal lattice based on the M13mp18 7429-nucleotide long scaffold plasmid (p7429), has been designed using CaDNAo [29] (figure S1). High purity salt free (HPSF) purified staple oligonucleotides needed for origami folding were purchased from Eurofins MWG Operon (Ebersberg, Germany), and single-stranded M13mp18 scaffold DNA was supplied by Bayou Biolabs (Metairie, LA, USA). The 5'-Atto488-functionalized oligonucleotides were

III. Binding and Diffusion of membrane-bound DNA nanostructures

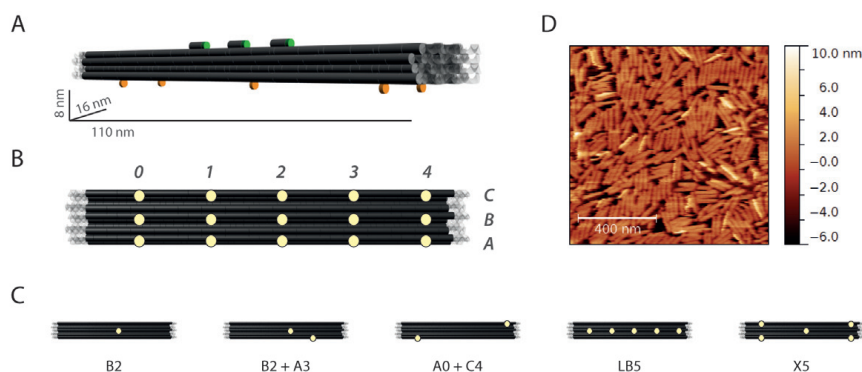


Figure 1. Structural characteristics of the elongated amphipathic 20-helix bundles. (A) 3D representation and predicted dimensions ($8\text{ nm} \times 16\text{ nm} \times 110\text{ nm}$) of the designed DNA origami nanostructures. The structures under investigation have three Atto488-modified oligonucleotides at the top facet for fluorescence detection and a maximum of five cholesterol anchors at the bottom facet for membrane-anchoring. (B) Localization of the 15 possible sites (marked with pale circles) for chol-TEG anchors insertion at the bottom facet of the elongated DNA origami. Five positions (numbered 0–4) were spaced along three different helices of the origami (named A–C). (C) Representative examples of some of the amphipathic DNA origami structures produced. Naming of the structures will correspond to the location of the chol-TEG anchors, except for LB5 (anchors at positions B0 + B1 + B2 + B3 + B4) and X5 (A0 + A4 + B2 + C0 + C4) (D) AFM image of the folded bare 20-helix bundle (structure N) deposited on mica. Experimentally measured dimensions of the nanostructures are in good agreement with predicted dimensions—see text.

acquired from Eurofins, while the 3'-chol-TEG functionalized and dual 5'-Cy5/3'-chol-TEG functionalized oligonucleotides (all HPLC-purified) were purchased from Sigma-Aldrich (Taufkirchen, Germany). All oligonucleotide staples were diluted in Milli-Q ultra pure water at concentration of $100\ \mu\text{M}$. The assembly of the origami structure was performed in a one-pot reaction mix. To this end, the components were mixed to the final concentrations of 20 nM p7429 scaffold plasmid and 200 nM staple oligonucleotides in a 5 mM Tris-HCl, 1 mM EDTA, 20 mM MgCl_2 , pH 8.0 buffer (folding buffer). Thermal annealing was performed over a 41 h cooling scheme on an Eppendorf Mastercycler Pro thermal cycler (Hamburg, Germany), from 65 to 40 °C [3]. The folded nanostructures were then purified from the excess of staple strands by centrifugation with Amicon Ultra 100 kDa MWCO filters (Merck Millipore, Darmstadt, Germany) using the buffer consisting of 5 mM Tris-HCl, 1 mM EDTA, 5 mM MgCl_2 , 300 mM NaCl, pH 8.0 (imaging buffer). The assembled origami structures were collected at the end of the fourth cycle of centrifugation (three cycles at a rate of 14000 g for 3 min, followed by one cycle at the same rate for 5 min) and stored at 4 °C. All produced DNA origami structures have three Atto488-labeled oligonucleotides attached to extended staples (16 nucleotide long) at positions close to the centre of the upper facet and contain none, single or multiple chol-TEG anchors at defined positions on the opposite facet (figures 1 and S1). The bulk concentration of the origami structures was estimated by fluorescence intensity using a one-drop measurement unit of a Jasco FP-8500 spectrofluorometer (Tokyo, Japan). To this end, undiluted samples of purified Atto488-labelled DNA origami were excited at 500 nm, and the respective emission intensities measured in the range of 510–620 nm. This value (corrected for the triple fluorescent labelling of the DNA origami structures) was compared to an intensity calibration curve obtained

for known Atto488 concentrations in the same imaging buffer using the same settings.

2.2. Atomic force microscopy (AFM) of the folded DNA origami

AFM was utilized in order to determine the structural properties and verify the correct assembly of the folded DNA origami nanostructures (figure 1(D)). To simplify the procedure and interpretation of results, here the topographical aspect of bare origami lacking cholesterol anchors (structure N) was assessed. To this end, 5 μl of the purified origami solution was mixed with 50 μl folding buffer (5 mM Tris-HCl, 1 mM EDTA, 20 mM MgCl_2 , pH 8.0), and deposited on top of a freshly cleaved mica sheet previously glued on top of a glass coverslip. Magnesium in the buffer solution is required to mediate adsorption of DNA origami to the mica surface. After 10 min incubation, most of DNA origami settled down and adsorbed on the surface, so that high-speed AFM imaging could be performed.

Measurements were performed on a JPK Nanowizard Ultra (Berlin, Germany) mounted on top of a Zeiss LSM 510 Meta microscope. High-speed imaging was done in the AC mode (also known as intermittent contact mode) using USC-F0.3-k0.3 ultra-short cantilevers (Nanoworld, Neuchâtel, Switzerland) with a typical stiffness of $0.3\ \text{N m}^{-1}$. The cantilever oscillation was turned to a frequency of 100–150 kHz and the amplitude kept below 10 nm. Scan rate was set to 5–10 Hz for imaging areas larger than $2\ \mu\text{m} \times 2\ \mu\text{m}$, while scanning rates of 10–25 Hz were used for smaller areas. The force applied on the sample was maintained at the lowest possible value by continuously adjusting the setpoint and gain during the imaging. Typically, setpoints close to 7–8 nm were utilized. Height, error, deflection and phase-shift signals were recorded

III.1 Effect of anchor positioning on binding and diffusion of elongated 3D DNA nanostructures on lipid membranes

and images were line-fitted as required. Analysis of the AFM images was performed using JPK SPM Data Processing (version 5.1.4) and Gwyddion (version 2.30). Average length of the DNA origami structures was estimated from topographical cross-sections along the long axis of individual structures.

2.3. Agarose gel electrophoresis analysis of DNA origami structures

The quality of folding of the DNA origami objects containing zero, one or multiple chol-TEG anchors was investigated through agarose gel electrophoresis (figure S2), as described elsewhere [3]. Briefly, the assembled DNA origami structures were loaded into 2% agarose gels containing $0.5 \times$ TBE buffer (40 mM Tris-Cl, 45 mM boric acid, 1 mM EDTA, pH 8.3) and 11 mM $MgCl_2$. The GeneRuler Express DNA ladder from ThermoFischer Scientifics was utilized. Electrophoresis was performed at 70V for approximately 4h, in an ice water bath. SYBR Safe for DNA staining (10 μ l of stock solution) was directly added to the gels prior electrophoresis. At the end of electrophoresis, gels were scanned using a Peqlab E-BOX VX2 Gel Documentation System (VWR International GmbH, Erlangen, Germany).

Fluorescence analysis of agarose gels was further used to verify the correct incorporation status of the chol-TEG anchors. For this specific experiment, instead of using DNA origami folded with simple 3'-chol-TEG modified staples, we folded DNA origami in which the chol-TEG staples had an extra Cy5-functionalization at their 5'-end. The newly assembled DNA origami objects with Cy5/chol-TEG anchors were loaded into a 2% agarose gel without SYBR Safe. The same electrophoresis procedure as above was then performed. Next, the gels were scanned with epi-illumination using Amersham 600 CCD Imager (GE Healthcare, Little Chalfont, UK) using a 460 nm or 630 nm LED light source for excitation of Atto488 or Cy5 fluorescence, respectively. After performing a background correction of the gel images, Atto488 and Cy5 fluorescence intensities within the bands of interest were integrated, and the normalized Cy5/Atto488 ratios were calculated (figure 2(C)). As all structures possess three Atto488 labels, this signal could be used as internal standard for fluorescence intensity normalization. In the end, the gel was incubated with SYBR Safe for two hours for DNA staining and imaged as described above.

2.4. Vesicle preparation and fluorescence imaging

GUVs composed of 1,2-dioleoyl-*sn*-glycero-3-phosphocholine (DOPC) (Avanti Polar Lipids, Alabaster, AL, USA), containing additional 0.005 mol% Atto655-DOPE (AttoTEC GmbH, Siegen, Germany) were produced by electroformation [30] in polytetrafluoroethylene chambers with Pt electrodes 4 nm apart as described previously [31]. Briefly, 6 μ l of the lipid mixture (2 mg ml^{-1} in chloroform) was spread onto two Pt wires and dried in a desiccator for 30 min. The chamber was then filled with 350 μ l of a 610 mOsm kg^{-1} aqueous solution of sucrose. An AC electric field of 2 V (RMS) was applied at a frequency of 10 Hz for 1.5h, followed by 2 Hz for 0.75h. Experiments

were carried out in 40 μ l MatriCal 384-multiwell plates with #1.5 glass bottom thickness (Brooks Life Science Systems, Spokane, WA, USA). Freshly plasma cleaned wells (10 min) were passivated with PLL(20)-g[3.5]-PEG(2) (SuSoS AG, Dübendorf, Switzerland) by incubation with a 0.5 mg ml^{-1} solution in PBS buffer for at least half an hour and consequently thoroughly washed with water and imaging buffer. 3 μ l of the GUV suspension (diluted 1:50 in 610 mOsm kg^{-1} sucrose solution from the original suspension in the electroformation chamber) were mixed with a 18 μ l DNA origami solution (0.1–5 nM total concentration) diluted in imaging buffer (iso-osmolar), and samples were incubated at 4 °C overnight. Before measurement, the samples were equilibrated at the microscope objective ($T = 27.5 \pm 1.0$ °C) for at least 30 min.

Confocal imaging was performed on a commercial laser scanning microscope LSM 780 with a ConfoCor3 unit (Zeiss, Jena, Germany) using a water immersion objective (C-Apochromat, $40 \times /1.2$ W UV-VIS-IR, Zeiss, Jena, Germany). Samples were excited with the 488 nm line of an Ar-ion-laser or with the 633 nm line of a He-Ne laser (for Atto488 and Atto655 excitation, respectively). To avoid the effect of polarization selection in excitation of the GUVs, an achromatic $\lambda/4$ plate (Edmund Optics, Barrington, NJ, USA) was installed in the excitation beam path. Images were recorded at the equatorial planes of GUVs, utilizing a 1 Airy unit pinhole, 512×512 pixel resolution and a scan rate of 3.15 μ s per pixel. In order to compare membrane affinities of different nanostructures, fluorescence intensities of membrane-bound DNA origami at a bulk concentration of 1 nM were determined using a semi-automated Matlab-based software [32]. Further image analysis was performed using the ImageJ software (<http://rsb.info.nih.gov/ij/>).

2.5. FCS

For FCS, the previously described confocal imaging setup was used. The laser lines with wavelength of 488 nm and 633 nm (for Atto488 and Atto655-DOPE excitation, correspondingly) were used at low laser power (1.2 μ W) to avoid photobleaching and fluorescence saturation effects [33]. The normalized pinhole size was kept at 1 Airy unit, which corresponds to the pinhole settings of 34 μ m for 488 and 45 μ m for 633 nm. The pinhole position and the correction collar were adjusted to maximize the detected fluorescence signal and the photon count rate per molecule, respectively. The lateral size of the FCS detection volume r_0 (207 ± 7 and 264 ± 6 nm for the green and red detection channels, respectively) was determined using fluorescent dyes with known diffusion coefficients in water: D (Alexa488) = $414 \mu m^2 s^{-1}$ at 25.0 ± 0.5 °C [34] and D (Atto655) = $426 \mu m^2 s^{-1}$ at 25 °C [35], as previously described [20]. The diffusion coefficients of the calibration dyes have been corrected for the working temperature at the objective (27.5 ± 1.0 °C) [33, 36, 37]. In order to eliminate the distorting effect of detector afterpulsing, in all experiments the fluorescent signal was split in two equivalent channels and the output of the two detectors was cross-correlated [33]. For data analysis, the average of the two resulting correlation functions (ACF) was considered.

FCS on membranes was performed at the upper pole of a GUV with a diameter of at least 20 μm (which is large enough to neglect membrane curvature within the FCS detection spot size). During acquisition of FCS data (minimum 15 runs, 15 s each for the green channel and minimum 3 runs, 30–60 s each for the red channel), the fluorescence count rate was monitored online, ensuring that no fluorescence fluctuations originated from the movements of the whole membrane or the presence of large aggregates on the membrane. In case such events were observed, the corresponding datasets were disregarded. Additionally, correct positioning of the confocal detection volume was checked after each set of three measurements.

Particle numbers (and consequently, surface densities) and translational diffusion coefficient (D) of the elongated 3D DNA nanostructures, as well as the diffusion coefficient of Atto655-DOPE on freestanding membranes were obtained from the analysis of the ACF using the freely available data analysis software PyCorrFit version 0.9.7 [38]. As virtually no unbound DNA origami was detected in solution, and its potential contribution to FCS curves was negligible (data not shown), a one-component 2D diffusion model [31, 33] was used to analyse the experimental results, as it was done in previous experiments with membrane-bound DNA origami particles [20, 21]:

$$G(\tau) = \frac{1}{N} \frac{1}{1 + \tau/\tau_D} \quad (1)$$

Here N is the number of particles in the 2D detection volume, and τ_D is the FCS diffusion time, which is determined by the translational diffusion coefficient D and the size of the 2D Gaussian detection volume r_0 as follows: $\tau_D = r_0^2/(4D)$. The relatively slow diffusion of membrane-bound DNA origami ($\tau_D \sim 3$ ms) allowed us to use equation (1) directly in the data analysis without including a triplet blinking component for the correlation times longer than 50 μs . To ensure proper determination of the concentration of membrane-bound DNA origami particles, amplitudes of autocorrelation functions were corrected for the presence of a noncorrelated background signal. As the origami length is known, $L = 110$ nm, the surface density of membrane-bound origami particles, $\sigma = N/(\pi r_0^2)$, expressed in particles per μm^2 , could be easily converted to the reduced surface density $\rho = \sigma L^2$ [21].

The Atto655 fluorophore is characterized by a negligible triplet state contribution [39]. We indeed found this to be the case for the fluorescently labelled lipid Atto655-DOPE in GUVs, and the same model (equation (1)) was used to analyse FCS results for translational diffusion of this fluorescently labelled lipid.

3. Results

3.1. Design and production of amphipathic elongated 3D DNA origami objects

The dimensions of the 20-helix bundle DNA origami structure here produced are approximately 110 nm (length) \times 16 nm (width) \times 8 nm (height) (figure 1(A)). 15 distinct positions,

equally oriented in the direction of the membrane, were implemented on the bottom facet for placing chol-TEG anchors (figure 1(B)). More specifically, five cholesterol anchoring sites (numbered 0–4) were spaced 21.4 nm apart along three defined bottom helices (named A–C). This strategy allowed us to produce nanostructures differing only in the number and membrane accessibility of the hydrophobic moieties, by simply substituting the respective staple sequences at defined position with their chol-TEG modified counterparts. To illustrate the naming convention, a chol-TEG anchor at position B2 is localized at the centre of the bottom facet of the origami structure, while position C4 refers to the location in the vicinity of one of the corners (for more examples, see figure 1(C)). Agarose gel analysis of the folded DNA origami after purification (figure S2) showed that all studied structures are able to assemble at high yield (fast running band corresponds to monomeric and correctly folded form of the object), although several structures with single (C3 and C4) or double chol-TEG (e.g. B2 + B4) anchors may form additional high-order aggregates (visible bands retained in wells). Note that no purification attempt to get rid of those aggregates was performed. Correct assembly of the structure was further confirmed by AFM imaging of the bare 20-helix bundle (structure N) deposited on mica (figure 1(D)). Experimentally measured dimensions of individual 43 structures ($L = 114 \pm 7$ nm; $h = 7\text{--}8$ nm) are in good agreement with the 20-helix bundle design prediction.

Correct incorporation of the chol-TEG modified oligonucleotides was also assessed for some of the assembled structures using fluorescence analysis in agarose gels (figure 2). For this special purpose, chol-TEG oligonucleotides labelled with an additional Cy5 dye were utilized during DNA origami assembly. Structures with double chol-TEG at the corner locations, with multiple chol-TEG at the helix B or positioned in an X-shape, as well as their counterparts bearing single chol-TEG anchors, were loaded into agarose gels for electrophoresis (figures 2(A) and (B), respectively). Quantitative analysis of the DNA origami gel bands (in terms of the normalized Cy5 fluorescence intensity) shows that the incorporation of individual chol-TEG modified oligonucleotides does not depend on the position of the staple within the structure (figure 2(C)). Note that all sequences in question are 21 nucleotide-long (figure S1), with T_m values between 48.1 $^\circ\text{C}$ and 66.4 $^\circ\text{C}$, which ensures a stable hybridization with the scaffold strand. Further analysis of the Cy5 fluorescence signals also confirms the predicted number of anchors for each object, as the intensities show a linear increase with the number of chol-TEG anchors.

3.2. Influence of number and positioning of chol-TEG anchors on the binding of an elongated 3D DNA origami to free standing lipid bilayers

In order to determine the minimal anchor number and accessibility requirements for efficient membrane attachment, binding to DOPC GUVs of the elongated DNA origami structures with various combinations of number and position of chol-TEG anchors was investigated by confocal fluorescence microscopy and the average fluorescence intensities of each nanostructure evaluated at the membrane surface.

III.1 Effect of anchor positioning on binding and diffusion of elongated 3D DNA nanostructures on lipid membranes

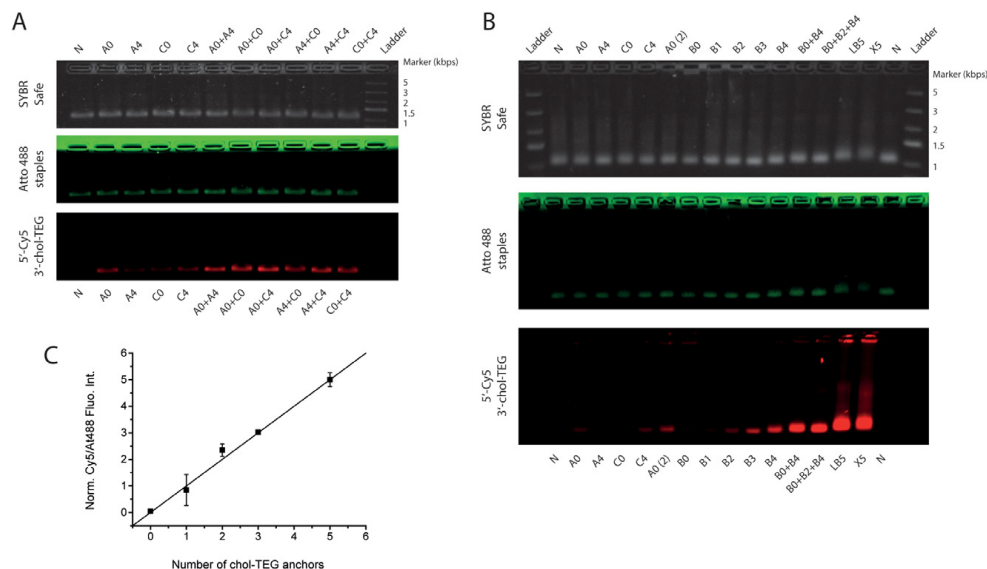


Figure 2. Incorporation of chol-TEG anchors within the 20-helix bundle DNA origami assessed via dual-colour fluorescence agarose gel analysis. Here, 2 nM of DNA origami with single or multiple chol-TEG anchor staples modified with a Cy5 dye at 5' end were analysed. This allowed not only to assess fluorescence from the three Atto488 dyes present on each origami, but also to follow the presence and number of chol-TEG anchors via the Cy5 signal. Gels were exposed to 460 nm and 630 nm LEDs, and Atto488 and Cy5 fluorescence was recovered. Different lanes in gels ((A)–(B)) correspond to the origami structures with chol-TEG anchors at defined positions. Lanes containing marker DNA ladder (Ladder) and DNA origami with no chol-TEG anchors (N) were also included. Overall, while Atto488 signal was constant along the different lanes, Cy5 fluorescence varied as a function of the number of chol-TEG anchors present in the structures. Gels were stained *a posteriori* with SYBR Safe for identification of the marker DNA bands and confirmation of the proper DNA origami folding. Special nomenclature: N (no anchors); LB5 (B0 + B1 + B2 + B3 + B4); X5 (A0 + A4 + B2 + C0 + C4). Numbers in brackets correspond to repeated samples. (C) Normalized Cy5/Atto488 recovered fluorescence intensities were plotted as a function of the chol-TEG anchor number. Linear increase of the fluorescence intensity as a function of anchor number is emphasized by adding the line $y = x$.

The bare elongated DNA origami structure lacking chol-TEG anchors (denoted as N) was by itself not capable of attaching to membranes (figure S6). Having performed this control, we assessed the membrane interaction capability of the DNA origami nanostructures with one chol-TEG anchor (figure S3). Considering our origami design, an optimized coverage of the most significant chol-TEG localizations was achieved by choosing 9 positions (figure 1), i.e. three different localizations (pos. 2–4) on each functionalisable helix A–C starting from the centre (pos. 2) to the most accessible end (pos. 4). No clear co-localization of these single-anchored DNA origami structures with the membrane was detected on the fluorescence images, suggesting that generally incorporation of a single chol-TEG modification does not drive binding of a large DNA-origami object into lipid bilayers (figures 3 and S3). Note that for the origami with a chol-TEG anchor at position C4 (the most accessible corner), an apparent weak increase of its mean fluorescence intensity at the membrane surface was retrieved (figure 3(B)), which could be explained by the increased accessibility of the anchor.

Next, the number of anchors in the structures was increased to a total of two. Using once again positions 2–4 at the helices

A–C, we produced a set of flat DNA origami structures containing two chol-TEG modifications, with one of the anchors always fixed at the central B2 position (figure S4). Previous studies have shown that two cholesterol anchors are sufficient for the attachment of different DNA origami structures to lipid membranes [21, 27]. We, however, observe that double-anchor positioning with a fixed central chol-TEG anchor on the lower facet of the object did not improve significantly the attachment of the rectangular-shaped DNA origami, as seen in figure 3(B). Note that the structures with a variable chol-TEG anchor on helix C (especially structures B2 + C2 and B2 + C4) seem to have increased fluorescence intensity at the membrane surface (figures 3(B) and S4). Helix C, due to its location at the end of the origami (figure S1), is intrinsically more flexible than helix A, which may explain this behaviour.

In order to further explore other possible double-anchor localizations, we produced a set of DNA origami structures bearing two chol-TEG anchors positioned near the corners of the lower facet (i.e. positions A0, A4, C0 and C4) (figure S5), as those would be the positions within our design with highest membrane accessibility. Interestingly, all the structures containing these anchoring combinations (with the exception of

III. Binding and Diffusion of membrane-bound DNA nanostructures

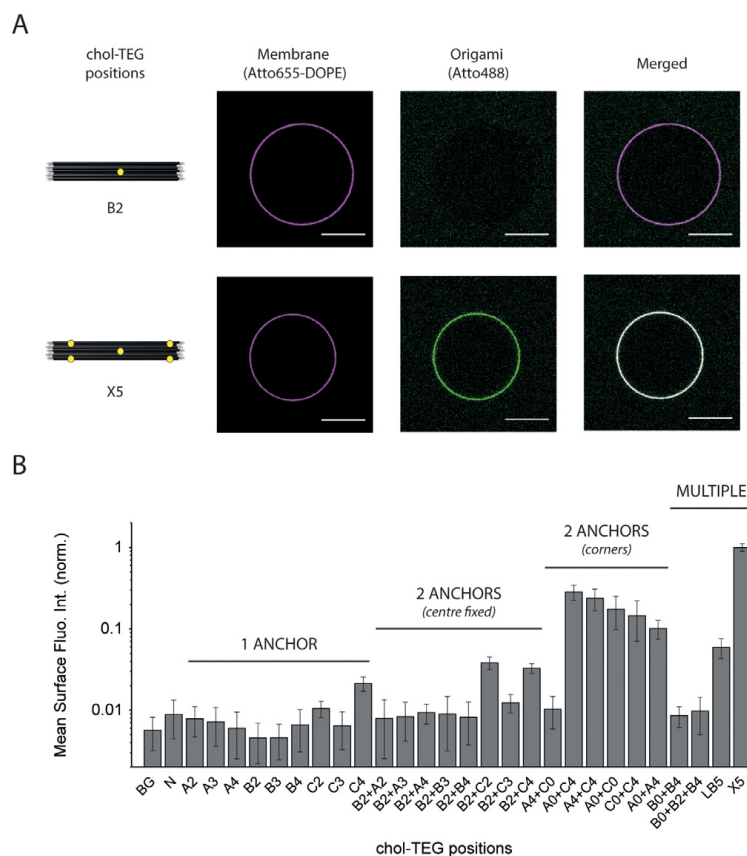


Figure 3. Membrane binding of the 20-helix bundle DNA origami as a function of the position and number of chol-TEG anchors. (A) Fluorescence confocal images of DOPC GUVs at the equatorial plane incubated with 1 nM DNA origami containing: (upper panel) one chol-TEG anchor at the central position B2 and (bottom panel) five chol-TEG anchors in a crossed orientation (A0, A4, B2, C0, C4, denoted as X5). GUVs contained 0.005 mol% Atto655-DOPE (violet colour) for fluorescence detection; while each origami structure had $3 \times$ Atto488 dyes (green colour). Merged images are further presented. Scale bar: $20 \mu\text{m}$. (B) Quantitative analysis of the mean fluorescence intensities at the membrane surface for all chol-TEG combinations utilized on the 20-helix bundle DNA origami. Structures with significantly increased membrane binding were A0 + C4, A4 + C4, A0 + C0, C0 + C4, A0 + A4, LB5 and X5. Note that the intensity axis in the plot is in logarithmic scale and that the mean intensities were normalized in relation to X5. Illustrative confocal images of GUVs incubated with DNA origami at all chol-TEG anchor combinations can be found in figures S3–S6. Special nomenclature: BG (background fluorescence); N (no anchors); LB5 (B0 + B1 + B2 + B3 + B4); X5 (A0 + A4 + B2 + C0 + C4).

the one having the anchors positioned at A4 + C0) showed strong membrane binding (figure S5), resulting in a significantly higher mean surface fluorescence intensity of DNA origami on top of the membrane when compared to the background signal (figure 3(B)). These results confirm that the incorporation of two cholesteryl anchors is generally enough for membrane attachment of large DNA origami structures; the binding efficiency, however, depends on the positioning and accessibility of the chol-TEG anchors within the membrane-facing side of the nanostructures.

Next, as two cholesteryl anchors near the ends of helix A (A0 + A4) and helix C (C0 + C4) enabled attachment of the nanostructures to lipid membranes, we investigated

if similar binding could be accomplished by incorporating cholesteryl anchors in the less accessible central helix B instead. For that reason, structures with two (B0 + B4), three (B0 + B2 + B4) and five (B1 + B2 + B3 + B4 + B5, referred to as LB5) chol-TEG anchors were chosen (figure S6). Surprisingly, significant membrane attachment was only possible when five anchors were positioned at helix B, yet the resulting fluorescence intensity at the membrane (figure 3(B)) was at least twofold lower when compared to the values obtained for the structures having two anchors near the ends of helix A or C (figures 3(B) and S5). Moreover, by analysing the membrane attachment behaviour of a structure designed to have five chol-TEG anchors positioned in an X-shape

III.1 Effect of anchor positioning on binding and diffusion of elongated 3D DNA nanostructures on lipid membranes

fashion (A0 + A4 + B2 + C0 + C4 referred to as X5) (figures 3(A) and S6) in comparison to the structures with two anchors near the corners (figure S5), we obtained a fourfold increase in origami fluorescence intensity at the membrane; in comparison to the LB5 structure, this increase is 17-fold (figure 3(B)). Importantly, note that the reported differences in membrane binding as a function of the chol-TEG positions are not caused by variations in the incorporation levels of individual cholesteryl-modified oligonucleotides during folding (figure 2).

To summarize, the comparison of all the studied 20-helix bundles with different combinations of chol-TEG anchors reveals that not only the number but also importantly the positioning (and hence accessibility) of the hydrophobic moieties to the membrane strongly influences the binding behaviour of large 3D DNA origami structures to lipid membranes.

3.3. Influence of number and positioning of chol-TEG anchors on the diffusion of an elongated 3D DNA origami on freestanding lipid bilayers

After determining that accessibility of the hydrophobic modifications influences the attachment of a DNA origami object to freestanding lipid bilayers (figure 3), we chose a set of structures with known numbers and positioning of cholesteryl anchors to assess the influence of these parameters on the dynamic behaviour of membrane-bound origami. The use of Atto488-modified staples around the centre of our elongated objects allows us to follow translational diffusion by FCS and eliminates potential complications in interpretation of the results due to rotational diffusion [20, 21]. The translational diffusion coefficients at the membrane surface were determined for four elongated DNA origami structures with different combinations of two (A0 + C4, A4 + C4 and C0 + C4) anchors and with five (X5) anchors, at a broad range of total concentrations (0.1 to 5nM).

At low surface densities of membrane-bound DNA origami ($\rho < 0.2$, dilute regime), FCS autocorrelation functions could be very well described by the 2D diffusion model (equation (1)) describing the translational Brownian motion of the Atto488-labeled DNA origami particles bound to the lipid membrane, which is exemplified by figure 4. At higher surface densities of membrane-bound origami particles, where crowding effects become important, an increase in the particle density lead to progressively stronger deviations from the simple diffusion model (data not shown). In this concentration regime, if all particles are fluorescently labelled (which is the case with our experiments), FCS autocorrelation functions reflect the collective (mutual) diffusion or membrane-bound particles, rather than their self-diffusion [21].

The diffusion coefficients of membrane-bound DNA origami structures in the dilute regime ($\rho < 0.2$) estimated from FCS measurements ($\sim 4 \mu\text{m}^2 \text{s}^{-1}$) are in good agreement with those reported previously for DNA nanoneedles [20, 21] and monoliths [26] on freestanding membranes. In our experiments GUVs were filled with 610 mOsm kg^{-1} solution of sucrose, whose refractive index is higher than that of water. As a result, we expect that the diffusion coefficients

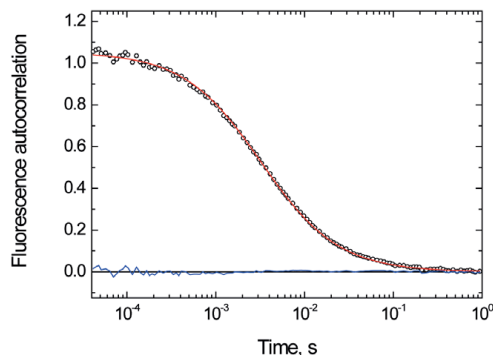


Figure 4. Diffusion of membrane-bound elongated DNA origami 20-helix bundle as detected by FCS. Representative FCS autocorrelation curve (symbols) for the membrane-bound X5 DNA origami structure, respective fit and residuals using the model described in the text are presented. Reduced surface density of DNA origami was $\rho = 0.09$, which corresponds to a dilute density regime at the membrane surface.

Table 1. Diffusion times of DNA origami with two or five chol-TEG anchors on freestanding DOPC membranes determined using FCS.

Membrane-bound origami	Diffusion time (ms)	Number of GUVs
A0 + C4	2.84 ± 0.08	15
A4 + C4	2.80 ± 0.11	11
C0 + C4	2.74 ± 0.08	17
X5	3.09 ± 0.08	22

Note: Values correspond to the average diffusion times determined for n number of GUVs at reduced surface densities $\rho < 0.2$ of membrane-bound DNA origami. Error values represent the standard error of the mean.

of membrane-bound origami structures obtained under these conditions are all underestimated by the same factor [33]. Therefore, we prefer to report the diffusion times directly measured in the FCS experiments (table 1) and present relative diffusion coefficients with respect to that of the A4 + C4 structure (figure 5). We find that, while DNA origami structures with two chol-TEG anchors positioned at the corners are characterized by very close diffusion coefficients, the X5 structure with five anchors making an X-cross pattern exhibits a 10% lower lateral mobility.

The membrane-bound origami structures do not perturb membrane properties even at high surface densities, as can be judged by the diffusion coefficient of the fluorescently labelled lipid (Atto655-DOPE) in the GUVs in presence of DNA origami. Indeed, the lipid diffusion coefficient in presence of the origami structures is within the experimental errors the same as the one measured on naked vesicles (table S1), which confirms previous experimental observations [20].

In summary, we confirmed that the number of hydrophobic anchors influences the translational diffusion of DNA origami objects on membranes, but no strong influence of anchor positioning is so far observed. Further comparative studies will be needed to clearly assess this effect.

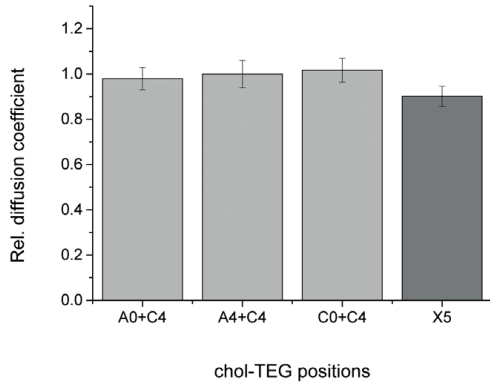


Figure 5. Relative translational diffusion coefficients of chol-TEG modified DNA origami structures on freestanding lipid bilayers. Diffusion coefficients were obtained from experimental FCS curves measured in the dilute regime (reduced surface densities of membrane-bound origami $\rho < 0.2$) and normalized with respect to that of the A4 + C4 structure.

4. Discussion

In this work we proposed to elucidate the effect of the number and positioning of cholesterol anchors on binding of an elongated DNA origami construct to freestanding lipid bilayers. By investigating nanostructures bearing one and different combinations of two, three or five chol-TEG anchors, we show that in general two anchors are necessary for efficiently binding DNA origami objects to lipid bilayers (figures 3 and S3–S6), as it had been suggested by previous studies [21, 27]. Moreover, incorporation of five chol-TEG moieties across the membrane-facing surface of the DNA origami object (i.e. X5 structure) leads to a four-fold increase in its binding ability to the GU surface, when compared to structures containing only two anchors near the corners (figures 3(B) and S5–S6). A similar dependency on the number of hydrophobic moieties was previously suggested to explain the incorporation of a DNA origami nanochannel into small unilamellar vesicles (SUVs) [27]. There, an increase from 20% to 40% of the number of SUVs with at least one incorporated nanochannel was achieved by increasing the number of chol-TEG modifications from 2 to 11, and an almost 80% incorporation efficiency was achieved with 26 anchors.

Remarkably, our results further reveal that the number of anchors alone is not enough to ensure efficient membrane binding. For example, structures containing combinations of two chol-TEG anchors, with one anchor fixed in the middle B2 position and the position of the second one varies (figure S4), do not significantly bind to the membrane surface. In contrast, all structures with two anchors near the corners (figure S5) display enhanced membrane attachment. Surprisingly, the exception is the A4 + C0 structure that presents a lack of membrane binding worth of future investigation. Furthermore, note that the corresponding chol-TEG positioning near the ends of the least accessible central helix B (i.e. B0 + B4)

was not enough for binding of the DNA origami to the GU membrane (figure S6). Even more striking is the difference between two DNA objects bearing five anchors positioned in a line (LB5) or making a cross (X5) (figures 3(B) and S6), where an almost 17-fold increase in membrane localization is accomplished by just changing the positioning of the anchors from LB5 to X5.

Altogether, these results strongly suggest that the anchor positioning within the bulky DNA origami object plays an important role in membrane binding, as the accessibility of the anchors to the membrane is conditioned by steric hindrances arising from the origami bulkiness and not just from the distance between the anchors. More specifically, the choice of corner positions with higher membrane accessibility is favourable for the DNA object attachment to lipid bilayers, which can then be further improved by increasing the number of membrane anchors. Note that in the previously described DNA nanoneedle design with two chol-TEG anchors [21] the locations chosen for anchor positioning were close to the ends of the structure. For the nanochannel with two cholesterol anchors [27], although the anchors are located in the centre of the membrane-facing surface, their distance to the edges of the structure is below 10 nm, in close agreement with the distances described for the corner positions of our structure (figure 1).

In order to determine if the number and positioning of anchors play a role in the membrane dynamics of the rectangular-shaped DNA origami structure, translational diffusion for three nanostructures with double anchor positioning at the corners (A0 + C4, A4 + C4 and C0 + C4) and the X5 nanostructure with five anchors was studied by FCS. Previous FCS studies on DNA nanoneedles [21] and particle tracking experiments on DNA origami blocks [25] showed that increasing the number of hydrophobic moieties (by a factor of four and two, respectively) slows down diffusion of the membrane-bound DNA objects. Our data confirm this trend, as the X5 structure, origami with best membrane binding efficiency, shows the slowest translational diffusion coefficient (reduction of approximately 10% when compared with the double anchored structures) (figure 5). No significant differences in diffusion coefficients were observed for the double-anchored structures—similar to what was found for their binding efficiencies. Regarding the structures with five anchors, on the other hand, as LB5 and X5 showed a strikingly different behaviour in terms of membrane binding (figures 3(B) and S6), it would be of great interest to further compare their membrane dynamics. Nevertheless, in order to do so, a tighter control of the experimental conditions would be needed.

Taken together, our findings provide a rational basis for interpretation of previously described membrane-attaching origami structures and for the prediction of membrane binding efficiencies in future designs. Further investigation of structures with different aspect ratios and protruding chol-TEG anchors may help corroborate the effect of steric hindrance described here and, in this way, contribute to the understanding of the minimal requirements necessary for the attachment of DNA origami objects to lipid membranes.

III.1 Effect of anchor positioning on binding and diffusion of elongated 3D DNA nanostructures on lipid membranes

5. Conclusions

In summary, the study of simple elongated DNA origami structures differing only in the number and positioning of chol-TEG anchors enabled us to decipher the role of hydrophobicity (number of anchors) and, for the first time, membrane accessibility (position of anchors) on the attachment and diffusive behaviour of a DNA origami structure to lipid membranes. Taken together, our results show that a strong and efficient binding of DNA origami objects to lipid bilayers requires at least two chol-TEG anchors positioned near the structure corners. Furthermore, increasing the number of highly accessible anchors enhances the DNA structure localization at the membrane. This work evidences the importance of the position-dependent steric hindrances within a 3D DNA object. Ultimately, this provides a rational basis for the design of efficient amphipathic DNA origami nanostructures, more specifically in terms of number and localization of the hydrophobic moieties. As the interaction of cholesterol moiety with membranes relies on nonspecific hydrophobic interactions, it is reasonable to speculate that the results obtained for chol-TEG anchors can be extended to other types of anchoring moiety employing the same binding mechanism.

Acknowledgments

This work has been supported by the collaborative research project SFB863 of the German Research Foundation (DFG). A K acknowledges the support of the Graduate School of Quantitative Biosciences Munich; H G F acknowledges the receipt of a Humboldt Research Fellowship. Further support was given by the Max Planck Society to P S. The authors specially thank Jonas Mücksch and members of the Munich DNA Node for fruitful discussions and expert advice.

References

- [1] Rothmund P W 2006 Folding DNA to create nanoscale shapes and patterns *Nature* **440** 297–302
- [2] Douglas S M, Dietz H, Liedl T, Högberg B, Graf F and Shih W M 2009 Self-assembly of DNA into nanoscale three-dimensional shapes *Nature* **459** 414–8
- [3] Castro C E, Kilchherr F, Kim D N, Shiao E L, Wauer T, Wortmann P, Bathe M and Dietz H 2011 A primer to scaffolded DNA origami *Nat. Methods* **8** 221–9
- [4] Simmel F C 2012 DNA-based assembly lines and nanofactories *Curr. Opin. Biotechnol.* **23** 516–21
- [5] Sharma J, Chhabra R, Andersen C S, Gothelf K V, Yan H and Liu Y 2008 Toward reliable gold nanoparticle patterning on self-assembled DNA nanoscaffold *J. Am. Chem. Soc.* **130** 7820–1
- [6] Kuzyk A, Laitinen K T and Törmä P 2009 DNA origami as a nanoscale template for protein assembly *Nanotechnology* **20** 235305
- [7] Steinhauer C, Jungmann R, Sobey T L, Simmel F C and Tinnefeld P 2009 DNA origami as a nanoscopic ruler for super-resolution microscopy *Angew. Chem., Int. Ed. Engl.* **48** 8870–3
- [8] Voigt N V, Tørring T, Rotaru A, Jacobsen M F, Ravnsbæk J B, Subramani R, Mamdouh W, Kjems J, Mokhir A, Besenbacher F and Gothelf K V 2010 Single-molecule chemical reactions on DNA origami *Nat. Nanotechnol.* **5** 200–3
- [9] Suzuki Y, Endo M and Sugiyama H 2015 Mimicking membrane-related biological events by DNA origami nanotechnology *ACS Nano* **9** 3418–20
- [10] Langecker M, Arnaut V, List J and Simmel F C 2014 DNA nanostructures interacting with lipid bilayer membranes *Acc. Chem. Res.* **47** 1807–15
- [11] Arumugam S, Chwastek G and Schwille P 2011 Protein-membrane interactions: the virtue of minimal systems in systems biology *Wiley Interdiscip. Rev.: Syst. Biol. Med.* **3** 269–80
- [12] Khan M S, Dosoky N S and Williams J D 2013 Engineering lipid bilayer membranes for protein studies *Int. J. Mol. Sci.* **14** 21561–97
- [13] Chan Y H, van Lengerich B and Boxer S G 2009 Effects of linker sequences on vesicle fusion mediated by lipid-anchored DNA oligonucleotides *Proc. Natl Acad. Sci. USA* **106** 979–84
- [14] Pfeiffer I and Höök F 2004 Bivalent cholesterol-based coupling of oligonucleotides to lipid membrane assemblies *J. Am. Chem. Soc.* **126** 10224–5
- [15] Banchelli M, Gambinossi F, Durand A, Caminati G, Brown T, Berti D and Baglioni P 2010 Modulation of density and orientation of amphiphilic DNA on phospholipid membranes. II. Vesicles *J. Phys. Chem. B* **114** 7348–58
- [16] Bunge A, Loew M, Pescador P, Arbuzova A, Brodersen N, Kang J, Dähne L, Liebscher J, Herrmann A, Stengel G and Huster D 2009 Lipid membranes carrying lipophilic cholesterol-based oligonucleotides—characterization and application on layer-by-layer coated particles *J. Phys. Chem. B* **113** 16425–34
- [17] Bunge A, Kurz A, Windeck A K, Korte T, Flasche W, Liebscher J, Herrmann A and Huster D 2007 Lipophilic oligonucleotides spontaneously insert into lipid membranes, bind complementary DNA strands, and sequester into lipid-disordered domains *Langmuir* **23** 4455–64
- [18] Börjesson K, Lundberg E P, Woller J G, Nordén B and Albinsson B 2011 Soft-surface DNA nanotechnology: DNA constructs anchored and aligned to lipid membrane *Angew. Chem., Int. Ed. Engl.* **50** 8312–5
- [19] Banchelli M, Betti F, Berti D, Caminati G, Bombelli F B, Brown T, Wilhelmsson L M, Nordén B and Baglioni P 2008 Phospholipid membranes decorated by cholesterol-based oligonucleotides as soft hybrid nanostructures *J. Phys. Chem. B* **112** 10942–52
- [20] Czogalla A, Petrov E P, Kauert D J, Uzunova V, Zhang Y, Seidel R and Schwille P 2013 Switchable domain partitioning and diffusion of DNA origami rods on membranes *Faraday Discuss.* **161** 31–43 discussion 113–50
- [21] Czogalla A, Kauert D J, Seidel R, Schwille P and Petrov E P 2015 DNA origami nanoneedles on freestanding lipid membranes as a tool to observe isotropic–nematic transition in two dimensions *Nano Lett.* **15** 649–55
- [22] Johnson-Buck A, Jiang S, Yan H and Walter N G 2014 DNA-cholesterol barges as programmable membrane-exploring agents *ACS Nano* **8** 5641–9
- [23] List J, Weber M and Simmel F C 2014 Hydrophobic actuation of a DNA origami bilayer structure *Angew. Chem., Int. Ed. Engl.* **53** 4236–9
- [24] Suzuki Y, Endo M, Yang Y and Sugiyama H 2014 Dynamic assembly/disassembly processes of photoresponsive DNA origami nanostructures directly visualized on a lipid membrane surface *J. Am. Chem. Soc.* **136** 1714–7
- [25] Kocabay S, Kempter S, List J, Xing Y, Bae W, Schiffels D, Shih W M, Simmel F C and Liedl T 2015 Membrane-assisted growth of DNA origami nanostructure arrays *ACS Nano* **9** 3530–9

III. Binding and Diffusion of membrane-bound DNA nanostructures

- [26] Czogalla A, Kauert D J, Franquelim H G, Uzunova V, Zhang Y, Seidel R and Schwille P 2015 Amphipathic DNA origami nanoparticles to scaffold and deform lipid membrane vesicles *Angew. Chem., Int. Ed. Engl.* **54** 6501–5
- [27] Langecker M, Arnaut V, Martin T G, List J, Renner S, Mayer M, Dietz H and Simmel F C 2012 Synthetic lipid membrane channels formed by designed DNA nanostructures *Science* **338** 932–6
- [28] Göpflich K, Zettl T, Meijering A E, Hernández-Ainsa S, Kocabey S, Liedl T and Keyser U F 2015 DNA-tile structures induce ionic currents through lipid membranes *Nano Lett.* **15** 3134–8
- [29] Douglas S M, Marblestone A H, Teerapittayanon S, Vazquez A, Church G M and Shih W M 2009 Rapid prototyping of 3D DNA-origami shapes with caDNAo *Nucleic Acids Res.* **37** 5001–6
- [30] Angelova M I and Dimitrov D S 1986 Liposome electroformation *Faraday Discuss.* **81** 303–11
- [31] García-Sáez A J, Carrer D C and Schwille P 2010 Fluorescence correlation spectroscopy for the study of membrane dynamics and organization in giant unilamellar vesicles *Methods Mol. Biol.* **606** 493–508
- [32] Thomas F A, Visco I, Petrášek Z, Heinemann F and Schwille P 2015 Introducing a fluorescence-based standard to quantify protein partitioning into membranes *Biochim. Biophys. Acta* **1848** 2932–41
- [33] Petrov E P and Schwille P 2008 State of the art and novel trends in fluorescence correlation spectroscopy *Standardization and Quality Assurance in Fluorescence Measurements II—Bioanalytical and Biomedical Applications* ed U Resch-Genger (Berlin: Springer) pp 145–97
- [34] Petrov E P, Ohrt T, Winkler R G and Schwille P 2006 Diffusion and segmental dynamics of double-stranded DNA *Phys. Rev. Lett.* **97** 258101
- [35] Dertinger T, Pacheco V, von der Hocht I, Hartmann R, Gregor I and Enderlein J 2007 Two-focus fluorescence correlation spectroscopy: a new tool for accurate and absolute diffusion measurements *ChemPhysChem* **8** 433–43
- [36] Heinemann F, Betaneli V, Thomas F A and Schwille P 2012 Quantifying lipid diffusion by fluorescence correlation spectroscopy: a critical treatise *Langmuir* **28** 13395–404
- [37] Korson L, Drosthan W and Millero F J 1969 Viscosity of water at various temperatures *J. Phys. Chem.* **73** 34–9
- [38] Müller P, Schwille P and Weidemann T 2014 PyCorrFit-generic data evaluation for fluorescence correlation spectroscopy *Bioinformatics* **30** 2532–3
- [39] Buschmann V, Weston K D and Sauer M 2003 Spectroscopic study and evaluation of red-absorbing fluorescent dyes *Bioconjug. Chem.* **14** 195–204

III.2 Control of membrane binding and diffusion of cholesteryl-modified DNA origami nanostructures by DNA spacers

The results discussed in this section have been published as:

Khmelinskaia, A., Mücksch, J., Petrov, E. P., Franquelim, H. G., Schwille, P. (2018) Control of membrane binding and diffusion of cholesteryl-modified DNA origami nanostructures by DNA spacers. Langmuir: doi: 10.1021/acs.langmuir.8b01850. A reprint permission has been granted by the publisher. The supplementary information can be found in Appendix C.

LANGMUIR

Subscriber access provided by MPI FUR BIOCHEMIE

Interface Components: Nanoparticles, Colloids, Emulsions, Surfactants, Proteins, Polymers

Control of membrane binding and diffusion of cholesteryl-modified DNA origami nanostructures by DNA spacers

Alena Khmelinskaia, Jonas Mücksch, Eugene P Petrov, Henri G. Franquelim, and Petra Schwill

Langmuir, **Just Accepted Manuscript** • DOI: 10.1021/acs.langmuir.8b01850 • Publication Date (Web): 25 Sep 2018

Downloaded from <http://pubs.acs.org> on September 27, 2018

Just Accepted

"Just Accepted" manuscripts have been peer-reviewed and accepted for publication. They are posted online prior to technical editing, formatting for publication and author proofing. The American Chemical Society provides "Just Accepted" as a service to the research community to expedite the dissemination of scientific material as soon as possible after acceptance. "Just Accepted" manuscripts appear in full in PDF format accompanied by an HTML abstract. "Just Accepted" manuscripts have been fully peer reviewed, but should not be considered the official version of record. They are citable by the Digital Object Identifier (DOI®). "Just Accepted" is an optional service offered to authors. Therefore, the "Just Accepted" Web site may not include all articles that will be published in the journal. After a manuscript is technically edited and formatted, it will be removed from the "Just Accepted" Web site and published as an ASAP article. Note that technical editing may introduce minor changes to the manuscript text and/or graphics which could affect content, and all legal disclaimers and ethical guidelines that apply to the journal pertain. ACS cannot be held responsible for errors or consequences arising from the use of information contained in these "Just Accepted" manuscripts.



ACS Publications

is published by the American Chemical Society, 1155 Sixteenth Street N.W., Washington, DC 20036

Published by American Chemical Society. Copyright © American Chemical Society.

However, no copyright claim is made to original U.S. Government works, or works produced by employees of any Commonwealth realm Crown government in the course of their duties.

1
2
3
4
5
6
7
8
9
10
11
12
13
14
15
16
17
18
19
20
21
22
23
24
25
26
27
28
29
30
31
32
33
34
35
36
37
38
39
40
41
42
43
44
45
46
47
48
49
50
51
52
53
54
55
56
57
58
59
60

Control of membrane binding and diffusion of cholesteryl-modified DNA origami nanostructures by DNA spacers

Alena Khmelinskaia¹, Jonas Mücksch¹, Eugene P. Petrov^{1,2}, Henri G. Franquelim¹, Petra Schwille^{1}*

¹ Max Planck Institute of Biochemistry, Am Klopferspitz 18, 82152 Martinsried, Germany

² Faculty of Physics, Ludwig Maximilian University of Munich, Geschwister-Scholl-Platz 1, 80539 Munich, Germany

ABSTRACT

DNA origami nanotechnology is increasingly used to mimic membrane-associated biophysical phenomena. Although a variety of DNA origami nanostructures has already been produced to target lipid membranes, the requirements for membrane binding have so far not been systematically assessed. Here, we used a set of elongated DNA origami structures with varying placement and number of cholesteryl-based membrane anchors to compare different strategies for their incorporation. Single and multiple cholesteryl anchors were attached to DNA nanostructures using single- and double-stranded DNA spacers of varying length. The produced DNA nanostructures were studied in terms of their membrane binding and diffusion. Our results

1
2
3 show that the location and number of anchoring moieties play a crucial role for membrane
4 binding of DNA nanostructures mainly if the cholesteryl anchors are in close proximity to the
5 bulky DNA nanostructures. Moreover, the use of DNA spacers largely overcomes local steric
6 hindrances and thus enhances membrane binding. Fluorescence correlation spectroscopy
7 measurements demonstrate that the distinct physical properties of single- and double-stranded
8 DNA spacers control the interaction of the amphipathic DNA nanostructures with lipid
9 membranes. Thus, we provide a rational basis for the design of amphipathic DNA origami
10 nanostructures to efficiently bind lipid membranes in various environments.
11
12
13
14
15
16
17
18
19
20
21
22
23
24
25
26
27
28
29
30
31
32
33
34
35
36
37
38
39
40
41
42
43
44
45
46
47
48
49
50
51
52
53
54
55
56
57
58
59
60

1
2
3
4
5
6
7
8
9
10
11
12
13
14
15
16
17
18
19
20
21
22
23
24
25
26
27
28
29
30
31
32
33
34
35
36
37
38
39
40
41
42
43
44
45
46
47
48
49
50
51
52
53
54
55
56
57
58
59
60

INTRODUCTION

The last decades' advances in DNA nanotechnology allowed for the production of customizable DNA nanostructures with nanometer-precision addressability, which can be modified with a wide variety of functional moieties, e.g. small biomolecules, fluorescent dyes, metallic nanoparticles, peptides, proteins or hydrophobic moieties¹⁻⁷. The versatility of DNA-based nanomaterials led to their use to investigate various biophysical processes in biologically relevant environments, such as lipid membranes, directly addressing cellular membranes or resorting to minimal lipid model systems⁸⁻⁹. For this purpose, DNA oligonucleotides have been previously covalently modified with lipophilic moieties, such as alkyl chains¹⁰, cholesterol¹¹⁻¹³, tocopherol¹⁴ and porphyrins¹⁵. Membrane-targeting of DNA nanostructures by cholesteryl anchors with a tetra-ethylene glycol linker (TEG-chol) became particularly popular, since such oligonucleotides are commercially available and have been extensively characterized in terms of their incorporation into lipid membranes and their effect on the lipid membrane reorganization^{12-13, 16}. Ranging from the study of the differential partitioning of a simple six-helix bundle in phase-separated membranes¹⁷ and its 2D organization upon crowding on homogeneous membranes¹⁸, to the achievement of controllable binding of DNA nanostructures to lipid membranes¹⁹⁻²⁰, cholesteryl-modified nanostructures have been used to mimic rather complex biological phenomena. For example, membrane-assisted oligomerization of amphipathic DNA nanostructures of various flat shapes has been previously shown^{19, 21-22}. More recently, this phenomenon has been demonstrated to induce shape deformation and bursting of small vesicles²³ as well as large scale deformation of giant unilamellar vesicles (GUVs)²⁴. Other membrane-shaping phenomena usually associated with protein scaffolds have been recently mimicked using curved DNA origami nanostructures, capable of tubulating lipid membranes²⁵⁻²⁶. DNA-based

1
2
3 membrane nanochannels, ranging from large hemolysin-inspired structures to tile-based
4 constructs²⁷⁻²⁹, can insert into lipid bilayers and conduct ion currents. A small 4-helix DNA tile
5
6
7 has been shown to facilitate the flip-flop of lipids between lipid leaflets outperforming natural
8
9
10 enzymes³⁰. Furthermore, DNA origami nanostructures have been used to modify the cell surface
11
12
13 function to promote cell-cell adhesion³¹.

14
15
16 Interestingly, despite the complexity of the phenomena described and the physical properties
17
18
19 unraveled in the above mentioned studies, a thorough analysis of the strategies chosen to
20
21
22 membrane-target DNA nanostructure in each of these studies reveals a lack of a systematic
23
24
25 approach towards this goal. For instance, DNA origami nanostructures of similar membrane-
26
27
28 facing areas have been targeted to lipid membranes using various numbers and types of
29
30
31 attachment of TEG-chol moieties: from a single cholesteryl-modified oligonucleotide to a total
32
33
34 of 47, directly incorporated in the DNA nanostructures or hybridized with a DNA extension of
35
36
37 18, 20 or 60 nucleotides^{19, 23-25, 31}. Previously, we have addressed a part of this problem by
38
39
40 studying the minimal steric requirements for the membrane-attachment of such DNA-based
41
42
43 nanostructures by the direct incorporation in an elongated 3D DNA origami nanostructure of
44
45
46 various configurations of cholesteryl-modified nucleotides³².

47
48
49 Here, we use the previously designed 20-helix bundle with 15 addressable locations to explore
50
51
52 the effect of single- and double-stranded DNA linkers between the TEG-chol anchors and the
53
54
55 bulky DNA nanostructures on membrane binding (Figure 1). Single- and multiple-cholesteryl-
56
57
58 modified DNA origami nanostructures were produced varying the length and flexibility of the
59
60
61 cholesteryl-anchors (Figure 1C). We study the binding, membrane density and dynamics of each
62
63
64 of these DNA nanostructures by fluorescence microscopy and fluorescence correlation
65
66
67 spectroscopy (FCS) on GUVs. Our results convincingly demonstrate that the accessibility and

1
2
3
4
5
6
7
8
9
10
11
12
13
14
15
16
17
18
19
20
21
22
23
24
25
26
27
28
29
30
31
32
33
34
35
36
37
38
39
40
41
42
43
44
45
46
47
48
49
50
51
52
53
54
55
56
57
58
59
60

number of the anchoring moieties within the bulky DNA nanostructures play a crucial role for their binding to lipid membranes. We further show that the DNA spacer type has a pronounced effect on the diffusion of the elongated DNA nanostructures on lipid membranes and response to cationic lipids.

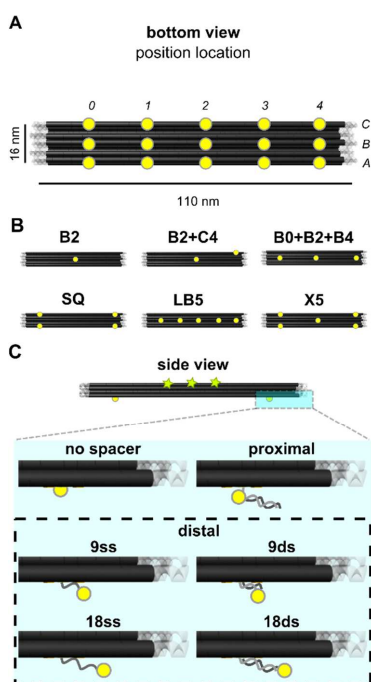


Figure 1. Structural characteristics of the elongated 20-helix bundle DNA origami nanostructure.

(A) Nomenclature and location of the 15 possible sites (yellow circles) for modification with TEG-chol anchors on the bottom facet of the elongated DNA origami (16 nm × 110 nm). Five locations along and three across the elongated DNA origami nanostructure were denoted by numbers (0-4) and letters (A–C), respectively. (B) Bottom view of some of the combinations of TEG-chol anchors used. Naming of the structures explicitly codes for the location of the TEG-

1
2
3
4
5
6
7
8
9
10
11
12
13
14
15
16
17
18
19
20
21
22
23
24
25
26
27
28
29
30
31
32
33
34
35
36
37
38
39
40
41
42
43
44
45
46
47
48
49
50
51
52
53
54
55
56
57
58
59
60

chol anchors, except for R4 (anchor locations A0 + A4 + C0 + C4), LB5 (anchors locations B0 + B1 + B2 + B3 + B4) and X5 (anchor locations A0 + A4 + B2 + C0 + C4). (C) Schematic representation of the side view of the different types of TEG-chol anchors used. Two different linkage strategies were employed: direct insertion into the DNA nanostructure of oligonucleotides with no, 9 or 18 nucleotide extensions TEG-chol modified at the free end (denoted no spacer, 9ss and 18ss, respectively); hybridization of TEG-chol oligonucleotides in a proximal position to the DNA nanostructure with 18 nucleotide extensions (denoted proximal) or in a distal position to the DNA nanostructure with 9 or 18 nucleotide extensions (denoted 9ds and 18ds, respectively). The list of strands used for assembly of each TEG-chol anchor can be found in the Supporting Table 1.

1
2
3
4
5
6
7
8
9
10
11
12
13
14
15
16
17
18
19
20
21
22
23
24
25
26
27
28
29
30
31
32
33
34
35
36
37
38
39
40
41
42
43
44
45
46
47
48
49
50
51
52
53
54
55
56
57
58
59
60

MATERIALS AND METHODS

DNA origami folding and purification – The previously described elongated DNA origami structure was used³². Some of the oligonucleotides in the bottom locations A0-4, B0-4, C0-4 (Figure 1) were substituted by the respective extended and/or TEG-modified oligonucleotides (Sigma-Aldrich, Taufkirchen, Germany) (Supporting Table 1) to assemble the required membrane anchors. For detection by fluorescence microscopy and spectroscopy, the nanostructures were functionalized respectively with three 5' ATTO488 or 5' Alexa488-modified GGGTTTGGTGTGTTTTT oligonucleotides (Eurofins, Planegg, Germany), that would attach to complementary extensions located on the top facet close to the center of the structure. DNA origami nanostructure folding, purification in imaging buffer (5 mM Tris-HCl, 1 mM EDTA, 5 mM MgCl₂, 300 mM NaCl, pH 8.0) and concentration determination were performed as previously described³².

Vesicle preparation and DNA origami nanostructure binding – Giant unilamellar vesicles (GUVs) composed of 1,2-dioleoyl-*sn*-glycero-3-phosphocholine (DOPC), and 9:1 mixtures of DOPC with 1,2-dioleoyl-*sn*-glycero-3-phospho-L-serine (DOPS) or 1,2-dioleoyl-3-trimethylammonium-propane (DOTAP) (all purchased from Avanti Polar Lipids, Alabaster, AL, USA), and additionally containing 0.005 mol% Atto655-DOPE (ATTO-TEC GmbH, Siegen, Germany) were produced by electroformation³³ in polytetrafluoroethylene chambers with Pt electrodes spaced 4 mm apart, as described previously³⁴. Briefly, 6 μL of the lipid mixture (2 $\text{mg}\cdot\text{mL}^{-1}$ in chloroform Uvasol) was spread onto two Pt wires and dried in a desiccator for 30 min. The chamber was then filled with 350 μL of a 605 $\text{mOsm}\cdot\text{kg}^{-1}$ aqueous solution of sucrose. A sinusoidal AC electric field of 2 V (RMS) was applied at a frequency of 10 Hz for 1.5 h, followed by 2 Hz for 45 min. Experiments were carried out in 40 μL 384-multiwell plates with

1
2
3 #1.5 glass coverslip bottom (MatriCal, Brooks Life Science Systems, Spokane, WA, USA and
4 Sensoplate, Greiner Bio-One GmbH, Frickenhausen, Germany). Freshly plasma-cleaned wells
5
6
7
8 (0.3 mbar, 10 min) (MiniFlecto-PC-MFC, Plasma Technology, Herrenberg-Gültstein, Germany)
9
10 were passivated with PLL(20)-g[3.5]-PEG(2) (SuSoS AG, Dübendorf, Switzerland) by
11
12 incubation with a 0.5 mg·mL⁻¹ solution in Milli-Q water (Merck Millipore, Darmstadt, Germany)
13
14 for at least half an hour and subsequently thoroughly washed with Milli-Q water and imaging
15
16 buffer. 3 μL of the GUV suspension (original suspension in the electroformation chamber diluted
17
18 1:50 in 605 mOsm·kg⁻¹ sucrose solution) were mixed with 18 μL of DNA origami solution (3
19
20 nM total concentration) diluted in imaging buffer (iso-osmolar). To reach a higher MgCl₂
21
22 concentration, 1 μL of buffer containing 5 mM Tris-HCl, 1 mM EDTA, 195 mM MgCl₂, pH 8.0
23
24 (iso-osmolar) was added to the chambers. Samples were incubated at 4 °C overnight and, before
25
26 measurement, equilibrated at the microscope objective (27.5 ± 1.0 °C) for at least 30 min. GUVs
27
28 were not disrupted by DNA origami. After overnight incubation, no penetration of DNA origami
29
30 nanostructures to the interior volume of the GUVs was found (Supporting Figure 1).
31
32
33
34
35

36 **Fluorescence imaging** – Confocal imaging was performed on a LSM 780 commercial laser
37
38 scanning microscope with a ConfoCor3 unit (Carl Zeiss AG, Oberkochen, Germany) using a
39
40 water immersion objective (C-Apochromat, 40×/1.2 W UV-VIS-IR, Zeiss, Jena, Germany).
41
42 Fluorophores were excited with the 488 nm line of an Ar-ion-laser or with the 633 nm line of a
43
44 He-Ne laser (for Atto488 and Atto655 excitation, respectively). To avoid the effect of
45
46 polarization selection in excitation of the GUVs, an achromatic λ/4 plate (Edmund Optics,
47
48 Barrington, NJ, USA) was installed in the excitation beam path to achieve circularly polarized
49
50 excitation in the sample. Images were recorded at the equatorial planes of GUVs, using a 1 Airy
51
52 unit pinhole, 512 × 512 pixel, pixel dwell time of 3.15 μs and GaAsP detectors. In order to
53
54
55
56
57
58
59
60

1
2
3 compare membrane affinities of different nanostructures, fluorescence intensities of membrane-
4 bound DNA origami at a bulk concentration of 3 nM were determined using an in-house
5 software based on Matlab (MathWorks, Naticks, USA)³⁵. The background signal was subtracted
6 from the obtained fluorescence intensity and independent measurements were normalized taking
7 into account the particle brightness of Alexa488 in solution as obtained by fluorescence
8 correlation spectroscopy. Further data normalization is specified for the respective figures. Image
9 brightness and contrast adjustment for better visualization was performed using ImageJ ([http://
10 rsb.info.nih.gov/ij/](http://rsb.info.nih.gov/ij/))³⁶. In Figures 2 and 3 the brightness and contrast levels were adjusted
11 individually for illustrative purposes.
12
13
14
15
16
17
18
19
20
21
22

23
24
25 **Fluorescence correlation spectroscopy** – For fluorescence correlation spectroscopy (FCS),
26 2 mm-thick silicon isolators with 4.5 mm diameter wells (Grace Bio-Labs, Oregon, USA) were
27 pressed on plasma cleaned high precision 22 mm × 22 mm #1.5 coverslides (Marienfeld
28 Superior, Germany). Samples were prepared as described above at total DNA nanostructure
29 concentrations ranging between 0.05 and 1 nM. This allowed us to assure the reduced density of
30 membrane-bound DNA nanostructures is in the regime $\rho < 0.5$ in which the effect of crowding
31 on the translational diffusion is expected to be below 10%¹⁸. Here $\rho = \sigma L^2$ is the reduced density
32 of particles on the membrane, σ is the surface density of membrane-bound DNA nanostructures
33 per μm^2 and L is the DNA nanostructure length. The localization of the three Alexa488 modified
34 nucleotides around the center of the structures allowed us to follow translational diffusion by
35 FCS and eliminated potential complications in interpretation of the results due to rotational
36 diffusion¹⁷⁻¹⁸. Samples were sealed with 18 mm × 18 mm plasma-cleaned coverslides to avoid
37 evaporation, and incubated overnight, as described above.
38
39
40
41
42
43
44
45
46
47
48
49
50
51
52
53
54
55
56
57
58
59
60

1
2
3 FCS measurements were performed on the same microscope setup as above, using avalanche
4 photodiode detectors (ConfoCor3, Carl Zeiss AG, Oberkochen, Germany). The internal pinholes
5 were set to 35 μm and 45 μm size, corresponding to 1 Airy unit for 488 nm and 633 nm
6 excitation wavelength, respectively. To eliminate the unwanted contribution of the detector
7 afterpulsing to the autocorrelation curve, we performed pseudo-crosscorrelation, i.e. we split
8 50/50 the collected fluorescence, directed it on two independent detectors and cross-correlated
9 their signals. For analysis, the average of the two resulting autocorrelation functions (ACFs) was
10 considered. The optical system was calibrated on a daily basis using Alexa Fluor 488 (Alexa488,
11 Thermo Fischer Scientific, Waltham, MA, EUA) or ATTO 655 carboxylic acid (Atto655,
12 ATTO-TEC, Siegen, Germany) freely diffusing in aqueous solution with known diffusion
13 coefficients³⁷⁻³⁹, corrected for the temperature at the microscope objective through the relation
14 $D(T) \propto T/\eta(T)$ ⁴⁰⁻⁴¹. The viscosity of water at 27.5 °C was calculated using the previously
15 published expression⁴². For calibration measurements, the confocal volume was positioned 50
16 μm above the bottom coverslip, the lateral pinhole position was optimized for maximum
17 fluorescence signal and the objective's correction collar was positioned for maximal count rate
18 per particle.

19
20
21 FCS on membranes was carried out at the upper poles of GUVs with diameter of at least 20 μm
22 (which is large enough to be considered as a flat surface in comparison with our DNA
23 nanostructures). The optimal axial focus position was determined by scanning the detection
24 volume in the axial direction to locate the intensity maximum. This procedure was repeated for
25 each FCS measurement, to compensate for potential sample drift. During acquisition of FCS data
26 (minimum 15 runs, 15 s each), the fluorescence count rate was monitored online, ensuring that
27 no fluorescence fluctuations originated from the movements of the whole membrane or the
28
29
30
31
32
33
34
35
36
37
38
39
40
41
42
43
44
45
46
47
48
49
50
51
52
53
54
55
56
57
58
59
60

1
2
3 presence of large aggregates of fluorescent particles. In case such events were observed, the
4
5 corresponding datasets were discarded. For both the initial calibration measurement and the FCS
6
7 measurements on GUVs, the sufficiently low excitation power density was chosen to minimize
8
9 photobleaching and fluorescence saturation⁴³⁻⁴⁵.

10
11
12
13 The recorded ACFs were analyzed using a home-written Matlab-based code (MathWorks,
14
15 Natick, USA) to obtain particle number (and consequently, membrane density) and the
16
17 translational diffusion coefficient (D) of membrane-bound DNA nanoparticles, as well as of the
18
19 lipid probe. As virtually no unbound DNA origami was detected in solution, and its potential
20
21 contribution to FCS curves was negligible (data not shown), a single-component two-
22
23 dimensional diffusion model was used as a fitting function.
24
25
26

27
28 In general, the model function for 3D diffusion reads⁴⁵:

$$G(\tau) = N^{-1} \left(1 + \frac{T}{1-T} e^{-\tau/\tau_T} \right) \left(1 + \tau/\tau_D \right)^{-1} \left(1 + \tau/(S^2\tau_D) \right)^{-1/2} \quad (\text{Eq. 1})$$

29
30
31
32 Here, $\tau_D = w_0^2/4D$ is the diffusion time, which depends on the diffusion coefficient D and the
33
34 lateral waist w_0 of the confocal detection volume, which assumed to be a 3D Gaussian. The
35
36 structure parameter S represents the ratio of axial to lateral extent of the detection volume, T is
37
38 the triplet fraction, and τ_T is the triplet blinking time. Under the experimental conditions, Atto655
39
40 does not show any triplet blinking, and experimental curves are therefore fitted with $T=0$. When
41
42 measuring on membranes the axial extent of the confocal volume is irrelevant ($S=\infty$). To ensure
43
44 proper determination of the concentration of membrane-bound DNA origami particles,
45
46
47
48
49
50
51
52
53
54
55
56
57
58
59
60

1
2
3 amplitudes of autocorrelation functions were corrected for the presence of a non-correlated
4 background⁴⁶.
5
6
7

8
9
10
11
12 Based on the FCS measurements, the diffusion coefficient of DNA origami nanostructures bound
13 to the lipid membrane (D_{DNA}) was calculated as follows:
14

$$D_{DNA} = D_{Alexa488} \frac{\tau_{DNA}}{\tau_{Alexa488}} \text{ (Eq. 2).}$$

15
16
17
18
19
20
21
22 The relative variations for $\tau_{Alexa488}$ within one measurement day were of about 1%. The
23 relative error in $D_{Alexa488}$ is about 2%. At the same time, τ_{DNA} showed $\approx 10\%$ variability
24 between measurements on individual GUVs. Thus, the error in D_{DNA} is dominated by the error in
25
26
27
28
29 τ_{DNA} .
30
31

32 **Statistical analysis** – The data presented has been statistically analyzed using one or two way
33 ANOVA with subsequent Bonferroni's test for the mean diffusion coefficients using Prism 7
34 (GraphPad, La Jolla, CA, USA). The summary tables can be found in the SA Tables.
35
36
37
38
39
40
41
42
43
44
45
46
47
48
49
50
51
52
53
54
55
56
57
58
59
60

1
2
3
4
5
6
7
8
9
10
11
12
13
14
15
16
17
18
19
20
21
22
23
24
25
26
27
28
29
30
31
32
33
34
35
36
37
38
39
40
41
42
43
44
45
46
47
48
49
50
51
52
53
54
55
56
57
58
59
60

RESULTS AND DISCUSSION

We used the elongated DNA nanostructure that has been previously described³² to study the effect of different TEG-chol anchors on the binding efficiency to lipid membranes (Figure 2 and Supporting Figure 2). The 20-helix bundle, with a membrane-facing surface of dimensions 110 nm × 16 nm, has 15 distinct locations for TEG-chol anchor placement (Figure 1A). More specifically, five sites (numbered 0–4) were spaced 21.4 nm apart along three helices (named A–C). The distances from the left (location 0) and right (location 4) locations to the structure edges are 26.3 and 16.9 nm, respectively. Structures containing combinations of one, two, three or five TEG-chol anchors in different locations have been produced (for particular examples, see Figure 1B), and their binding efficiency to DOPC GUVs was assessed by fluorescence confocal microscopy.

Number and location of TEG-chol moieties in the proximal position strongly influence the membrane binding of elongated DNA nanostructures

– First, we assessed DNA nanostructures displaying cholesteryl-modified oligonucleotides in a proximal position hybridized with 18 nucleotide-long overhangs at the modification sites (Figure 1C). The fluorescence intensity of GUVs incubated with 3 nM solution of DNA nanostructures featuring various numbers and locations of proximal TEG-chol anchors was analyzed (Figure 2A,C, Supporting Figure S2B). Our results show that under these conditions, one proximal TEG-chol anchor was not enough to achieve significant membrane binding. Furthermore, although higher numbers of proximal TEG-chol anchors increased the affinity of the DNA nanostructures to the membrane surface, anchor location also played a crucial role. More specifically, nanostructures with proximal TEG-chol anchors at locations near the edges (such as A0 + C4) were more efficient in membrane attachment than those with TEG-chol anchors closer to the center of the

1
2
3 structure (B2 + C4, where B2 is the central location). Among the configurations tested, the
4
5 highest membrane binding was achieved by the configuration X5 (A0 + A4 + B2 + C0 + C4).
6
7 Taken together, there is a strong dependence of membrane binding on the number and location of
8
9 the TEG-chol anchors, with binding efficiencies differing up to a factor of 100 compared to a
10
11 single TEG-chol at B2. Previously we studied the effect of TEG-chol moieties directly attached
12
13 to the DNA nanostructure, with strikingly similar findings³² (Figure 2E, Supporting Figure
14
15 S2A,B). Notably, in the proximal localization, the distance between the TEG-chol anchors and
16
17 the DNA nanostructures should be comparable with the distance upon direct modification of the
18
19 structure as in our previous study (“proximal” and “no spacer” anchors in Figure 1C,
20
21 respectively). Variations in the binding efficiency of anchor combinations with less accessible
22
23 locations, such as B0 + B2 + B4, may come from an incomplete hybridization of the 18
24
25 nucleotide-long strands due to steric hindrance and electrostatic repulsion in the proximal
26
27 orientation.
28
29
30
31
32
33

34 **DNA spacers increase membrane binding efficiency of elongated DNA origami**
35 **nanostructures** – Although proximal localization of TEG-chol moieties has been used in the
36
37 special instance of electrically stable insertion of DNA-based nanopores in lipid vesicles²⁷,
38
39 usually a distal localization of TEG-chol moieties has been chosen to efficiently bind DNA
40
41 nanostructures to lipid membranes^{19, 23, 25-26, 31}. Switching the attachment of the cholesteryl-
42
43 modified nucleotide from a proximal to a distal position (denoted 18ds, Figure 1C) drastically
44
45 changed the membrane-binding behavior of the elongated DNA nanostructures (Figure 2B,D,
46
47 Supporting Figure S2F). Here, a single TEG-chol anchor yielded significant membrane binding,
48
49 irrespectively of its location. Additionally, the membrane binding efficiency of structures bearing
50
51 two, three or five TEG-chol anchors was only one order of magnitude higher in comparison to a
52
53
54
55
56
57
58
59
60

1
2
3
4
5
6
7
8
9
10
11
12
13
14
15
16
17
18
19
20
21
22
23
24
25
26
27
28
29
30
31
32
33
34
35
36
37
38
39
40
41
42
43
44
45
46
47
48
49
50
51
52
53
54
55
56
57
58
59
60

single TEG-chol anchor at location B2, showing a very low effect of the total number or location of the anchors (Figure 2E). The comparison of these results with those obtained for the proximal positioning of TEG-chol moieties, suggests that the distance between the TEG-chol anchor and the bulky DNA nanostructure may play a role for the membrane binding efficiency.

To study the effect of the distance between the TEG-chol moieties and the DNA nanostructure, we systematically varied the DNA spacer length. Three different types of TEG-chol anchors were tested (Figure 1C, 2E and Supporting Figure 2C-E): 9ss and 18ss anchors, produced through direct insertion into the DNA nanostructures of oligonucleotides with 9 or 18 nucleotide extensions, respectively, cholesteryl-modified at the free end; and 9ds anchors, produced through the extension of the neighboring oligonucleotide for hybridization with the directly inserted 9 nucleotide extended cholesteryl-modified oligonucleotide in the DNA nanostructure (Supporting Figure 3). Just as observed for the 18ds DNA spacer, attachment of a single TEG-chol anchor through the 9ds DNA spacer resulted in efficient membrane binding of DNA nanostructures, although the spacer was shorter by a factor of two. The shorter DNA spacer also resulted in lower membrane binding efficiencies, although in the same order of magnitude as for 18ds DNA spacer. Importantly, the effect of the number of anchors and their location was more pronounced for 9ds than for 18ds DNA spacers. This difference may be additionally due to the distinct rigidity of the TEG-chol anchors at their attachment points to the DNA nanostructure. Interestingly, the higher flexibility of 9ss and 18ss DNA spacers, in comparison to their double-stranded counterparts, did not further enhance membrane binding. For both 9ss and 18ss DNA spacers, a minimum of two TEG-chol anchors were necessary for an efficient membrane binding (nearly two orders of magnitude increase in membrane binding efficiency upon addition of the second TEG-chol anchor), irrespectively of their localization. Further increasing the number of

1
2
3 anchors had a small effect on the membrane binding efficiency, as observed for 18ds DNA
4
5 spacers. Indeed, it appeared that DNA spacers providing better binding to the lipid membrane
6
7 showed a smaller dependence on the number and positioning of cholesteryl anchors (Figure 1E
8
9 and Supporting Figure 2). Notably, the use of 9ss and 18ss DNA spacers resulted in very similar
10
11 membrane-binding behaviors, even though the contour length of the spacers differed by a factor
12
13 of two. The membrane binding efficiency of multiple TEG-chol anchors attached via 9ss or 18ss
14
15 DNA spacers was higher than with no DNA spacer or in proximal position, especially when
16
17 comparing configurations involving less accessible locations, such as B0 + B2 + B4 or LB5.
18
19 Nonetheless, the flexibility of the single-stranded DNA spacers and consequent lower
20
21 accessibility to the membrane of the TEG-chol anchors resulted in a less efficient membrane
22
23 binding in comparison to the double-stranded counterparts. We thus suggest that the flexibility of
24
25 short TEG-chol modified DNA spacers can be used to control the binding efficiency of DNA
26
27 nanostructures to lipid membranes. So far, single-stranded DNA spacers consisting of a single
28
29 nucleotide (A) or short sequences (AAA) have only been used in small DNA tile designs, to
30
31 ensure a higher flexibility of the anchors²⁹⁻³⁰.
32
33
34
35
36
37

38
39 Our results can be used to rationalize the previous choices of TEG-chol attachment to DNA
40
41 nanostructures. Direct incorporation of one or two cholesteryl anchors (no DNA spacer) have
42
43 been used in rather small or quasi-one-dimensional structures, such as DNA tile nanoparticles²²
44
45 and DNA nanoneedles¹⁸, where steric hindrance does not play a major role. Other bulkier
46
47 structures, like DNA hexagons²¹ and monolith²⁴, were also attached to lipid membranes using
48
49 this strategy, but with a larger number of anchors (6 and 9, respectively). In all other studies, the
50
51 extension of oligonucleotides for hybridization with TEG-chol-modified oligonucleotides was
52
53 preferred, most probably to reduce the costs for structure functionalization and increase the
54
55
56
57
58
59
60

III.2 Control of membrane binding and diffusion of cholesteryl-modified DNA origami nanostructures by DNA spacers

1
2
3
4
5
6
7
8
9
10
11
12
13
14
15
16
17
18
19
20
21
22
23
24
25
26
27
28
29
30
31
32
33
34
35
36
37
38
39
40
41
42
43
44
45
46
47
48
49
50
51
52
53
54
55
56
57
58
59
60

modularity of the structures. On the one hand, proximal positioning of cholesteryl anchors has been used to achieve stable insertion of DNA-based nanopores, most probably due to the tighter interaction between the nanostructure and the lipid bilayer²⁷⁻²⁸. However, it has been shown that the incorporation of large numbers of cholesteryl moieties in a proximal position reduced the folding efficiency of DNA nanostructures²⁰. On the other hand, distal positioning of cholesterol on DNA spacers of 18 to 21 nucleotides has been used to achieve membrane binding¹⁹, self-assembly²³ and even shaping of model lipid membranes²⁵⁻²⁶, although the number of anchors varied from 1 to a total of 47. To achieve attachment to cell membranes, 60ds DNA spacers have been used, to avoid any steric hindrance in the crowded environment of the cell surface³¹.

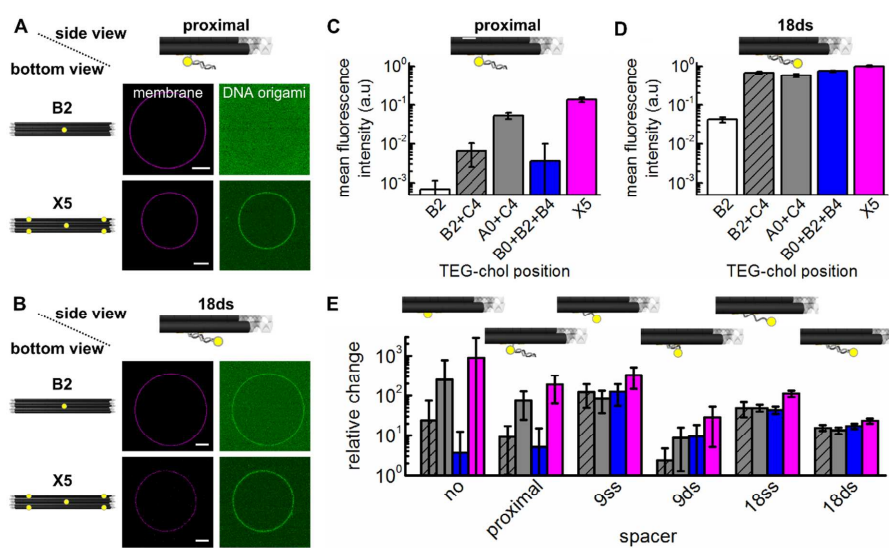


Figure 2. Control of membrane binding efficiency of elongated DNA origami nanostructures by cholesteryl-modified DNA spacers. (A,B) Confocal fluorescence microscopy images of DOPC GUVs at the equatorial plane incubated with 3 nM solution of DNA nanostructures modified

1
2
3 with: one TEG-chol anchor at the central location B2 and five TEG-chol anchors in a crossed
4 shape configuration (A0 + A4 + B2 + C0 + C4, named X5). Two conditions are shown for
5 comparison: proximal (A) and distal (18ds DNA spacer, B) location of the TEG-chol anchor
6 upon hybridization of the modified DNA strand with the complementary 18 nucleotide-long
7 extension. GUVs contained 0.005 mol% Atto655-DOPE for fluorescence imaging (magenta),
8 while each DNA origami structure carried three Atto488 dyes (green). Scale bar: 10 μm . (C,D)
9 Mean fluorescence intensity of DOPC GUVs for several TEG-chol combinations with proximal
10 (C) and distal (18ds, D) location. Note the logarithmic scale of the intensity axis. Error bars
11 correspond to the standard deviation of measurements on typically 15-30 GUVs. (E) Changes in
12 binding upon an increase in the number of anchors for each type of spacer. The measured
13 fluorescence intensities on the GUV are normalized to that of the respective DNA nanostructure
14 with one TEG-chol anchor at the central location B2. For each spacer studied (Figure 1C,
15 Supporting Figure 2) the following TEG-chol anchor configurations are compared: B2 + C4
16 (shaded grey), A0 + C4 (grey), B0+B2+B4 (blue) and X5 (magenta). Note the logarithmic scale
17 of the relative change axis. The significance analysis of the data is summarized in SA Tables 1-3.
18
19
20
21
22
23
24
25
26
27
28
29
30
31
32
33
34
35
36
37
38
39
40
41
42
43
44
45
46
47
48
49
50
51
52
53
54
55
56
57
58
59
60

1
2
3
4
5
6
7
8
9
10
11
12
13
14
15
16
17
18
19
20
21
22
23
24
25
26
27
28
29
30
31
32
33
34
35
36
37
38
39
40
41
42
43
44
45
46
47
48
49
50
51
52
53
54
55
56
57
58
59
60

Short DNA spacers affect the sensitivity of TEG-chol modified DNA nanostructures to charges in the environment – Membrane-associated processes in living cells frequently involve protein interaction with negatively charged lipids⁴⁷⁻⁴⁸ and/or require the presence of divalent cations in the vicinity of the interaction site⁴⁹. To test the compatibility of cholesteryl-modified DNA nanostructures with such biologically-inspired settings, we assessed the binding of DNA nanostructures with TEG-chol anchors attached at locations A0 + C4 with no spacer, as well as with 18ss and 18ds DNA spacers to DOPC GUVs at low MgCl₂ concentration (imaging buffer, 5 mM), DOPC GUVs at higher MgCl₂ concentration (MgCl₂ enriched imaging buffer, 14 mM) and DOPC GUVs containing 10 mol% of the negatively charged lipid DOPS (imaging buffer, 5 mM MgCl₂) (Figure 3).

Generally, under all the above three conditions, membrane binding efficiency followed the trend outlined above: the use of DNA spacers (either 18ds or 18ss) increased the binding efficiency of the DNA nanostructures compared to no spacers, with 18ds DNA spacers being most efficient (Figure 3A,B). An increase in Mg²⁺ concentration enhanced the binding to DOPC GUVs of A0 + C4 DNA nanostructures. It is known that divalent cations can mediate the interaction between DNA and zwitterionic lipid molecules⁵⁰, which explains the effect of Mg²⁺. The presence of negatively charged DOPS lipids in the membrane reduced the binding efficiency of DNA nanostructures, as previously reported^{17, 51}, which can be explained by electrostatic repulsion between negatively charged membrane and negatively charged DNA origami. Interestingly, the charge effect on the membrane binding of A0 + C4 nanostructure was much stronger in the absence of a DNA spacer than in the presence of 18ss and 18ds DNA spacers (Figure 3C). Indeed, in absence of DNA spacers the length of TEG-chol anchor is in the order of the Debye

1
2
3
4
5
6
7
8
9
10
11
12
13
14
15
16
17
18
19
20
21
22
23
24
25
26
27
28
29
30
31
32
33
34
35
36
37
38
39
40
41
42
43
44
45
46
47
48
49
50
51
52
53
54
55
56
57
58
59
60

length (≈ 0.5 nm). Notably, under all three conditions tested, bare structure N without TEG-chol anchors, did not show any binding to the lipid membrane (Figure 3B).

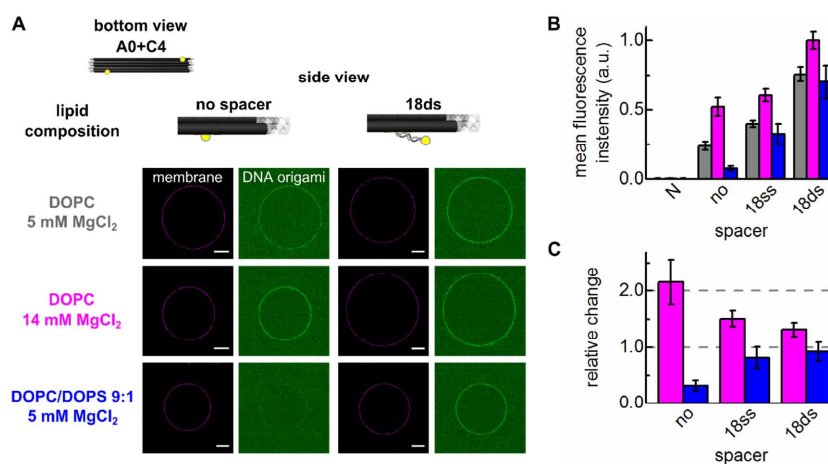


Figure 3. Response of TEG-chol modified DNA nanostructures to charge in the environment.

(A) Confocal fluorescence microscopy images of DOPC GUVs in buffer containing 5 mM MgCl₂ (upper panel), or 14 mM MgCl₂ (middle panel) or containing 10 mol% of the negatively charged lipid DOPS (DOPC/DOPS 9:1) in buffer containing 5 mM MgCl (lower panel). Images were taken at the equatorial plane of GUVs incubated with 3 nM solution of DNA nanostructures modified with two TEG-chol anchors at locations A0 + C4. Two conditions are shown for comparison: DNA nanostructure modification using no spacer (left panel) and 18ds DNA spacer (right panel). GUVs contained 0.005 mol% Atto655-DOPE (magenta) for fluorescence imaging, while each origami structure carried three Atto488 dyes (green). Scale bar: 10 μ m. (B) Mean fluorescence intensities of A0 + C4 nanostructures bound to DOPC GUVs in buffer containing 5 mM (grey) or 14 mM (magenta) MgCl₂ or containing 10mol% of negatively charged lipid DOPS (DOPC/DOPS 9:1) in imaging buffer containing 5 mM MgCl₂ (blue). A0+C4 structure with no

III.2 Control of membrane binding and diffusion of cholesteryl-modified DNA origami nanostructures by DNA spacers

1
2
3
4
5
6
7
8
9
10
11
12
13
14
15
16
17
18
19
20
21
22
23
24
25
26
27
28
29
30
31
32
33
34
35
36
37
38
39
40
41
42
43
44
45
46
47
48
49
50
51
52
53
54
55
56
57
58
59
60

spacer, as well as with 18ss and 18ds DNA spacer are compared. Bare DNA nanostructure N is shown under all conditions for reference. Error bars correspond to the standard deviation of measurements on typically 20 GUVs. (C) Effect of charges in the environment on the membrane binding of cholesteryl-modified DNA nanostructures, relative to the binding efficiency of DNA nanostructures to DOPC GUVs in buffer containing 5 mM MgCl₂. Color coding is the same as in B. Dashed lines for ratio 1 and 2 are present for guidance. The significance analysis of the data is summarized in SA Tables 4,5.

1
2
3 **Single- and double-stranded DNA spacers differently influence diffusion of TEG-chol**
4 **modified DNA nanostructures on lipid membranes** – Membrane-related processes are
5
6 dependent on the diffusion of biomolecules. We used fluorescence correlation spectroscopy
7
8 (FCS) to study the effect of DNA spacers on the translational diffusion of a chosen set of
9
10 membrane-bound DNA nanostructures. All measurements were performed in a dilute regime,
11
12 with reduced surface density of DNA nanostructures $\rho < 0.5$ (see Materials and Methods for
13
14 more details), in which the effect of crowding on the translational diffusion is expected to be
15
16 below 10%¹⁸. In this regime, FCS autocorrelation functions for membrane-bound nanostructures
17
18 could be well described by the 2D diffusion model (Equation 1 with $S=\infty$). This allowed us to
19
20 obtain the translational diffusion coefficients of Alexa488-labeled DNA origami particles bound
21
22 to lipid membranes (Figure 4A).
23
24
25
26
27
28

29
30 In order to assess the effects of the number and locations of the anchors on the translational
31
32 diffusion of membrane-bound nanostructures, we analyzed the diffusion of DNA nanostructures
33
34 bearing two and five TEG-chol anchors attached with 9ss and 18ds DNA spacers: B2 + C4 vs A0
35
36 + C4 combinations and LB5 (five anchors attached along the center helix B: B0 + B1 + B2 + B3
37
38 + B4) vs X5 combinations (Figure 4B). For cholesteryl-modified DNA nanostructures with 18ds
39
40 DNA spacers, the diffusion coefficient of membrane-bound DNA nanostructure was generally
41
42 lower with five TEG-chol anchors (specifically structure X5) than with two, in good agreement
43
44 with previous studies^{18, 23, 32}. Interestingly, when the TEG-chol anchors were attached using 9ss
45
46 DNA spacers, the diffusion of membrane-bound DNA nanostructures was independent of the
47
48 number of anchors, within the error bounds (see SA Table 7 for details). The diffusion
49
50 coefficients of structures with the same number of TEG-chol anchors but different locations
51
52 showed no clear trend, although some differences were evident, as for the cases of B2 + C4 and
53
54
55
56
57
58
59
60

III.2 Control of membrane binding and diffusion of cholesteryl-modified DNA origami nanostructures by DNA spacers

1
2
3
4
5
6
7
8
9
10
11
12
13
14
15
16
17
18
19
20
21
22
23
24
25
26
27
28
29
30
31
32
33
34
35
36
37
38
39
40
41
42
43
44
45
46
47
48
49
50
51
52
53
54
55
56
57
58
59
60

A0 + C4 with 9ss DNA spacers or LB5 and X5 with 18ds DNA spacers. Additionally, we observed that cholesteryl-modified X5 DNA nanostructures with single-stranded DNA spacers (9ss and 18ss) showed 10-20% faster diffusion in comparison to structures lacking additional DNA spacer (no spacer), while in the case of 18ds DNA spacers the diffusion was slower (Figure 4C).

We attribute the differences observed between nanostructures carrying single- and double-stranded DNA spacers to their distinct physical properties. On the one hand, we attribute the differences observed between nanostructures carrying single- and double-stranded DNA spacers to their distinct physical properties. On the one hand, the diameter of single-stranded DNA is ≈ 1.3 nm⁵², while the diameter of double-stranded DNA is ≈ 2.5 nm⁵³. Thus, when pulled into the lipid bilayer by the TEG-chol anchor, single-stranded DNA spacers being comparable by diameter with the dimensions of a lipid headgroup will move more readily through the lipid leaflet in comparison to thicker double-stranded DNA spacers, resulting in a smaller diffusion coefficient for the structures with double-stranded DNA spacers. On the other hand, single-stranded DNA spacers are more flexible than the 18ds DNA spacer, which may result in a loss of orientation of the TEG-chol anchors towards the membrane. Although the contour lengths of the 9ss and 18ds DNA spacers are similar (5.4 nm for 9ss DNA spacers, taking into account the length per base of 0.6 nm⁵⁴; 6.1 nm for 18ds DNA spacers, taking into account the length per base pair of 0.34 nm⁵³), the persistence length of single- and double-stranded DNA is strikingly different (2.2 nm and 50 nm, respectively)⁵³⁻⁵⁷. Indeed, 9ss DNA spacers can be described using the worm-like chain model⁵⁸, which gives the root mean square end-to-end distance of ≈ 3.9 nm, only 1.6 times smaller than the length of the stiff-rod 18ds DNA spacer. For 18ss DNA spacers

1
2
3 with a contour length of 10.8 nm, the root mean square end-to-end distance (≈ 6.2 nm) is
4
5 essentially the same as the length of the 18ds DNA spacer.
6
7

8
9 Measuring diffusion coefficients of membrane-bound DNA origami nanostructures allows one to
10
11 semi-quantitatively characterize their binding to the lipid bilayer. Indeed, it is well known that
12
13 the diffusion coefficient of a membrane inclusion depends on the surface membrane viscosity,
14
15 the viscosities of the surrounding bulk media, as well on the membrane inclusion size⁵⁹⁻⁶⁰. If the
16
17 membrane surface viscosity and bulk viscosities of the surrounding media are known, knowledge
18
19 of the diffusion coefficient allows one to determine the *effective* inclusion size of the membrane-
20
21 bound nanostructure. This effective inclusion size, i.e. the size of a cylindrical inclusion that
22
23 would have the same diffusion coefficient under the same conditions, depends not only on the
24
25 size of the nanostructure, but also on how tightly it is bound to the lipid bilayer. To do this, we
26
27 use the analytical approximation⁶¹⁻⁶² of the exact model⁶⁰ for the diffusion coefficient of a
28
29 circular membrane inclusion for all combinations of the viscosities and inclusion sizes. In doing
30
31 this, we assume the surface viscosity of the DOPC membranes to be $\eta_m = 5.9 \times 10^{-10}$ Pa s m⁶³
32
33 and the viscosity of the surrounding bulk medium (aqueous solution) $\eta = 8.42 \times 10^{-4}$ Pa s (at 27.5
34
35 °C)⁴². From the experimentally determined diffusion coefficients, the estimated effective radii of
36
37 membrane inclusions are $a = 3.5 \pm 1.5$ nm in case of the 18ds DNA spacers ($D = 2.7 \pm 0.2$
38
39 $\mu\text{m}^2/\text{s}$) and $a = 0.8 \pm 0.4$ nm in case of the 18ss DNA spacers ($D = 3.4 \pm 0.3$ $\mu\text{m}^2/\text{s}$). Thus, by
40
41 simply changing the DNA spacer, we can vary the effective inclusion size of the membrane-
42
43 bound DNA nanostructures by a factor of three.
44
45
46
47
48
49
50
51
52
53
54
55
56
57
58
59
60

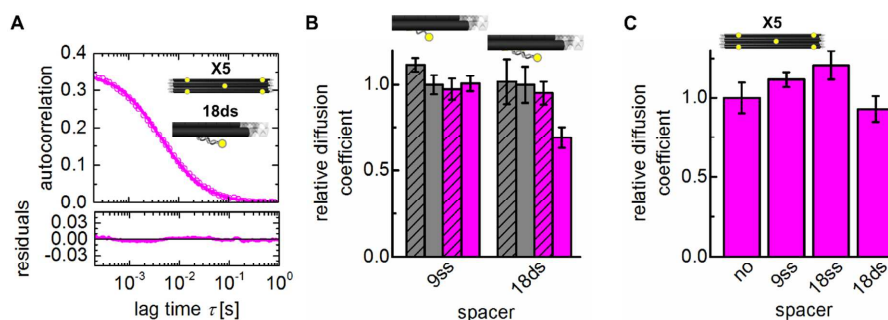


Figure 4. Effects of TEG-chol number and DNA spacer type on the translational diffusion of membrane-bound DNA nanostructures on DOPC GUVs. (A) Representative autocorrelation curve (circles), single-component 2D diffusion fit (line) and the respective residuals for membrane-bound DNA nanostructure X5 (A0 + A4 + B2 + C0 + C4) with 18ds DNA spacer. Reduced surface density $\rho = 0.3$. Each origami structure was labeled with three Alexa488 dyes. (B) Relative diffusion coefficient of membrane-bound DNA nanostructures bearing two TEG-cholesterol anchors at locations B2 + C4 (shaded grey) and A0 + C4 (grey) or five TEG-cholesterol anchors located along helix B (B0 + B1 + B2 + B3 + B4, denoted LB5) (shaded magenta) or in a cross-shape (X5) (magenta). Each data set is normalized to the diffusion coefficient of the respective A0 + C4 DNA nanostructure. (C) Relative diffusion coefficient of membrane-bound TEG-cholesterol-modified DNA nanostructures X5 using no, 9ss, 18ss and 18ds DNA spacers. Data sets were normalized to the diffusion coefficient of the nanostructure modified carrying no DNA spacers. Error bars in B and C typically correspond to the standard deviation of measurements on 6 GUVs. The significance analysis of the data is summarized in SA Tables 6-9.

1
2
3 Finally, we studied diffusion coefficients of X5 DNA nanostructures on DOPC GUVs containing
4
5 10 mol% of negatively charged lipid DOPS or positively charged lipid DOTAP. Previously, it
6
7 has been shown that the membrane surface viscosity of DOPC/DOTAP mixtures is the same as
8
9 that of pure DOPC at least up to 10 mol% of cationic lipid ⁶³. It is reasonable to assume that the
10
11 same situation holds also for DOPC/DOPS mixtures. The presence of the negatively charged
12
13 lipid DOPS did not influence the diffusion of membrane-bound DNA nanostructures,
14
15 irrespectively of the DNA spacer used (Supporting Figure 4, see also SA Tables 11). On the
16
17 contrary, the presence of the positively charged lipid DOTAP had a strikingly different effect on
18
19 TEG-chol modified DNA nanostructures (Figure 5A): while DOTAP slowed down the diffusion
20
21 of the X5 nanostructure with 9ss DNA spacers, the X5 nanostructure with 18ds DNA spacers
22
23 diffused faster on DOPC/DOTAP 9:1 GUVs than on pure zwitterionic DOPC GUVs. Notably,
24
25 the presence of 10 mol% of negatively or positively charged lipid did not influence the lipid
26
27 diffusion (Supporting Figure 5, see also SA Table 12). Interestingly, efficient membrane binding
28
29 of DNA nanostructures to DOPC/DOTAP 9:1 GUVs can be achieved even without TEG-chol
30
31 anchors. Indeed, binding of bare DNA nanostructure N to cationic membranes was almost as
32
33 strong as for DNA nanostructures with five cholesteryl modifications, independently of the DNA
34
35 spacer used (Supporting Figure 6, see also SA Table 14). Taking this into account, we suggest
36
37 that the mode of interaction of DNA nanostructures with DOPC/DOTAP GUVs is fundamentally
38
39 different compared to DOPC or DOPC/DOPS membranes, where binding of DNA
40
41 nanostructures occurred only upon modification with TEG-chol anchors. If one considers that the
42
43 binding to DOPC/DOTAP 9:1 GUVs is achieved via the bottom facet where the TEG-chol
44
45 anchors are attached ⁶⁴, in addition to the TEG-chol insertion, tight attraction between the lipids
46
47 and the membrane-facing side of the DNA nanostructure can be established as a result of strong
48
49
50
51
52
53
54
55
56
57
58
59
60

III.2 Control of membrane binding and diffusion of cholesteryl-modified DNA origami nanostructures by DNA spacers

1
2
3
4
5
6
7
8
9
10
11
12
13
14
15
16
17
18
19
20
21
22
23
24
25
26
27
28
29
30
31
32
33
34
35
36
37
38
39
40
41
42
43
44
45
46
47
48
49
50
51
52
53
54
55
56
57
58
59
60

electrostatic forces between DNA and the oppositely charged membrane^{63, 65-69}. This results in a slower diffusion of membrane-bound DNA nanostructures on DOPC/DOTAP GUVs in comparison to pure DOPC. In the case of 18ds DNA spacers in DNA nanostructures binding to DOPC/DOTAP 9:1 GUVs, a stiff double stranded DNA is present at location B2. This center spacer is subject to electrostatic repulsion away from the bulky DNA nanostructure. Consequently, the effective cross-section of interaction with the lipid bilayer is reduced, resulting in a faster DNA nanostructure diffusion compared to the bare DNA nanostructure N on the same cationic membrane (Figure 5B). Note that the lower charge density and higher flexibility of 9ss DNA spacers will result in a smaller influence of the modification at location B2 on the surface area interacting with the lipid membrane, and consequently on the translational diffusion coefficient, than in absence of this modification. Strikingly, the removal of the TEG-chol anchor in location B2 (structure R4, combination of locations A0 + A4 + C0 + C4) resulted in a slower diffusion of membrane-bound DNA nanostructures than with combination X5, displaying a TEG-chol anchor at location B2 (Figure 5B). Moreover, the diffusion coefficient of SQ nanostructures with 9ss DNA spacers resembled that of the bare DNA origami nanostructure N. Indeed, for nanostructure R4 TEG-chol with 9ss DNA spacers, the estimated effective radius of membrane inclusion ($a = 6 \pm 3$ nm for $D = 2.4 \pm 0.3 \mu\text{m}^2/\text{s}$) matches that of the bare structure N ($a = 6 \pm 5$ nm for $D = 2.3 \pm 0.4 \mu\text{m}^2/\text{s}$) (Figure 5C). In comparison, for nanostructure X5 with TEG-chol anchors attached using 18ds DNA spacers, the effective radius is considerably smaller $a = 1.3 \pm 0.6$ nm ($D = 3.2 \pm 0.2 \mu\text{m}^2/\text{s}$). Notably the effective inclusion radii of nanostructure N and R4 with 9ss DNA spacers on such cationic membranes are larger than for the DNA nanostructures and DOPC membranes discussed above, suggesting a tighter interaction with the lipid bilayer dominated by electrostatic interactions.

1
2
3 Theoretical and experimental results show that for a rod-like particle with large enough aspect
4 ratio (in our case ≈ 7) fully inserted into a lipid bilayer, the effective radius is expected to be \approx
5
6
7
8
9
10
11
12
13
14
15
16
17
18
19
20
21
22
23
24
25
26
27
28
29
30
31
32
33
34
35
36
37
38
39
40
41
42
43
44
45
46
47
48
49
50
51
52
53
54
55
56
57
58
59
60

(0.3-0.5) L , provided that $L/l_{SD} \lesssim 1$, where l_{SD} is the Saffman-Delbrück length $l_{SD} = \eta_m / (\eta_1 + \eta_2)$, where $\eta_{1,2}$ are the viscosities of the surrounding media (in our case $L/l_{SD} \approx 0.4$, and the latter condition is satisfied reasonably well)⁷⁰⁻⁷⁴. The effective inclusion radii in all cases discussed above are much smaller than the expected effective inclusion size for our DNA nanostructures in case they are fully inserted into the lipid bilayer, which means that the DNA nanostructures are gliding over the membrane surface, as previously suggested¹⁸. Note that, since the distance between individual anchors is considerably smaller than the Saffman-Delbrück length l_{SD} , the drag on the membrane bound DNA origami nanostructure cannot be represented as a sum of the drags on the individual cholesteryl anchors.

It would be instructive to compare these results of diffusion of DNA nanostructures on lipid bilayers with their diffusion on lipid monolayers. Recently, we found the effective inclusion size of X5 with 18ds DNA spacers in low density DMPC monolayers to be of ≈ 28 nm⁷⁵, which suggests that in this case the DNA nanostructure is almost fully inserted into the lipid monolayer. This manifests the crucial difference in the molecular organization of lipid monolayers, featuring a relatively loose arrangement of lipids, and bilayers, where lipid molecules are tightly packed together.

1
2
3
4
5
6
7
8
9
10
11
12
13
14
15
16
17
18
19
20
21
22
23
24
25
26
27
28
29
30
31
32
33
34
35
36
37
38
39
40
41
42
43
44
45
46
47
48
49
50
51
52
53
54
55
56
57
58
59
60

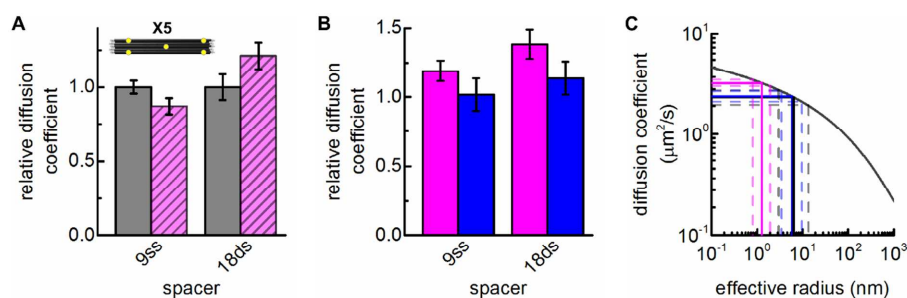


Figure 5. Influence of single- and double-stranded DNA spacers on the dynamics of cholesteryl-modified DNA nanostructures bound to DOPC/DOTAP 9:1 GUVs. (A) Relative diffusion coefficient of membrane-bound X5 DNA nanostructures on pure DOPC GUVs (grey) and DOPC/DOTAP 9:1 GUVs (shaded magenta). Each data set is normalized to the respective diffusion coefficient in pure DOPC. (B) Relative diffusion coefficient of membrane-bound X5 (magenta) and R4 (combination of locations A0 + A4 + C0 + C4, blue) DNA nanostructures on DOPC/DOTAP 9:1 GUVs. The data are normalized to the diffusion coefficient of bare structure N under the same conditions. (C) The dependence of the diffusion coefficient of a membrane inclusion on its size (grey line) allows one to estimate the effective inclusion size of membrane-bound DNA nanostructures. The estimates of the effective radii of bare DNA nanostructure N (black line), X5 using 18ds DNA spacers (magenta line) and R4 using 9ss DNA spacers (blue line) bound to DOPC/DOTAP 9:1 GUVs are superimposed with the respective standard deviations (dashed lines). The significance analysis of the data is summarized in SA Tables 15,16.

1
2
3
4
5
6
7
8
9
10
11
12
13
14
15
16
17
18
19
20
21
22
23
24
25
26
27
28
29
30
31
32
33
34
35
36
37
38
39
40
41
42
43
44
45
46
47
48
49
50
51
52
53
54
55
56
57
58
59
60

CONCLUSIONS

Here, we presented an extensive study of the effect of anchor placement and spacer length on the binding and diffusion of cholesteryl-modified DNA origami nanostructures on lipid membranes. Our results show that attaching cholesteryl anchors via DNA spacers overcomes local steric hindrances, i.e. limited accessibility of the anchors positioned closer to the bulky DNA nanostructure. Indeed, the use of DNA spacers increases the membrane binding efficiency of cholesteryl-modified DNA nanostructures, even when only a single anchor in the center of the structure is present. Importantly, we show that double-stranded DNA spacers in TEG-chol modified nanostructures are more efficient for membrane binding and less sensitive to charge variations in the environment, in comparison with single-stranded spacers. Furthermore, our results on membrane binding efficiencies and diffusion of cholesteryl-modified DNA nanostructures allowed us to unravel details of the mechanism of their interaction with lipid membranes. Ultimately, we hereby provide a modular approach to control the membrane affinity and dynamics of amphipathic DNA nanostructures using DNA spacers.

ASSOCIATED CONTENT

The following files are available free of charge.

Supporting information (PDF)

Statistical analysis (PDF)

AUTHOR INFORMATION

Corresponding Author

*e-mail: schwille@biochem.mpg.de

1
2
3
4
5
6
7
8
9
10
11
12
13
14
15
16
17
18
19
20
21
22
23
24
25
26
27
28
29
30
31
32
33
34
35
36
37
38
39
40
41
42
43
44
45
46
47
48
49
50
51
52
53
54
55
56
57
58
59
60

Author Contributions

A K, H G F and P S conceived the study. A K designed and performed all experiments. A K, J M and H G F analyzed the data. A K, J M, H G F and E P P interpreted the data. All authors contributed to the writing of the manuscript. All authors have given approval to the final version of the manuscript.

ACKNOWLEDGMENTS

This work has been supported by the collaborative research project SFB 863 of the Deutsche Forschungsgemeinschaft. A K acknowledges the support of the Graduate School of Quantitative Biosciences Munich; J.M. acknowledges support from the excellence cluster Nanosystems Initiative Munich and the International Max Planck Research School for Molecular Life Sciences; H G F acknowledges the receipt of a Humboldt Research Fellowship (PTG/1152511/STP); E P P acknowledges the financial support by the Deutsche Forschungsgemeinschaft within the SFB 1032 TP B01 and A09. Further support was given by the Max Planck Society to P S. The authors specially thank Prof. Joachim Rädler and the members of the Munich DNA Node for fruitful discussions and expert advice.

1
2
3
4
5
6
7
8
9
10
11
12
13
14
15
16
17
18
19
20
21
22
23
24
25
26
27
28
29
30
31
32
33
34
35
36
37
38
39
40
41
42
43
44
45
46
47
48
49
50
51
52
53
54
55
56
57
58
59
60

REFERENCES

1. Rothemund, P. W. K., Folding DNA to create nanoscale shapes and patterns. *Nature* **2006**, *440* (7082), 297-302.
2. Douglas, S. M.; Dietz, H.; Liedl, T.; Högberg, B.; Graf, F.; Shih, W. M., Self-assembly of DNA into nanoscale three-dimensional shapes. *Nature* **2009**, *459* (7245), 414-418.
3. Dietz, H.; Douglas, S. M.; Shih, W. M., Folding DNA into Twisted and Curved Nanoscale Shapes. *Science* **2009**, *325* (5941), 725-730.
4. Czogalla, A.; Franquelim, Henri G.; Schwille, P., DNA Nanostructures on Membranes as Tools for Synthetic Biology. *Biophys. J.* **2016**, *110* (8), 1698-1707.
5. Simmel, F. C., DNA-based assembly lines and nanofactories. *Curr. Opin. Biotechnol.* **2012**, *23* (4), 516-521.
6. Hong, F.; Zhang, F.; Liu, Y.; Yan, H., DNA Origami: Scaffolds for Creating Higher Order Structures. *Chem. Rev.* **2017**, *117* (20), 12584-12640.
7. Nummelin, S.; Kommeri, J.; Kostiainen, M. A.; Linko, V., Evolution of Structural DNA Nanotechnology. *Adv. Mater.* **2018**, doi: 10.1002/adma.201703721.
8. Lagny, T. J.; Bassereau, P., Bioinspired membrane-based systems for a physical approach of cell organization and dynamics: usefulness and limitations. *Interface Focus* **2015**, *5* (4), 20150038.
9. Göpfrich, K.; Platzman, I.; Spatz, J. P., Mastering Complexity: Towards Bottom-up Construction of Multifunctional Eukaryotic Synthetic Cells. *Trends Biotechnol.* **2018**, doi: 10.1016/j.tibtech.2018.03.008.
10. Chan, Y.-H. M.; van Lengerich, B.; Boxer, S. G., Effects of linker sequences on vesicle fusion mediated by lipid-anchored DNA oligonucleotides. *Proc. Natl. Acad. Sci.* **2009**, *106* (4), 979-84.
11. Pfeiffer, I.; Höök, F., Bivalent Cholesterol-Based Coupling of Oligonucleotides to Lipid Membrane Assemblies. *J. Am. Chem. Soc.* **2004**, *126* (33), 10224-10225.
12. Banchelli, M.; Gambinossi, F.; Durand, A.; Caminati, G.; Brown, T.; Berti, D.; Baglioni, P., Modulation of Density and Orientation of Amphiphilic DNA on Phospholipid Membranes. II. Vesicles. *J. Phys. Chem. B* **2010**, *114* (21), 7348-7358.
13. Bunge, A.; Loew, M.; Pescador, P.; Arbizova, A.; Brodersen, N.; Kang, J.; Dähne, L.; Liebscher, J.; Herrmann, A.; Stengel, G.; Huster, D., Lipid Membranes Carrying Lipophilic Cholesterol-Based Oligonucleotides—Characterization and Application on Layer-by-Layer Coated Particles. *J. Phys. Chem. B* **2009**, *113* (51), 16425-16434.
14. Bunge, A.; Kurz, A.; Windeck, A.-K.; Korte, T.; Flasche, W.; Liebscher, J.; Herrmann, A.; Huster, D., Lipophilic Oligonucleotides Spontaneously Insert into Lipid Membranes, Bind Complementary DNA Strands, and Sequester into Lipid-Disordered Domains. *Langmuir* **2007**, *23* (8), 4455-4464.

III.2 Control of membrane binding and diffusion of cholesteryl-modified DNA origami nanostructures by DNA spacers

1
2
3
4
5
6
7
8
9
10
11
12
13
14
15
16
17
18
19
20
21
22
23
24
25
26
27
28
29
30
31
32
33
34
35
36
37
38
39
40
41
42
43
44
45
46
47
48
49
50
51
52
53
54
55
56
57
58
59
60

15. Börjesson, K.; Lundberg, E. P.; Woller Jakob, G.; Nordén, B.; Albinsson, B., Soft-Surface DNA Nanotechnology: DNA Constructs Anchored and Aligned to Lipid Membrane. *Angew. Chem. Int. Ed.* **2011**, *50* (36), 8312-8315.
16. Banchelli, M.; Betti, F.; Berti, D.; Caminati, G.; Bombelli, F. B.; Brown, T.; Wilhelmsson, L. M.; Nordén, B.; Baglioni, P., Phospholipid Membranes Decorated by Cholesterol-Based Oligonucleotides as Soft Hybrid Nanostructures. *J. Phys. Chem. B* **2008**, *112* (35), 10942-10952.
17. Czogalla, A.; Petrov, E. P.; Kauert, D. J.; Uzunova, V.; Zhang, Y.; Seidel, R.; Schwille, P., Switchable domain partitioning and diffusion of DNA origami rods on membranes. *Faraday Discuss.* **2013**, *161*, 31-43.
18. Czogalla, A.; Kauert, D. J.; Seidel, R.; Schwille, P.; Petrov, E. P., DNA Origami Nanoneedles on Freestanding Lipid Membranes as a Tool To Observe Isotropic–Nematic Transition in Two Dimensions. *Nano Lett.* **2015**, *15* (1), 649-655.
19. Johnson-Buck, A.; Jiang, S.; Yan, H.; Walter, N. G., DNA–Cholesterol Barges as Programmable Membrane-Exploring Agents. *ACS Nano* **2014**, *8* (6), 5641-5649.
20. List, J.; Weber, M.; Simmel, F. C., Hydrophobic Actuation of a DNA Origami Bilayer Structure. *Angew. Chem. Int. Ed.* **2014**, *53* (16), 4236-4239.
21. Suzuki, Y.; Endo, M.; Yang, Y.; Sugiyama, H., Dynamic Assembly/Disassembly Processes of Photoresponsive DNA Origami Nanostructures Directly Visualized on a Lipid Membrane Surface. *J. Am. Chem. Soc.* **2014**, *136* (5), 1714-1717.
22. Avakyan, N.; Conway, J. W.; Sleiman, H. F., Long-Range Ordering of Blunt-Ended DNA Tiles on Supported Lipid Bilayers. *J. Am. Chem. Soc.* **2017**, *139* (34), 12027-12034.
23. Kocabay, S.; Kempter, S.; List, J.; Xing, Y.; Bae, W.; Schiffels, D.; Shih, W. M.; Simmel, F. C.; Liedl, T., Membrane-Assisted Growth of DNA Origami Nanostructure Arrays. *ACS Nano* **2015**, *9* (4), 3530-3539.
24. Czogalla, A.; Kauert, D. J.; Franquelim, H. G.; Uzunova, V.; Zhang, Y.; Seidel, R.; Schwille, P., Amphipathic DNA Origami Nanoparticles to Scaffold and Deform Lipid Membrane Vesicles. *Angew. Chem. Int. Ed.* **2015**, *54* (22), 6501-6505.
25. Franquelim, H. G.; Khmelinskaia, A.; Sobczak, J.-P.; Dietz, H.; Schwille, P., Membrane sculpting by curved DNA origami scaffolds. *Nat. Commun.* **2018**, *9* (1), 811.
26. Grome, M. W.; Zhang, Z.; Pincet, F.; Lin, C., Vesicle Tubulation with Self-Assembling DNA Nanosprings. *Angew. Chem. Int. Ed.* **2018**, *57* (19), 5330-5334.
27. Langecker, M.; Arnaut, V.; Martin, T. G.; List, J.; Renner, S.; Mayer, M.; Dietz, H.; Simmel, F. C., Synthetic Lipid Membrane Channels Formed by Designed DNA Nanostructures. *Science* **2012**, *338* (6109), 932-936.
28. Göpfrich, K.; Li, C.-Y.; Ricci, M.; Bhamidimarri, S. P.; Yoo, J.; Gyenes, B.; Ohmann, A.; Winterhalter, M.; Aksimentiev, A.; Keyser, U. F., Large-Conductance Transmembrane Porin Made from DNA Origami. *ACS Nano* **2016**, *10* (9), 8207-8214.

- 1
2
3
4
5
6
7
8
9
10
11
12
13
14
15
16
17
18
19
20
21
22
23
24
25
26
27
28
29
30
31
32
33
34
35
36
37
38
39
40
41
42
43
44
45
46
47
48
49
50
51
52
53
54
55
56
57
58
59
60
29. Göpfrich, K.; Zettl, T.; Meijering, A. E. C.; Hernández-Ainsa, S.; Kocabey, S.; Liedl, T.; Keyser, U. F., DNA-Tile Structures Induce Ionic Currents through Lipid Membranes. *Nano Lett.* **2015**, *15* (5), 3134-3138.
30. Ohmann, A.; Li, C.-Y.; Maffeo, C.; Al Nahas, K.; Baumann, K. N.; Göpfrich, K.; Yoo, J.; Keyser, U. F.; Aksimentiev, A., A synthetic enzyme built from DNA flips 107 lipids per second in biological membranes. *Nat. Commun.* **2018**, *9* (1), 2426.
31. Akbari, E.; Mollica, M. Y.; Lucas, C. R.; Bushman, S. M.; Patton, R. A.; Shahhosseini, M.; Song, J. W.; Castro, C. E., Engineering Cell Surface Function with DNA Origami. *Adv. Mater.* **2017**, *29* (46), 1703632.
32. Khmelinskaia, A.; Franquelim, H. G.; Petrov, E. P.; Schwille, P., Effect of anchor positioning on binding and diffusion of elongated 3D DNA nanostructures on lipid membranes. *J. Phys. D: Appl. Phys.* **2016**, *49* (19), 194001.
33. Angelova, M. I.; Dimitrov, D. S., Liposome electroformation. *Faraday Discuss. Chem. Soc.* **1986**, *81*, 303-311.
34. Garcia-Saez, A. J.; Carrer, D. C.; Schwille, P., Fluorescence correlation spectroscopy for the study of membrane dynamics and organization in giant unilamellar vesicles. *Methods Mol. Biol.* **2010**, *606*, 493-508.
35. Thomas, F. A.; Visco, I.; Petrášek, Z.; Heinemann, F.; Schwille, P., Introducing a fluorescence-based standard to quantify protein partitioning into membranes. *Biochim. Biophys. Acta, Biomembr.* **2015**, *1848* (11, Part A), 2932-2941.
36. Schindelin, J.; Rueden, C. T.; Hiner, M. C.; Eliceiri, K. W., The ImageJ ecosystem: An open platform for biomedical image analysis. *Mol. Reprod. Dev.* **2015**, *82* (7-8), 518-529.
37. Petrov, E. P.; Ohrt, T.; Winkler, R. G.; Schwille, P., Diffusion and Segmental Dynamics of Double-Stranded DNA. *Phys. Rev. Lett.* **2006**, *97* (25), 258101.
38. Petrášek, Z.; Schwille, P., Precise Measurement of Diffusion Coefficients using Scanning Fluorescence Correlation Spectroscopy. *Biophys. J.* **2008**, *94* (4), 1437-1448.
39. Müller, C. B.; Loman, A.; Pacheco, V.; Koberling, F.; Willbold, D.; Richtering, W.; Enderlein, J., Precise measurement of diffusion by multi-color dual-focus fluorescence correlation spectroscopy. *Europhys. Lett.* **2008**, *83* (4), 46001.
40. Sutherland, W., LXXV. A dynamical theory of diffusion for non-electrolytes and the molecular mass of albumin. *The London, Edinburgh, and Dublin Philosophical Magazine and Journal of Science* **1905**, *9* (54), 781-785.
41. Einstein, A., Über die von der molekularkinetischen Theorie der Wärme geforderte Bewegung von in ruhenden Flüssigkeiten suspendierten Teilchen. *Annalen der Physik* **1905**, *322* (8), 549-560.
42. Kestin, J.; Sokolov, M.; Wakeham, W. A., Viscosity of liquid water in the range $-8\text{ }^{\circ}\text{C}$ to $150\text{ }^{\circ}\text{C}$. *J. Phys. Chem. Ref. Data* **1978**, *7* (3), 941-948.

III.2 Control of membrane binding and diffusion of cholesteryl-modified DNA origami nanostructures by DNA spacers

1
2
3
4
5
6
7
8
9
10
11
12
13
14
15
16
17
18
19
20
21
22
23
24
25
26
27
28
29
30
31
32
33
34
35
36
37
38
39
40
41
42
43
44
45
46
47
48
49
50
51
52
53
54
55
56
57
58
59
60

43. Widengren, J.; Mets, U.; Rigler, R., Fluorescence correlation spectroscopy of triplet states in solution: a theoretical and experimental study. *J. Phys. Chem.* **1995**, *99* (36), 13368-13379.
44. Gregor, I.; Patra, D.; Enderlein, J., Optical Saturation in Fluorescence Correlation Spectroscopy under Continuous-Wave and Pulsed Excitation. *ChemPhysChem* **2005**, *6* (1), 164-170.
45. Petrov, E. P.; Schwille, P., State of the Art and Novel Trends in Fluorescence Correlation Spectroscopy. In *Standardization and Quality Assurance in Fluorescence Measurements II: Bioanalytical and Biomedical Applications*, Resch-Genger, U., Ed. Springer Berlin Heidelberg: Berlin, Heidelberg, 2008; pp 145-197.
46. Thompson, N. L., Fluorescence Correlation Spectroscopy. In *Topics in Fluorescence Spectroscopy*, Lakowicz, J. R., Ed. Plenum Press: New York, 1991; Vol. 1: Techniques, pp 337-378.
47. Harayama, T.; Riezman, H., Understanding the diversity of membrane lipid composition. *Nat. Rev. Mol. Cell Biol.* **2018**, *19* (5), 281-296.
48. van Meer, G.; Voelker, D. R.; Feigenson, G. W., Membrane lipids: where they are and how they behave. *Nat. Rev. Mol. Cell Biol.* **2008**, *9* (2), 112-124.
49. Harries, D.; May, S.; Ben-Shaul, A., Counterion release in membrane-biopolymer interactions. *Soft Matter* **2013**, *9* (39), 9268-9284.
50. Gromelski, S.; Brezesinski, G., DNA Condensation and Interaction with Zwitterionic Phospholipids Mediated by Divalent Cations. *Langmuir* **2006**, *22* (14), 6293-6301.
51. Hirtz, M.; Brglez, J.; Fuchs, H.; Niemeyer, C. M., Selective Binding of DNA Origami on Biomimetic Lipid Patches. *Small* **2015**, *11* (43), 5752-5758.
52. Arnott, S.; Chandrasekaran, R.; Leslie, A. G., Structure of the single-stranded polyribonucleotide polycytidylic acid. *J. Mol. Biol.* **1976**, *106* (3), 735-748.
53. Bloomfield, V. A.; Crothers, D. M.; Hearst, J. E.; Tinoco, I., *Nucleic acids : structures, properties, and functions*. Univ. Science Books: Sausalito, Calif, 2000.
54. Chi, Q.; Wang, G.; Jiang, J., The persistence length and length per base of single-stranded DNA obtained from fluorescence correlation spectroscopy measurements using mean field theory. *Physica A Stat. Mech. Appl.* **2013**, *392* (5), 1072-1079.
55. Smith, S. B.; Cui, Y.; Bustamante, C., Overstretching B-DNA: the elastic response of individual double-stranded and single-stranded DNA molecules. *Science* **1996**, *271* (5250), 795-799.
56. Tinland, B.; Pluen, A.; Sturm, J.; Weill, G., Persistence length of single-stranded DNA. *Macromolecules* **1997**, *30* (19), 5763-5765.
57. Murphy, M.; Rasnik, I.; Cheng, W.; Lohman, T. M.; Ha, T., Probing single-stranded DNA conformational flexibility using fluorescence spectroscopy. *Biophys. J.* **2004**, *86* (4), 2530-2537.
58. van der Maarel, J. R. C., *Introduction to Biopolymer Physics*. WORLD SCIENTIFIC: 2008; p 264.

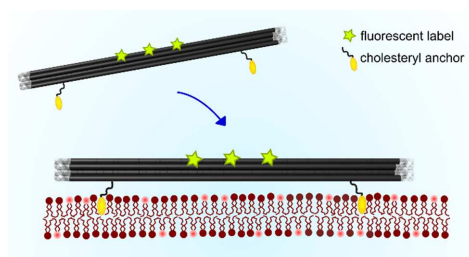
- 1
2
3
4
5
6
7
8
9
10
11
12
13
14
15
16
17
18
19
20
21
22
23
24
25
26
27
28
29
30
31
32
33
34
35
36
37
38
39
40
41
42
43
44
45
46
47
48
49
50
51
52
53
54
55
56
57
58
59
60
59. Saffman, P. G.; Delbrück, M., Brownian motion in biological membranes. *Proc. Natl. Acad. Sci.* **1975**, *72* (8), 3111-3113.
60. Hughes, B. D.; Pailthorpe, B. A.; White, L. R., The translational and rotational drag on a cylinder moving in a membrane. *J. Fluid Mech.* **1981**, *110*, 349-372.
61. Petrov, E. P.; Schwille, P., Translational Diffusion in Lipid Membranes beyond the Saffman-Delbrück Approximation. *Biophys. J.* **2008**, *94* (5), L41-L43.
62. Petrov, E. P.; Petrosyan, R.; Schwille, P., Translational and rotational diffusion of micrometer-sized solid domains in lipid membranes. *Soft Matter* **2012**, *8* (29), 7552-7555.
63. Herold, C.; Schwille, P.; Petrov, E. P., DNA Condensation at Freestanding Cationic Lipid Bilayers. *Phys. Rev. Lett.* **2010**, *104* (14), 148102.
64. Gopinath, A.; Miyazono, E.; Faraon, A.; Rothmund, P. W. K., Engineering and mapping nanocavity emission via precision placement of DNA origami. *Nature* **2016**, *535* (7612), 401-405.
65. Herold, C.; Schwille, P.; Petrov, E. P., Single DNA molecules on freestanding and supported cationic lipid bilayers: diverse conformational dynamics controlled by the local bilayer properties. *J. Phys. D: Appl. Phys.* **2016**, *49* (7), 074001.
66. Kahl, V.; Hennig, M.; Maier, B.; Rädler, J. O., Conformational dynamics of DNA-electrophoresis on cationic membranes. *Electrophoresis* **2009**, *30* (8), 1276-1281.
67. Maier, B.; Rädler, J. O., DNA on fluid membranes: a model polymer in two dimensions. *Macromolecules* **2000**, *33* (19), 7185-7194.
68. Maier, B.; Rädler, J. O., Conformation and self-diffusion of single DNA molecules confined to two dimensions. *Phys. Rev. Lett.* **1999**, *82* (9), 1911.
69. Chang, C.-M.; Lau, Y.-G.; Tsai, J.-C.; Juan, W.-T., Relaxation of DNA on a supported lipid membrane. *Europhys. Lett.* **2012**, *99* (4), 48008.
70. Levine, A. J.; Liverpool, T.; MacKintosh, F., Mobility of extended bodies in viscous films and membranes. *Phys. Rev. E* **2004**, *69* (2), 021503.
71. Levine, A. J.; Liverpool, T.; MacKintosh, F. C., Dynamics of rigid and flexible extended bodies in viscous films and membranes. *Phys. Rev. Lett.* **2004**, *93* (3), 038102.
72. Fischer, T. M., The drag on needles moving in a Langmuir monolayer. *J. Fluid Mech.* **2004**, *498*, 123-137.
73. Dhar, P.; Fischer, T. M.; Wang, Y.; Mallouk, T.; Paxton, W.; Sen, A., Autonomously moving nanorods at a viscous interface. *Nano Lett.* **2006**, *6* (1), 66-72.
74. Klopp, C.; Stannarius, R.; Eremin, A., Brownian dynamics of elongated particles in a quasi-two-dimensional isotropic liquid. *Phys. Rev. Fluids* **2017**, *2* (12), 124202.
75. Khmelinskaia, A.; Mücksch, J.; Conci, F.; Chwastek, G.; Schwille, P., FCS Analysis of Protein Mobility on Lipid Monolayers. *Biophys. J.* **2018**, *114* (10), 2444-2454.

III.2 Control of membrane binding and diffusion of cholesteryl-modified DNA origami nanostructures by DNA spacers

1
2
3
4
5
6
7
8
9
10
11
12
13
14
15
16
17
18
19
20
21
22
23
24
25
26
27
28
29
30
31
32
33
34
35
36
37
38
39
40
41
42
43
44
45
46
47
48
49
50
51
52
53
54
55
56
57
58
59
60

1
2
3
4
5
6
7
8
9
10
11
12
13
14
15
16
17
18
19
20
21
22
23
24
25
26
27
28
29
30
31
32
33
34
35
36
37
38
39
40
41
42
43
44
45
46
47
48
49
50
51
52
53
54
55
56
57
58
59
60

For table of contents only



III.3 FCS analysis of protein mobility on lipid monolayers

The results discussed in this section are the outcome of an equal-contribution collaboration with Jonas Mücksch and have been published as:

Khmelinskaia, A. , Mücksch, J.* , Conci, F., Chwastek, G., Schwille, P. (2018) FCS analysis of protein mobility on lipid monolayers. Biophys. J., 114: 2444-2454. doi: 10.1016/j.bpj.2018.02.031. *indicates equal contributions. A reprint permission has been granted by the publisher. The supplementary information can be found in Appendix D.*

FCS Analysis of Protein Mobility on Lipid Monolayers

Alena Khmelinskaia,¹ Jonas Mücksch,¹ Franco Conci,¹ Grzegorz Chwastek,¹ and Petra Schwille^{1,*}

¹Department of Cellular and Molecular Biophysics, Max Planck Institute of Biochemistry, Martinsried, Germany

ABSTRACT In vitro membrane model systems are used to dissect complex biological phenomena under controlled unadulterated conditions. In this context, lipid monolayers are a powerful tool to particularly study the influence of lipid packing on the behavior of membrane proteins. Here, monolayers deposited in miniaturized fixed area-chambers, which require only minute amounts of protein, were used and shown to faithfully reproduce the characteristics of Langmuir monolayers. This assay is ideally suited to be combined with single-molecule sensitive fluorescence correlation spectroscopy (FCS) to characterize diffusion dynamics. Our results confirm the influence of lipid packing on lipid mobility and validate the use of FCS as an alternative to conventional surface pressure measurements for characterizing the monolayer. Furthermore, we demonstrate the effect of lipid density on the diffusional behavior of membrane-bound components. We exploit the sensitivity of FCS to characterize protein interactions with the lipid monolayer in a regime in which the monolayer physical properties are not altered. To demonstrate the potential of our approach, we analyzed the diffusion behavior of objects of different nature, ranging from a small peptide to a large DNA-based nanostructure. Moreover, in this work we quantify the surface viscosity of lipid monolayers. We present a detailed strategy for the conduction of point FCS experiments on lipid monolayers, which is the first step toward extensive studies of protein-monomer interactions.

INTRODUCTION

Biological membranes have been a predominant focus of biophysical research in the last few decades. Highly complex in their organization, as an interplay between numerous lipid and protein partners, biological membranes are not only a physical barrier between cellular compartments but also directly or indirectly play a fundamental role in several key cellular mechanisms. To facilitate the study of complex membrane-associated phenomena under defined and controlled conditions, a variety of minimal model membrane systems have been developed (1).

From the available in vitro membrane model systems, support-free model membranes are especially attractive as additional interactions with the support can strongly influence the studied behaviors (2,3). Lipid vesicles, black lipid membranes, suspended lipid bilayers and lipid monolayers are some of the most common free-standing model membranes, with each of them bearing particular limitations. Small unilamellar vesicles and large unilamellar vesicles,

with diameters smaller than 1 μm , are mainly used to study protein-membrane interactions in which curvature plays a significant role in the binding (e.g., (4,5)). In contrast, giant unilamellar vesicles (GUVs) with diameters larger than 10 μm are quasi-planar, can be produced at high yields under several salt conditions and are stable over long periods of time (6). Black lipid membranes also do not have an intrinsic curvature but often contain an undefined amount of residual solvent trapped within the lipid leaflets, which is linked to the preparation protocol (7). Solvent-free suspended lipid bilayers, on the other hand, can be formed from the rupture of lipid vesicles but have very limited sizes, up to only a few μm (e.g., (8)).

To study lipid-protein interactions, it is generally desirable to vary a plethora of membrane conditions, including lipid packing density and mobility. In cells, both are strongly related to the local lipid composition and lateral organization (9–11). In vitro, lipid mobility can potentially be controlled through external factors such as membrane composition, ambient bulk viscosity, temperature, and ionic strength (12–14). However, all these factors generally also affect the protein behavior itself, which renders the interpretation of experiments challenging. More importantly, the effect of lipid packing is not accessible by typical model membranes. An elegant system to study its effect is the

Submitted December 6, 2017, and accepted for publication February 27, 2018.

*Correspondence: schwille@biochem.mpg.de

Alena Khmelinskaia and Jonas Mücksch contributed equally to this work.
Editor: Claudia Steinem.

<https://doi.org/10.1016/j.bpj.2018.02.031>

© 2018 Biophysical Society.



III.3 FCS analysis of protein mobility on lipid monolayers

FCS Study of Proteins on Monolayers

Langmuir lipid monolayer, in which a single layer of lipids, deposited on an air-water interface, is mechanically compressed to tune both lipid packing and lipid mobility (15). Typically, experiments on lipid monolayers are performed in Langmuir-Blodgett troughs that require large quantities of precious sample volume (of order of tens of milliliters per sample), which usually precludes them from studies on proteins and peptides. With the recent introduction of miniaturized chambers (16), lipid monolayers are of easy handling and preparation, and require considerably smaller amounts of protein, making them compatible with recombinant proteins, which are typically produced on small lab scales. Notably, although lipid monolayers lack essential features of biological membranes, complex biological networks (such as a minimal actin cortex (17,18), the dynamic behavior of pattern-forming Min proteins, and the assembly of FtsZ filaments (19)) have been successfully reconstituted using this model system.

Changes in lipid packing were proposed to influence the diffusion behavior of protein components in the membrane (15). However, measuring the lateral diffusion of molecules in lipid monolayers has been to date restricted to lipids, which were studied to a minor degree only (15,16,20,21). Here, to quantify mobilities in lipid monolayers, we used fluorescence correlation spectroscopy (FCS) (22). In this method, a fluorescence time trace is recorded from a small detection volume, typically a confocal volume (23,24). Signal fluctuations originating from, e.g., diffusion of fluorescent species through the detection volume are analyzed by means of autocorrelation. The characteristic decay time of the autocorrelation curve is directly linked to the hydrodynamic properties of the fluorescent molecules, whereas the fluorescence intensity is proportional to the average number of molecules in the detection volume. Thus, knowing the size and shape of the confocal volume, estimated through a calibration procedure, and applying an appropriate model function, one gains direct access to the diffusion coefficient D of a given fluorescent species. The amplitude G_0 of the autocorrelation curve scales with the inverse number N of particles in the confocal volume.

In this study, we demonstrate the use of confocal point FCS to study protein mobilities in lipid monolayers. We used miniaturized chambers to measure hitherto unknown diffusion coefficients of proteins on lipid monolayers and correlated the results with the lipid packing and mobility. Furthermore, we characterized the compatibility of several membrane-binding molecules with the lipid monolayer system.

MATERIALS AND METHODS

Chemicals

The lipids 1,2-dimyristoyl-sn-glycero-3-phosphocholine (DMPC), 1,2-dioleoyl-sn-glycero-3-[(N-(5-amino-1-carboxypentyl)iminodiacetic acid)suc-

ciny] (DOGS-NTA(Ni)), ovine brain ganglioside G_{M1} , *Escherichia coli* polar lipid extract, were purchased from Avanti Polar Lipids (Alabaster, AL). ATTO655 and ATTO488 head labeled 1,2-dioleoyl-sn-glycero-3-phosphoethanolamine (DOPE) were purchased from ATTO-TEC (Siegen, Germany). Lipid mixtures were prepared in high purity chloroform (Merck KGaA, Darmstadt, Germany) and their concentration was determined by gravimetry.

Bovine serum albumin was purchased from Sigma-Aldrich (Taufkirchen, Germany). Labeled cholera toxin β (Alexa Fluor 488) was purchased from Invitrogen (Carlsbad, CA). The membrane proximal external region (MPER) of the envelope glycoprotein gp41 of HIV-1, namely the peptide Atto488CELDKAWSLWNWF (underscored sequence corresponds to aa 662–673 by HXBc2 numbering), which presumably dimerizes through a disulfide bond, was purified by the Biochemistry Core Facility of the Max Planck Institute of Biochemistry with degree of purity >90%. The Biochemistry Core Facility of the Max Planck Institute of Biochemistry also purified the MinD, MinE (25), and eGFP-MinD (26) proteins according to the reported protocols. Ramm et al. developed the construct and purification protocol for the chimeric fluorescent protein mCherry carrying the membrane targeting sequence (Mts) of the protein MinD from *Bacillus subtilis* (mCherry-Mts) (B. Ramm, P. Glock, J.M., P. Blumhardt, M. Heymann, and P.S., unpublished data). Purified mNeonGreen was kindly provided by Magnus-Carsten Huppertz, Max Planck Institute of Biochemistry (Martinsried, Germany).

Q buffer (10 mM HEPES, 150 mM NaCl, pH 7.4) was used for most described measurements. M buffer (25 mM Tris-HCl, 150 KCl, 5 mM $MgCl_2$, pH 7.5) was used when working with Min proteins or mCherry-Mts constructs (Table S1). For DNA origami, D buffer (5 mM Tris-HCl, 1 mM EDTA, 5 mM $MgCl_2$, 300 mM NaCl, pH 8.0) was used.

DNA origami folding and purification

The elongated DNA origami structure described in (27) was used. Two variations were produced: unmodified (N) and cholesterol (Chol)-modified (X5) DNA nanostructure. For X5, the oligonucleotides in the bottom positions A0, A4, B2, C0, and C4 (Fig. S1) were extended with an 18 nucleotide sequence complementary to the 5' TEG-Chol modified oligonucleotide AACGAGACCACCCATAGC (Sigma-Aldrich). For detection by fluorescence microscopy and spectroscopy, both N and X5 were functionalized by $3 \times 5'$ ATTO488-modified oligonucleotides GGGTTTGGTGTITTTT (Eurofins, Planegg, Germany), positioned on the top facet close to the center of the structure. Folding, purification, and quantification of DNA nanostructures was performed as previously reported (27).

Monolayer preparation in miniaturized chambers

Customized miniaturized chambers inspired by (16) were manufactured by laser cutting a 15 mm diameter hole into a 5 mm-high polytetrafluoroethylene (PTFE) sheet (Fig. S2). Before every use, the PTFE spacers were cleaned in a series of sonication steps (30 min each) in acetone, chloroform, isopropanol, and ethanol. A chamber was completed by gluing a #1.5 cover glass (Menzel Gläser, Braunschweig, Germany) to the bottom of the PTFE spacer using picodent twinsil 22 two component glue (picodent, Wipperfuerth, Germany). Directly before use, the miniaturized chamber was thoroughly rinsed with distilled milliQ water and 99% ethanol, dried under airflow and plasma cleaned (MiniFlecto-PC-MFC; plasma technology, Herrenberg-Gültstein, Germany) for 10 min to make the glass hydrophilic. The cleaned chambers were filled with 200 μ L of aqueous buffer. The lipid mixture (0.1 mg/mL, containing 0.01 mol% of ATTO655-DOPE or ATTO488-DOPE) was deposited drop-by-drop on the air-buffer interface (Fig. 1 A; see also (16)) to reach the desired lipid density. If required, 20–40 μ L of the aqueous phase were pipetted out after complete evaporation of chloroform to adjust the interface position. The

III. Binding and Diffusion of membrane-bound DNA nanostructures

Khmelinskaia et al.

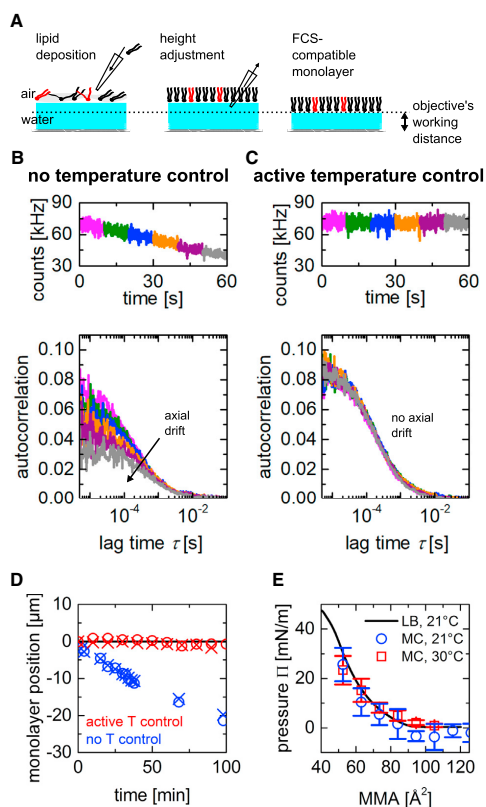


FIGURE 1 Stabilization of the lipid monolayer positioning by using an active temperature control. (A) Schematic representation of lipid monolayer deposition on an air-water interface is shown. A known amount of lipids dissolved in chloroform was deposited drop-by-drop on the air-water interface. If necessary, a small volume (20–40 μ L) of the aqueous subphase was pipetted out to bring the monolayer within the working distance of the used objective. (B and C) Representative intensity traces (upper panels) and corresponding autocorrelation curves (lower panels) of 0.01 mol% Atto655-DOPE in DMPC obtained by point FCS without and with active temperature (T) control, respectively, are shown. The effect of the axial drift on the autocorrelation curves is highlighted in (B), whereas the autocorrelation curves obtained with T control (C) are indistinguishable. (D) Monolayer positions over time without and with active T control are shown. Circles and crosses correspond to independent time series. (E) Surface pressure (Π) measured for DMPC monolayers deposited in miniaturized chambers (MC) with a fixed area at 21°C (circles) and 30°C (squares) is shown. The average of typically four independent samples and respective standard deviations are shown. As a reference, the DMPC Langmuir isotherm (LB) at 21°C is shown (black line). To see this figure in color, go online.

miniaturized chamber was covered with a cover slip and sealed with grease. For addition of biomolecules to the system, biomolecule solution was pipetted into the aqueous phase of known volume to reach the desired concentration.

FCS and confocal imaging

Confocal imaging was performed on a laser-scanning microscope (LSM780; Zeiss AG, Oberkochen, Germany), equipped with gallium arsenide phosphide detectors and a water immersion objective with a long working distance of 620 μ m (LD C-Apochromat 40X, NA 1.1; Zeiss AG). The monolayer interface was located by imaging the back-reflection of the excitation laser. For presentation purposes, the brightness and contrast of images was adjusted by using ImageJ software (28).

FCS measurements were performed on the same microscope stand using avalanche photodiode detectors (ConfoCor3; Zeiss AG). The internal pinholes were set to 35 and 45 μ m for 488 and 633 nm excitation wavelength, respectively. To circumvent detector afterpulsing, we performed pseudo-cross correlation, i.e., we split the collected fluorescence, projected it on two independent avalanche photodiode detectors, and cross correlated their signals. The optical system was calibrated on a daily basis by using Alexa Fluor 488 (Alexa488; Thermo Fischer, Waltham, MA) or ATTO 655 carboxylic acid (Atto655; ATTO-TEC), freely diffusing with known diffusion coefficients (29–31) in aqueous solution, corrected for the respective temperature through the relation $D(T) \propto T/\eta(T)$ (32,33). The viscosity of water $\eta(T)$ at any temperature was calculated (34). In brief, the confocal volume was positioned 50 μ m above the bottom cover slip, the lateral pinhole position was optimized for maximal fluorescence signal and the objective's correction collar was positioned for maximal count rate per particle, and finally the FCS measurement was taken.

For FCS measurements on lipid monolayers, the optimal axial focus position was determined by scanning the volume in the axial direction to locate the intensity maximum. This procedure was repeated in between FCS measurements because of sample drift. For both the initial calibration measurement and the FCS measurements on lipid monolayers, the irradiance was chosen sufficiently low to minimize photobleaching and fluorescence saturation (35–37).

To control the temperature, the miniaturized chambers were placed in a heating system (Ibidi, Martinsried, Germany) compatible with the commercial microscopy stage.

The recorded correlation curves were analyzed by using PyCorrFit 0.9.7 (38). The used fitting function reads as follows:

$$G(\tau) = N^{-1} \left(1 + \frac{T}{1-T} e^{-\tau/\tau_T} \right) \times \left(1 + \tau/\tau_D \right)^{-1} \left(1 + \tau/(S^2\tau_D) \right)^{-1/2}. \quad (1)$$

Here, $\tau_D = w_0^2/4D$ is the diffusion time, which depends on the lateral e^{-2} -value of the confocal detection volume. Moreover, we introduced the structure parameter S , which represents the ratio of axial/lateral extent of the detection volume, the triplet fraction T , and the triplet decay time τ_T . Atto655 does not show triplet blinking and experimental curves were therefore fitted with $T=0$. Moreover, when measuring on membranes, the axial extent of the confocal volume is irrelevant ($S=\infty$).

Langmuir compression isotherms

Compression isotherms were measured using a Kibron Micro-Trough XL Langmuir-Blodgett trough equipped with a dyne probe and the analytical software FilmWareX 4.0 (Kibron, Helsinki, Finland). Before every measurement, the trough was thoroughly cleaned by three washing steps with Kimtech paper tissues soaked with chloroform and ethanol. Powder-free gloves were used to avoid any contaminations. The dyne probe was cleaned by flaming it with a butane torch. The instrument was calibrated daily and the surface pressure (Π) zeroed in the aqueous subphase before every measurement. To verify the subphase purity, an isotherm was recorded in absence of lipids with a compression rate of 5 cm^2/min . Lipids

III.3 FCS analysis of protein mobility on lipid monolayers

were deposited on the air-water interface from a 1 mg/mL stock solution in high purity chloroform. After complete evaporation of chloroform, the isotherm was recorded with a compression rate of 5 cm²/min until the monolayer collapsed. Isotherms were measured at least in duplicate at room temperature (21°C).

Surface pressure measurements in miniaturized chambers

For Π measurement in the miniaturized chambers, we used the dyne probe and detection system described above. After system calibration (see above), Π was zeroed in a miniaturized chamber filled with 200 μ L of Q buffer before every measurement. Lipids were deposited on the interface as described above. After full solvent evaporation (\sim 5 min), the resulting Π value was recorded. We measured Π at room temperature (21°C) and at 30°C. For measurements at 30°C, the miniaturized chamber was placed on a hot plate together with tissue soaked in water and was covered by a petri dish to achieve a humidity-saturated environment (Fig. S3). A small hole in the petri dish ensured accessibility for the dyne probe. Under these settings, evaporation was negligible.

Determination of the interface area in miniaturized chambers

A monolayer of defined packing was deposited in a miniaturized chamber and imaged with a Zeiss Plan Apo 10X/0.45 objective (Zeiss AG). We acquired several adjacent tile images of the interface to image the entire cross section of the miniaturized chamber ($R = 7.5$ mm). This procedure was repeated in 19 different z -planes, each of them 100 μ m apart. A circle was imaged in each z -plane, corresponding to the section of the meniscus with the confocal plane (Fig. S4 B). The center of mass of each circle was determined and the intensity values were plotted versus their distance to this center. To reduce the noise, the radial distance was binned (bin width five pixels). The resulting radial intensity distribution was baseline corrected and fitted by a Gaussian, which is centered around the radius of the circle. Based on the known nominal focus position and the determined radii, we determined the radial meniscus profile $h(r)$ (Fig. S4 C), which was extrapolated to the physical size of the chamber $R = 7.5$ mm. This function is well behaved and the corresponding meniscus area A was calculated

$$\text{numerically: } A = 2\pi \int_0^R r \sqrt{1 + |\partial h(r)/\partial r|^2} dr.$$

RESULTS AND DISCUSSION

Temperature control improves FCS performance on lipid monolayers

Here, we used a miniaturized chamber with a fixed area (16) to study biomolecule mobility on lipid monolayers by FCS. The use of such miniaturized chambers has the major advantage that considerably smaller amounts of lipids and proteins are required compared to conventional Langmuir-Blodgett troughs. Because of the fixed-area of the chamber, we controlled the lipid density by the amount of lipid deposited on the air-water interface (Fig. 1 A). To avoid lipid oxidation by carbon-chain exposure at the air-water interface, we chose to use the fully saturated lipid DMPC.

When performing FCS on two-dimensional systems such as lipid membranes, the z position of the confocal volume

needs to be accurately adjusted to the membrane position because axial mismatches between both bias the obtained number of particles N and diffusion coefficient D (39). For monolayers, it is particularly challenging to keep the confocal volume centered on the monolayer. Upon evaporation of the subphase, the air-water interface is lowered, leading to a reduction of the autocorrelation amplitude G_0 and thus an increase in N detected (Eq. 1; Fig. 1 B). Thus, when working with lipid monolayers, the evaporation of the subphase, because of the high surface area/volume ratio is a major concern. Moreover, almost all confocal setups feature a temperature above the ambient temperature, mainly because of active elements hosted in the microscope body. Consequently, the monolayer chamber is exposed to a temperature gradient in which the bottom cover slip is warmer than the top lid of the chamber. Therefore, water condensation occurs on the top lid of the chamber, preventing the gas phase above the monolayer from reaching a humidity-saturated state. The resulting permanent axial drift of the monolayer with respect to the confocal volume renders long high-quality FCS measurements almost impossible and wastes valuable measurement time because the operator constantly needs to refocus on the lipid monolayer.

We avoided this major bottleneck by actively heating the sample and its surroundings to a constant temperature ($T = 30^\circ\text{C}$) above room temperature. By this strategy, we stabilized the lipid monolayer position and eliminated the artifacts arising from axial drift (Fig. 1, C and D). The stable positioning of the focus allowed us to measure for considerably longer periods of time and thus to access long correlation times, e.g., due to low diffusion coefficients (40,41). Gudmand et al. had previously taken advantage of the natural subphase evaporation to apply a modification of z -scan FCS (39) to determine lipid mobility in monolayers (15). In their approach, each series of intensity trace measurements started with the lipid monolayer above and finished below the fixed focus position such that the maximal autocorrelation amplitude and counts per particle could be found. Although this approach is simple and elegantly makes use of the inherent evaporation, it comes at the cost of very long measurement times (30 min). In contrast, our approach of focus stabilization and point FCS analysis maximizes the counts per particle because the lipid monolayer is constantly in focus and thus reduces the total measurement time per sample considerably. Nonetheless, both approaches are expected to yield identical results (42).

Lipid diffusion coefficient is an effective tool to characterize the monolayer state

To confirm the quality of the obtained lipid monolayers, we measured the surface pressure (Π) of monolayers deposited at different mean molecular areas per molecule (MMA, in \AA^2) in the miniaturized chambers (see Materials and Methods; Fig. S2). Because the area of the chamber is

III. Binding and Diffusion of membrane-bound DNA nanostructures

Khmelinskaia et al.

constant, the MMA is controlled by the amount of lipids deposited on the air-water interface. We compared the Π - A dependence from the miniaturized chambers with the corresponding Langmuir Π - A isotherm (Fig. 1 E). Since the air-water interface forms a meniscus, its area is larger than the cross section of the chamber, in particular in the miniaturized chambers. As a result, the actual MMA is larger than predicted from the amount of lipid deposited, which directly reflects in an overall lower Π . It would be desirable to apply a correction factor taking into account the real interface area of the meniscus in the miniaturized chambers. However, whereas the meniscus shape in capillaries (i.e., cavity radius much smaller than the height of the liquid) has been subject to theoretical studies (43,44), no analytical expression is known for a cylindrical well structure as used in this study. Additionally, the contact angle of aqueous buffer and plasma cleaned PTFE is unknown. In this study, we estimated the actual interface area by imaging the entire monolayer at different lipid packings (Fig. S4). Interestingly, the lipid packing of the monolayer had only a very minor impact on the meniscus shape. Relative to the miniaturized chamber cross section πR^2 , the monolayer area was $(4 \pm 1)\%$ larger at $90 \text{ \AA}^2/\text{molecule}$. As at $50 \text{ \AA}^2/\text{molecule}$, the meniscus shape was similar, we corrected all MMAs by a factor of 1.05.

The compression isotherm of DMPC behaved as previously described (15). The monolayers deposited in the fixed-area chambers follow the general trend of the Langmuir isotherm and confirm the reproducibility of the deposition protocol of the lipid monolayers in fixed-area chambers. We attribute the small discrepancies at low MMA to the difference between the two assays in the physical process of increasing lipid packing. In a Langmuir monolayer, the lipids rearrange upon slow physical compression, whereas in the fixed-area chambers, lipid molecules need to incorporate and find their arrangement during the much faster process of lipid spreading on the interface upon organic solvent evaporation. Consequently, when depositing low MMA lipid monolayers, a fraction of the lipid molecules may not insert into the monolayer, resulting in an effective increase of the MMA.

The measurement of Π in our miniaturized chambers although conceptually simple (Fig. S3), is rather impractical when combined with confocal microscopy at temperature-controlled conditions. Instead, we used confocal microscopy and FCS to monitor the lipid monolayer quality. DMPC lipid monolayers deposited at 30°C were homogeneous between 50 and $100 \text{ \AA}^2/\text{molecule}$ (Fig. S5). The FCS curves obtained for DMPC monolayers with different MMAs showed an increased N with higher lipid packing (Fig. 2, A and B). Moreover, the measured N is inversely proportional to the estimated MMA, as highlighted in Fig. 2 B by a fit of the inverse proportionality. However, the determined number of particles is consistently lower than the theoretically predicted number of particles.

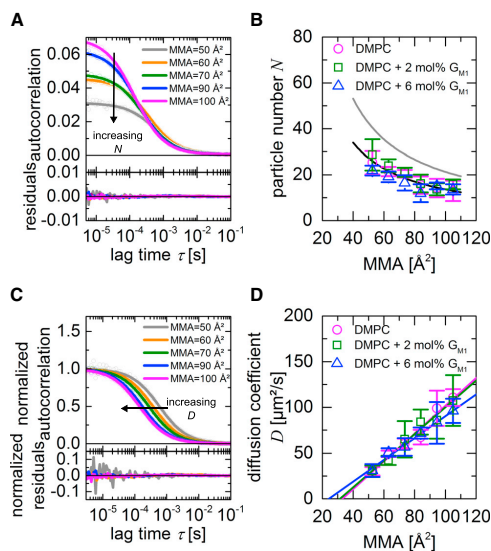


FIGURE 2 Characterization of DMPC lipid monolayers deposited in fixed-area chambers at 30°C by point FCS. (A) Representative autocorrelation curves, single-component diffusion fit, and the respective residuals obtained by point FCS for DMPC lipid monolayers deposited at different MMAs in fixed area-chambers are shown. The monolayers were doped with 0.01 mol% Atto655-DOPE. The increase of autocorrelation amplitude (G_0) with increasing MMA is highlighted and corresponds to the decrease in the number of particles N in the confocal volume. (B) Number of particles N obtained for lipid monolayers at different MMA by fitting a single-component diffusion model (Eq. 1) is shown. Measurements were performed on pure DMPC, and 2 mol% and 6 mol% content of G_{M1} . Overall N follows the trend of an expected $1/\text{MMA}$ -dependence (black line). The theoretically predicted N is shown by the gray line. (C) Normalized autocorrelation curves for DMPC monolayers deposited at different MMA are shown. The shift of the autocorrelation curves to smaller diffusion times (τ_D) and correspondingly larger diffusion coefficient (D) with increasing MMA is highlighted. (D) Lipid diffusion coefficient varies linearly with lipid monolayer MMA. Measurements were performed on pure DMPC, 2 and 6 mol% content of G_{M1} . The lines are linear fits (Table S2) for each data set. The obtained critical areas (a_c) can be found in Table S2. The average of typically four independent samples and respective standard deviations are shown in (B) and (D). To see this figure in color, go online.

Another observed feature was the shift of the correlation curves toward larger diffusion times with increasing lipid packing, resulting in slower lipid mobility, as previously shown (15,16) (Fig. 2, C and D). As described by the free-area model, D varied linearly with the lipid density (15,16,45). As surface pressure Π is a monotonic function of the MMA, there is a monotonic relationship between D and Π (15). Consequently, the cumbersome measurement of Π in fixed-area chambers can be replaced by an FCS measurement of lipid diffusion to characterize the current state of the monolayer.

III.3 FCS analysis of protein mobility on lipid monolayers

When analyzing the linear dependence of D on the MMA (Table S2), we obtained the intersection of the linear extrapolation to $D = 0 \mu\text{m}^2/\text{s}$, which yields an estimate for the critical area a_c , below which the translational diffusion of lipids in a fluid monolayer can theoretically no longer occur. The obtained a_c of $(33.0 \pm 8.0) \text{ \AA}^2/\text{molecule}$ for DMPC is in good agreement with previously reported values (15,16,20).

Protein mobility is modulated by lipid monolayer packing

Lipid Langmuir monolayer studies generally suggest that protein/peptide adsorption and potential insertion into lipid membranes changes lateral pressure and lipid packing (e.g., (21,46,47)). Therefore, when studying the effect of lipid packing, careful controls need to be performed to ensure that the addition of biomolecules at a certain concentration does not change the macroscopic properties of the monolayer. Moreover, it has been proposed that the mobility of protein components in membranes is influenced by lipid packing (15). To further investigate this hypothesis, we studied the influence of lipid packing, and consequently of lipid mobility, on the mobility of monolayer-bound biomolecules using point FCS.

First, the binding of molecules to lipid monolayers through head-group specific interaction or the insertion of a hydrophobic moiety was tested (Table S1). Independently of the nature of the interaction with the lipid monolayer, the studied molecules can be divided into two groups: homogeneously distributed or aggregated at the lipid interface. Importantly, the presence of protein clusters precludes quantitative FCS measurements. The aggregates have statistically ill-defined size and brightness distributions, distorting both amplitude and shape of the autocorrelation curve

(Eq. 1; Fig. S6). Under special circumstances, the effect of aggregates can be corrected by postprocessing of the photon-arrival times (48,49). However, even these approaches may only deal with the effect of very bright particles passing through the center of the confocal volume. Although passivation strategies to reduce unspecific interactions with the interface and consequent protein aggregation could be conceived, these are of low relevance as the effective MMA of the monolayer is modified. Generally, it is thus advisable to spend considerable efforts to prevent the formation of or to remove aggregates.

We found that the model protein CtxB falls into the category of proteins that do not aggregate at the lipid monolayer interface and is thus suitable for analysis by point FCS. Previously, binding of CtxB to lipid monolayers has been qualitatively assessed in phase-separated lipid mixtures (16). However, to date, the diffusion behavior of CtxB at the lipid monolayer has not been studied. Here, we varied the density of the lipids at the interface and studied its effect on the mobility of CtxB (Fig. 3). To eliminate the influence of protein binding on lipid diffusion, low protein concentrations ($\leq 10 \text{ nM}$) were used. Indeed, the lipid diffusion in the monolayer does not change upon addition of CtxB, as highlighted by the perfectly superimposed autocorrelation curves (Fig. 3 A; Fig. S7). Consequently, protein binding in these conditions did not change the surface pressure Π . Furthermore, the use of a low protein concentration allowed us to use a simple single-component diffusion model (with a triplet component, in accordance with the used dye molecule) (Eq. 1) to fit the obtained autocorrelation curves for the protein channel because there was virtually no contribution from protein in solution to the autocorrelation curve.

As expected, the autocorrelation curve obtained for CtxB was shifted to larger decay times compared to the lipid monolayer curves, indicating a slower protein diffusion

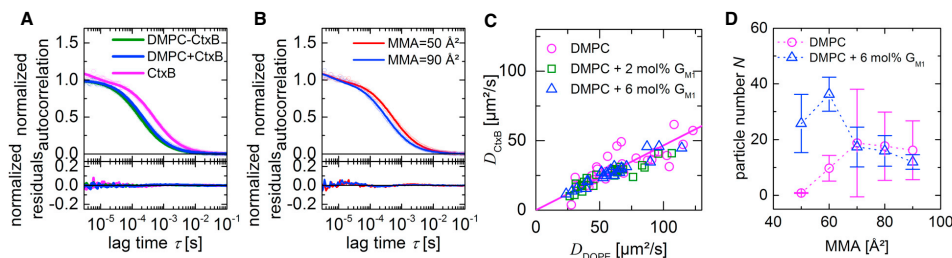


FIGURE 3 Cholera toxin β (CtxB) interaction with DMPC lipid monolayers in absence or presence of the specific ligand G_{M1} analyzed by point FCS. (A) Autocorrelation curves obtained by point FCS for a DMPC monolayer at $70 \text{ \AA}^2/\text{molecule}$ with 0.01 mol\% Atto655-DOPE, before and after addition of 10 nM CtxB-Alexa488, and for the protein CtxB-Alexa488 are shown. Fits with single diffusion component and respective residuals are shown. (B) Autocorrelation curves obtained for CtxB (10 nM) bound to DMPC monolayers at 90 and $50 \text{ \AA}^2/\text{molecule}$. Fits with single diffusion component and respective residuals are shown. (C) Shown is the relationship between lipid diffusion and CtxB diffusion on a pure DMPC monolayer (magenta) and in the presence of 2 mol\% or 6 mol\% of the specific ligand G_{M1} . The diffusion coefficients of CtxB and lipids show a linear relation (Table S3) as highlighted by the linear fit for a pure DMPC monolayer. (D) Shown is the relationship between the detected CtxB number of particles N bound to the lipid monolayer and the lipid MMA in presence and absence of the ligand G_{M1} . The average of typically three independent samples and respective standard deviations are shown. To see this figure in color, go online.

III. Binding and Diffusion of membrane-bound DNA nanostructures

Khmelniskaia et al.

(Fig. 3 A). The decrease in lipid MMA, and consequent reduction of lipid mobility, again resulted in a shift of the autocorrelation curves of CtxB to larger diffusion times (Fig. 3 B). The CtxB diffusion coefficient (D_{CtxB}) scaled linearly with the lipid diffusion in the monolayer; less dense lipid monolayers allowed for a faster diffusion of the protein (Fig. 3 C). A similar linear dependence on D_{DOPE} was observed for another membrane-targeted molecule, the MPER of the envelope glycoprotein gp41 of HIV-1 (Fig. S8). Relative to D_{DOPE} , D_{CtxB} was approximately 60% lower, whereas D_{MPER} was only 40% lower (Fig. 4).

Next, we analyzed the influence of a specific ligand, the ganglioside G_{M1} , on the diffusion behavior of CtxB. Supposedly, the pentameric CtxB binds up to five G_{M1} as each monomer exhibits a binding site with a reported dissociation constant $K_{\text{D}} = 0.1\text{--}1\text{ nM}$ (50–52). As all experiments were conducted above K_{D} , CtxB should prevalently bind to its ligand when G_{M1} is present in the membrane. Interestingly, the addition of G_{M1} does not significantly influence the diffusion coefficient D_{CtxB} . In theory, the two-dimensional diffusion of a molecule correlates with the size of the molecule's inclusion in the membrane (12). One can thus hypothesize that the similar diffusion coefficients obtained in presence and absence of the ligand G_{M1} indicate that the insertion size of the pentameric CtxB nonspecifically bound to the lipid monolayer is similar to the effective insertion size of the lipid group codiffusing upon binding of the pentameric CtxB to five G_{M1} molecules.

Although the diffusion coefficients are similar, the analysis of the amplitude of CtxB correlation curves unravels a significant difference in CtxB binding to the lipid monolayer in presence and absence of G_{M1} (Fig. 3 D). In absence of

G_{M1} , CtxB binding to DMPC monolayers is dependent on the lipid packing, with higher binding observed at low lipid density. This can be explained by the affinity of CtxB to the air-water interface that is shielded at higher lipid densities (Fig. S9). In presence of G_{M1} , on the other hand, CtxB binds stronger to the lipid monolayer at low MMA, as the total amount of G_{M1} present in the lipid monolayer is inversely proportional to the lipid packing. For $100\text{ \AA}^2/\text{molecule}$, a larger scatter of N was obtained in both conditions, as G_0 is particularly sensitive to small density variations and occasional protein clusters were encountered at the monolayer.

Although these are the first steps toward the analysis of protein-lipid interactions on monolayers, the role of specific ligands in the modulation of protein behavior should be subject to future studies. Additionally, as the lipid density has a strong impact on the diffusion of membrane interacting proteins/peptides, the rate of chemical reactions in the membrane may also be sensitive to lipid packing. Furthermore, the single molecule sensitivity of FCS enables the detection and quantification of protein/peptide interaction with lipid monolayers in a regime in which no diffusion coefficient variation and, consequently, no surface pressure variation is detected.

Hydrodynamic length scale is different in lipid monolayers and bilayers

When inspecting the diffusion coefficients discussed above, it becomes clear that the surface viscosity η_s of the lipid monolayer is considerably lower than the surface viscosity of a bilayer, in good agreement with previous studies (53–55). Specifically, the diffusion coefficients of lipids

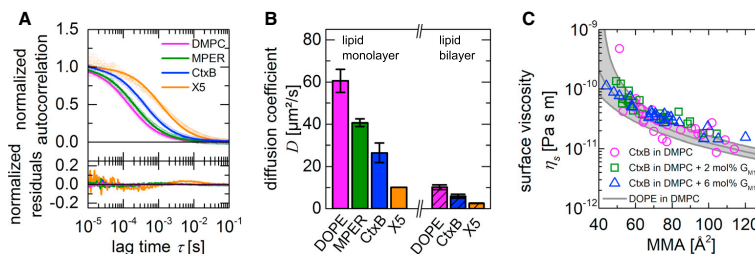


FIGURE 4 Comparison of the mobility of biomolecules of different dimensions on lipid monolayers at $70\text{ \AA}^2/\text{molecule}$ by point FCS. (A) Shown are autocorrelation curves obtained by point FCS for 0.01 mol% Atto655-DOPE, 10 nM of the membrane proximal external region (MPER) of the envelope glycoprotein gp41 of HIV-1 and G_{M1} -bound CtxB, both labeled with Alexa488, and 40 pM DNA structure X5 three-fold labeled with Atto488 in a DMPC monolayer at $70\text{ \AA}^2/\text{molecule}$. Fits with single diffusional component and respective residuals are shown. (B) Diffusion coefficients obtained for each analyzed biomolecule in a DMPC monolayer at $70\text{ \AA}^2/\text{molecule}$ (filled bars). The studied biomolecules cover a range of sizes and number of membrane insertion points. The average of typically three independent samples and respective standard deviations are shown. Diffusion coefficients determined by others for Atto655-DOPE (23.5°C) (42), G_{M1} -bound CtxB (23.5°C) (77), and DNA structure X5 (27.5°C; A.K., J.M., Henri G. Franquelim, and P.S., unpublished data) in 1,2-dioleoyl-sn-glycero-3-phosphocholine free-standing lipid bilayers are shown for comparison (shadowed bars). (C) Surface viscosity η_s of DMPC monolayers based on FCS experiments on CtxB (open symbols, Fig. 3 C) and ATTO655-DOPE (gray line with 95% confidence intervals, Fig. 2 D; Table S2) are shown. η_s was obtained numerically by finding the zero between predicted and measured diffusion coefficients using Newton's method. As expected, η_s increases with increasing lipid packing. Empirically, the η_s roughly follows a bi-exponential: $\eta_s = a_1 \exp(-a_2 \cdot \text{MMA}) + a_3 \exp(-a_4 \cdot \text{MMA})$ with $a_1 = 1.2 \cdot 10^{-8}\text{ Pa s m}$, $a_2 = 0.104\text{ \AA}^{-2}$, $a_3 = 1.7 \cdot 10^{-10}\text{ Pa s m}$, $a_4 = 0.025\text{ \AA}^{-2}$. All values correspond to 30°C. To see this figure in color, go online.

2450 Biophysical Journal 114, 2444–2454, May 22, 2018

III.3 FCS analysis of protein mobility on lipid monolayers

and CtxB are at least threefold larger in the lipid monolayer (Fig. 4) depending on the MMA. Accordingly, the characteristic hydrodynamic length of the system $l = \eta_s / (\mu_1 + \mu_2)$ (56,57) is shorter in lipid monolayers than bilayers. Here, we introduced the bulk viscosities μ_1 and μ_2 below and above the membrane, respectively. Assuming that the monolayer has half the thickness of a bilayer and that the viscosity of air is negligible compared to the viscosity of water, a lower viscosity of the lipid monolayer compared to the lipid bilayer is reasonable. Moreover, in lipid monolayers, no interleaflet coupling occurs and the packing density is lower, especially at high MMA.

For a more quantitative approach, we estimated the surface viscosity η_s of DMPC lipid monolayers at different MMAs based on the measured diffusion coefficients. Notably, the major models used to describe diffusion in lipid membranes, more specifically the Saffman-Delbrück model (12) and the Hughes-Pailthorpe-White model (HPW model) (56), are weakly dependent on the size of the membrane insertion. Thus, having in hand a reasonable estimation of the membrane inclusion radius r should yield a good approximation of η_s . As the Saffman-Delbrück model becomes inapplicable at high MMA, the values have been estimated numerically by using an empirical expression for the HPW model (57). The estimation was based on the determined D_{CtxB} assuming the previously reported radius $r = 3.1$ nm of pentameric CtxB (58). Overall, the η_s of DMPC lipid monolayers decreases with increasing MMA as expected (Fig. 4 C). In detail, the η_s of DMPC ranges from 1×10^{-10} Pa s m at $50 \text{ \AA}^2/\text{molecule}$ to 2×10^{-11} Pa s m at $100 \text{ \AA}^2/\text{molecule}$. The estimated values are relatively low compared to previously reported data (53,54,59–61). However, these reported values scatter considerably and it has been previously discussed that the surface viscosity was frequently overestimated (53). Interestingly, the surface viscosity at $62 \text{ \AA}^2/\text{molecule}$, which is around the expected MMA for DMPC bilayers (62), compared to $70 \text{ \AA}^2/\text{molecule}$ changes only by around 31%. Consequently, all larger differences in diffusion coefficients between lipid monolayers and bilayers can be mainly attributed to interleaflet coupling and the surrounding environments. Gudmand et al. made a similar observation when they found that a DMPC monolayer needs to have an MMA as small as 50 \AA^2 to yield the same diffusion coefficients in bilayers and monolayer (15). Moreover, the estimation of η_s based on D_{CtxB} is surprisingly in good agreement with the estimation based on D_{DOPE} (Fig. 2 D). With an assumed $r = 0.36$ nm (15,20,63–66), the size of the lipid probe is not much larger than the lipids themselves and thus violates a key assumption of the HPW model. The corresponding hydrodynamic length scale l of DMPC lipid monolayers will range from 120 nm at $50 \text{ \AA}^2/\text{molecule}$ to 24 nm at $100 \text{ \AA}^2/\text{molecule}$, in comparison to estimated 250 nm for lipid bilayers assuming $\eta_s = 5 \times 10^{-10}$ Pa s m (67–69). The smaller hydrodynamic length

scale of the lipid monolayer implies a slightly larger sensitivity of the lipid monolayer system to size variations on relevant length scales (12,57).

To test this hypothesis, we studied the interaction of a relatively large synthetic DNA origami-based nanoparticle (70). For simplicity, we chose a flat three-dimensional DNA origami structure (Fig. S1), which was previously studied on free-standing lipid bilayers (27). The bare nanostructure (denoted N), which has no affinity to GUVs in the used buffer conditions, showed no enrichment at the lipid monolayer interface and therefore did not alter the lipid diffusion (Fig. S10, A and B). The highly charged nature of such DNA nanostructures is likely to be the cause of this low affinity to the air-water interface. Interestingly, we also did not observe significant structure clustering.

Next, we functionalized the DNA origami structure with five cholesterol (Chol)-modified oligonucleotides (structure X5) to directly compare its diffusion behavior to that of pentameric CtxB. As a result, the DNA nanostructure did bind to the lipid monolayer (Fig. S10 C), which is in line with the previously shown binding to GUVs (27). As in the case of CtxB and MPER, although of considerably larger dimensions, structure X5 did not influence the lipid mobility upon binding to the lipid monolayer (Fig. S10 D). The autocorrelation curve obtained for the structure X5 decayed at larger diffusion times than CtxB, corresponding to a smaller diffusion coefficient (Fig. 4). As no significant binding has been observed with structure N, we did not expect a full insertion of X5 into the lipid monolayer. X5 is rather likely binding to the lipid monolayer by the insertion of the five Chol-modified oligonucleotides into the lipid monolayer, gliding on the interface as proposed for lipid bilayers (71).

Both the X5 structure and pentameric CtxB bound to G_{M1} have five membrane anchors of comparable insertion sizes. In free-standing bilayers of similar nature, their diffusion coefficients differ by a factor of 2.2. Interestingly, their diffusion coefficients measured in DMPC monolayers of $70 \text{ \AA}^2/\text{molecule}$ differ by a factor of 3. This small but significant difference between lipid bilayers and monolayers is consistent with the discussed difference in hydrodynamic length scale. Moreover, having determined the η_s of the lipid monolayer (3.8×10^{-11} Pa s m at $70 \text{ \AA}^2/\text{molecule}$), we can now estimate the inclusion size for both MPER and X5. For MPER, $r = 0.8$ nm, in good agreement with estimations based on the alignment of MPER in lipid bilayers (72). For X5, $r = 28.3$ nm, which is larger than the combined inclusion of five cholesterol anchors. For a more quantitative understanding, the compatibility of current membrane diffusion models with lipid monolayers needs to be addressed in future studies.

We note that the fit to the autocorrelation curve of the structure X5 shows systematic residuals up to 4% of the amplitude, which is considerably larger than for the other studied biomolecules. However, we do not expect any

Khmelinskaia et al.

contribution from rotational diffusion to the autocorrelation curve, as the fluorescent labels are located close to the center of the rod (71,73). On the other hand, when recording autocorrelation curves at different concentrations of nanostructure X5, the autocorrelation function shifted toward larger diffusion times at higher X5 concentration (Fig. S10 E). A similar behavior was previously described on GUVs for long DNA nanoneedles and has been attributed to crowding effects on particle diffusion at high surface densities (73). Thus, lipid monolayers appear to also support the study of more complex diffusional behaviors by point FCS.

CONCLUSIONS

In this work, we have established conditions under which reproducible, long, high-quality point FCS measurements can be performed on lipid monolayer systems. Most importantly, we discussed the necessity to reach an equilibrated system in which the lipid monolayer stays at a constant height to minimize focus drift. To reach this state, it is necessary to heat the closed monolayer chamber to the working temperature or above, in our case 30°C. Provided the biomolecule of interest is exclusively located at the lipid monolayer, the throughput of protein-monolayer studies could even be increased by camera detection schemes similar to, e.g., refs (74–76), coupled with wide-field illumination. In a set of proof-of-principle experiments, we applied FCS to study the lateral diffusion of selected biomolecules at the lipid monolayer. The use of FCS can not only complement canonical *D* measurements to characterize the monolayer state but also allows the quantitative characterization of protein-lipid monolayer interactions in a regime in which the physical properties of the monolayer are not modified. To cover a wide range of sizes and membrane insertion points of diffusing particles, we studied not only the diffusion of the rather small peptide MPER but also the model protein CtxB and a large DNA origami construct. We showed that the viscosity and consequently the hydrodynamic length scale in lipid monolayers are smaller than in lipid bilayers. Furthermore, we investigated the effect of lipid packing on protein diffusion in the lipid monolayer and found a linear dependence between the diffusion coefficient of bound protein and the diffusion coefficients of the lipids themselves. The direct impact of lipid packing on the mobility of monolayer-associated biomolecules may have implications on intermolecular reaction rates. We believe that this study forms a basis for novel research on the effects of lipid packing on protein-monolayer interactions.

SUPPORTING MATERIAL

10 figures and three tables are available at [http://www.biophysj.org/biophysj/supplemental/S0006-3495\(18\)30259-5](http://www.biophysj.org/biophysj/supplemental/S0006-3495(18)30259-5).

AUTHOR CONTRIBUTIONS

A.K. and J.M. contributed to the project design, conducted experiments, analyzed data, and wrote the manuscript. F.C. conducted experiments and wrote the manuscript. G.C. and P.S. contributed to the project design and wrote the manuscript.

ACKNOWLEDGMENTS

This article is dedicated to Jörg Langowski, a wonderful colleague and highly original FCS/FCCS researcher from very early on. Our friendly competition over several years had always been inspiring and certainly helped to promote FCCS further in the biophysics community. We will miss him and his critical mind.

A.K. acknowledges the support of the Graduate School of Quantitative Biosciences Munich. J.M. acknowledges support from the excellence cluster Nanosystems Initiative Munich and the International Max Planck Research School for Molecular Life Sciences. The authors thank Beatrice Ramm, Kristina Ganztzinger, Philipp Glock, Magnus-Carsten Huppertz and Sonal for the provided protein aliquots, namely for the mCherry constructs (BR and PG), NWASP constructs (KG and S), mNeonGreen (MH). The authors thank the Biochemistry Core Facility of the Max Planck Institute of Biochemistry for the synthesis of Alexa488 labeled MPER and for purification of the proteins MinD and MinE. The authors also thank Eugene P. Petrov and Henri G. Franquelim for helpful discussions.

REFERENCES

- Lagny, T. J., and P. Bassereau. 2015. Bioinspired membrane-based systems for a physical approach of cell organization and dynamics: usefulness and limitations. *Interface Focus*. 5:20150038.
- Dertinger, T., I. von der Hocht, ..., J. Enderlein. 2006. Surface sticking and lateral diffusion of lipids in supported bilayers. *Langmuir*. 22:9339–9344.
- Przybylo, M., J. Sýkora, ..., M. Hof. 2006. Lipid diffusion in giant unilamellar vesicles is more than 2 times faster than in supported phospholipid bilayers under identical conditions. *Langmuir*. 22:9096–9099.
- Bhatia, V. K., K. L. Madsen, ..., D. Stamou. 2009. Amphipathic motifs in BAR domains are essential for membrane curvature sensing. *EMBO J*. 28:3303–3314.
- Henne, W. M., H. M. Kent, ..., H. T. McMahon. 2007. Structure and analysis of FCHo2 F-BAR domain: a dimerizing and membrane recruitment module that effects membrane curvature. *Structure*. 15:839–852.
- Jørgensen, I. L., G. C. Kemmer, and T. G. Pomorski. 2017. Membrane protein reconstitution into giant unilamellar vesicles: a review on current techniques. *Eur. Biophys. J*. 46:103–119.
- Winterhalter, M. 2000. Black lipid membranes. *Curr. Opin. Colloid Interface Sci*. 5:250–255.
- Heinemann, F., and P. Schwill. 2011. Preparation of micrometer-sized free-standing membranes. *ChemPhysChem*. 12:2568–2571.
- Holthuis, J. C., and A. K. Menon. 2014. Lipid landscapes and pipelines in membrane homeostasis. *Nature*. 510:48–57.
- van den Brink-van der Laan, E., J. A. Killian, and B. de Kruijff. 2004. Nonbilayer lipids affect peripheral and integral membrane proteins via changes in the lateral pressure profile. *Biochim. Biophys. Acta*. 1666:275–288.
- Bigay, J., and B. Antonny. 2012. Curvature, lipid packing, and electrostatics of membrane organelles: defining cellular territories in determining specificity. *Dev. Cell*. 23:886–895.
- Saffman, P. G., and M. Delbrück. 1975. Brownian motion in biological membranes. *Proc. Natl. Acad. Sci. USA*. 72:3111–3113.

III.3 FCS analysis of protein mobility on lipid monolayers

FCS Study of Proteins on Monolayers

13. Böckmann, R. A., A. Hac, ..., H. Grubmüller. 2003. Effect of sodium chloride on a lipid bilayer. *Biophys. J.* 85:1647–1655.
14. Machán, R., and M. Hof. 2010. Lipid diffusion in planar membranes investigated by fluorescence correlation spectroscopy. *Biochim. Biophys. Acta.* 1798:1377–1391.
15. Gudmand, M., M. Fidorra, ..., T. Heimburg. 2009. Diffusion and partitioning of fluorescent lipid probes in phospholipid monolayers. *Biophys. J.* 96:4598–4609.
16. Chwastek, G., and P. Schwille. 2013. A monolayer assay tailored to investigate lipid-protein systems. *ChemPhysChem.* 14:1877–1881.
17. Vogel, S. K., F. Heinemann, ..., P. Schwille. 2013. The design of MACs (minimal actin cortices). *Cytoskeleton.* 70:706–717.
18. Vogel, S. K., F. Greiss, ..., P. Schwille. 2017. Control of lipid domain organization by a biomimetic contractile actomyosin cortex. *eLife.* 6:e24350.
19. Zieske, K., G. Chwastek, and P. Schwille. 2016. Protein patterns and oscillations on lipid monolayers and in microdroplets. *Angew. Chem. Int. Engl.* 55:13455–13459.
20. Ke, P. C., and C. A. Naumann. 2001. Single molecule fluorescence imaging of phospholipid monolayers at the air–water interface. *Langmuir.* 17:3727–3733.
21. Huang, Z., K. H. Pearce, and N. L. Thompson. 1992. Effect of bovine prothrombin fragment I on the translational diffusion of phospholipids in Langmuir-Blodgett monolayers. *Biochim. Biophys. Acta.* 1112:259–265.
22. Magde, D., E. Elson, and W. W. Webb. 1972. Thermodynamic fluctuations in a reacting system—measurement by fluorescence correlation spectroscopy. *Phys. Rev. Lett.* 29:705–708.
23. Rigler, R., Ü. Mets, ..., P. Kask. 1993. Fluorescence correlation spectroscopy with high count rate and low background: analysis of translational diffusion. *Eur. Biophys. J.* 22:169–175.
24. Eigen, M., and R. Rigler. 1994. Sorting single molecules: application to diagnostics and evolutionary biotechnology. *Proc. Natl. Acad. Sci. USA.* 91:5740–5747.
25. Loose, M., E. Fischer-Friedrich, ..., P. Schwille. 2008. Spatial regulators for bacterial cell division self-organize into surface waves in vitro. *Science.* 320:789–792.
26. Zieske, K., J. Schweizer, and P. Schwille. 2014. Surface topology assisted alignment of Min protein waves. *FEBS Lett.* 588:2545–2549.
27. Khmelinskaia, A., H. G. Franquelim, ..., P. Schwille. 2016. Effect of anchor positioning on binding and diffusion of elongated 3D DNA nanostructures on lipid membranes. *J. Phys. D Appl. Phys.* 49:194001.
28. Schindelin, J., C. T. Rueden, ..., K. W. Eliceiri. 2015. The ImageJ ecosystem: an open platform for biomedical image analysis. *Mol. Reprod. Dev.* 82:518–529.
29. Petrov, E. P., T. Ohr, ..., P. Schwille. 2006. Diffusion and segmental dynamics of double-stranded DNA. *Phys. Rev. Lett.* 97:258101.
30. Petrášek, Z., and P. Schwille. 2008. Precise measurement of diffusion coefficients using scanning fluorescence correlation spectroscopy. *Biophys. J.* 94:1437–1448.
31. Müller, C., A. Loman, ..., J. Enderlein. 2008. Precise measurement of diffusion by multi-color dual-focus fluorescence correlation spectroscopy. *Europhys. Lett.* 83:46001.
32. Sutherland, W. 1905. LXXV. A dynamical theory of diffusion for non-electrolytes and the molecular mass of albumin. *Lond. Edinb. Dublin Philos. Mag. J. Sci.* 9:781–785.
33. Einstein, A. 1905. Über die von der molekularinetischen Theorie der Wärme geforderte Bewegung von in ruhenden Flüssigkeiten suspendierten Teilchen. *Ann. Phys.* 322:549–560.
34. Kestin, J., M. Sokolov, and W. A. Wakeham. 1978. Viscosity of liquid water in the range -8°C to 150°C . *J. Phys. Chem. Ref. Data.* 7:941–948.
35. Widengren, J., U. Mets, and R. Rigler. 1995. Fluorescence correlation spectroscopy of triplet states in solution: a theoretical and experimental study. *J. Phys. Chem.* 99:13368–13379.
36. Gregor, I., D. Patra, and J. Enderlein. 2005. Optical saturation in fluorescence correlation spectroscopy under continuous-wave and pulsed excitation. *ChemPhysChem.* 6:164–170.
37. Petrov, E., and P. Schwille. 2008. State of the art and novel trends in fluorescence correlation spectroscopy. In *Standardization and Quality Assurance in Fluorescence Measurements II, Volume 6*. U. Resch-Genger, ed. Springer Series on Fluorescence. (Springer), pp. 145–197.
38. Müller, P., P. Schwille, and T. Weidemann. 2014. PyCorrFit-generic data evaluation for fluorescence correlation spectroscopy. *Bioinformatics.* 30:2532–2533.
39. Benda, A., M. Beneš, ..., M. Hof. 2003. How to determine diffusion coefficients in planar phospholipid systems by confocal fluorescence correlation spectroscopy. *Langmuir.* 19:4120–4126.
40. Oliver, C. 1979. Spectral analysis with short data batches (photon correlation spectroscopy). *J. Phys. Math. Gen.* 12:591–617.
41. Schätzel, K., M. Drewel, and S. Stimac. 1988. Photon correlation measurements at large lag times: improving statistical accuracy. *J. Mod. Opt.* 35:711–718.
42. Heinemann, F., V. Betaneli, ..., P. Schwille. 2012. Quantifying lipid diffusion by fluorescence correlation spectroscopy: a critical treatise. *Langmuir.* 28:13395–13404.
43. Erikson, T. A. 1965. The surface area of liquids in circular tubes. *J. Phys. Chem.* 69:1809–1813.
44. Kashin, V. V., K. M. Shakirov, and A. I. Poshevneva. 2011. The capillary constant in calculating the surface tension of liquids. *Steel Transl.* 41:795–798.
45. Galla, H. J., W. Hartmann, ..., E. Sackmann. 1979. On two-dimensional passive random walk in lipid bilayers and fluid pathways in biomembranes. *J. Membr. Biol.* 48:215–236.
46. Vázquez, R. F., M. A. Daza Millone, ..., S. M. Maté. 2017. Interaction of acylated and unacylated forms of E. coli alpha-hemolysin with lipid monolayers: a PM-IRRAS study. *Colloids Surf. B Biointerfaces.* 158:76–83.
47. Alvares, D. S., N. Wilke, ..., M. L. Fanani. 2017. The insertion of Polybia-MP1 peptide into phospholipid monolayers is regulated by its anionic nature and phase state. *Chem. Phys. Lipids.* 207:38–48.
48. Persson, G., P. Thyberg, ..., J. Widengren. 2009. Modulation filtering enables removal of spikes in fluorescence correlation spectroscopy measurements without affecting the temporal information. *J. Phys. Chem. B.* 113:8752–8757.
49. Laurence, T. A., Y. Kwon, ..., D. Barsky. 2007. Correlation spectroscopy of minor fluorescent species: signal purification and distribution analysis. *Biophys. J.* 92:2184–2198.
50. Fishman, P. H., J. Moss, and J. C. Osborne, Jr. 1978. Interaction of cholera toxin with the oligosaccharide of ganglioside GM1: evidence for multiple oligosaccharide binding sites. *Biochemistry.* 17:711–716.
51. Ludwig, D. S., H. O. Ribi, ..., R. D. Kornberg. 1986. Two-dimensional crystals of cholera toxin B-subunit-receptor complexes: projected structure at 17-Å resolution. *Proc. Natl. Acad. Sci. USA.* 83:8585–8588.
52. Reed, R. A., J. Mattai, and G. G. Shipley. 1987. Interaction of cholera toxin with ganglioside GM1 receptors in supported lipid monolayers. *Biochemistry.* 26:824–832.
53. Sickert, M., and F. Rondelez. 2003. Shear viscosity of langmuir monolayers in the low-density limit. *Phys. Rev. Lett.* 90:126104.
54. Sickert, M., and F. Rondelez. 2004. Sickert and Rondelez reply. *Phys. Rev. Lett.* 92.
55. Wilke, N., F. Vega Mercado, and B. Maggio. 2010. Rheological properties of a two phase lipid monolayer at the air/water interface: effect of the composition of the mixture. *Langmuir.* 26:11050–11059.
56. Hughes, B. D., B. A. Pailthorpe, and L. R. White. 1981. The translational and rotational drag on a cylinder moving in a membrane. *J. Fluid Mech.* 110:349–372.
57. Petrov, E. P., and P. Schwille. 2008. Translational diffusion in lipid membranes beyond the Saffman-Delbruck approximation. *Biophys. J.* 94:L41–L43.

III. Binding and Diffusion of membrane-bound DNA nanostructures

Khmelniskaia et al.

58. Zhang, R. G., M. L. Westbrook, ..., G. G. Shipley. 1995. The 2.4 Å crystal structure of cholera toxin B subunit pentamer: cholera toxin. *J. Mol. Biol.* 251:550–562.
59. Brooks, C. F., G. G. Fuller, ..., C. R. Robertson. 1999. An interfacial stress rheometer to study rheological transitions in monolayers at the air–water interface. *Langmuir*. 15:2450–2459.
60. Wurlitzer, S., P. Steffen, and Th. M. Fischer. 2000. Line tension of Langmuir monolayer phase boundaries determined with optical tweezers. *J. Chem. Phys.* 112:5915–5918.
61. Schwartz, D. K., C. M. Knobler, and R. Bruinsma. 1994. Direct observation of Langmuir monolayer flow through a channel. *Phys. Rev. Lett.* 73:2841–2844.
62. Nagle, J. F., and S. Tristram-Nagle. 2000. Structure of lipid bilayers. *Biochim. Biophys. Acta.* 1469:159–195.
63. Peters, R., and K. Beck. 1983. Translational diffusion in phospholipid monolayers measured by fluorescence microphotolysis. *Proc. Natl. Acad. Sci. USA.* 80:7183–7187.
64. Kim, S., and H. Yu. 1992. Lateral diffusion of amphiphiles and macromolecules at the air/water interface. *J. Phys. Chem.* 96:4034–4040.
65. Tanaka, K., P. A. Manning, ..., H. Yu. 1999. Lipid lateral diffusion in dilaurylphosphatidylcholine/cholesterol mixed monolayers at the air/water interface. *Langmuir*. 15:600–606.
66. Boguslavsky, V., M. Rebecchi, ..., S. McLaughlin. 1994. Effect of monolayer surface pressure on the activities of phosphoinositide-specific phospholipase C-beta 1, -gamma 1, and -delta 1. *Biochemistry*. 33:3032–3037.
67. Peters, R., and R. J. Cherry. 1982. Lateral and rotational diffusion of bacteriorhodopsin in lipid bilayers: experimental test of the Saffman-Delbrück equations. *Proc. Natl. Acad. Sci. USA.* 79:4317–4321.
68. Waugh, R. E. 1982. Surface viscosity measurements from large bilayer vesicle tether formation. II. Experiments. *Biophys. J.* 38:29–37.
69. Herold, C., P. Schwille, and E. P. Petrov. 2010. DNA condensation at freestanding cationic lipid bilayers. *Phys. Rev. Lett.* 104:148102.
70. Rothmund, P. W. 2006. Folding DNA to create nanoscale shapes and patterns. *Nature*. 440:297–302.
71. Czogalla, A., E. P. Petrov, ..., P. Schwille. 2013. Switchable domain partitioning and diffusion of DNA origami rods on membranes. *Faraday Discuss.* 161:31–43, discussion 113–150.
72. Sun, Z. Y., K. J. Oh, ..., E. L. Reinherz. 2008. HIV-1 broadly neutralizing antibody extracts its epitope from a kinked gp41 ectodomain region on the viral membrane. *Immunity*. 28:52–63.
73. Czogalla, A., D. J. Kauert, ..., E. P. Petrov. 2015. DNA origami nanoneedles on freestanding lipid membranes as a tool to observe isotropic-nematic transition in two dimensions. *Nano Lett.* 15:649–655.
74. Capoulade, J., M. Wachsmuth, ..., M. Knop. 2011. Quantitative fluorescence imaging of protein diffusion and interaction in living cells. *Nat. Biotechnol.* 29:835–839.
75. Bag, N., J. Sankaran, ..., T. Wohland. 2012. Calibration and limits of camera-based fluorescence correlation spectroscopy: a supported lipid bilayer study. *ChemPhysChem*. 13:2784–2794.
76. Krieger, J. W., A. P. Singh, ..., J. Langowski. 2014. Dual-color fluorescence cross-correlation spectroscopy on a single plane illumination microscope (SPIM-FCCS). *Opt. Express*. 22:2358–2375.
77. Heinemann, F., S. K. Vogel, and P. Schwille. 2013. Lateral membrane diffusion modulated by a minimal actin cortex. *Biophys. J.* 104:1465–1475.

IV

SELF-ORGANIZATION OF MEMBRANE-BOUND DNA NANOSTRUCTURES

The results discussed in this section are a result of a collaborative work with Renukka Yaadav (intern under supervision of the author of this thesis), Henri G. Franquelim and Eugene P. Petrov. The project was designed by AK, HGF and EPP. AK designed all DNA origami nanostructures, AK and RY performed high speed atomic force microscopy (HSAFM) imaging assisted by HGF. AK and EPP contributed for data interpretation. The information about materials and methods can be found in Appendix E.

IV.1 Introduction

In recent years, there has been an increased interest in the mechanisms of nanoscale organization of the cell membrane and especially in the role played in it by membrane proteins [McMahon and Gallop, 2005, Graham and Kozlov, 2010, Antonny, 2011]. It has been established that the shape of highly curved lipid membrane structures in living cells are controlled and modulated by several types of scaffolding proteins [Prinz and Hinshaw, 2009, Baumgart et al., 2011], such as the BAR domain superfamily (II.1.3). These proteins are generally strongly elongated and banana shaped. As a result, in the membrane plane these proteins possess a strongly elongated rod shape.

Recent theoretical, simulation-based, and experimental studies [Ramakrishnan et al., 2013, Simunovic et al., 2013a, Cui et al., 2013, Lipowsky, 2013] suggest that protein-controlled membrane shape transformation starts with membrane-mediated self-organization of membrane-bound protein molecules into a nematic domain. This self-organization on the nanoscale enhances the effect of individual molecules and generates an anisotropic spontaneous curvature of the protein-decorated membrane. Thus, in spite of the different chemical structure of scaffolding proteins, their membrane-bending effect largely relies on one and the same physical mechanism, which is governed by their shape-controlled collective be-

haviour. Therefore, the basic properties of the phenomenon can be understood using a model synthetic biology-inspired approach [Schwille and Diez, 2009, Schwille, 2011].

Interestingly, although several theoretical studies have predicted membrane-driven self-organization of rigid rodlike particles [Dommersnes and Fournier, 1999, Wen et al., 2012, Ramakrishnan et al., 2013, Yue et al., 2013, Simunovic et al., 2013b, Simunovic and Voth, 2015, Zhang et al., 2015, Olinger et al., 2016, Ghosh et al., 2016], only recently Petrova *et al.* showed the first experimental evidences for such processes [Petrova et al., 2017]. In this work, rodlike *fd*-virus particles electrostatically bound to a freestanding cationic lipid membrane have been observed to form tip-to-tip linear chain aggregates.

Here, we address the organization of rigid rodlike DNA origami nanoparticles on supported lipid bilayers (SLBs). To cover a range of shapes, DNA nanoparticles of aspect ratios 1, 7 and 22 were studied (Figure IV.1). DNA nanoparticles were adsorbed through electrostatic interactions to mica or SLBs, let diffuse and their organization at different surface densities was observed using high speed atomic force microscopy (HSAFM). Our results show that although on a rigid and passive surface, i.e. mica, the DNA nanoparticles have purely repulsive interactions and distribute homogeneously, on an elastic lipid membrane tip-to-tip and side-by-side attraction takes place creating organized aggregates. Moreover, we confirm the anisotropic phase type dependency on particle aspect ratio at high surface densities [Bates and Frenkel, 2000].

IV.2 Results and Discussion

To cover a range of shapes, three DNA origami nanostructures of aspect ratios 1, 7 and 22 (AR1, AR7 and AR22, respectively) were designed (Figure IV.1, Supplementary Figures E.1-E.3). To avoid staking interactions between monomers of each structure [Woo and Rothmund, 2011, Gerling et al., 2015], the oligonucleotides at the tips of each structure have been extended with two adenines (As). Additionally, AR1 has been designed with irregular helix length to reduce the number of possible staking interactions due to shape complementarity. Agarose gel electrophoresis and transmission electron microscopy (TEM) confirmed the correct structure folding in predominantly monomeric form. It is important to note that no further efforts were done to eliminate the small percentage of dimeric AR1 and of higher order AR22 aggregates.

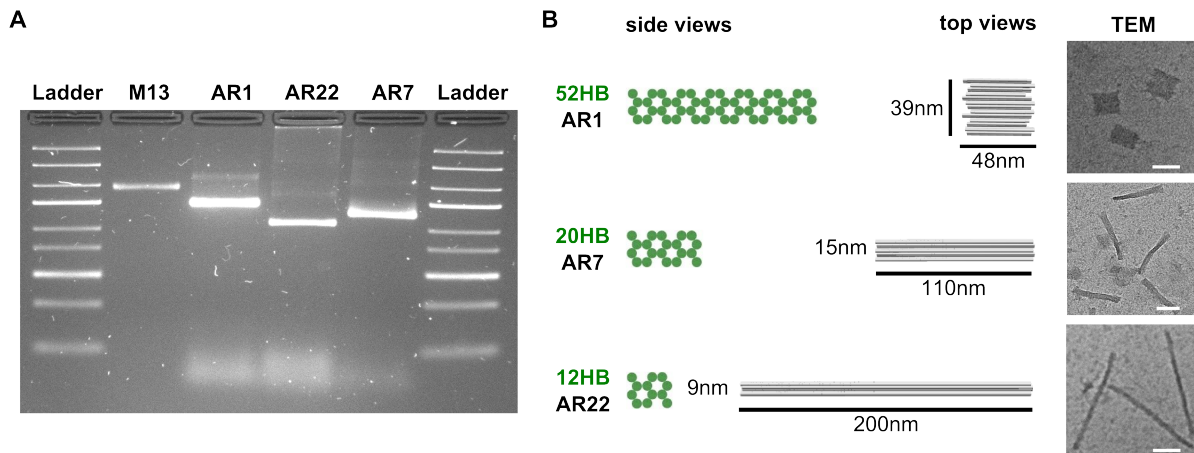


Figure IV.1: DNA nanostructures of different aspect ratios. A) Confirmation of DNA origami folding into a preferential monomeric form. Lanes were loaded with DNA nanostructures with aspect ratio 1, 7 and 22 (respectively AR1, AR7 and AR22). Lanes containing marker DNA ladder (Ladder) and the unfolded plasmid M13 (M13) are shown for comparison. B) Schematic representation and TEM images of each DNA nanostructure. Estimated dimensions are shown in the schematic representation. Scale bars correspond to 50 nm.

IV.2.1 Density-dependent organization of rodlike DNA nanostructures on mica

In order to confirm the absence of attractive interactions between the designed DNA nanostructures, AR7 nanostructures were imaged at different surface densities on mica using HSAFM (Figure IV.2). Notably, the organization of purely-repulsive rodlike structures on a rigid substrate is dictated by their aspect ratio and their surface density [Bates and Frenkel, 2000]. Typically, DNA origami nanostructures are strongly adsorbed to negatively charged mica through electrostatic interactions mediated by Mg^{2+} ions, enabling for stable imaging. Here, the FOB buffer is doped with NaCl reaching approximately 10:1 ratio with $MgCl_2$ (150 mM NaCl 16 mM $MgCl_2$). The addition of monovalent ions, i.e. Na^+ , weakens the interactions between the DNA origami nanostructures and the support through replacement of Mg^{2+} ions [Pastré et al., 2003]. In result, DNA origami nanostructures become mobile on the mica surface and can reorganize themselves [Aghebat Rafat et al., 2014, Woo and Rothmund, 2014].

AR7 nanostructures distribute themselves homogeneously on the mica surface, indepen-

dently of their surface density (Figure IV.2). At higher surface densities, although the translational diffusion appears to be limited, no higher order structures are formed. This observation supports that the interactions between AR7 nanostructures are purely repulsive. Indeed, the Debye length at the imaging buffer condition is ≈ 0.7 nm.

It has been theoretically predicted [Frenkel and Eppenga, 1985, Bates and Frenkel, 2000, Khandkar and Barma, 2005, Vink, 2009] and experimentally confirmed [Czogalla et al., 2015b] that the isotropic-nematic transition (IN transition) for rodlike particles occurs at a reduced surface density $\rho = \sigma L^2 \approx 7$, where σ is the surface density in particles/ μm^2 and L is the rod length (for AR7, 110 nm). In agreement, at the highest surface densities ($\rho \approx 2.4$), although a certain degree of orientation is gained, the system is still far from the IN transition (Figure IV.2C).

IV.2.2 Self-organization of rodlike DNA nanostructures on SLBs

Next, we studied the organization of rodlike DNA nanostructures on SLBs at different surface densities using HSAFM (Figure IV.3). As described above for mica, AR7 was adsorbed to SLBs through electrostatic interactions mediated by MgCl_2 , in this case between the negatively charged backbone of DNA and the zwitterionic headgroup of the phospholipids [Gromelski and Brezesinski, 2006, Suzuki et al., 2015]. Such an approach has been previously used to observe the organization of square, triangle, hexagonal and cross-shaped DNA structures into large lattices when deposited at high densities on SLBs [Suzuki et al., 2015, Dohno et al., 2017, Avakyan et al., 2017, Sato et al., 2018]. Here, FOB buffer containing 20 mM MgCl_2 and no NaCl was used. Additionally, SLBs composed of DSPC were used. Such gel SLBs (phase transition temperature $(T_m)_{\text{DSPC}} = 55$ °C and working temperature $T = 20$ °C) not only increase the interaction of DNA nanostructures with the membrane, as gel phase has a higher charge density when compared to less ordered phases [Pisani et al., 2006, Kato et al., 2010, Dohno et al., 2017, Avakyan et al., 2017, Sato et al., 2018], but also allowed us to track the diffusion and organization of individual nanoparticles.

At low surface densities (Figure IV.3A), no clear attractive interactions were observed and the overall organization was identical to the described for mica at similar surface densities (Figure IV.2A). Notably, stable tip-to-tip attraction could be observed, although they may originate from local entrapment in defects on the membrane, i.e. grain boundaries formed

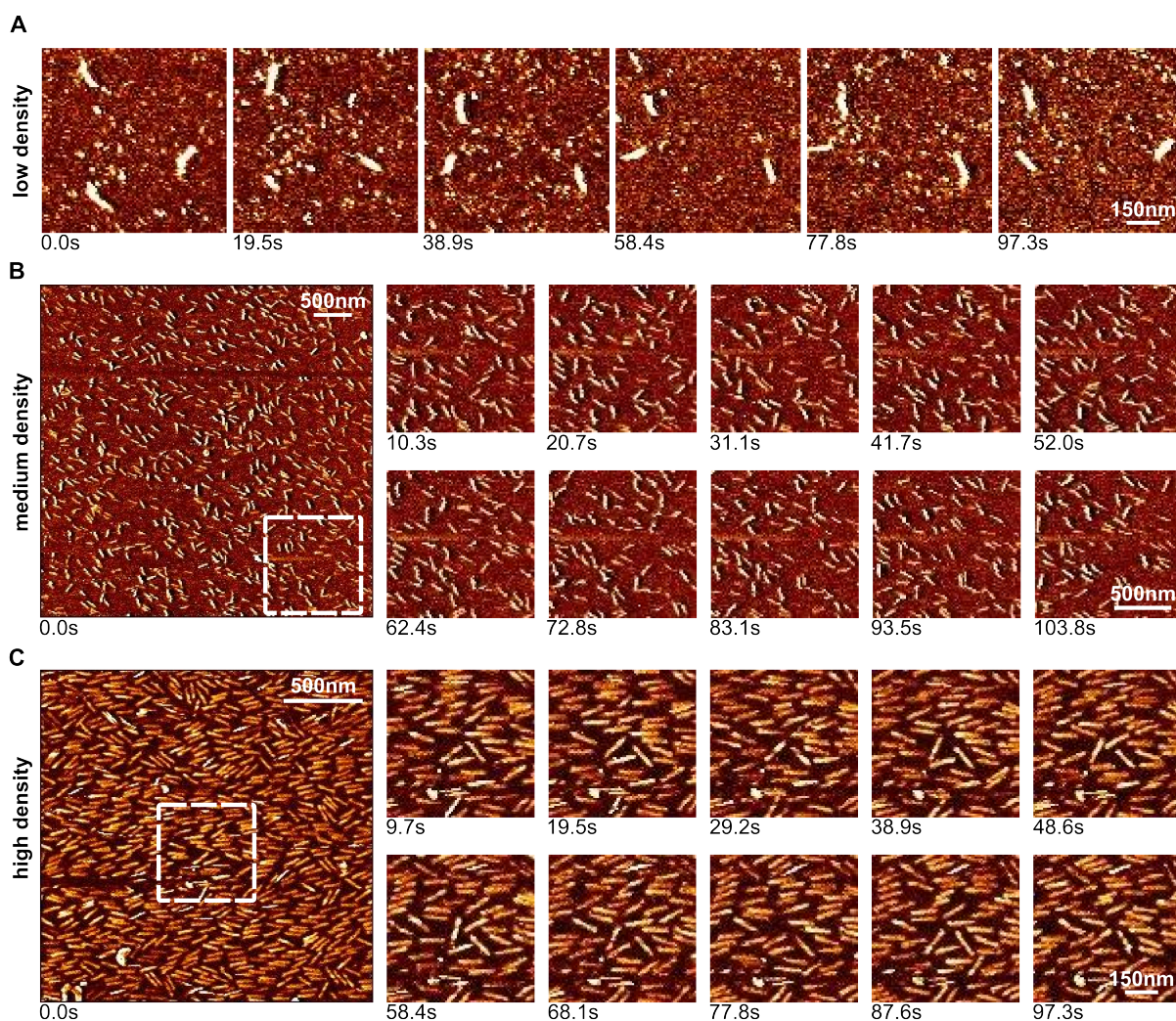


Figure IV.2: DNA nanostructure show purely repulsive interactions on a rigid surface. HSAFM images of DNA nanostructure AR7 diffusing on a mica surface at different surface densities: A) low (2-3 particles/ μm^2), B) medium (30-50 particles/ μm^2) and C) high (100-200 particles/ μm^2) surface area coverage. Snapshots in time are shown for each condition. White dashed boxes correspond to the area chosen for illustration. All experiments are performed at 16 mM MgCl_2 and 150 mM NaCl.

upon membrane deposition.

At higher surface densities, the organization of AR7 nanostructures on SLBs (Figure IV.3B,C) is strikingly different from what was observed on mica (Figure IV.2B,C). On SLBs, AR7 nanostructures are no longer homogeneously distributed and higher order aggregates are formed at surface densities in the regime > 30 particles/ μm^2 . While at medium

surface densities (30-50 particles/ μm^2) no clear preference between tip-to-tip and side-by-side attraction is observed, at high surface densities (100-200 particles/ μm^2) side-by-side attraction seems to prevail. As a result, AR7 domains of anisotropic organization are formed. Notably, the formation of such domains has been suggested to play an important role in the early steps of membrane shaping by scaffolding proteins [Ramakrishnan et al., 2013, Simunovic et al., 2013a, Cui et al., 2013, Lipowsky, 2013].

Theoretical works predict that the local deformation of elastic surfaces upon adhesion of rodlike particles results in attractive interactions between those particles and that the character of such interactions will depend on the membrane tension γ [Cherstvy and Petrov, 2014, Simunovic and Voth, 2015, Ghosh et al., 2016]. At low γ , tip-to-tip attraction should dominate while at higher γ side-by-side attraction is more probable. Recently, tip-to-tip attraction between rodlike *fd*-viruses has been observed on low tension free-standing lipid bilayers [Petrova et al., 2017]. Considering an elastic membrane that, upon nanoparticle adhesion, cannot be stretched, the resulting deformation will increase the membrane tension. Thus, with the number of bound nanoparticles, γ increases and consequently side-by-side attraction may become more probable. Our observation of prevalent side-by-side attraction at high membrane densities is in very good agreement with this line of reasoning.

The characteristic length-scale l at which membrane-mediated attraction of membrane-bound nanoparticles takes place scales as $l \sim \sqrt{\kappa/\gamma}$, where κ is the bending rigidity of the elastic membrane [Cherstvy and Petrov, 2014]. From our observations, we estimate that $l \approx 100\text{nm}$, at least two orders of magnitude larger than the Debye length in the used buffer (1.2 nm). For a lipid well below its T_m , such as DSPC at 20 °C, the bending rigidity κ is estimated to be $\approx 10^3 k_B T$ [Dimova et al., 2000, Mecke et al., 2003, Dimova, 2014]. As a result, the membrane tension is estimated to be in the order of 10^{-4} – 10^{-3} N/m, at least one order of magnitude below the typical membrane rupture tension (10^{-2} N/m [Evans et al., 2003]). Notably, mica is rigid and does not respond to particle adhesion, thus no attractive interactions are expected. Thus, overall our results are in good agreement with the current interaction models.

Interestingly, self-organization phenomena of rigid rodlike nanostructures, to the best of our knowledge, have never been previously observed on SLBs [Herold et al., 2016] and even on free-standing lipid bilayers, only tip-to-tip attraction was observed [Petrova et al., 2017]. Importantly, although SLBs do not allow for large scale deformations due to the

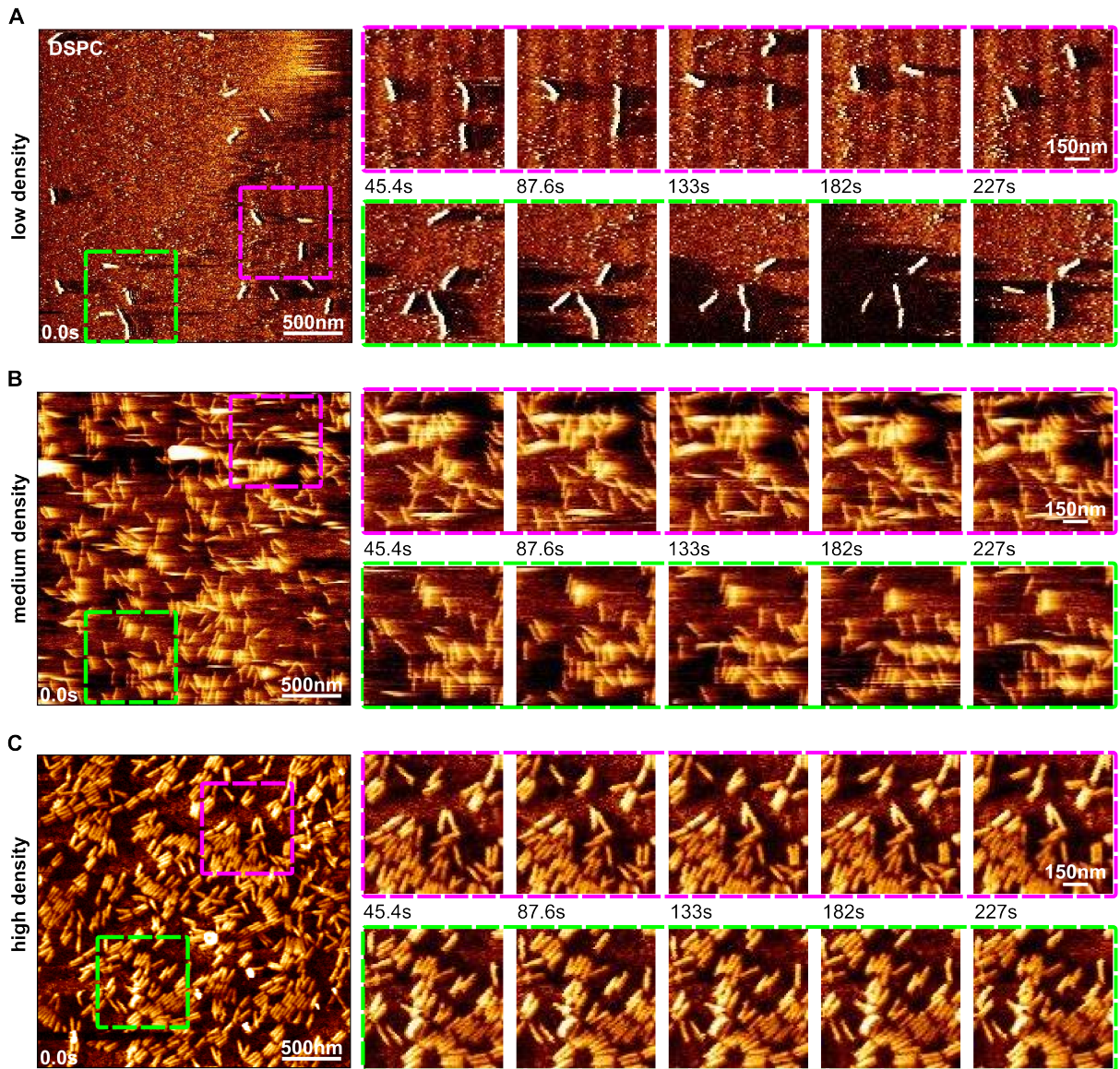


Figure IV.3: DNA nanostructure show tip-to-tip and side-by-side attraction on SLBs. HSAFM images of DNA nanostructure AR7 diffusing on 1,2-distearoyl-*sn*-glycero-3-phosphocholine (DSPC) SLBs at different surface densities: A) low (2-3 particles/ μm^2), B) medium (30-50 particles/ μm^2) and C) high (100-200 particles/ μm^2) surface area coverage. Snapshots in time are shown for each condition. Two different regions are chosen as examples and delimited by dashed boxes. All experiments are performed at 20 mM MgCl_2 .

presence of a solid support, small range deformations are possible due to the presence of an hydration layer of 1–3 nm thickness between the support and the phospholipid headgroups [Johnson et al., 1991, Koenig et al., 1996, Kiessling and Tamm, 2003, Zwang et al., 2010].

At fixed membrane rigidity and tension, the strength of the interaction between the elastic membrane and the adsorbed nanoparticle plays a crucial role on the type of interactions observed [Cherstvy and Petrov, 2014, Ghosh et al., 2016, Petrova et al., 2017]. Using the approach described by [Bellot et al., 2013], the linear charge density of our DNA nanostructure AR7 is estimated to be $16 e^-/\text{nm}$ and is higher than that of *fd*-bacteriophage particles ($10 e^-/\text{nm}$ [Zimmermann et al., 1986]). Furthermore, while in the previous studies the membrane binding was mediated through electrostatic interactions with positively charged lipids, the amount of which never exceeded a few %, in this study the membrane is covered with Mg^{2+} cations that coordinate with the phosphate group of the phospholipids [McLaughlin et al., 1978, Lis et al., 1981]. In other words, each lipid bears a net positive charge. Thus, the possibly higher positive charge density in the SLBs used in this study will result in stronger interaction with the DNA nanoparticles, and thus higher surface tension and different regimes of self-organization.

IV.2.3 Dependence of the anisotropic phase formation on the aspect ratio of DNA nanostructures

Our experimental system can also be used to study the influence of the aspect ratio of the particle on the formed anisotropic phase at high surface densities, where diffusion is mainly eliminated. The 2D isotropic-anisotropic phase transition of rodlike particles has been theoretically predicted to take place at different surface densities depending on the particle's aspect ratio [Frenkel and Eppenga, 1985, Bates and Frenkel, 2000, Khandkar and Barma, 2005, Vink, 2009, Avendaño and Escobedo, 2012, Xu et al., 2013]. In all previous experiments [Kwan et al., 2001, Kim et al., 2001, Tao et al., 2003, Yoo et al., 2006, Hore and Composto, 2010, Zhao et al., 2011, Czogalla et al., 2016] such isotropic-anisotropic phase transitions have been observed by varying the surface density of particles of a fixed aspect ratio (1 to 70). To the best of our knowledge, to date no experimental study has been carried out where isotropic-anisotropic phase transitions of particles of different aspect ratio were observed for particles with the same properties under identical conditions.

DNA origami nanotechnology is the perfect tool for a comprehensive study covering a range of aspect ratios, as structures of virtually any shape can be produced at high yields [Rothemund, 2006, Douglas et al., 2009a, Dietz et al., 2009]. In this chapter, we study the organization of three particles of aspect ratios 1, 7 and 22 (AR1, AR7 and AR22

- Figure IV.1) on SLBs using HSAFM. Phase separated lipid bilayers (1,2-dioleoyl-*sn*-glycero-3-phosphocholine (DOPC)/DSPC/cholesterol (Chol) 2:2:1) were used in order to limit the total surface area and assure the possibility of nanoparticle reorganization at high local surface densities. Although DNA origami nanostructures preferentially bind to the liquid ordered phase (l_o) where the charge density is higher [Pisani et al., 2006, Kato et al., 2010, Dohno et al., 2017, Avakyan et al., 2017, Sato et al., 2018], DNA nanostructures can cross the border back and forth to the liquid disordered (l_d) phase [Dohno et al., 2017, Avakyan et al., 2017, Sato et al., 2018].

For all three DNA nanoparticles, anisotropic phases were observed at high surface densities. Generally, for elongated particles three different phases (isotropic, nematic and smectic), which transform into one another upon increase of surface density and variation of aspect ratio, can be observed. From the theoretically predicted phase diagram, for rodlike particles an IN transition is expected to occur at high surface densities of particles of aspect ratio bigger than 7, before the formation of a smectic phase [Bates and Frenkel, 2000]. Indeed, for AR22 we observed a nematic phase (Figure IV.1C), while for AR7 we observed a smectic phase (Figure IV.1B).

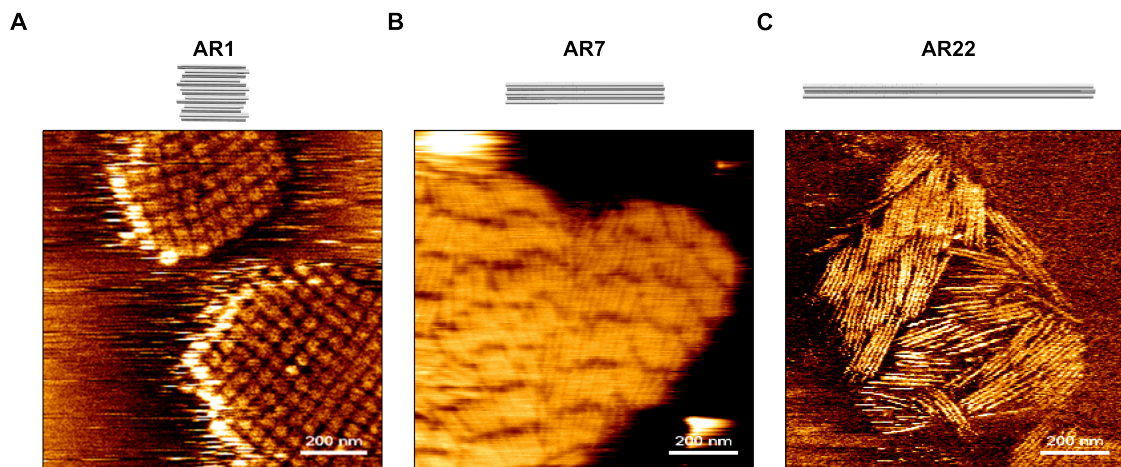


Figure IV.4: Anisotropic phases formed by DNA nanostructures at high surface densities. HSAFM images of a square crystalline phase formed by DNA nanostructures AR1 (A), smectic phase formed by DNA nanostructure AR7 (B), and nematic phase formed by DNA nanostructure AR22 (C) on DOPC: DSPC: Chol (2:2:1) SLBs.

In contrast, the seemingly simple case of Brownian squares (particle aspect ratio 1) shows an unexpectedly rich succession of phases depending on their packing density [Zhao et al.,

2011, Avendaño and Escobedo, 2012, Walsh and Menon, 2016]. At high densities square-shaped particles have been shown to freeze into the translationally and orientationally ordered square crystalline phase with suppressed translational diffusion [Walsh and Menon, 2016]. Indeed, this is what we observed in our experiments with DNA nanoparticles AR1 (Figure IV.1A).

Taken together, these results are the first step towards the study of isotropic-anisotropic phase transition of particles with the same properties and varying aspect ratios in 2D.

IV.3 Conclusions

Here, we have used HSAFM to study the organization of rodlike DNA nanoparticles on rigid (mica) and elastic (SLB) supports. We have shown that DNA nanoparticle interaction depends on the responsiveness of the underlying support. While on mica DNA nanoparticles showed purely repulsive interactions, on DSPC SLBs stable tip-to-tip and side-by-side contacts were established. Moreover, the type of preferred interaction is dependent on the particle surface density and thus membrane tension γ , supporting that the γ influences the self-organization of rodlike particles adhering to elastic membranes [Simunovic and Voth, 2015, Ghosh et al., 2016]. To our knowledge, this is the first time that anisotropic domains of rodlike particles, suggested to play a role in the early steps of membrane curvature-induction mechanisms [Ramakrishnan et al., 2013, Simunovic et al., 2013a, Cui et al., 2013, Lipowsky, 2013], are observed on 2D elastic surfaces. Ultimately, we show the possibility of using DNA nanoparticles in combination with SLBs to study membrane-driven self-organization of particles of different aspect-ratio and their isotropic-anisotropic phase transition.

DNA-BASED SCAFFOLDS FOR SHAPING LIPID MEMBRANES

The greatest promise of creating arbitrary structures with biological molecules is held by the recognition that structure encodes function. One of the most intriguing questions in DNA nanotechnology is whether it can be used to mimic complex biological functions based on structural motifs. Thus, we set out to design DNA origami nanostructures that mimic structure-based protein functionality: the shaping of biological membranes by protein scaffolds (chapter V.1). We developed curved DNA origami nanostructures in various shapes that imitated the banana-shaped Bin/Amphiphysin/Rvs (BAR) proteins (see section II.1.3) and studied their ability to induce membrane transformations. We showed that dependent on the curvature, membrane affinity and surface density, coats of DNA nanostructures controllably tubulate membranes reproducing the activity of BAR proteins. Our results provided direct proof that the curvature of membrane binding macromolecules can alone induce macroscopic transformations.

In chapter V.2, I aimed to advance the design of DNA-based scaffolds by integrating a conformational switch to trigger membrane shaping. Notably, the final step of clathrin-mediated endocytosis, e.g., is performed by dynamin, whose concerted GTPase activity and conformational change results in the fission of the enclosed membrane [Pawlowski, 2010, Schmid and Frolov, 2011, Ferguson and De Camilli, 2012]. I thus set out to implement a conformational switch into DNA origami nanostructures, to control the shaping of lipid membranes. In this chapter, DNA nanostructures that can be switched between an "open" and a "closed" conformation were designed. The conformational switch is driven by the removal of strategically positioned single-stranded DNA. The design of individual modules was tuned based on its step-by-step characterization using transmission electron microscopy (TEM) and oxDNA molecular dynamic simulations (MD simulations). The effect of each module on the shape of lipid membranes was studied using confocal microscopy. Taken together, these are the first steps towards a DNA origami machine that can shape flat lipid membranes in a precise and temporally controlled manner.

V.1 Membrane sculpting by curved DNA origami scaffolds

The results discussed in this section are the result of a close collaboration with the leading author Henri G. Franquelim and have been published as:

Franquelim, H. G., Khmelinskaia, A., Sobczak, J.-P., Dietz, H., Schwille, P. (2018) Membrane sculpting by curved DNA origami scaffolds. Nat. Commun., 9: 811. doi: 10.1038/s41467-018-03198-9. A reprint permission has been granted by the publisher. The supplementary information can be found in Appendix F. The author of this thesis contributed to the experimental design of the project, performed and analyzed the fluorescence imaging and FCS-based experiments for determining surface densities, binding and tubulation efficiencies of different DNA origami scaffolds.



ARTICLE

DOI: [10.1038/s41467-018-03198-9](https://doi.org/10.1038/s41467-018-03198-9)

OPEN

Membrane sculpting by curved DNA origami scaffolds

Henri G. Franquelim ¹, Alena Khmelinskaia ^{1,2}, Jean-Philippe Sobczak ³, Hendrik Dietz ³ & Petra Schwille ¹

Membrane sculpting and transformation is essential for many cellular functions, thus being largely regulated by self-assembling and self-organizing protein coats. Their functionality is often encoded by particular spatial structures. Prominent examples are BAR domain proteins, the 'banana-like' shapes of which are thought to aid scaffolding and membrane tubulation. To elucidate whether 3D structure can be uncoupled from other functional features of complex scaffolding proteins, we hereby develop curved DNA origami in various shapes and stacking features, following the presumable design features of BAR proteins, and characterize their ability for membrane binding and transformation. We show that dependent on curvature, membrane affinity and surface density, DNA origami coats can indeed reproduce the activity of membrane-sculpting proteins such as BAR, suggesting exciting perspectives for using them in bottom-up approaches towards minimal biomimetic cellular machineries.

¹Max Planck Institute of Biochemistry, D-82152 Martinsried near Munich, Planegg, Germany. ²Graduate School of Quantitative Biosciences, Ludwig-Maximilians-University, D-81337 Munich, Germany. ³Physics Department and Institute of Advanced Study, Technische Universität München, D-85748 Garching near Munich, Germany. Correspondence and requests for materials should be addressed to P.S. (email: schwille@biochem.mpg.de)

The curvatures of biological membranes vary strongly, from predominantly flat in the plasma membrane to highly curved in the endoplasmic reticulum or in the Golgi apparatus. The transformation of membranes from one shape to another, for example during cell division, belongs to the most fundamental processes in living cells. Numerous factors that regulate membrane curvature have been identified, with scaffolding proteins being the most obvious ones^{1–3}. An important class of scaffolding proteins which presumably imprint their shape on lipid membranes is the BAR (Bin/Amphiphysin/Rvs) domain superfamily^{4, 5}. When dimerized, BAR proteins form characteristic banana-shaped scaffolds that induce and stabilize membrane curvature through electrostatic and hydrophobic interactions^{4–6}. Several BAR proteins were shown to tubulate membranes *in vitro*^{7–10}. BAR proteins presumably rely on their curved shape for their activity: different types of BAR modules adopt folds with different degrees of curvature^{4, 5}. By using BAR domains as model proteins^{11, 12}, recent studies emphasized the relevance of physical-chemical foundations for membrane bending. From the minimalistic perspective of bottom-up synthetic biology^{13, 14}, it is tempting to speculate about the simplest way to induce specific membrane curvatures, and thus engineer a minimal membrane sculpting machinery *de novo*. The goal of this work is to mimic structural and functional features of BAR domain proteins by rationally designed DNA origami objects (Supplementary Fig. 1), in order to decipher the essential properties of artificial scaffolds for curving lipid membranes.

Programmable self-assembly with DNA origami may be employed to produce a variety of two-dimensional and three-dimensional structures on the nanometer-scale, including objects with custom curvature^{15–19}. This molecular toolkit now serves as the starting point for our goal of constructing membrane-sculpting machinery from the bottom-up. DNA origami has been previously employed to create nanoscale channels in lipid membranes^{20, 21} and to guide the assembly of nanoscale lipid compartments^{22–25}. In contrast to DNA origami nanocages^{24, 25} that template small liposomes via detergent removal, our designed origami structures act on preexisting cell-sized vesicles, imitating the mechanism of action of protein coats. Subsequently, in this work, we achieve the transformation of membrane shape on much larger scales, reminiscent of deformations observed in cells^{2, 3}.

Taking inspiration from the different degrees of curvature covered by BAR domain proteins, three DNA origami designs (20-helix bundles with hexagonal lattice; Supplementary Figs. 2–4 and Supplementary Tables 1–3) were here developed (Fig. 1): (i) a ‘semi-circle’ named HALF (origami H) with curvature (C) $\approx 21.7 \mu\text{m}^{-1}$; (ii) a ‘quarter-circle’ named QUARTER (origami Q) with $C \approx 11.6 \mu\text{m}^{-1}$ and (iii) a ‘stick’ named LINEAR (origami L) with $C \approx 0$ (Fig. 1a–c and Supplementary Fig. 5). Despite their fivefold increased length when compared to BAR proteins ($\sim 110 \text{ nm}$ vs. $\sim 20 \text{ nm}$, respectively), these origami structures (H, Q and L) mimic the typical shapes of highly-curved BAR/N-BAR dimers, moderately curved F-BAR dimers and flat PinkBAR/I-BAR dimers,

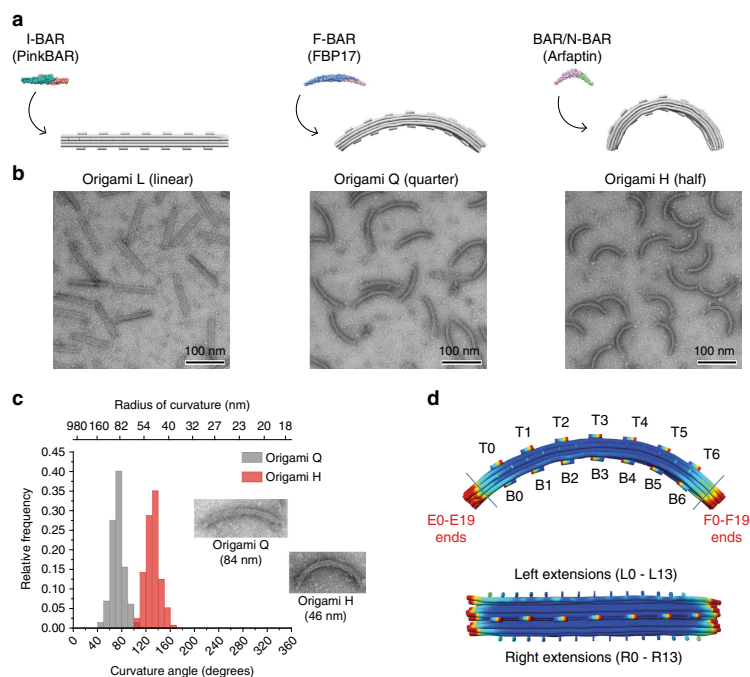


Fig. 1 BAR-mimicking DNA origami nanoscaffolds. **a** Structures of origami L (linear), Q (quarter) and H (half), which mimic the shape of I-BAR, F-BAR and BAR/N-BAR domains, respectively. **b** Corresponding negative-stain TEM images of the folded curved nanostructures. **c** The angle of curvature and respective radius of origami structures Q and H (84 and 46 nm, respectively) were experimentally determined from TEM images ($n = 110$ – 130). **d** Schematic representation of marked positions on the top convex (T0–T7), bottom concave (B0–B7), lateral sides (L0–L13, R0–R13) and tips used on the nanoscaffolds (here origami Q) for attaching fluorophores, membrane-anchoring moieties or oligomerizing staples. Scale bars: 100 nm

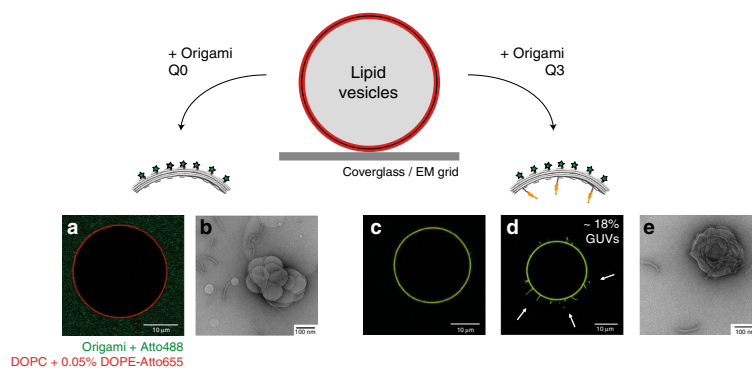


Fig. 2 Binding of curved origami structures to lipid model membranes. Interaction of the BAR-mimicking curved origami structures (labeled with Atto488; green) with DOPC model membranes (labeled with DOPE-Atto655; red) assessed using confocal microscopy and TEM. Bare DNA origami nanostructures (Q0) did not interact with GUVs, as observed on GUVs imaged at the equatorial plane by confocal microscopy (**a**) and on MLVs by negative-stain TEM (**b**). Incorporation of three TEG-chol moieties at the distal 5'-end of 18 bps-long linker sequences extending from the origami backbone (structure Q3), rendered optimal binding of the DNA origami structures to lipid bilayers (**c, e**). After incubation for at least 1 h with origami structure Q3 (**d**), circa 18 % of the GUVs presented outwards lipidic tubules (marked by arrows). Scale bars: (**b, e**) 100 nm; (**a, c, d**) 10 μ m

respectively (Fig. 1a and Supplementary Fig. 1). Each design further includes positions at the different curved facets for attaching fluorophores, membrane-anchoring moieties or for oligomerizing the objects laterally (Fig. 1d and Supplementary Notes). Thereupon, we studied the interaction of the DNA origami-based scaffolds with lipid model systems and demonstrate the ability for membrane bending in vitro. We determined quantitatively the requirements in terms of shape, membrane-attachment and oligomerization needed for a synthetic scaffold to induce specific membrane curvature. As we explore reconstitution assays with model membranes similar to the ones employed for studying scaffolding proteins in vitro^{8–10}, direct comparison with the mechanism of action of BAR domain proteins can be drawn.

Our results demonstrate that DNA nanotechnology has reached the degree of sophistication to reproduce complex biological functionality, which has so far been thought to be reserved for proteins. We show that structure- and function-specific DNA origami devices, biomimetic of proteins targeting and remodeling biological membranes, can be rationally designed and reconstituted into cell-sized model membrane environments. This opens up exciting perspectives for bottom-up synthetic biology approaches, as even more complex fundamental biomimetic nanosystems, such as protein-less membrane trafficking and protocell division machineries, may be within reach.

Results

Efficient binding of curved DNA origami to membranes. We assessed the interaction of curved DNA nanostructures with lipid membranes, mainly giant unilamellar vesicles (GUVs) composed of 1,2-dioleoyl-*sn*-glycero-3-phosphocholine (DOPC), via fluorescence confocal microscopy (Fig. 2). Incorporation of 7 \times Atto488-modified staples on positions T0–6 enabled fluorescence detection of the origami structures (Fig. 1d). Similarly to what was described elsewhere²⁶, bare DNA origami structures lacking membrane anchors were adsorbing to lipid bilayers in the presence of 20 mM MgCl₂ (Supplementary Fig. 6). We avoided such unspecific membrane attachment (Supplementary Fig. 7) and ensured long-term stability of the nanostructures²⁷ with an imaging buffer containing 5 mM MgCl₂ and 300 mM NaCl in

which the Na⁺ outcompetes membrane-adsorbed divalent cations via a counterion release mechanism to break up Mg²⁺-promoted interactions between DNA and the phospholipids^{28,29}. To achieve side-specific binding of the curved DNA origami structures to lipid membranes, we tested various methods including neutravidin-mediated attachment^{21,30} of biotinylated origami H to biotinylated lipids (Supplementary Fig. 8a) and covalent attachment^{24,31} of thiolated origami H to maleimide-modified lipids (Supplementary Fig. 8b). However, preferred membrane anchors were oligonucleotides linked to a cholesterol moiety via a tetraethylene glycol spacer (TEG-chol), as they have been already extensively characterized³² and allowed for a steady binding of nanostructure H to lipid bilayers (Supplementary Fig. 9) in comparison to the other approaches.

In order to enhance attachment of curved DNA origami scaffolds to model membranes and avoid steric hindrance (Supplementary Figs. 10–12), we placed TEG-chol moieties at the distant 5'-end of 18 bps-long linker sequences extending from the origami backbone (anchor orientation called TC5). Placing the anchors closer to the origami backbone, i.e., at the proximal 3'-end of the linker sequences (Supplementary Fig. 10a and Supplementary Fig. 11d–f), or shortening the linker length from 18 to 9 bps (Supplementary Fig. 12b, d), severely reduced binding of nanostructures H and Q to membranes. This effect was particularly prevalent for membrane binding through the concave origami surface.

Since anchor accessibility plays a decisive role for attaching DNA origami structures to lipid membranes³³, we further evaluated how number and positioning of TC5 anchors along the concave origami facet may influence binding of nanostructures H and Q to GUVs. When single TC5 anchors were introduced (Supplementary Fig. 13b–d and h–j), no significant attachment of our curved nanoscaffolds to membranes was observed (Supplementary Fig. 14). In contrast, when three TC5 anchors were incorporated (Supplementary Fig. 13e–f and k–l), membrane affinity was significantly increased, especially if the anchors were placed at positions B0, B3 and B6 (combination from here on called X3) (Fig. 2c and Supplementary Fig. 13f, l). Using negative-stain TEM imaging, we further corroborated the attachment of construct Q3 to lipid vesicles (Fig. 2e).

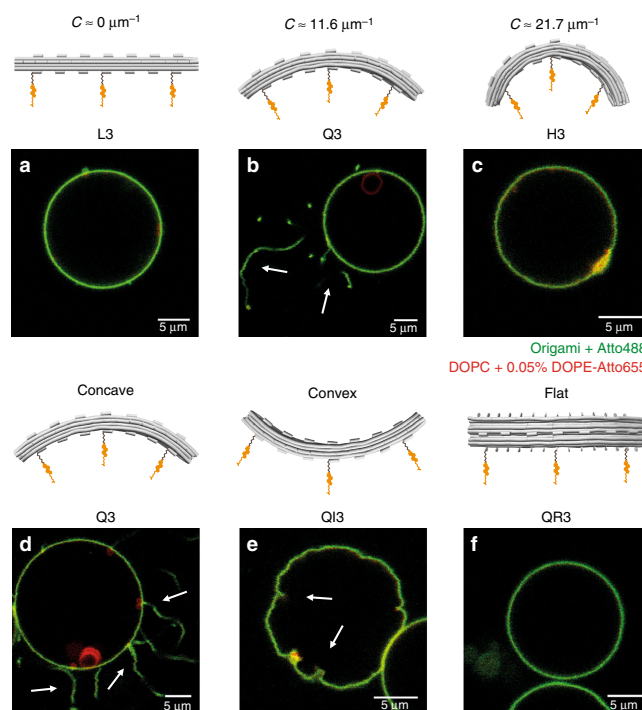


Fig. 3 Triggering of membrane deformations depends on the degree of curvature of the BAR-mimicking DNA nanoscaffolds. DNA origami structures (labeled with Atto488; green) of varying curvature (L3, Q3 and H3; here at 5 nM bulk concentration) were incubated with DOPC GUVs (labeled with DOPE-Atto655; red) for at least 1 h. After membrane binding was achieved, the surface tension of the GUVs was lowered by applying a hyperosmotic stress (10% increase in buffer osmolarity) and consequent changes in vesicle shape were monitored. No significant changes in vesicle shape were observed with membrane-bound origami L3 (**a**) and H3 (**c**). Vesicles covered with the moderately curved structure Q3 presented long tubular outward structures upon hyperosmotic stress (**b**; marked by arrows). Similarly, membrane interaction of origami Q variants displaying three cholesterol anchors on different curved facets was further investigated. Strong binding to GUVs was achieved for all nanostructures, independently of the facet where anchors are localized (**d–f**). Upon vesicle deflation, the concave structure (Q3) triggered outwards membrane tubules (**d**; marked by arrows); the convex structure (QI3) triggered evagination/invagination-type of deformation (**e**; marked by arrows); and the structure with null curvature (QR3) led to no significant changes in vesicle shape (**f**). Scale bars: 5 μm

Taken together, we identified some of the major requirements for efficiently attaching curved origami structures to lipid bilayers and we observed indications of curvature-mediated deformations of membranes induced by the F-BAR mimicking structure Q3 (Fig. 2d and Supplementary Fig. 13m). Notably, incubation of GUVs with Q3 for at least 1 h led to the appearance of outwards tubular deformations within a significant fraction of vesicles (~18%; 22 out of 121 GUVs); deformations similar to the positively curved tubules reported for several F-BAR proteins^{7, 8, 10, 34}.

Membrane deformations as a function of DNA origami curvature. As different classes of BAR domains curve membranes in distinct manners⁴, we further investigated whether the appearance of membrane deformations, as reported in Fig. 2d, can be correlated with the direction and degree of curvature of our BAR-mimicking DNA origami structures. Membrane tension has been previously implicated in influencing the assembly of BAR domain proteins^{35, 36}. To provide a controllable trigger for assessing vesicle deformations, we lowered the membrane tension by

increasing osmolarity of the outer buffer in 10%. Subsequently, shape variations of the deflated GUVs were monitored.

After the hyperosmotic stress, lipid vesicles without membrane-bound DNA origami (no origami in solution or incubated with nanostructures lacking cholesterol anchors) rapidly regained their spherical shape, suffering only minor shrinkage or blebbing (Supplementary Fig. 16h–j and Supplementary Movie 1). Bursting events were seldom (~13%; 5 out of 40 GUVs). For vesicles incubated with a structure lacking curvature (L3), a comparable effect was observed (Fig. 3a and Supplementary Fig. 15i, j), independently of the total DNA origami concentration.

Remarkably, moderately curved origami quarter-circles (Q) displaying a concave membrane-binding surface were able to trigger tubulation of GUVs upon hyperosmotic shock (Fig. 3b and Supplementary Movie 2). As seen for structure Q3, this process depended on the total origami concentration. At Q3 concentrations ≤ 3 nM, most vesicles presented no significant deformations, with only a minor fraction (~18%) displaying outwards tubules (43 out of 244 GUVs). By contrast, at Q3

concentrations ≥ 5 nM, $\sim 70\%$ of all GUVs (128 out of 189) displayed outwards tubules (Supplementary Fig. 19a–d and Supplementary Fig. 15k–m). If additional cholesterol moieties were used on the concave surface (as observed for Q7 with $7 \times$ TC5), due to the increase in hydrophobicity and consequently enhanced membrane binding, lower total concentrations of DNA origami were able to induce membrane tubulation (Supplementary Fig. 19i–l and Supplementary Fig. 17g–i). Indeed, most vesicles incubated with Q7 (97 out of 191 GUVs) displayed tubular deformations at concentrations ≥ 2 nM.

In the same way, we investigated origami Q constructs displaying either a convex membrane-binding interface (QI3; anchors at top positions T0, T3, and T6), or a flat membrane-binding interface perpendicular to the curvature (QR3; anchors at lateral positions R0, R6, and R12). For the latter (QR3), no significant membrane deformations were observed upon osmotic trigger (Fig. 3f; Supplementary Fig. 16m, n and Supplementary Movie 3), consistent with the results reported for the non-curved structure L3 (Fig. 3a and Supplementary Fig. 15i, j). For structure QI3 with convex membrane-binding interface, on the other hand, $\sim 60\%$ of the vesicles (55 out of 92 GUVs; at 5 nM QI3) presented evagination/invagination-type shallow deformations upon hyperosmotic stress (Fig. 3e; Supplementary Fig. 16k–l and Supplementary Movie 4). Such deformations effectively contrasted with the outward tubules observed for structure Q3 (Fig. 3b, d) and were somewhat reminiscent of the negatively curved membrane deformations reported for inverted I-BAR domains^{37,38}.

Contrary to the origami Q structures, the more curved origami half-circle (H) structures with concave membrane-binding interface were not capable of inducing the formation of tubular deformation on GUVs (Fig. 3c): neither at high H3 total concentrations (Supplementary Fig. 15n–p), nor for H7 displaying enhanced membrane binding (Supplementary Fig. 17j–l). For instance, with the exception of seldom vesicle bursting ($\sim 15\%$; 20 out of 134 GUVs) and minor flaccid deformations ($\sim 10\%$; 14 out of 134 GUVs), vesicles incubated with H3 ($\sim 75\%$; 100 out of 134 GUVs) remained spherical upon osmotic change and did not display any tubular deformations. Adsorption of these highly curved origami structures to DOPC vesicles seemed therefore insufficient to overcome the energetic barrier required for bending a flat membrane into a positively curved tube. Indeed, assuming a typical bending modulus for lipid bilayers of $\sim 10^{-19}$ J, the estimated energy cost for bending a flat membrane segment of surface area (A) ~ 1800 nm² (corresponding to the surface area of our DNA origami scaffolds) into a membrane tube with $R \approx 46$ nm (radius of curvature fitting origami H) is $\sim 38 k_B T$, based on the area-difference elasticity (ADE) model of membrane bending^{39,40} (equation 3). For origami Q ($R \approx 84$ nm), however, the estimated membrane bending cost is $\sim 11 k_B T$, ~ 3.5 -fold lower than structure H and comparable with the membrane bending costs expected for a BAR domain protein (amphiphysin: $9 k_B T$, for $R \approx 11$ nm and $A \approx 23$ nm²)⁴¹.

Taken together, our data show a clear connection between the curvature of the membrane-binding interface of our BAR-mimicking DNA-based scaffolds and the resulting membrane deformations (e.g. tubulation, invagination, etc.).

Hierarchical oligomerization of curved DNA origami scaffolds.

Self-assembly of membrane scaffolding proteins into higher-order structures was suggested to play an important role in the mechanism of action of BAR domains^{7,10}. Both lateral and tip-to-tip linear intermolecular interactions were described to stabilize their assembly into protein lattices^{7,10}. To test the influence of such higher-order linkages, we designed variants of curved DNA origami Q that could oligomerize, similar to BAR proteins,

tip-to-tip (Supplementary Fig. 18b–d) and laterally (Supplementary Fig. 18e). Overall, four constructs capable of multimerizing in solution were created: origami Q-E5 (Supplementary Fig. 18b), Q-E7 (Supplementary Fig. 18c) and Q-E13 (Supplementary Fig. 18d) able to linearly multimerize from the tips forming arc-like oligomers of tunable size; plus origami Q-S14 (Supplementary Fig. 18e) able to multimerize laterally forming sheet-like oligomers. Constructs Q-E5/7/13 possess 2×5 , 7 and 13 blunt ends at defined helices, enabling intermolecular stacking at the origami tips. Construct Q-S14, on the other hand, displays 2×14 TATATA overhangs, enabling complementary lateral interactions along the origami sides.

Subsequently, we tested whether the inclusion of those polymerizing staples would enhance the ability of origami Q3 with concave membrane-binding interface to produce tubular membrane deformations on GUVs upon deflation. Altogether, no significant differences in terms of total bulk concentration required to induce tubulation of vesicles were observed for constructs with or without tip-to-tip oligomerizing staples (i.e., structures Q3-E5/7/13 vs. Q3, respectively; Supplementary Fig. 18g–i and Supplementary Fig. 20). In contrast, for the construct with lateral oligomerizing staples (Q3-S14), lower bulk concentrations were required for inducing membrane tubulation upon osmotic stress (Supplementary Fig. 19e–h and Supplementary Fig. 18j). Indeed, $\sim 70\%$ of the vesicles incubated with Q3-S14 presented tubular deformations at concentrations ≥ 3 nM (135 out of 193 GUVs). Likewise, inclusion of lateral polymerizing overhangs on origami QI3 with convex membrane-binding interface (i.e., QI3-S14) also affected the generation of membrane deformations (Supplementary Fig. 21). Here while most vesicles displayed evagination-type membrane deformations upon hyperosmotic stress (Supplementary Fig. 21e, f), $\sim 15\%$ of vesicles (36 out of 244 GUVs; at 5 nM QI3-S14) additionally presented inward tubules (Supplementary Fig. 21d, g) resembling protruding nanotubes described for convex I-BAR proteins^{42,43}, which could not be observed for the structure QI3 lacking lateral overhangs. Incubation with lower bulk concentrations of QI3-S14 (i.e., 2 nM), on the other hand, did not promote significant membrane deformations, similar to what was observed for convex structure Q-I3 lacking polymerizing overhangs (Supplementary Fig. 16k).

In summary, our data indicate that in particular the presence of lateral interactions influences the ability of curved membrane-bound DNA origami to deform membranes. However, this effect seems to be of minor significance, as structures having additional membrane anchors but lacking polymerization strands (i.e., Q7; Supplementary Fig. 19i–l), were able to deform lipid vesicles as efficiently (in terms of total origami concentrations required) as the structures with polymerization strands (i.e., Q3-S14).

Membrane density and binding affinity of curved DNA origami.

Our results so far strongly suggest that a critical membrane density of curved nanostructures is required for triggering membrane bending. To test this hypothesis, variable surface densities of our BAR-mimicking DNA-based scaffolds to DOPC GUVs were quantitatively investigated at equilibrium (after overnight incubation), by fluorescence imaging and single molecule detection.

Apparent membrane dissociation constants at equilibrium ($K_d \pm$ s.d.) were obtained for L3, Q3, and H3 structures by fitting the fluorescence intensity values on the surface of GUVs⁴⁴ as a function of bulk concentration to a Langmuir isotherm (equation 1): K_d (L3) = 0.39 ± 0.07 nM ($n_{\text{total}} = 288$ GUVs; $n = 131$ –157 GUVs per fit, 2 repeats), K_d (Q3) = 0.68 ± 0.18 nM ($n_{\text{total}} = 277$ GUVs; $n = 83$ –100 GUVs per fit, 3 repeats) and K_d

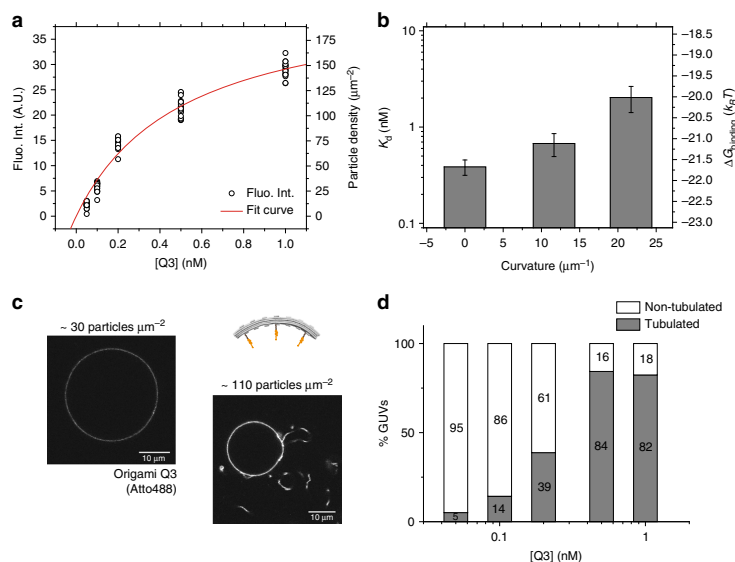


Fig. 4 Tubulation of flat membranes depends on surface density of membrane-bound curved origami Q. Fluorescence intensities of membrane-bound DNA origami (labeled with $3 \times$ Atto-488 dyes) at equilibrium (incubated overnight) were extracted using image analysis and represented as a function of total bulk concentration (**a**; here depicted for one independent set of measurements with Q3). Representative confocal images at the equatorial plane for membrane-bound Q3 nanostructures are depicted in **c**. Membrane binding of the DNA nanostructures was quantitatively investigated by fitting the data to a Langmuir isotherm (equation 1), enabling the determination of apparent membrane dissociation constants K_d (\pm s.d.): L3 ($n_{\text{total}} = 288$ GUVs; $n = 131$ –157 GUVs per fit, 2 repeats), Q3 ($n_{\text{total}} = 277$ GUVs; $n = 83$ –100 GUVs per fit, 3 repeats) and H3 ($n_{\text{total}} = 106$ GUVs; $n = 48$ –58 GUVs per fit, 2 repeats) (**b**). $\Delta G_{\text{binding}}$ was calculated via $\Delta G = RT \ln K_d$. Regarding efficiencies of membrane tubulation (**d**), high yields ($> 80\%$) were retrieved for Q3 bulk concentrations ≥ 0.5 nM, or, upon conversion to surface densities, for ≥ 90 membrane-bound DNA origami particles per μm^2 (as illustrated in **c**). Scale bars: 10 μm . Error bars in **b** correspond to s.d.

(H3) = 2.0 ± 0.6 nM ($n_{\text{total}} = 106$ GUVs; $n = 48$ –58 GUVs per fit, 2 repeats). Thus, for the same combination of cholesteryl anchors, increasing curvature of the DNA nanoscaffolds from flat ($C \approx 0$) to highly curved ($C \approx 21.7 \mu\text{m}^{-1}$) prompted a fivefold weaker binding to flat freestanding membranes (Fig. 4b and Supplementary Fig. 24).

By image analysis, we further quantified the efficiencies of vesicle tubulation by the curved DNA origami Q3 nanostructures (Fig. 4d; $n_{\text{total}} = 445$ GUVs, $n = 78$ –108 GUVs per origami concentration). When compared to the results obtained at a shorter incubation period (Fig. 2c, d and Fig. 3), after overnight incubation lower origami bulk concentrations and no additional osmotic perturbation were required to achieve high yields of membrane tubulation. At equilibrium, $> 80\%$ of vesicles (154 out of 185 GUVs) presented tubular deformation for Q3 bulk concentrations ≥ 0.5 nM (value close to K_d). Despite slightly increased membrane affinities (lower K_d values; Supplementary Fig. 24) when compared to structure Q3, structures with increased numbers of anchors (Q7) or with polymerizing overhangs (Q3–S14) yielded similar membrane tubulation efficiencies (Supplementary Fig. 25).

As the number of fluorescent particles is proportional to the fluorescence intensity, we performed additional FCS measurements in order to calibrate the measured fluorescence values and recover the corresponding densities of membrane-bound DNA origami at the surface of GUVs⁴⁴ (see calibration curve in Supplementary Fig. 22). Considering the average fluorescence intensities of single DNA origami structures, for Q3 with

moderate curvature, we estimated 50 ± 20 particles per μm^2 bound to GUVs ($n = 51$) to be sufficient for initiating tubulation, and 90 ± 20 particles per μm^2 ($n = 50$ GUVs) for almost all vesicles ($> 80\%$) to present tubules (representative curve depicted in Fig. 4a and confocal images in Fig. 4c). At these surface densities, our curved nanoscaffolds cover 9–16 % of the total membrane surface area. Interestingly, this surface fraction matches the previously reported coverage required for BAR domains to induce membrane deformations on model membranes (2–4 \times higher than for amphiphysin⁹). Flat structure L and highly curved structure H, on the contrary, were not capable of inducing membrane tubulation on GUVs even at surface coverages ≥ 100 particles per μm^2 (Supplementary Fig. 23), promoting at best flaccid membrane deformations analogous to the non-spherical shapes previously reported for flat PinkBAR domains⁴⁵. For structure L3, due to its ‘zero’ curvature, no tubulation was to be expected. For highly curved structures H3 and H7, a simple energetic cost-benefit analysis estimates the apparent free energies of membrane adhesion ($\Delta G = RT \ln K_d$, $-20 k_B T$ and $-21.5 k_B T$, respectively) to be clearly insufficient to allow for membrane bending ($38 k_B T$). For the moderately curved origami structure Q3, to the contrary, membrane adhesion ($-21.1 k_B T$) is strong enough to compensate for the energetic cost of membrane bending ($11 k_B T$), hence enabling tubular deformations to be generated.

Finally, we investigated the ultrastructure of membrane tubules decorated with origami Q3 at high surface densities (i.e., after overnight incubation of GUVs with 5 nM Q3), using cryo-

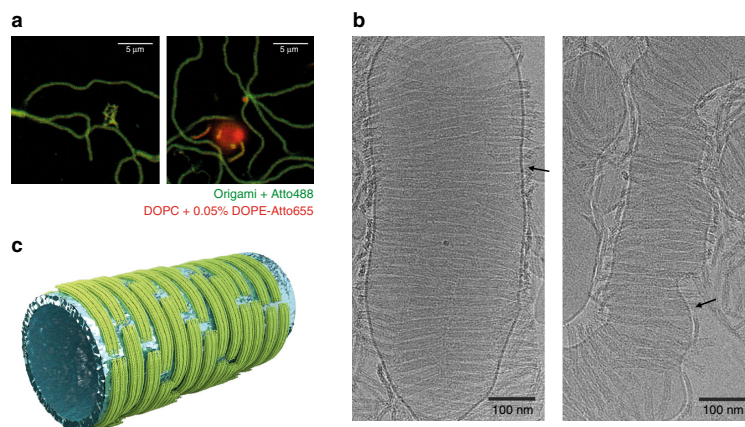


Fig. 5 Ultrastructure of lipid nanotubes decorated with DNA origami Q. **a** From confocal images, the membrane tubules obtained from GUVs (labeled with DOPE-Atto655; red) upon overnight incubation with structure Q3 (labeled with Atto488) appeared homogeneously covered with membrane-bound DNA origami. **b** Further cryo-EM imaging confirmed that the surface of the membrane tubules (black arrows) is densely covered with curved DNA nanostructures perpendicularly aligned along the long axis. **c** Based on the cryo-EM electron microscopy observations and radius of curvature of nanostructure Q3, a schematic representation of a lipid nanotube decorated with DNA origami Q is here depicted. Scale bars: **(a)** 5 μm ; **(b)** 100 nm

electron microscopy (cryo-EM). From the confocal images (Fig. 5a), the grown tubules appeared homogeneously covered with membrane-bound fluorescently labeled Q3. Further cryo-EM imaging (Fig. 5b) confirmed that the surface of the membrane tubules was densely covered with DNA nanostructures, preferentially aligning perpendicularly to the long axis of the tubular structures. Additionally, the recovered tubular diameter (220 ± 70 nm; $n_{\text{total}} = 35$ parallel cross-sections, 4 membrane tubules) was in good agreement with the predictions based on the objects curvature (~ 170 nm; Fig. 1a–c).

Discussion

This work demonstrates that curvature generation and topological transformation of biological membranes, as required for many cellular functions, can be achieved in a well-controlled fashion by curved synthetic scaffolds made of DNA. The action of these scaffolds may be tuned by varying shape, density, membrane affinity, and the propensity for self-assembly of the scaffolds on membrane surfaces. In contrast to earlier work exploring the deformation of membranes by flat nanostructures^{46, 47}, concerted lateral oligomerization by self-assembly plays only a minor role for the specific membrane transforming activity by curved DNA-based scaffolds. Moreover, in spite of producing larger tubular deformations than BAR domains, our curved structures operate at similar membrane bending energy levels. We have established three main requirements for the induction of tubular membrane deformations (Fig. 5c) by scaffolding elements: curvature, membrane affinity and surface density. Remarkably, we provide direct proof that the curvature of membrane associating macromolecular objects plays a decisive role, helping us understand the minimal physical–chemical laws underlying membrane deformations.

In this manuscript, we validate the usage of custom-designed DNA origami as a tool to overcome the limited predictability of engineered proteins. The ability of our developed structures to precisely control local membrane curvature will have great impact in the investigation of all kinds of biological membrane shaping phenomena. For example, sequential binding of proteins involved

in deformation cascades (e.g., clathrin-mediated endocytosis⁴⁸, FtsZ-mediated bacterial division⁴⁹) depends on the degree of curvature locally displayed by membranes. In this regard, BAR-mimicking DNA origami scaffoldings could allow detailed investigation of such proteins on model membranes or even cells⁵⁰, as a function of local curvature.

Altogether, our work has great significance for the growing field of bionanoengineering, opening up an avenue of research in synthetic biology. Our present achievements add exciting perspectives towards minimal biomimetic cellular machineries, involved in membrane shaping and beyond; pushing the limits of nanotechnology into cellular biology. As we laid down new foundations on manipulating DNA origami in lipid environments, design of even more elaborate DNA origami supramolecular assemblies targeting lipid membranes (e.g., artificial clathrin coated pits, enzymatic membrane complexes), and novel approaches for developing hybrid DNA-lipid-based drug delivery vehicles directed towards biological membrane barriers, will hence likely emerge in the near-future.

Methods

Materials. 1,2-dioleoyl-*sn*-glycero-3-phosphocholine (DOPC), 1,2-distearoyl-*sn*-glycero-3-phosphocholine (DSPC), cholesterol from ovine wool, 1,2-dioleoyl-*sn*-glycero-3-phosphoethanolamine-*N*-[4-(*p*-maleimidophenyl)butyramide] (MPB-DOPE) and 1,2-dioleoyl-*sn*-glycero-3-phosphoethanolamine-*N*-(cap biotinyl) (Biotin-DOPE) were purchased from Avanti Polar Lipids (Alabaster, AL, USA). Atto655-DOPE was acquired from AttoTEC GmbH (Siegen, Germany) and DiIC18(5) (DiD) from Thermo Fischer Scientifics (Waltham, MA, USA). Single-stranded M13mp18 scaffold plasmid (p7249) was supplied from Bayou Biolabs (Metairie, LA, USA), as well prepared by Florian Praetorius using high-cell-density fermentation of *Escherichia coli* in stirred-tank bioreactors according to reference⁵¹. High purity salt free (HPSF) purified staple oligonucleotides for origami preparation, as well as 5'-Atto488, 5'-Alexa488 and 3'-Biotin-TEG-functionalized oligonucleotides (all HPLC-purified) were purchased from Eurofins Genomics (Ebersberg, Germany). 5'/3'-Chol-TEG and 3'-Thiol-Modifier-C3 S-S-functionalized oligonucleotides (all HPLC purified) were acquired from Sigma-Aldrich (Taufkirchen, Germany).

Design and production of the DNA origami nanoscaffolds. The DNA origami structures employed throughout this work consisted in a 20-helix bundle with hexagonal lattice. As described in the main text, three curved designs were here

developed: origami H (curvature $C = 21.7 \mu\text{m}^{-1}$; curvature angle $\theta \approx 131^\circ$; radius of curvature $R = 46 \text{ nm}$; Supplementary Fig. 4; Supplementary Table 3), origami Q ($C \approx 11.6 \mu\text{m}^{-1}$; $\theta \approx 73^\circ$; $R = 84 \text{ nm}$; Supplementary Fig. 3; Supplementary Table 3) and origami L ($C \approx 0$; Supplementary Fig. 2; Supplementary Table 1). Those structures were based on the M13 p7249 plasmid and designed using CaDNA⁵² (Supplementary Figs. 2–4). Initial 3D models (Supplementary Fig. 1) were predicted using CanDo^{17,19}. Each design further included marked positions for attaching fluorophores, membrane-anchoring moieties or oligomerizing staples (Fig. 1d). More precisely, 7 sites on the bottom (concave) and top (convex) facets of the DNA origami (B0–B6 and T0–T6, respectively), plus 14 sites on the left and right facets (L0–L13 and R0–R13, respectively) were defined. This strategy allowed us to manipulate the functionality of the origami structures by exchanging the staple sequences at those defined external positions with functionalized counterparts (Supplementary Notes), without compromising the shape of the nanostructures stabilized by the core staples. The edges of each of the 20 helical bundles, usually kept as single-stranded segments to avoid blunt end interactions, could be similarly hybridized with functionalized staples. Folding of all the DNA origami structures was performed in a one-pot reaction mix³³. Briefly, 20 nM p7249 plasmid and 200 nM staple oligonucleotides were mixed in a 5 mM Tris-HCl, 1 mM EDTA, 20 mM MgCl₂, pH 8.0 buffer (folding buffer). Thermal annealing was performed over a cooling cycle scheme from 65 to 60 °C in 1 h and from 59 to 40 °C in 40 h, on a Eppendorf Mastercycler Pro (Hamburg, Germany) or Bio-Rad Tetrad 2 (München, Germany) thermal cycler. Purification of the folded structures from the excess of staple strands was performed using size-exclusion centrifugal filtration with Amicon Ultra 100 kDa MWCO filters (Merck Millipore, Darmstadt, Germany) or PEG precipitation⁵³ using a buffer consisting of 5 mM Tris-HCl, 1 mM EDTA, 5 mM MgCl₂, 300 mM NaCl, pH 8.0 (imaging buffer). Bulk concentrations of DNA origami were determined via fluorescence spectroscopy using a Jasco FP-8500 spectrofluorometer (Tokyo, Japan)³³. Correct assembly of the folded nanostructures was evaluated by agarose gel electrophoresis^{17,33} (Supplementary Fig. 5), negative-stain transmission electron microscopy (TEM)^{17,54} (Fig. 1b and Supplementary Fig. 5) and atomic force microscopy (AFM)³³ (Supplementary Fig. 5).

Preparation of lipid membranes for fluorescence microscopy. Supported lipid bilayers (SLBs) were obtained via fusion of small unilamellar vesicles deposited on top of freshly cleaved mica, as described elsewhere⁵⁵. Giant unilamellar vesicles (GUVs), the preferred membrane model system utilized throughout this work, were produced by electroformation in PTFE chambers with Pt electrodes^{33,56}. Six microliter of lipid mixture (2 mg mL⁻¹ in chloroform) was spread onto two Pt wires and dried in a desiccator for 30 min. The chamber was filled with 350 μL of an aqueous solution of sucrose. An AC electric field of 2 V (RMS) was applied at a frequency of 10 Hz for 1.5 h, followed by 2 Hz for 0.75 h. Unless otherwise stated, vesicles composed of DOPC, containing additional 0.005 mol% (for FCS experiments) or 0.05 mol% (for confocal imaging) Atto655-DOPE, were electroformed in an aqueous solution of sucrose iso-osmolar compared to imaging buffer (~575 mOsm kg⁻¹). Experiments were carried out in 40 μL MatriCal 384-multiwell plates with # 1.5 glass bottom thickness (Brooks Life Science Systems, Spokane, WA, USA). Prior usage, wells were freshly plasma cleaned, then passivated with bovine serum albumin (Sigma-Aldrich) or PLL(20)-g[3.5]-PEG(2) (SuSo AG, Dübendorf, Switzerland). Typically, 3 μL of the GUV suspension (pre-diluted at least 1:10 in iso-osmolar sucrose solution) were mixed with 18 μL DNA origami solution at a final 0.5–10 nM concentration diluted in imaging buffer. Unless otherwise stated, samples were incubated for at least 1 h at room temperature. Hyperosmotic stress of GUVs incubated with DNA origami structures was achieved by gently adding 3 μL of a glucose solution diluted in imaging buffer (1000 mOsm kg⁻¹) into the imaging chambers.

Typically, at least two independent sets of measurements were performed for evaluating a specific experimental condition under confocal microscopy (see following section). Overall, for the characterization of the type of membrane anchor (Supplementary Figs. 8–10), an average $n = 15$ vesicles was analyzed per each sample ($n_{\text{total}} = 277$ GUVs). For the characterization of the number, position and linker length required for cholesterol-functionalized DNA origami structures (Fig. 2a, c, d and Supplementary Figs. 11–14), an average $n = 26$ vesicles was analyzed per each sample ($n_{\text{total}} = 1023$ GUVs). For the membrane deformation assays triggered upon hyperosmotic stress (Fig. 3 and Supplementary Figs. 15–21), an average $n = 42$ vesicles was analyzed per each sample concentration ($n_{\text{total}} = 2352$ GUVs). For the determination of the binding coefficients (Fig. 4a, b and Supplementary Figs. 23, 24), an average $n = 13$ vesicles was analyzed per each sample concentration ($n_{\text{total}} = 975$ GUVs). Finally, for the determination of the tubulation efficiencies after overnight incubation (Fig. 4c, d and Supplementary Fig. 25), an average $n = 22$ vesicles was analyzed per each sample concentration ($n_{\text{total}} = 860$ GUVs).

Laser scanning confocal fluorescence microscopy. Confocal imaging was performed on a commercial laser scanning microscope LSM 780 with a ConfoCor3 unit (Zeiss, Jena, Germany) using a water immersion objective (C-Apochromat, 40 \times 1.2 W UV-VIS-IR, Zeiss, Jena, Germany). Samples were excited with the 488 nm line of an Ar-ion-laser (for Atto488 and Alexa488 excitation) or with the 633 nm line of a He-Ne laser (for Atto655 and DiD excitation). To avoid the effect of

polarization selection in excitation of the GUVs, an achromatic $\lambda/4$ plate (Edmund Optics, Barrington, NJ, USA) was installed in the excitation beam path. Images were typically recorded at the equatorial planes of GUVs, utilizing a 1 Airy unit pinhole, 512 \times 512 pixel resolution and a scan rate of 3.15 μs per pixel. Further image analysis was performed using the ImageJ software (<http://rsb.info.nih.gov/ij/>).

As fluorescence signal measured using confocal microscopy is proportional to the number of fluorescent molecules in the confocal volume, fluorescence intensity of membrane-bound DNA origami was determined in order to infer membrane affinities of different nanostructures and assess particle densities on membranes (see FCS section). For this purpose, GUVs incubated overnight (4 °C) with different bulk concentrations of DNA origami, ranging from 0.01 to 50 nM, were imaged at the equatorial plane and the corresponding fluorescence intensities extracted from the confocal images using a semi-automated Matlab-based software⁴⁴. As illustrated in Fig. 4a and Supplementary Fig. 23, apparent membrane dissociation constants at equilibrium (K_d ; Fig. 4b and Supplementary Fig. 24) for the different DNA origami nanostructures were then determined by fitting the fluorescence intensities of membrane-bound origami (I) as a function of total DNA origami concentrations in bulk (C_{bulk}) to a Langmuir isotherm⁶:

$$I = I_{\text{max}} / (1 + K_d / C_{\text{bulk}}), \quad (1)$$

Fluorescence correlation spectroscopy. Fluorescence correlation spectroscopy (FCS) measurements were carried out as described in our recent publication³³, using the LSM 780/ConfoCor 3 system mentioned above. Briefly, the laser line with wavelength of 488 nm for Atto488 excitation was used at low laser power (<1.2 μW) to avoid photobleaching and fluorescence saturation effect⁵⁷. The radius of the waist of the FCS detection volume, r_0 (207 \pm 7 nm), was calibrated using a fluorescent dye (Alexa488) with known diffusion coefficient (D) in water (D (Alexa488) = 414 $\mu\text{m}^2 \text{s}^{-1}$ at 25.0 \pm 0.5 °C)⁵⁸ and corrected for the working temperature at the objective (27.5 \pm 1.0 °C)^{57,59,60}. FCS on membranes was performed at the upper pole of a GUV with a diameter of at least 20 μm (which is large enough to neglect membrane curvature within the detection spot size). Particle numbers, N , (and consequently, surface densities, σ) of the BAR-mimicking DNA nanostructures were obtained from the analysis of the autocorrelation functions, using the freely available data analysis software PyCorrFit version 0.8.261. In order to eliminate the contribution of rotational diffusion to the correlation curves, DNA origami structures labeled at positions T2–4 were used³³. Furthermore, as virtually no unbound DNA origami was detected in solution, and its potential contribution to FCS curves was negligible, a one-component two-dimensional diffusion model^{56,57} was used (equation 2) to analyze the obtained correlation curves, as it was done in previous studies of membrane-bound DNA origami particles^{33,62,63}.

$$G(\tau) = \frac{1}{N} \frac{1}{1 + \frac{\tau}{\tau_D}}, \quad (2)$$

Here N is the number of particles in the 2D detection volume, and τ_D is the FCS diffusion time, which is determined by the translational diffusion coefficient D and the size of the 2D Gaussian detection volume r_0 as follows: $\tau_D = r_0^2 / (4D)$.

Knowing the origami length, $L = 110 \text{ nm}$, surface densities of membrane-bound particles ($\sigma = N / (\pi r_0^2)$; expressed in particles per μm^2) could be easily converted to the reduced surface densities $\rho = \sigma L^2$ ⁶². At higher surface densities ($\rho > 0.2$), crowding effects resulted in progressively stronger deviations from the one-component 2D diffusion model used to describe the translational Brownian motion of the Atto488-labeled DNA origami particles⁶². As particle density is proportional to the fluorescence intensity, average surface densities of membrane-bound DNA origami could be estimated at a high-density regime ($\rho > 0.2$) from the fluorescence intensity data obtained via confocal microscopy. Shortly, a calibration curve was obtained (Supplementary Fig. 22b) from the linear fit of the fluorescence intensity of membrane-bound DNA origami determined by confocal microscopy for single GUVs ($n = 45$) and the respective surface densities of membrane-bound DNA origami determined by FCS in the valid density regime ($\rho < 0.2$ —Supplementary Fig. 22a).

Atomic force and transmission electron microscopies. Atomic force microscopy (AFM) imaging of structures L0, Q0, and H0, deposited on top of freshly cleaved mica, was performed on a Nanowizard Ultra (JPK, Berlin, Germany) using the high-speed AC mode with USC-F0.3-k0.3 cantilevers (Nanoworld, Neuchâtel, Switzerland)³³. The cantilever oscillation was turned to a frequency of 100–150 kHz, the amplitude kept below 10 nm. Scan rate was set to 5–25 Hz and setpoints close to 7–8 nm were utilized. Analysis of the AFM images was performed using JPK SPM Data Processing (version 5.1.4) and Gwyddion (version 2.30).

Negative-stain transmission electron microscopy (TEM) imaging was performed on a Philips CM100 transmission electron microscope operated at 100 kV^{17,54}. Images were recorded with an AMT 4 \times 4 Megapixel CCD camera. Typically, 3 μL of folded DNA origami nanostructures were adsorbed on glow-discharged formvar-supported carbon coated Cu400 TEM grids (Science Services, Munich, Germany) and stained using a 2% aqueous uranyl formate solution containing 25 mM sodium hydroxide. For the experiments involving multimellar vesicles (MLV),

4 nM of origami Q0 or Q3 were pre-incubated for 30 min with DOPC MLV (at 0.5 mM lipid concentration) before deposition on the EM grids and negative staining.

For cryo-electron microscopy (cryo-EM), 5 nM Q3 was pre-incubated overnight in a tube with DOPC GUVs. Samples were then adsorbed for 4 min on glow-discharged lacy carbon grids (Plano, Wetzlar, Germany) and vitrified by plunge freezing the grid in liquid ethane. Imaging was performed on a Titan Halo electron microscope (FEI, Eindhoven, Netherlands), equipped with a Falcon II camera and a Gatan 626 cryo holder (Pleasanton, CA, USA). The microscope was operated at 300 kV, with a magnification of $\times 45,000$, giving a pixel size of 0.237 nm at the specimen level. Data were collected using SerialEM, at nominal $-3 \mu\text{m}$ target defocus with an electron dose of $20 \text{ e}^- \text{ \AA}^{-2}$. Tubular diameter (average \pm s.d.) was obtained analyzing $n_{\text{total}} = 35$ parallel cross-sections along four Q3-decorated membrane tubules.

Estimation of the energetic costs for membrane bending. The energy required for membrane bending by curved DNA origami scaffolds Q and H and a BAR domain protein were calculated using the Area-difference Elasticity (ADE) model^{39,40}. This model, based on the classical Helfrich-Canham-Evans elastic membrane model (spontaneous curvature model)⁶⁴, takes into consideration the finite thickness of the lipid bilayer and consequent additional penalty arising from the area difference between its two leaflets upon bending (i.e., negatively curved leaflet being compressed, while positively curved leaflet being expanded). The ADE model describes bending energy (ϵ_{bc}) as:

$$\epsilon_{\text{bc}} = \kappa \left(\frac{1}{2} \int dA (C_1 + C_2 - C_0)^2 + \frac{\alpha}{2AD^2} (\Delta A - \Delta A_0)^2 \right), \quad (3)$$

where κ is the bending modulus of DOPC bilayers ($23.1 \text{ k}_B T$)⁶⁵, A is the area of the membrane segment, C_1 and C_2 are the principal curvatures (for a membrane tube, $C_1 = 1/R$ and $C_2 = 0$). C_0 is spontaneous curvature of the membrane, which relates to the intrinsic curvature of the lipid molecules. For a homogenous non-symmetric bilayer, $C_0 = 0$. In the second term, ΔA is the differential monolayer area (determined by the difference in number of molecules of the outer and the inner monolayers) and ΔA_0 its value at equilibrium. D corresponds to the membrane thickness. $\alpha = \bar{\kappa}/\kappa$, with $\bar{\kappa}$ being the non-local bending rigidity modulus. α is estimated to be in the order of unity and the approximation $\alpha = 3/\pi$ ⁶⁶ was used.

Data availability. Data supporting the findings of this manuscript are available from the corresponding author upon reasonable request.

Received: 21 December 2017 Accepted: 24 January 2018
Published online: 23 February 2018

References

- Baumgart, T., Capraro, B. R., Zhu, C. & Das, S. L. Thermodynamics and mechanics of membrane curvature generation and sensing by proteins and lipids. *Annu. Rev. Phys. Chem.* **62**, 483–506 (2011).
- McMahon, H. T. & Gallop, J. L. Membrane curvature and mechanisms of dynamic cell membrane remodelling. *Nature* **438**, 590–596 (2005).
- Zimmerberg, J. & Kozlov, M. M. How proteins produce cellular membrane curvature. *Nat. Rev. Mol. Cell. Biol.* **7**, 9–19 (2006).
- Qualmann, B., Koch, D. & Kessels, M. M. Let's go bananas: revisiting the endocytic BAR code. *Embo. J.* **30**, 3501–3515 (2011).
- Frost, A., Unger, V. M. & De Camilli, P. The BAR domain superfamily: membrane-molding macromolecules. *Cell* **137**, 191–196 (2009).
- Zimmerberg, J. & McLaughlin, S. Membrane curvature: how BAR domains bend bilayers. *Curr. Biol.* **14**, R250–R252 (2004).
- Frost, A. et al. Structural basis of membrane invagination by F-BAR domains. *Cell* **132**, 807–817 (2008).
- Wang, Q. et al. Molecular mechanism of membrane constriction and tubulation mediated by the F-BAR protein Pacsin/Syndapin. *Proc. Natl. Acad. Sci. USA* **106**, 12700–12705 (2009).
- Sorre, B. et al. Nature of curvature coupling of amphiphysin with membranes depends on its bound density. *Proc. Natl. Acad. Sci. USA* **109**, 173–178 (2012).
- McDonald, N. A., Vander Kooi, C. W., Ohi, M. D. & Gould, K. L. Oligomerization but not membrane bending underlies the function of certain F-BAR proteins in cell motility and cytokinesis. *Dev. Cell* **35**, 725–736 (2015).
- Simunovic, M., Voth, G. A., Callan-Jones, A. & Bassereau, P. When physics takes over: BAR proteins and membrane curvature. *Trends Cell. Biol.* **25**, 780–792 (2015).
- Traub, L. M. F-BAR/EFC domain proteins: some assembly required. *Dev. Cell* **35**, 664–666 (2015).
- Schwille, P. Bottom-up synthetic biology: engineering in a tinkerer's world. *Science* **333**, 1252–1254 (2011).
- Schwille, P. & Diez, S. Synthetic biology of minimal systems. *Crit. Rev. Biochem. Mol. Biol.* **44**, 223–242 (2009).
- Rothmund, P. W. Folding DNA to create nanoscale shapes and patterns. *Nature* **440**, 297–302 (2006).
- Douglas, S. M. et al. Self-assembly of DNA into nanoscale three-dimensional shapes. *Nature* **459**, 414–418 (2009).
- Castro, C. E. et al. A primer to scaffolded DNA origami. *Nat. Methods* **8**, 221–229 (2011).
- Dietz, H., Douglas, S. M. & Shih, W. M. Folding DNA into twisted and curved nanoscale shapes. *Science* **325**, 725–730 (2009).
- Kim, D. N., Kilcherr, F., Dietz, H. & Bathe, M. Quantitative prediction of 3D solution shape and flexibility of nucleic acid nanostructures. *Nucleic Acids Res.* **40**, 2862–2868 (2012).
- Langecker, M. et al. Synthetic lipid membrane channels formed by designed DNA nanostructures. *Science* **338**, 932–936 (2012).
- Krishnan, S. et al. Molecular transport through large-diameter DNA nanopores. *Nat. Commun.* **7**, 12787 (2016).
- Dong, Y. et al. Cuboid vesicles formed by frame-guided assembly on DNA origami scaffolds. *Angew. Chem. Int. Ed.* **56**, 1586–1589 (2016).
- Perrault, S. D. & Shih, W. M. Virus-inspired membrane encapsulation of DNA nanostructures to achieve in vivo stability. *ACS Nano* **8**, 5132–5140 (2014).
- Yang, Y. et al. Self-assembly of size-controlled liposomes on DNA nanotemplates. *Nat. Chem.* **8**, 476–483 (2016).
- Zhang, Z., Yang, Y., Pincet, F., M. C. L. & Lin, C. Placing and shaping liposomes with reconfigurable DNA nanocages. *Nat. Chem.* **9**, 653–659 (2017).
- Suzuki, Y., Endo, M. & Sugiyama, H. Lipid-bilayer-assisted two-dimensional self-assembly of DNA origami nanostructures. *Nat. Commun.* **6**, 8052 (2015).
- Martin, T. G. & Dietz, H. Magnesium-free self-assembly of multi-layer DNA objects. *Nat. Commun.* **3**, 1103 (2012).
- Mengistu, D. H., Bohinc, K. & May, S. Binding of DNA to zwitterionic lipid layers mediated by divalent cations. *J. Phys. Chem. B.* **113**, 12277–12282 (2009).
- Harries, D., May, S. & Ben-Shaul, A. Counterion release in membrane-biopolymer interactions. *Soft Matter* **9**, 9268–9284 (2013).
- Hirtz, M., Brglez, J., Fuchs, H. & Niemeyer, C. M. Selective binding of DNA origami on biomimetic lipid patches. *Small* **11**, 5752–5758 (2015).
- Dave, N. & Liu, J. Biomimetic sensing based on chemically induced assembly of a signaling DNA aptamer on a fluid bilayer membrane. *Chem. Commun.* **48**, 3718–3720 (2012).
- Czogalla, A., Franquelim, H. G. & Schwille, P. DNA Nanostructures on Membranes as Tools for Synthetic Biology. *Biophys. J.* **110**, 1698–1707 (2016).
- Khmelnikaia, A., Franquelim, H. G., Petrov, E. P. & Schwille, P. Effect of anchor positioning on binding and diffusion of elongated 3D DNA nanostructures on lipid membranes. *J. Phys. D: Appl. Phys.* **49**, 194001 (2016).
- Zhao, H. et al. Membrane-sculpting BAR domains generate stable lipid microdomains. *Cell Rep.* **4**, 1213–1223 (2013).
- Shi, Z. & Baumgart, T. Membrane tension and peripheral protein density mediate membrane shape transitions. *Nat. Commun.* **6**, 5974 (2015).
- Simunovic, M. & Voth, G. A. Membrane tension controls the assembly of curvature-generating proteins. *Nat. Commun.* **6**, 7219 (2015).
- Mattila, P. K. et al. Missing-in-metastasis and IRSp53 deform PI(4,5)P2-rich membranes by an inverse BAR domain-like mechanism. *J. Cell. Biol.* **176**, 953–964 (2007).
- Saarikangas, J. et al. Molecular mechanisms of membrane deformation by I-BAR domain proteins. *Curr. Biol.* **19**, 95–107 (2009).
- Miao, L., Seifert, U., Wortis, M. & Döbereiner, H. G. Budding Transitions of Fluid-Bilayer Vesicles - the Effect of Area-Difference Elasticity. *Phys. Rev. E* **49**, 5389–5407 (1994).
- Döbereiner, H. G., Lehmann, A., Goedel, W., Selchow, O. & Lipowsky, R. Membrane curvature induced by sugar and polymer solutions. *Mater. Res. Soc. Symp. P.* **489**, 101–106 (1998).
- Lipowsky, R. Spontaneous tubulation of membranes and vesicles reveals membrane tension generated by spontaneous curvature. *Faraday Discuss.* **161**, 305–331 (2013).
- Barooji, Y. F., Rørvig-Lund, A., Semsey, S., Reihani, S. N. & Bendix, P. M. Dynamics of membrane nanotubes coated with I-BAR. *Sci. Rep.* **6**, 30054 (2016).
- Prévost, C. et al. IRSp53 senses negative membrane curvature and phase separates along membrane tubules. *Nat. Commun.* **6**, 8529 (2015).
- Thomas, F. A., Visco, I., Petrásek, Z., Heinemann, F. & Schwille, P. Introducing a fluorescence-based standard to quantify protein partitioning into membranes. *Biochim. Biophys. Acta* **1848**, 2932–2941 (2015).

45. Pykäläinen, A. et al. Pinkbar is an epithelial-specific BAR domain protein that generates planar membrane structures. *Nat. Struct. Mol. Biol.* **18**, 902–907 (2011).
46. Czogalla, A. et al. Amphipathic DNA origami nanoparticles to scaffold and deform lipid membrane vesicles. *Angew. Chem. Int. Ed.* **54**, 6501–6505 (2015).
47. Kocabay, S. et al. Membrane-assisted growth of DNA origami nanostructure arrays. *ACS Nano* **9**, 3530–3539 (2015).
48. Saleem, M. et al. A balance between membrane elasticity and polymerization energy sets the shape of spherical clathrin coats. *Nat. Commun.* **6**, 6249 (2015).
49. Arumugam, S. et al. Surface topology engineering of membranes for the mechanical investigation of the tubulin homologue FtsZ. *Angew. Chem. Int. Ed.* **51**, 11858–11862 (2012).
50. Akbari, E. et al. Engineering Cell Surface Function with DNA Origami. *Adv. Mater.* **29**, 1703632 (2017).
51. Kick, B., Praetorius, F., Dietz, H. & Weuster-Botz, D. Efficient production of single-stranded phage DNA as scaffolds for DNA origami. *Nano. Lett.* **15**, 4672–4676 (2015).
52. Douglas, S. M. et al. Rapid prototyping of 3D DNA-origami shapes with caDNA. *Nucleic Acids Res.* **37**, 5001–5006 (2009).
53. Stahl, E., Martin, T. G., Praetorius, F. & Dietz, H. Facile and scalable preparation of pure and dense DNA origami solutions. *Angew. Chem. Int. Ed.* **53**, 12735–12740 (2014).
54. Sobczak, J. P., Martin, T. G., Gerling, T. & Dietz, H. Rapid folding of DNA into nanoscale shapes at constant temperature. *Science* **338**, 1458–1461 (2012).
55. Franquelim, H. G., Gaspar, D., Veiga, A. S., Santos, N. C. & Castanho, M. A. Decoding distinct membrane interactions of HIV-1 fusion inhibitors using a combined atomic force and fluorescence microscopy approach. *Biochim. Biophys. Acta* **1828**, 1777–1785 (2013).
56. García-Sáez, A. J., Carrer, D. C. & Schwille, P. Fluorescence correlation spectroscopy for the study of membrane dynamics and organization in giant unilamellar vesicles. *Methods Mol. Biol.* **606**, 493–508 (2010).
57. Petrov, E. P. & Schwille, P. In Standardization and quality assurance in fluorescence measurements II—bioanalytical and biomedical applications. (ed. U. Resch-Genger) 145–197 (Springer, Berlin Heidelberg, 2008).
58. Petrov, E. P., Ohrt, T., Winkler, R. G. & Schwille, P. Diffusion and segmental dynamics of double-stranded DNA. *Phys. Rev. Lett.* **97**, 258101 (2006).
59. Heinemann, F., Betaneli, V., Thomas, F. A. & Schwille, P. Quantifying lipid diffusion by fluorescence correlation spectroscopy: a critical treatise. *Langmuir* **28**, 13395–13404 (2012).
60. Korson, L., Drosthan, W. & Millero, F. J. Viscosity of water at various temperatures. *J. Phys. Chem.* **73**, 34–39 (1969).
61. Müller, P., Schwille, P. & Weidemann, T. PyCorrFit-generic data evaluation for fluorescence correlation spectroscopy. *Bioinformatics* **30**, 2532–2533 (2014).
62. Czogalla, A., Kauert, D. J., Seidel, R., Schwille, P. & Petrov, E. P. DNA origami nanoneedles on freestanding lipid membranes as a tool to observe isotropic-nematic transition in two dimensions. *Nano. Lett.* **15**, 649–655 (2015).
63. Czogalla, A. et al. Switchable domain partitioning and diffusion of DNA origami rods on membranes. *Faraday Discuss.* **161**, 31–43 (2013).
64. Helfrich, W. Elastic properties of lipid bilayers: theory and possible experiments. *Z. Naturforsch. C* **28**, 693–703 (1973).
65. Fa, N. et al. Decrease of elastic moduli of DOPC bilayers induced by a macrolide antibiotic, azithromycin. *Biochim. Biophys. Acta* **1768**, 1830–1838 (2007).
66. Seifert, U. & Lipowsky, R. In Structure and dynamics of membranes. (eds R. Lipowsky & E. Sackmann) 403–462 (Elsevier Science, Amsterdam; New York, 1995).

Acknowledgements

This project was mainly funded by the collaborative research center SFB863 of the German Research Foundation (DFG). Additional support was given by the Nanosystems Initiative Munich (NIM), Center for NanoScience (CeNS) and Center for Integrated Protein Science Munich (CIPSM). H.G.F. was awarded a Humboldt Research Fellowship (PTG/1152511/STP) from the Alexander von Humboldt Foundation. A.K. was supported by the Graduate School of Quantitative Biosciences Munich (QBM). H.D. acknowledges the European Research Council (ERC Starting Grant #256270). P.S. acknowledges the Max Planck Society for further support. We thank Mike Strauss and the CEM facility at the Max Planck Institute of Biochemistry for the assistance during cryo-EM experiments, Aleksander Czogalla and Veikko Linko for initial assistance and support, and Eugene P. Petrov for expert advice and fruitful discussions.

Author contributions

P.S. and H.G.F. initially conceived the project. P.S. supervised and coordinated the project. H.D. supervised the development of curved DNA origami-based scaffolds. Experimental design was carried out largely by H.G.F., with contribution of A.K. H.G.F. designed the DNA origami structures, performed and analyzed the fluorescence microscopy experiments for studying requirements for membrane binding and curvature generation, executed the membrane deformation assays upon osmotic trigger and carried out the cryo-EM experiment. A.K. performed and analyzed the fluorescence imaging and FCS-based experiments for determining surface densities, binding and tubulation efficiencies. J.-P.S. developed the strategies for lateral self-assembly in solution and carried out negative-stain TEM experiments. All authors contributed to the writing and revision of the manuscript.

Additional information

Supplementary Information accompanies this paper at <https://doi.org/10.1038/s41467-018-03198-9>.

Competing interests: The authors declare no competing financial interests.

Reprints and permission information is available online at <http://ngp.nature.com/reprintsandpermissions/>

Publisher's note: Springer Nature remains neutral with regard to jurisdictional claims in published maps and institutional affiliations.



Open Access This article is licensed under a Creative Commons Attribution 4.0 International License, which permits use, sharing, adaptation, distribution and reproduction in any medium or format, as long as you give appropriate credit to the original author(s) and the source, provide a link to the Creative Commons license, and indicate if changes were made. The images or other third party material in this article are included in the article's Creative Commons license, unless indicated otherwise in a credit line to the material. If material is not included in the article's Creative Commons license and your intended use is not permitted by statutory regulation or exceeds the permitted use, you will need to obtain permission directly from the copyright holder. To view a copy of this license, visit <http://creativecommons.org/licenses/by/4.0/>.

© The Author(s) 2018

V.2 Integration of a conformational switch into DNA origami scaffolds

The results discussed in this section are the result of a close collaboration with Megan C. Engel and Garima Mishra, from the group of Jonathan P.K. Doye, in the University of Oxford, England. DNA origami nanostructure design and all in vitro experimental work has been performed by AK. All in silico experiments have been performed by MCE and GM. All contributed to the project design and data interpretation. Assistance on transmission electron microscopy (TEM) was given by Mike Strauss, head of the TEM facility in the Max Planck Institute for Biochemistry.

V.2.1 Introduction

Bin/Amphiphysin/Rvs (BAR) proteins are passive scaffolds that transmit their shape to the lipid membrane by binding to it (see section II.1.3). Another classical example of scaffolding proteins is the fission protein dynamin. In opposition to proteins from the BAR domain family, dynamin is an active scaffold which changes conformation upon GTP hydrolysis [Pawlowski, 2010, Schmid and Frolov, 2011, Ferguson and De Camilli, 2012]. Several models suggest that the helical dynamin coat can constrict, extend, turn, twist or perform other movements, resulting in the physical cleavage of the enclosed lipid tube and its final vesiculation.

Previously, DNA origami has been used to design scaffolds to shape free-standing lipid membranes [Kocabey et al., 2015, Czogalla et al., 2015a, Franquelim et al., 2018, Grome et al., 2018]. In these studies, the designed scaffolds passively shaped the lipid membranes either by imprinting their curved shape and thus inducing tubulation [Franquelim et al., 2018, Grome et al., 2018], or by polymerizing on lipid membranes thus resulting in planar deformations and even vesicle rupture [Kocabey et al., 2015, Czogalla et al., 2015a]. However, to our knowledge, no reconfigurable DNA-based membrane scaffolding system has been designed so far.

The first DNA nanomachine was based on the conversion from B to Z-DNA [Mao et al., 1999] and, shortly after, the first DNA tweezer driven by a strand displacement mechanism

was demonstrated [Yurke et al., 2000]. However, only a decade later the first reconfigurable DNA origami nanostructures emerged [Liedl et al., 2010, Marini et al., 2011]. Since then, a number of DNA origami machines have been designed, such as tweezers to study protein complexes (e.g. nucleosomes) [Funke et al., 2016b, Funke et al., 2016a, Le et al., 2016] or control enzymatic activity [Liu et al., 2013], cages for molecular delivery [Douglas et al., 2012, Andersen et al., 2009] or enzymatic control [Grossi et al., 2017], or even molecular sensors [Kuzuya et al., 2011, Kuzyk et al., 2014], to name only a few (for a recent review on dynamic DNA nanostructures, see [Ijäs et al., 2018]). Nonetheless, to date, only two reconfigurable structures have been designed to interact with lipid membranes. DNA origami bilayer structures have been developed to unfold in the presence of lipid bilayers thus triggering DNA nanostructure binding [List et al., 2014]. On the other hand, cages that capture small unilamellar vesicles (SUVs) have been programmed to further change their configuration promoting fusion and reshaping of liposome [Zhang et al., 2017].

Several mechanisms have been proposed to manipulate the conformation of DNA based structures, such as Z-B DNA transition [Mao et al., 1999], toehold-mediated strand displacement mechanism [Yurke et al., 2000], pH [Liedl and Simmel, 2005, Elbaz et al., 2009, Kuzuya et al., 2014b], temperature [Turek et al., 2018], DNA polymerase assisted gap-filling [Agarwal et al., 2018], DNA intercalators [Chen et al., 2016, Zadegan et al., 2017], light regulation [Kohman and Han, 2015, Kuzyk et al., 2016, Willner et al., 2017], and UV light damage [Chen et al., 2017]. From those, mainly the strand displacement mechanism has been used for a vast range of applications [Castro et al., 2015].

Here, we propose to develop a three-state structure that can change its configuration from a passive state, where it binds but does not affect the shape of the lipid membrane, to a set of active states that can deform the lipid membrane. Three modules were designed based on the strand displacement mechanism (Figure V.1) and fine-tuned through structural characterization, combining TEM and oxDNA modelling. Furthermore, the effect of each module on lipid bilayers was assessed using confocal fluorescence microscopy.

V.2.2 Results and Discussion

V.2.2.1 Modular design and characterization of a DNA origami nanostructure with an integrated conformational switch

Here, I designed a modular DNA origami nanostructure based on a 22-helix bundle nunchuck, constituted by two rigid halves with a connecting flexible hinge (Figure V.1A, Supplementary figure G.1). This flexible basic module with a 5 nucleotide (nt) gap (module N) can be further stabilized in several conformations by other modules (Figure V.1B). Lateral double-helices are added to stabilize a flat "rigid" conformation that can be further switched to a single-stranded "flexible" conformation (short module S). On the other side, the introduction of helices below the structure can stabilize a specific angle in an "open" conformation, which can be switched to a "closed" conformation through programmed hairpin folding (long module L) (Supplementary figure G.2). For both modules, the toehold-mediated strand displacement mechanism is used to trigger the conformational change (Figure V.1C). The strands to be removed were designed to bear 7/8 nucleotide overhangs on the 3'-end that act as a toehold for docking and consequent hybridization of the removal strand (R). As a result, the strands exposing toeholds are displaced, thus leaving single-stranded portions in the DNA nanostructure (Supplementary tables G.1 and G.2). Notably, single-stranded DNA has previously been demonstrated to keep the structural arrangement of rigid DNA rods in 3D [Liedl et al., 2010] and to generate force for bending DNA nanostructures [Liedl et al., 2010, Zhou et al., 2014].

To validate the design strategy, we pursued a combined simulation and experimental approach, in order to characterize the bending angle of each structural module. We used oxDNA [Ouldridge et al., 2011, Sulc et al., 2012], a nucleotide-level coarse-grained model. oxDNA has previously been successfully used to model DNA nanostructures and their bending angles [Seifert et al., 2015, Schreck et al., 2016, Sharma et al., 2017], to capture DNA mechanical response to tension [Romano et al., 2013, Mosayebi et al., 2015] and to describe DNA twisting [Matek et al., 2012, Matek et al., 2015]. The *in silico* results of angle distribution (Supplementary figure G.3) were confirmed using TEM imaging (Figure V.2). For this, each configuration was individually folded and imaged.

In agreement with the simulated data (oxDNA), TEM analysis of module N revealed a bending angle of $\approx 150^\circ$ (Figure V.2A). Interestingly, the structural flexibility of module

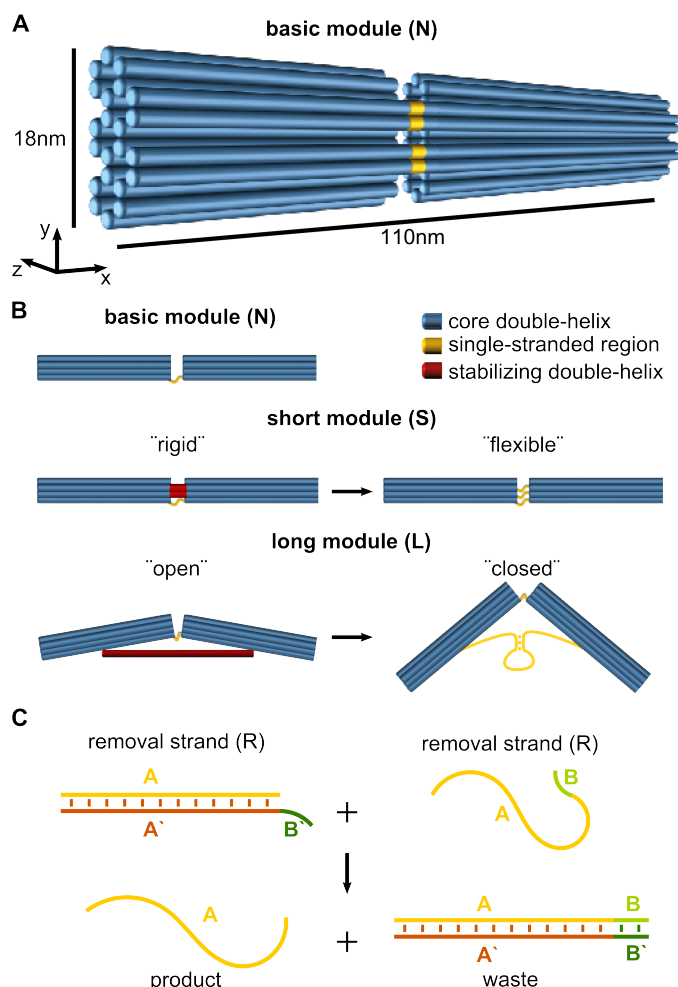


Figure V.1: Design principles for a DNA origami nanostructure with an integrated conformational switch. A) Schematic representation of the basic module (N) consisting of a core DNA nuchuck of 18 nm width and 110 nm length. B) Side view of each of the designed modules: basic module (N); short module (S) where lateral double-helices are added to stabilize a flat "rigid" conformation that can be switched to a single-stranded "flexible" form; long module (L) where a specific "open" bending angle is stabilized by additional double-helices that can be switched to a smaller "closed" angle through hairpin folding. In A) and B) blue cylinders correspond to core double-helices, yellow is used to highlight single-stranded regions and red cylinders depict stabilizing double-helices. C) Schematic representation of the general mechanism of toehold-mediated strand displacement, employed to achieve the confirmation changes depicted in B).

N was limited, with bending angles varying between 120° and 180° . Indeed, oxDNA simulations suggest that nt-stacking across the short 5nt gap may limit the bending angle of module N. Indeed, stacking interactions have been described to stabilize the conformation

of single-stranded DNA [McIntosh et al., 2014, Plumridge et al., 2017], to determine the configuration of mismatched bases in a DNA double-helix [Zacharias and Sklenar, 1997, Jiao et al., 2002] and even to drive the assembly of DNA nanostructure arrays [Woo and Rothmund, 2011, Gerling et al., 2015]. Moreover, due to DNA helix splaying from the connector helices, module N has a preferential bending direction downwards.

In its "rigid" conformation, module S presents an almost flat conformation of $\approx 180^\circ$ in oxDNA simulations, corroborated by TEM images (Figure V.2B, left panel). Interestingly, the removal of the stabilizing strand (highlighted in magenta in the snapshot from the oxDNA simulation) only marginally increases the structural flexibility of module S (Figure V.2B, right panel). Indeed, in the "flexible" conformation of S, the lateral single-strands appear to counteract the helix splaying.

According to oxDNA simulations, the DNA helices introduced under the basic module stabilized a bending angle of $\approx 130^\circ$ in the "open" configuration of module L, as expected from the design (Figure V.2C, left panel). However, TEM imaging suggests a broader angle distribution, most probably due to differences in the yield of strand incorporation [Wagenbauer et al., 2014, Strauss et al., 2018]. In the "closed" configuration of module L, the bending angle is stabilized at $\approx 50^\circ$ according to oxDNA simulations and at $\approx 40^\circ$ from TEM imaging. Notably, in this simulation the sequence, and thus hairpin folding, has not been taken into account.

To confirm the strand displacement upon addition of the corresponding removal strands (R), we used dual-colour agarose gel electrophoresis. For this purpose, DNA nanostructures have been labelled with Cy3-modified oligonucleotides. Additionally, Cy5-modified protecting strands (that will be removed upon addition of R) were used (Figure V.3A). Through analysis of the fluorescence signal, we determined a removal efficiency of 97% and 75% in module S and L, respectively. Notably, the lower strand displacement efficiency for module L can be explained by the staple routing (Figure G.1, Supplementary table G.1). For module S, each removed strand is short (P_s^*) and only introduces one crossover between adjacent helices. On the other hand, each protecting strand (P_{l_1} and P_{l_2}) in module L establishes two crossovers, which may result in the thermodynamic entrapment of the formed double-stranded product upon addition of R.

TEM imaging further confirmed the conformational switch upon addition of R (Figure V.3B). The initial configuration of each module ("rigid" for module S and "open" for module

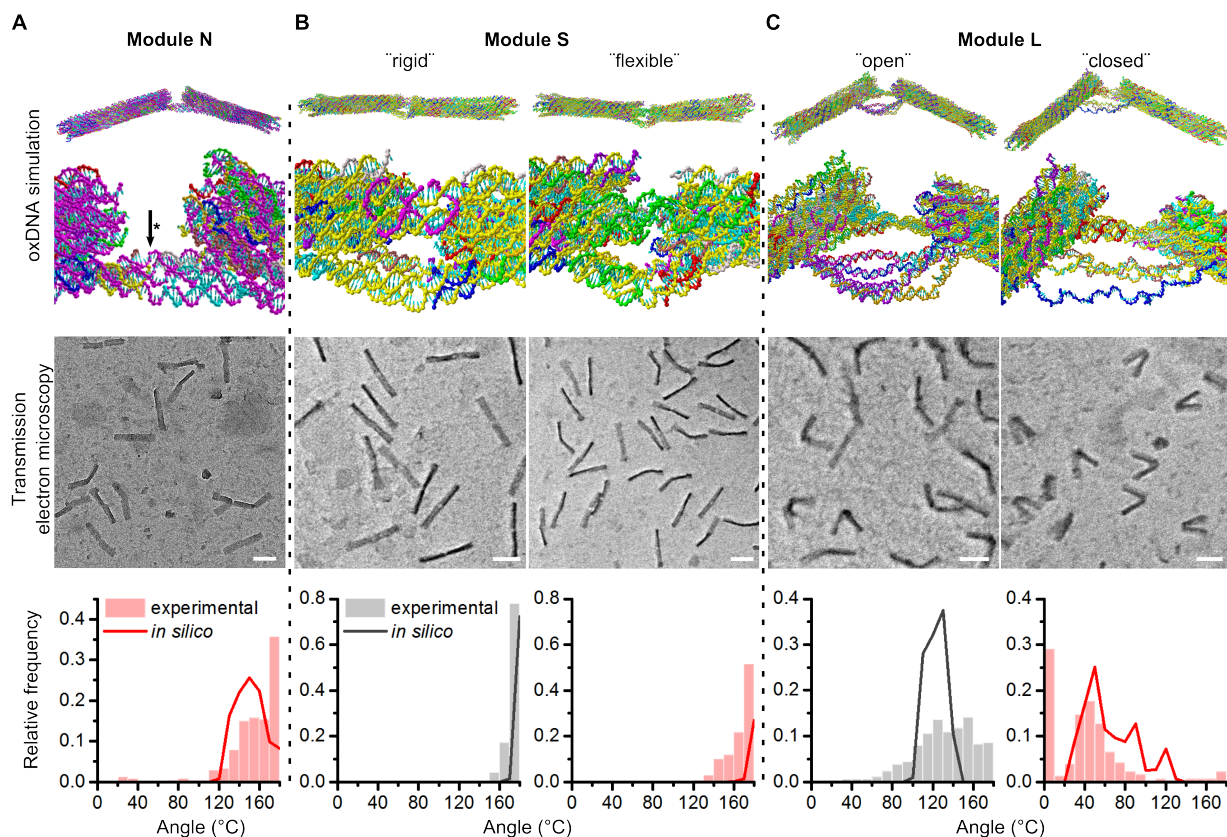


Figure V.2: Structure characterization of individual DNA origami modules. Snapshots of oxDNA simulations (top), TEM images (middle) and relative angle frequencies (bottom) observed for module N (A), "rigid" and "flexible" conformations of module S (B) as well as "open" and "closed" conformations of module L (C). The arrow in A points to the 5nt-long single-stranded gap between the two halves of the structure. Scale bars in the TEM images correspond to 50 nm. Relative angle frequencies were obtained from TEM image analysis (bars - experimental) and from oxDNA simulations (lines - *in silico*).

L) has been incubated overnight with 100× excess of corresponding removal strands. The obtained angle distribution for the "rigid" module S incubated with R reproduced the one obtained for the "flexible" module S (Figure V.5B, right panel). Incubation of the "open" module L with R resulted in a broad angle distribution, between the angles obtained for the folded "open" and "closed" conformations (Figure V.5C). These results corroborate the 75% displacement efficiency determined by gel electrophoresis.

Taken together, our results validate our design strategy of a dynamic DNA nanostructure and the use of oxDNA to structurally characterize designs *in silico*.

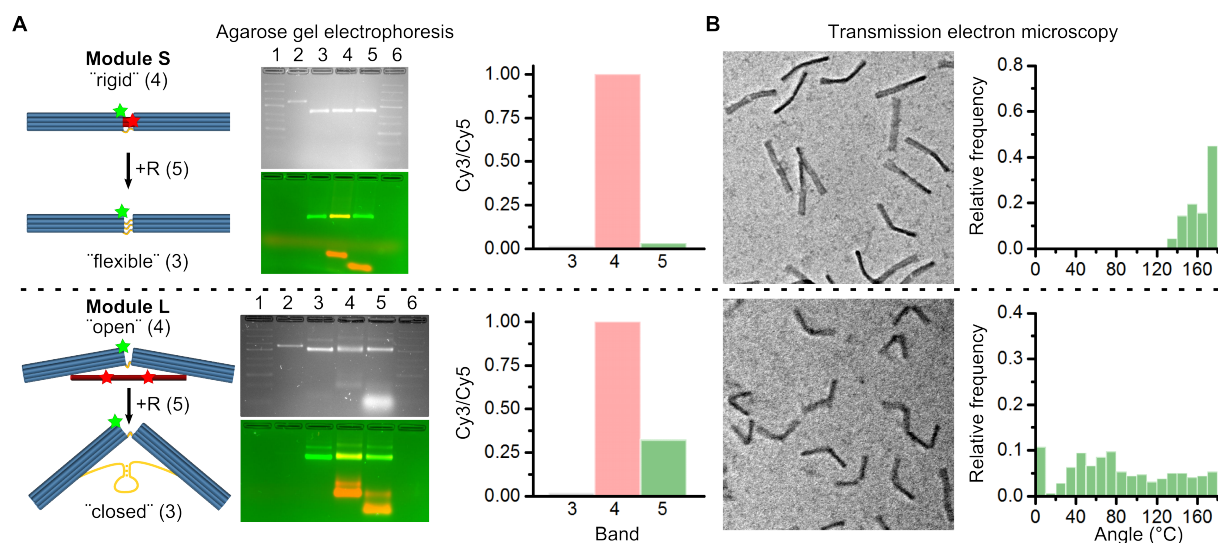


Figure V.3: DNA origami nanostructures switch their conformation upon toehold-mediated strand displacement. A) Confirmation of strand displacement by agarose gel dual-colour imaging. Module S (top) and L (bottom) are permanently labelled with Cy3 while Cy5-labelled strands are expected to be removed upon addition of the removal strand R. In lane 3, we loaded the "flexible" or "closed" (single labelled) conformation of module S or L, respectively. "Rigid" or "open" (double labelled) conformation of module S or L, respectively, were loaded on lane 4. In lane 5, "rigid" or "open" conformations of module S or L, respectively, incubated with the corresponding removal strands (R) were loaded. The unfolded plasmid M13 (2) and the ladder (1 and 6) are shown for reference. B) TEM images and respective observed relative angle frequencies for "rigid"/"open" conformation of module S/L (top/bottom, respectively) incubated with R strands.

V.2.2.2 DNA nanostructure fine-tuning towards a three-state structure

To generate a three-state structure, we proposed to combine the three individual modules. While the lateral helices of module S would assure a starting flat conformation ("open"), the central gap of the module N will allow the switch to different bending angles ("flexible") and the helices below the structure of module L will enable the stabilization of small bending angles ("closed"). However, the combination of the three modules resulted in an equal angle distribution $\approx 165^\circ$ before and after strand displacement (data not shown). Our hypothesis is that, while the insertion of the helices below the structure causes strain on the "open" conformation closing the structure by 10° , the lateral helices and nt-stacking across the gap strongly restrain the flexibility of the "closed" conformation.

In order to improve the structural flexibility, we varied the size of the gap in module

N from 0 to 42 nt and simulated the angle distribution using oxDNA (Figure V.4A). We observed that, while increasing the gap length from 5 to 21 nt, the range of accessible angles (and thus the flexibility) of module N increased from 60° to 120° . Further increasing the gap length to 42 nt did not significantly impact the flexibility of the DNA nanostructure. Interestingly, total closing of the gap did not result in a fully flat conformation but rather in an angle of $\approx 150^\circ$, due to splaying of DNA helices. Thus, we hypothesize that lateral double-helices are indispensable to keep a straight conformation.

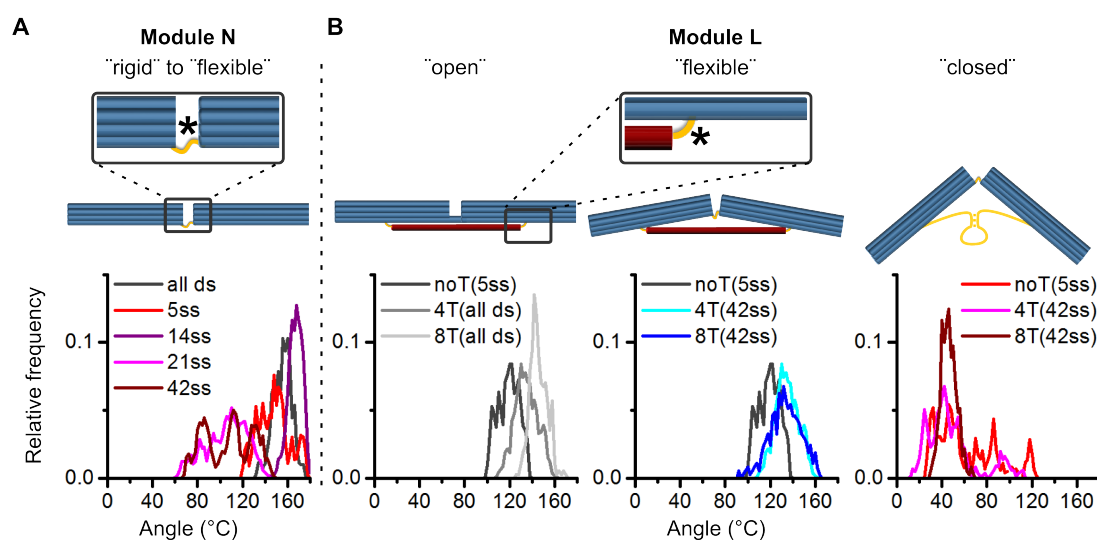


Figure V.4: oxDNA modelling reveals that small modifications in design result in major structural changes. A) Changes in relative angle frequencies upon changes in the single-stranded gap length (marked by *) in module N. Gap length is varied from 0 to 42 nt. B) Changes in relative angle frequencies of each module L conformation upon insertion of none, 4 or 8 thymine (T) nucleotides at the insertion point (marked by *) of the stabilizing helices under the structure. The size of the gap is specified in the legend.

To relax the tension in the insertion point of the helices under the module L, we modified the strand sequence to include extra T nts on each side. The conformations of structures with a 42 nts gap and additional 4 or 8 Ts in the insertion points (marked as *) were simulated using oxDNA (Figure V.4B). The introduction of additional Ts shifted the angle distribution of the "rigid" conformation closer to a flat structure, confirming the tension in the original structure (no Ts). Indeed, the angle distribution obtained by introduction of additional 8 Ts is similar to the one of "rigid" (closed gap) module N (Figure V.4A). Notably, the introduction of Ts in the insertion points shifted the angle distribution of the "flexible" configuration by only $\approx 10^\circ$, although accompanied by a slight broadening of the angle distribution. Furthermore, the angle stabilized by hairpin folding in the "closed"

configuration was not influenced by the introduction of Ts.

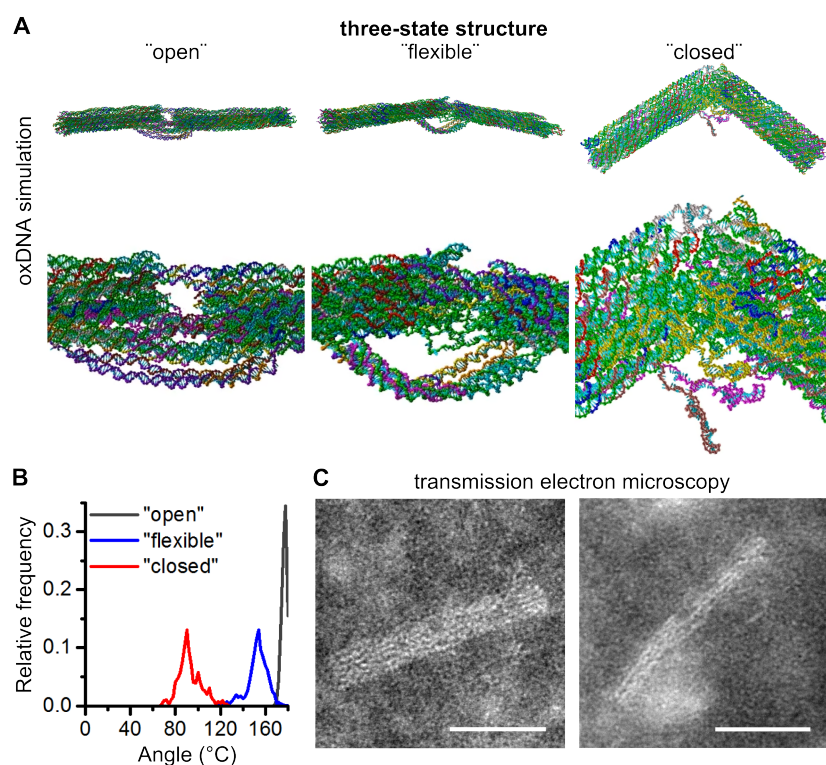


Figure V.5: Three-state DNA origami nanostructure achieved by combination of modules N, S and L. A) Snapshots of oxDNA simulations of "open", "flexible" and "closed" conformations of the three-state DNA origami nanostructure. B) Angle distribution obtained from oxDNA simulations for the three conformations of the DNA origami nanostructure. C) TEM images of the "open" conformation. Scale bars correspond to 50 nm.

By combining together all three modules N, S and L with the respective modifications, a structure with three defined states was achieved (Figure V.5A,B). Thus, in the basic module we incorporate not only side DNA helix braces, but also helices below the structure. To define an initial "open" configuration, the gap in the structure is fully closed and the structure is fully double-stranded. The presence of the lateral double-helices counteract the splaying of the helices. The helices below the structure, necessary for further conformational changes, possess 8 Ts at the insertion point to avoid any strain in the structure. Indeed, oxDNA simulations confirm a flat conformation of $\approx 180^\circ$ for this combination of modules. Upon removal of the oligonucleotides in the central gap region (42 nt gap), the conformation of the DNA nanostructure will be stabilized ("flexible" conformation) by the presence of the rigid helices below the structure. According to the oxDNA simulations,

the angle of this conformation is stabilized at $\approx 150^\circ$. Interestingly, the displacement of the protecting oligonucleotides in the lateral helices does not significantly impact the structure conformation, probably due to the presence of the rigid helices under the structure (data not shown). The final switch occurs by removal of the protecting strands in the helices under the structure. The hairpin folding stabilizes the "closed" conformation angle at $\approx 90^\circ$. Preliminary TEM imaging of the folded three-state nanostructure in its "open" conformation confirms the initial rigid 180° state. Further design and conformational switch validation using TEM and agarose gel electrophoresis will be necessary prior to the transition to lipid membranes.

Taken together, we propose a robust design of a dynamic three-state structure with defined bending angles. Other multi-state DNA origami tweezers have been previously proposed [Kuzuya et al., 2014a, Kuzyk et al., 2014, Kuzuya et al., 2014b]. However, such structures could not stabilize different bending angles and have never been studied in combination with lipid membranes.

V.2.2.3 Bent DNA nanostructures bind and deform lipid membranes

In this section, we studied the effect of the designed DNA nanostructures on the shape of 1,2-dioleoyl-*sn*-glycero-3-phosphocholine (DOPC) giant unilamellar vesicles (GUVs) using confocal microscopy (Figure V.6). For this purpose, DNA origami nanostructures were functionalized with eight cholesterol modified with a tetra-ethylene glycol linker (chol-TEG) anchors. To ensure high membrane affinity, 18 double-stranded DNA spacers were used (see chapter III.2 for more details). Furthermore, these anchors were distributed across either the bottom (concave) or the top (convex) surface, as previously done with curved scaffolds (see chapter V.1). Initial conformations of DNA module S and L ("rigid" and "open", respectively) were incubated overnight (5 nM) with GUVs.

We observed that binding of "rigid" module S does not affect the shape of GUVs (Figure V.6B, left). These observations are in good agreement with previously published results for other flat monomeric structures [Kocabey et al., 2015, Czogalla et al., 2015a, Khmelinskaia et al., 2016, Franquelim et al., 2018]. Interestingly, the concave surface of the "open" conformation of module L did not change the shape of lipid membranes neither (Figure V.6B, top-right). Previous studies, have shown that curved DNA nanostructures bound through

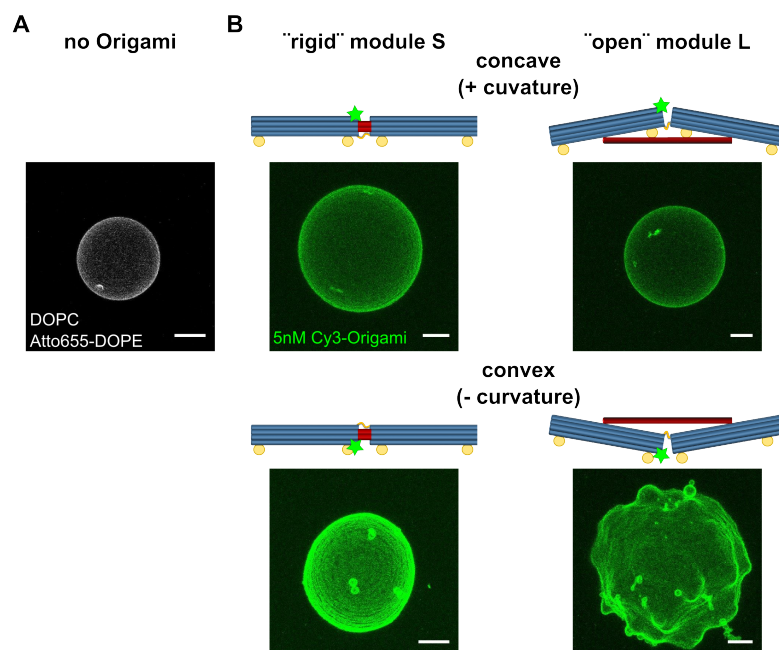


Figure V.6: Binding of the "open" conformation of module L by the negatively curved surface causes large scale deformations on GUVs. Maximum projections of the upper pole of DOPC GUVs incubated overnight with no DNA origami nanostructures (A), 5nM of "rigid" module S (B) or "open" module L (C) chol-TEG modified on the concave (top) and convex (bottom) surface. GUVs are stained with 0.005 %mol ATTO655-1,2-dioleoyl-*sn*-glycero-3-phosphoethanolamine (DOPE) while DNA origami nanostructures are labelled with Cy3. Images were obtained by confocal microscopy and scale bars corresponds to 10 μm .

the concave facet are able to tubulate lipid membranes [Franquelim et al., 2018, Grome et al., 2018]. In contrast, the helices below the structure in our design may hinder the binding of the anchors positioned near the centre of module L to the lipid membrane. As a result, the membrane cannot follow the scaffold shape. On the other hand, the binding of module L through the convex facet results in large scale deformations on GUVs (Figure V.6B, bottom-right). Similarly, curved structures with negative curvature deformed lipid membranes, although the effect was rather described as membrane invagination [Franquelim et al., 2018]. The flexibility of our structure and the possible second primary curvature formed upon bending may explain the observed difference.

In the next step, the effect of each conformation of the designed three-state structure should be assessed. Additionally, we are currently developing a Förster resonance energy transfer (FRET)-based assay to correlate the conformational change with the observed

deformations of GUVs. Importantly, the force generated by single-stranded DNA has been theoretically described and experimentally validated [Smith et al., 1996] (II.2.2). The displacement of a single strand results in the generation of a free energy of $\approx 1k_B T$ /strand at room temperature, according to the modified freely-jointed chain model (mFJC model) (equation II.4, see section II.2.2). Although the generated free energy from the single-stranded DNA segments is low, according to the Area-difference elasticity model (ADE model) (equation II.3, see section II.1.3), it should be enough to bend a piece of membrane into a shallow curvature. Indeed, the expected bending penalty to curve a piece of membrane into a segment with $C_1 = 5.6\mu\text{m}^{-1}$ is $E \approx 4k_B T$). Indeed, the binding of DNA scaffolds with shallow curvature have been shown to be enough to tubulate lipid membranes [Franquelim et al., 2018]. On the other hand, hairpin folding generates high amounts of free-energy ($\approx 20k_B T$ /hairpin, Supplementary figure G.2) which is predicted to be enough to model lipid membranes into highly curved segments (for $C_1 = 23.0\mu\text{m}^{-1}$, $E \approx 40k_B T$). We propose to further complement the *in vitro* studies described above with *in silico* experiments, in which the lipid membrane resistance to deformation (generally characterized by the bending rigidity κ) will be simulated by force applied in points distributed across the membrane binding surface and the changes in angle distribution of the DNA nanostructure conformation are analyzed. These results will be compared with current models for membrane shaping energy requirements.

V.2.3 Conclusions

In recent years, DNA origami nanostructures have been used to mimic the action of scaffolding proteins. However, to date only non-reconfigurable structures have been used. Here, we used a mixture of *in vitro* and *in silico* studies to establish a robust design for a reconfigurable three-state structure. Three modules were designed and combined to achieve a DNA origami nanostructure with three conformations of $\approx 180^\circ$, 150° and 90° . We further showed that structures with shallow bending angle ($\approx 130^\circ$) cause large scale deformations on free-standing lipid membranes, when bound through the convex surface. Further experiments will be necessary to correlate the conformational changes of the three-state structure with effects on the shape of lipid membranes. Taken together, these are the first steps towards the dynamic control of membrane shape.

VI

CONCLUSIONS AND OUTLOOK

In this thesis, we designed DNA origami nanostructures with the intention of mimicking membrane-shaping protein scaffolds, and thus getting new insights on their mode of action. Several aspects of such structures were studied, from their binding, diffusion and self-organization on lipid membranes, to their effect on the shape of lipid bilayers.

First, I established a set of parameters that can be varied to tune the membrane-binding efficiency and the diffusion of highly negatively charged DNA nanostructures on lipid membranes (chapters III.1 and III.2). I showed that the number, the location within the bulky DNA nanostructure, the positioning and the DNA spacers used in the attachment of cholesterol modified with a tetra-ethylene glycol linker (chol-TEG) to the nanostructures play a crucial role on the binding efficiency of the DNA nanostructures to the lipid bilayers. Additionally, I showed that positively charged lipids and the type of DNA spacer used to attach chol-TEG anchors impact the diffusion of membrane-bound DNA origami nanostructures. These effects result from different levels of interaction of the DNA nanostructures with the lipid membrane and are reflected in the effective membrane insertion size. It is of interest to explore the influence of other parameters, such as the structure's aspect ratio, curvature and function, as well as the distance between chol-TEG anchors, or between anchors and the edges of the structure, on the membrane-binding efficiency and 2D dynamics of DNA nanostructures. E.g., our previous results with curved DNA nanostructures showed that the degree of curvature plays a crucial role for the membrane affinity (chapter V.1 and appendix F). Furthermore, the applicability of the drawn conclusions to the use of other functional moieties for membrane-binding (e.g. amphipathic helices) and even to the establishment of other types of interactions should be validated.

DNA origami has been used to control enzymatic reactions [Grossi et al., 2017, Liu et al., 2013, Linko et al., 2015], to study the function of proteins [Hariadi et al., 2016, Funke et al., 2016a, Le et al., 2016, Kremmentsova et al., 2017], their interactions [Funke et al., 2016b] and organization [Ketterer et al., 2018, Fisher et al., 2018]. So far, on lipid membranes, DNA origami has been used to organize pore forming proteins [Henning-Knechtel et al.,

2017, Kurokawa et al., 2018], study SNARE mediated membrane fusion [Xu et al., 2016] and as a platform for analysis of 2D dynamics in membrane tethered enzymatic cascades [Sun et al., 2017]. However, in all these applications DNA origami played the role of a scaffold to proteins. In the future, one can expect that DNA origami can be incorporated into complex membrane associated phenomena, such as symmetry breaking, pattern formation and membrane shaping. Indeed, the set of parameters discussed in this thesis can be used to control the affinity to the lipid membrane and the 2D dynamics of DNA origami nanostructures. Importantly, both processes are fundamental for the establishment of interactions and reaction rates at the membrane. Moreover, my results demonstrate the compatibility of DNA origami binding to lipid membranes in biologically relevant conditions, such as the presence of negatively charged lipids or divalent cations.

Second, the achieved expansion of fluorescence correlation spectroscopy (FCS) to lipid monolayer-bound macromolecules (chapter III.3), are the first steps towards the routine study of protein-monolayer interactions. Importantly, not only lipid monolayers can be used to investigate several parameters common to other model systems, e.g. pH, temperature, ionic strength and modulation by specific ligands, but also enable the tuning of the lipid packing density, which is otherwise not accessible. Interestingly, DNA origami nanostructures seem to be specially suitable to be combined with lipid monolayers as, in opposition to a number of proteins, they do not aggregate on the air-water interface. Thus, DNA origami may be used as a tool to study a wide range of hydrophobic interactions, otherwise difficult to handle at such an interface.

Third, we showed that DNA origami nanostructures, electrostatically-bound to the membrane, self-organize on supported lipid bilayers (SLBs) into anisotropic domains through tip-to-tip and side-by-side attraction (chapter IV). In this context, gel lipid membranes were used to slow down the diffusion of DNA nanorods to a range that can be assessed by high speed atomic force microscopy (HS-AFM). The expansion of the study to other lipid membrane compositions as well as other membrane-anchoring mechanisms (e.g. hydrophobic interactions) would allow us to establish the influence of the membrane biophysical properties on the self-organization mode of DNA nanostructure and the robustness of the observed phenomenon. Furthermore, the use of SLBs reduces the scale of membrane deformation upon DNA origami nanostructure adhesion. Using other model systems, such as cushioned bilayers or even free-standing lipid bilayers, as the substrate would allow one to explore other regimes of deformation and shed new light on the process of self-

organization. For example, assays on giant unilamellar vesicles (GUVs) of 1-5 μm diameter could be combined with cryo-electron microscopy (cryo-EM) to visualize the formation of such domains. Furthermore, such levels of membrane-assisted self-organization have been previously suggested to play an important role in the early steps of membrane shaping mechanisms [Ramakrishnan et al., 2013, Simunovic et al., 2013a, Cui et al., 2013, Lipowsky, 2013]. Thus, it would be of great interest to combine the assays here described with DNA based scaffolds mimicking proteins in their membrane shaping function (chapter V).

From a fundamental physics perspective, we further show that our experimental platform can be used to observe different anisotropic phases formed at high membrane densities of DNA nanostructures of varying aspect-ratio. This is the first step towards the study of isotropic-anisotropic phase transition of particles with the same properties and varying aspect ratios in 2D. Moreover, the same platform can be used to study the effects of membrane-mediated interactions on conformations of DNA nanostructures with an established degree of flexibility or bending angle (see chapter V.2), similarly to what has been previously done for other membrane adsorbed polymers [Herold et al., 2010, Herold et al., 2016, Petrova et al., 2017]. Here, the additional control over the particle conformation offered by DNA origami enables one to explore a range of conditions otherwise difficult to access while working with particles of identical properties.

Last, we designed DNA origami scaffolds that are capable of shaping lipid membranes, mimicking the function of protein scaffolds (chapter V). We showed that curved DNA nanostructures can deform lipid membranes, forming tubules or invagination-like deformations. We further correlated these shapes with the degree and type of curvature, as well as membrane-density of the DNA. In this thesis, chol-TEG anchors were used to attach DNA-based scaffolds to lipid membranes. It would be natural to further use membrane binding moieties similar to the naturally occurring in protein scaffolds, e.g. amphipathic helices. From a structural perspective, the current knowledge about the membrane curvature and specially scaffold arrangement in regions of membrane deformation is rather sparse. Thus, it would be of great interest to use, e.g., cryo-EM to observe the architecture of the connection point of the formed membrane tubules with the mother vesicle. Additionally, our curved scaffolds can be used to dissect the differences between the mechanisms of curvature induction and curvature sensing.

Moreover, we extended the design of DNA-based scaffolds by integrating a conformational

switch that enables the triggering of the membrane-sculpting function. Although the action of the designed three-state structure on the shape of the lipid membrane has not yet been demonstrated, our approach seems to be promising. Indeed, our first results with bent DNA nanostructures show that mild bending angles can cause large scale deformations on lipid membranes. Moreover, the possible transmission of the dynamic conformational switch onto the lipid membrane shape is supported by the energetic considerations on the contractile element and the membrane bending penalty. Aiming towards membrane fission seems to be the most exciting future direction. It would then be interesting to upscale the action of such a contractile element to $> \mu\text{m}$ regime, e.g. by polymerization of individual DNA nanostructures. With this approach, one could possibly mimick large scale machineries, such as the cell division ring. Interestingly, cellular membrane shaping processes are performed by a number of proteins. Thus, it is tempting to combine the so far developed nanostructures to obtain a larger variety of membrane shapes.

Bibliography

- [Agarwal et al., 2018] Agarwal, N. P., Matthies, M., Joffroy, B., and Schmidt, T. L. (2018). Structural transformation of wireframe DNA origami via DNA polymerase assisted gap-filling. *ACS Nano*, 12(3):2546–2553.
- [Aghebat Rafat et al., 2014] Aghebat Rafat, A., Pirzer, T., Scheible, M. B., Kostina, A., and Simmel, F. C. (2014). Surface-assisted large-scale ordering of DNA origami tiles. *Angew. Chem.*, 53(29):7665–7668.
- [Akbari et al., 2017] Akbari, E., Mollica, M. Y., Lucas, C. R., Bushman, S. M., Patton, R. A., Shahhosseini, M., Song, J. W., and Castro, C. E. (2017). Engineering cell surface function with DNA origami. *Adv. Mater.*, 29(46):1703632.
- [Andersen et al., 2009] Andersen, E. S., Dong, M., Nielsen, M. M., Jahn, K., Subramani, R., Mamdouh, W., Golas, M. M., Sander, B., Stark, H., Oliveira, C. L. P., Pedersen, J. S., Birkedal, V., Besenbacher, F., Gothelf, K. V., and Kjems, J. (2009). Self-assembly of a nanoscale DNA box with a controllable lid. *Nature*, 459:73–76.
- [Ando et al., 2001] Ando, T., Kodera, N., Takai, E., Maruyama, D., Saito, K., and Toda, A. (2001). A high-speed atomic force microscope for studying biological macromolecules. *Proc. Natl. Acad. Sci.*, 98(22):12468–12472.
- [Ando et al., 2014] Ando, T., Uchihashi, T., and Scheuring, S. (2014). Filming biomolecular processes by high-speed atomic force microscopy. *Chem. Rev.*, 114(6):3120–3188.
- [Angelova and Dimitrov, 1986] Angelova, M. I. and Dimitrov, D. S. (1986). Liposome electroformation. *Faraday Discuss. Chem. Soc.*, 81:303–311.
- [Antonny, 2011] Antonny, B. (2011). Mechanisms of membrane curvature sensing. *Annu. Rev. Biochem.*, 80:101–123.
- [Avakyan et al., 2017] Avakyan, N., Conway, J. W., and Sleiman, H. F. (2017). Long-range ordering of blunt-ended DNA tiles on supported lipid bilayers. *J. Am. Chem. Soc.*, 139(34):12027–12034.

- [Avendaño and Escobedo, 2012] Avendaño, C. and Escobedo, F. A. (2012). Phase behavior of rounded hard-squares. *Soft Matter*, 8(17):4675–4681.
- [Banchelli et al., 2008] Banchelli, M., Betti, F., Berti, D., Caminati, G., Bombelli, F. B., Brown, T., Wilhelmsson, L. M., Norden, B., and Baglioni, P. (2008). Phospholipid membranes decorated by cholesterol-based oligonucleotides as soft hybrid nanostructures. *J. Phys. Chem. B*, 112(35):10942–10952.
- [Banchelli et al., 2010] Banchelli, M., Gambinossi, F., Durand, A., Caminati, G., Brown, T., Berti, D., and Baglioni, P. (2010). Modulation of density and orientation of amphiphilic DNA on phospholipid membranes. II. Vesicles. *J. Phys. Chem. B*, 114(21):7348–7358.
- [Bates and Frenkel, 2000] Bates, M. A. and Frenkel, D. (2000). Phase behavior of two-dimensional hard rod fluids. *J. Chem. Phys.*, 112(22):10034–10041.
- [Baumgart et al., 2011] Baumgart, T., Capraro, B. R., Zhu, C., and Das, S. L. (2011). Thermodynamics and mechanics of membrane curvature generation and sensing by proteins and lipids. *Annu. Rev. Phys. Chem.*, 62:483–506.
- [Bellot et al., 2013] Bellot, G., McClintock, M. A., Chou, J. J., and Shih, W. M. (2013). DNA nanotubes for NMR structure determination of membrane proteins. *Nat. Protoc.*, 8(4):755–770.
- [Bhatia et al., 2010] Bhatia, V. K., Hatzakis, N. S., and Stamou, D. (2010). A unifying mechanism accounts for sensing of membrane curvature by BAR domains, amphipathic helices and membrane-anchored proteins. *Semin. Cell Dev. Biol.*, 21(4):381–390.
- [Bhushan, 2017] Bhushan, B. (2017). *Springer handbook of nanotechnology*. Springer.
- [Bloomfield et al., 2000] Bloomfield, V., Crothers, D., and Tinoco Jr, I. (2000). *Nucleic Acids: Structures, Properties, and Functions*. Calif: University Science Books.
- [Bozec et al., 2007] Bozec, L., van der Heijden, G., and Horton, M. (2007). Collagen fibrils: nanoscale ropes. *Biophys. J.*, 92(1):70–75.
- [Braga and Ricci, 2004] Braga, P. C. and Ricci, D. (2004). *Atomic Force Microscopy: Biomedical Methods and Applications*. Springer Science & Business Media.

BIBLIOGRAPHY

- [Brown, 1828] Brown, R. (1828). XXVII. A brief account of microscopical observations made in the months of june, july and august 1827, on the particles contained in the pollen of plants; and on the general existence of active molecules in organic and inorganic bodies. *The Philosophical Magazine and Annals of Phylosophy*, 4(21):161–173.
- [Bunge et al., 2009] Bunge, A., Loew, M., Pescador, P., Arbuzova, A., Brodersen, N., Kang, J., Dahne, L., Liebscher, J., Herrmann, A., Stengel, G., and Huster, D. (2009). Lipid membranes carrying lipophilic cholesterol-based oligonucleotides – characterization and application on layer-by-layer coated particles. *J. Phys. Chem. B*, 113(51):16425–16434.
- [Burns et al., 2014] Burns, J. R., Al-Juffali, N., Janes, S. M., and Howorka, S. (2014). Membrane-spanning DNA nanopores with cytotoxic effect. *Angew. Chem.*, 53(46):12466–12470.
- [Burns et al., 2013a] Burns, J. R., Göpfrich, K., Wood, J. W., Thacker, V. V., Stulz, E., Keyser, U. F., and Howorka, S. (2013a). Lipid-bilayer-spanning DNA nanopores with a bifunctional porphyrin anchor. *Angew. Chem.*, 52(46):12069–12072.
- [Burns et al., 2013b] Burns, J. R., Stulz, E., and Howorka, S. (2013b). Self-assembled DNA nanopores that span lipid bilayers. *Nano Lett.*, 13(6):2351–2356.
- [Burstyn and Sengers, 1983] Burstyn, H. C. and Sengers, J. V. (1983). Time dependence of critical concentration fluctuations in a binary liquid. *Phys. Rev. A*, 27(2):1071–1085.
- [Castellana and Cremer, 2006] Castellana, E. T. and Cremer, P. S. (2006). Solid supported lipid bilayers: From biophysical studies to sensor design. *Surf. Sci. Rep.*, 61(10):429–444.
- [Castro et al., 2015] Castro, C. E., Su, H.-J., Marras, A. E., Zhou, L., and Johnson, J. (2015). Mechanical design of DNA nanostructures. *Nanoscale*, 7(14):5913–5921.
- [Chen et al., 2017] Chen, H., Li, R., Li, S., Andréasson, J., and Choi, J. H. (2017). Conformational effects of UV light on DNA origami. *J. Am. Chem. Soc.*, 139(4):1380–1383.
- [Chen et al., 2016] Chen, H., Zhang, H., Pan, J., Cha, T.-G., Li, S., Andréasson, J., and Choi, J. H. (2016). Dynamic and progressive control of DNA origami conformation by modulating DNA helicity with chemical adducts. *ACS Nano*, 10(5):4989–4996.

- [Cherstvy and Petrov, 2014] Cherstvy, A. G. and Petrov, E. P. (2014). Modeling DNA condensation on freestanding cationic lipid membranes. *Phys. Chem. Chem. Phys.*, 16(5):2020–2037.
- [Chi et al., 2013] Chi, Q., Wang, G., and Jiang, J. (2013). The persistence length and length per base of single-stranded DNA obtained from fluorescence correlation spectroscopy measurements using mean field theory. *Physica A Stat. Mech. Appl.*, 392(5):1072–1079.
- [Chiantia et al., 2005] Chiantia, S., Kahya, N., and Schwille, P. (2005). Dehydration damage of domain-exhibiting supported bilayers: An AFM study on the protective effects of disaccharides and other stabilizing substances. *Langmuir*, 21(14):6317–6323.
- [Chiantia et al., 2006] Chiantia, S., Ries, J., Kahya, N., and Schwille, P. (2006). Combined AFM and two-focus SFCS study of raft-exhibiting model membranes. *ChemPhysChem*, 7(11):2409—2418.
- [Chwastek and Schwille, 2013] Chwastek, G. and Schwille, P. (2013). A monolayer assay tailored to investigate lipid-protein systems. *ChemPhysChem*, 14(9):1877–1881.
- [Cicuta et al., 2007] Cicuta, P., Keller, S. L., and Veatch, S. L. (2007). Diffusion of liquid domains in lipid bilayer membranes. *J. Phys. Chem. B*, 111(13):3328–3331.
- [Costantini et al., 2012] Costantini, L. M., Fossati, M., Francolini, M., and Snapp, E. L. (2012). Assessing the tendency of fluorescent proteins to oligomerize under physiologic conditions. *Traffic*, 13(5):643–649.
- [Cui et al., 2013] Cui, H., Mim, C., Vázquez, F. X., Lyman, E., Unger, V. M., and Voth, G. A. (2013). Understanding the role of amphipathic helices in N-BAR domain driven membrane remodeling. *Biophys. J.*, 104(2):404–411.
- [Czogalla et al., 2016] Czogalla, A., Franquelim, H. G., and Schwille, P. (2016). DNA nanostructures on membranes as tools for synthetic biology. *Biophys. J.*, 110(8):1698–1707.
- [Czogalla et al., 2015a] Czogalla, A., Kauert, D. J., Franquelim, H. G., Uzunova, V., Zhang, Y., Seidel, R., and Schwille, P. (2015a). Amphipathic DNA origami nanoparticles to scaffold and deform lipid membrane vesicles. *Angew. Chem.*, 54(22):6501–6505.

BIBLIOGRAPHY

- [Czogalla et al., 2015b] Czogalla, A., Kauert, D. J., Seidel, R., Schwille, P., and Petrov, E. P. (2015b). DNA origami nanoneedles on freestanding lipid membranes as a tool to observe isotropic–nematic transition in two dimensions. *Nano Lett.*, 15(1):649–655.
- [Czogalla et al., 2013] Czogalla, A., Petrov, E. P., Kauert, D. J., Uzunova, V., Zhang, Y., Seidel, R., and Schwille, P. (2013). Switchable domain partitioning and diffusion of DNA origami rods on membranes. *Faraday Discuss.*, 161(0):31–43.
- [Davidson, 1979] Davidson, R. S. (April 1979). Mechanisms of photo-oxidation reactions. *Pestic. Sci.*, 10(2):158–170.
- [de Almeida and Loura, 2004] de Almeida, R. and Loura, L. (2004). *Tópicos de Biofísica de Membranas*. LIDEL, Lisboa.
- [Dertinger et al., 2007] Dertinger, T., Pacheco, V., von der Hocht, I., Hartmann, R., Gregor, I., and Enderlein, J. (2007). Two-focus fluorescence correlation spectroscopy: A new tool for accurate and absolute diffusion measurements. *ChemPhysChem*, 8(3):433–443.
- [Dertinger et al., 2006] Dertinger, T., von der Hocht, I., Benda, A., Hof, M., and Enderlein, J. (2006). Surface sticking and lateral diffusion of lipids in supported bilayers. *Langmuir*, 22(22):9339–9344.
- [Dietz et al., 2009] Dietz, H., Douglas, S. M., and Shih, W. M. (2009). Folding DNA into twisted and curved nanoscale shapes. *Science*, 325(5941):725–730.
- [Dimova, 2014] Dimova, R. (2014). Recent developments in the field of bending rigidity measurements on membranes. *Adv. Colloid Interface Sci.*, 208:225–234.
- [Dimova et al., 2000] Dimova, R., Pouligny, B., and Dietrich, C. (2000). Pretransitional effects in dimyristoylphosphatidylcholine vesicle membranes: Optical dynamometry study. *Biophys. J.*, 79(1):340–356.
- [Doherty and McMahon, 2009] Doherty, G. J. and McMahon, H. T. (2009). Mechanisms of endocytosis. *Annu. Rev. Biochem.*, 78:857–902.
- [Dohno et al., 2017] Dohno, C., Makishi, S., Nakatani, K., and Contera, S. (2017). Amphiphilic DNA tiles for controlled insertion and 2D assembly on fluid lipid membranes: The effect on mechanical properties. *Nanoscale*, 9(9):3051–3058.

- [Dommersnes and Fournier, 1999] Dommersnes, P. G. and Fournier, J.-B. (1999). N-body study of anisotropic membrane inclusions: Membrane mediated interactions and ordered aggregation. *Eur. Phys. J. B.*, 12(1):9–12.
- [Douglas et al., 2012] Douglas, S. M., Bachelet, I., and Church, G. M. (2012). A logic-gated nanorobot for targeted transport of molecular payloads. *Science*, 335(6070):831–834.
- [Douglas et al., 2009a] Douglas, S. M., Dietz, H., Liedl, T., Högberg, B., Graf, F., and Shih, W. M. (2009a). Self-assembly of DNA into nanoscale three-dimensional shapes. *Nature*, 459:414–418.
- [Douglas et al., 2009b] Douglas, S. M., Marblestone, A. H., Teerapittayanon, S., Vazquez, A., Church, G. M., and Shih, W. M. (2009b). Rapid prototyping of 3D DNA-origami shapes with caDNAno. *Nucleic Acids Res.*, 37(15):5001–5006.
- [Drin and Antonny, 2010] Drin, G. and Antonny, B. (2010). Amphipathic helices and membrane curvature. *FEBS Lett.*, 584(9):1840–1847.
- [Eaton and West, 2010] Eaton, P. and West, P. (2010). *Atomic Force Microscopy*. Oxford University Press.
- [Eggeling et al., 1999] Eggeling, C., Widengren, J., Rigler, R., Seidel, C. A. M., Rettig, W., Strehmel, B., Schrader, S., and Seifert, H. (1999). *Photostability of Fluorescent Dyes for Single-Molecule Spectroscopy: Mechanisms and Experimental Methods for Estimating Photobleaching in Aqueous Solution*, pages 193–240. Springer Berlin Heidelberg, Berlin, Heidelberg.
- [Eigen and Rigler, 1994] Eigen, M. and Rigler, R. (1994). Sorting single molecules: application to diagnostics and evolutionary biotechnology. *Proc. Natl. Acad. Sci.*, 91(13):5740–5747.
- [Einstein, 1905] Einstein, A. (1905). Über die von der molekularkinetischen theorie der wärme geforderte bewegung von in ruhenden flüssigkeiten suspendierten teilchen. *Ann. Phys.*, 322(8):549–560.
- [Elbaz et al., 2009] Elbaz, J., Wang, Z.-G., Orbach, R., and Willner, I. (2009). pH-stimulated concurrent mechanical activation of two DNA "tweezers". a "SETRESET" logic gate system. *Nano Lett.*, 9(12):4510–4514.

BIBLIOGRAPHY

- [Elson and Magde, 1974] Elson, E. L. and Magde, D. (January 1974). Fluorescence correlation spectroscopy. I. Conceptual basis and theory. *Biopolymers*, 13(1):1–27.
- [Evans et al., 2003] Evans, E., Heinrich, V., Ludwig, F., and Rawicz, W. (2003). Dynamic tension spectroscopy and strength of biomembranes. *Biophys. J.*, 85(4):2342–2350.
- [Fa et al., 2007] Fa, N., Lins, L., Courtoy, P. J., Dufrene, Y., Van Der Smissen, P., Brasseur, R., Tyteca, D., and Mingeot-Leclercq, M.-P. (2007). Decrease of elastic moduli of DOPC bilayers induced by a macrolide antibiotic, azithromycin. *Biochim. Biophys. Acta*, 1768(7):1830–1838.
- [Feigenson, 2006] Feigenson, G. W. (2006). Phase behavior of lipid mixtures. *Nat. Chem. Biol.*, 2:560–563.
- [Ferguson and De Camilli, 2012] Ferguson, S. M. and De Camilli, P. (2012). Dynamin, a membrane-remodelling GTPase. *Nat. Rev. Mol. Cell Biol.*, 13(2):75–88.
- [Fick, 1855] Fick, A. (1855). Über diffusion. *Ann. Phys.*, 170(1):59–86.
- [Fisher et al., 2018] Fisher, P. D. E., Shen, Q., Akpınar, B., Davis, L. K., Chung, K. K. H., Baddeley, D., Saric, A., Melia, T. J., Hoogenboom, B. W., Lin, C., and Lusk, C. P. (2018). A programmable DNA origami platform for organizing intrinsically disordered nucleoporins within nanopore confinement. *ACS Nano*, 12(2):1508–1518.
- [Franquelim et al., 2018] Franquelim, H. G., Khmelinskaia, A., Sobczak, J.-P., Dietz, H., and Schwille, P. (2018). Membrane sculpting by curved DNA origami scaffolds. *Nat. Commun.*, 9(1):811.
- [Frenkel and Eppenga, 1985] Frenkel and Eppenga (1985). Evidence for algebraic orientational order in a two-dimensional hard-core nematic. *Phys. Rev. A Gen. Phys.*, 31(3):1776–1787.
- [Frost et al., 2008] Frost, A., Perera, R., Roux, A., Spasov, K., Destaing, O., Egelman, E. H., De Camilli, P., and Unger, V. M. (2008). Structural basis of membrane invagination by F-BAR domains. *Cell*, 132(5):807–817.
- [Funke et al., 2016a] Funke, J. J., Ketterer, P., Lieleg, C., Korber, P., and Dietz, H. (2016a). Exploring nucleosome unwrapping using DNA origami. *Nano Lett.*, 16(12):7891–7898.

- [Funke et al., 2016b] Funke, J. J., Ketterer, P., Lieleg, C., Schunter, S., Korber, P., and Dietz, H. (2016b). Uncovering the forces between nucleosomes using DNA origami. *Sci. Adv.*, 2(11):e1600974.
- [Gauvin, 1997] Gauvin, R. (1997). Review of transmission electron microscopy for the characterization of materials. *Proc.SPIE*, 10291:200–229.
- [Gennis, 2013] Gennis, R. B. (2013). *Biomembranes: Molecular Structure and Function*. Springer Science & Business Media.
- [Gerling et al., 2015] Gerling, T., Wagenbauer, K. F., Neuner, A. M., and Dietz, H. (2015). Dynamic DNA devices and assemblies formed by shape-complementary, non-base pairing 3D components. *Science*, 347(6229):1446–1452.
- [Ghosh et al., 2016] Ghosh, S. K., Cherstvy, A. G., Petrov, E. P., and Metzler, R. (2016). Interactions of rod-like particles on responsive elastic sheets. *Soft Matter*, 12(38):7908–7919.
- [Göpfrich et al., 2016a] Göpfrich, K., Li, C.-Y., Mames, I., Bhamidimarri, S. P., Ricci, M., Yoo, J., Mames, A., Ohmann, A., Winterhalter, M., Stulz, E., Aksimentiev, A., and Keyser, U. F. (2016a). Ion channels made from a single membrane-spanning DNA duplex. *Nano Lett.*, 16(7):4665–4669.
- [Göpfrich et al., 2016b] Göpfrich, K., Li, C.-Y., Ricci, M., Bhamidimarri, S. P., Yoo, J., Gyenes, B., Ohmann, A., Winterhalter, M., Aksimentiev, A., and Keyser, U. F. (2016b). Large-conductance transmembrane porin made from DNA origami. *ACS Nano*, 10(9):8207–8214.
- [Göpfrich et al., 2018] Göpfrich, K., Platzman, I., and Spatz, J. P. (2018). Mastering complexity: Towards bottom-up construction of multifunctional eukaryotic synthetic cells. *Trends Biotechnol.*, 36(9):938–951.
- [Göpfrich et al., 2015] Göpfrich, K., Zettl, T., Meijering, A. E. C., Hernández-Ainsa, S., Kocabey, S., Liedl, T., and Keyser, U. F. (2015). DNA-tile structures induce ionic currents through lipid membranes. *Nano Lett.*, 15(5):3134–3138.
- [Gorter and Grendel, 1925] Gorter, E. and Grendel, F. (1925). On biomolecular layers of lipoids on the chromocytes of the blood. *J. Exp. Med.*, 41(4):439–443.

BIBLIOGRAPHY

- [Graham and Kozlov, 2010] Graham, T. R. and Kozlov, M. M. (2010). Interplay of proteins and lipids in generating membrane curvature. *Curr. Opin. Cell Biol.*, 22(4):430–436.
- [Grome et al., 2018] Grome, M. W., Zhang, Z., Pincet, F., and Lin, C. (2018). Vesicle tubulation with self-assembling DNA nanosprings. *Angew. Chem.*, 57(19):5330–5334.
- [Gromelski and Brezesinski, 2006] Gromelski, S. and Brezesinski, G. (2006). DNA condensation and interaction with zwitterionic phospholipids mediated by divalent cations. *Langmuir*, 22(14):6293–6301.
- [Grossi et al., 2017] Grossi, G., Dalgaard Ebbesen Jepsen, M., Kjems, J., and Andersen, E. S. (2017). Control of enzyme reactions by a reconfigurable DNA nanovault. *Nat. Commun.*, 8(1):992.
- [Gudmand et al., 2009] Gudmand, M., Fidorra, M., Bjørnholm, T., and Heimburg, T. (2009). Diffusion and partitioning of fluorescent lipid probes in phospholipid monolayers. *Biophys. J.*, 96(11):4598–4609.
- [Guigas and Weiss, 2006] Guigas, G. and Weiss, M. (2006). Size-dependent diffusion of membrane inclusions. *Biophys. J.*, 91(7):2393–2398.
- [Harayama and Riezman, 2018] Harayama, T. and Riezman, H. (2018). Understanding the diversity of membrane lipid composition. *Nat. Rev. Mol. Cell Biol.*, 19:281–296.
- [Hariadi et al., 2016] Hariadi, R. F., Appukutty, A. J., and Sivaramakrishnan, S. (2016). Engineering circular gliding of actin filaments along myosin-patterned dna nanotube rings to study long-term actin–myosin behaviors. *ACS Nano*, 10(9):8281–8288.
- [Haupts et al., 1998] Haupts, U., Maiti, S., Schwille, P., and Webb, W. W. (1998). Dynamics of fluorescence fluctuations in green fluorescent protein observed by fluorescence correlation spectroscopy. *Proc. Natl. Acad. Sci.*, 95(23):13573–13578.
- [Helfrich, 1973] Helfrich, W. (1973). Elastic properties of lipid bilayers: theory and possible experiments. *Z. Naturforsch. C*, 28(11):693–703.
- [Henning-Knechtel et al., 2017] Henning-Knechtel, A., Knechtel, J., and Magzoub, M. (2017). DNA-assisted oligomerization of pore-forming toxin monomers into precisely-controlled protein channels. *Nucleic Acids Res.*, 45(21):12057–12068.

- [Herold et al., 2010] Herold, C., Schwille, P., and Petrov, E. P. (2010). DNA condensation at freestanding cationic lipid bilayers. *Phys. Rev. Lett.*, 104(14):148102.
- [Herold et al., 2016] Herold, C., Schwille, P., and Petrov, E. P. (2016). Single DNA molecules on freestanding and supported cationic lipid bilayers: diverse conformational dynamics controlled by the local bilayer properties. *J. Phys. D*, 49:074001.
- [Hinterdorfer and Dufrene, 2006] Hinterdorfer, P. and Dufrene, Y. F. (2006). Detection and localization of single molecular recognition events using atomic force microscopy. *Nat. Methods*, 3(5):347–355.
- [Hong et al., 2017] Hong, F., Zhang, F., Liu, Y., and Yan, H. (2017). DNA origami: Scaffolds for creating higher order structures. *Chem. Rev.*, 117(20):12584–12640.
- [Hore and Composto, 2010] Hore, M. J. A. and Composto, R. J. (2010). Nanorod self-assembly for tuning optical absorption. *ACS Nano*, 4(11):6941–6949.
- [Hughes et al., 1981] Hughes, B. D., Pailthorpe, B. A., and White, L. R. (1981). The translational and rotational drag on a cylinder moving in a membrane. *J. Fluid Mech.*, 110:349–372.
- [Ijäs et al., 2018] Ijäs, H., Nummelin, S., Shen, B., Kostiainen, M. A., and Linko, V. (2018). Dynamic DNA origami devices: from strand-displacement reactions to external-stimuli responsive systems. *Int. J. Mol. Sci.*, 19(7):2114.
- [Jadidi et al., 2014] Jadidi, T., Seyyed-Allaei, H., Tabar, M. R. R., and Mashaghi, A. (2014). Poisson’s ratio and Young’s modulus of lipid bilayers in different phases. *Front. Bioeng. Biotechnol.*, 2:8.
- [Jiang et al., 2017] Jiang, S., Hong, F., Hu, H., Yan, H., and Liu, Y. (2017). Understanding the elementary steps in DNA tile-based self-assembly. *ACS Nano*, 11(9):9370–9381.
- [Jiao et al., 2002] Jiao, Y., Stringfellow, S., and Yu, H. (2002). Distinguishing “looped-out” and “stacked-in” DNA bulge conformation using fluorescent 2-aminopurine replacing a purine base. *J. Biomol. Struct. Dyn.*, 19(5):929–934.
- [Johnson et al., 1991] Johnson, S. J., Bayerl, T. M., McDermott, D. C., Adam, G. W., Rennie, A. R., Thomas, R. K., and Sackmann, E. (1991). Structure of an adsorbed dimyristoylphosphatidylcholine bilayer measured with specular reflection of neutrons. *Biophys. J.*, 59(2):289–294.

- [Johnson-Buck et al., 2014] Johnson-Buck, A., Jiang, S., Yan, H., and Walter, N. G. (2014). DNA-cholesterol barges as programmable membrane-exploring agents. *ACS Nano*, 8(6):5641–5649.
- [Jørgensen et al., 2017] Jørgensen, I. L., Kemmer, G. C., and Pomorski, T. G. (2017). Membrane protein reconstitution into giant unilamellar vesicles: a review on current techniques. *Eur. Biophys. J.*, 46(2):103–119.
- [Kato et al., 2010] Kato, A., Tsuji, A., Yanagisawa, M., Saeki, D., Juni, K., Morimoto, Y., and Yoshikawa, K. (2010). Phase separation on a phospholipid membrane inducing a characteristic localization of DNA accompanied by its structural transition. *J. Phys. Chem. Lett.*, 1(23):3391–3395.
- [Ketterer et al., 2018] Ketterer, P., Ananth, A. N., Laman Trip, D. S., Mishra, A., Bertosin, E., Ganji, M., van der Torre, J., Onck, P., Dietz, H., and Dekker, C. (2018). DNA origami scaffold for studying intrinsically disordered proteins of the nuclear pore complex. *Nat. Commun.*, 9(1):902.
- [Khandkar and Barma, 2005] Khandkar, M. D. and Barma, M. (2005). Orientational correlations and the effect of spatial gradients in the equilibrium steady state of hard rods in two dimensions: a study using deposition-evaporation kinetics. *Phys. Rev. E Stat. Nonlin. Soft Matter Phys.*, 72(5):051717.
- [Khmelinskaia et al., 2016] Khmelinskaia, A., Franquelim, H. G., Petrov, E. P., and Schwille, P. (2016). Effect of anchor positioning on binding and diffusion of elongated 3D DNA nanostructures on lipid membranes. *J. Phys. D*, 49:194001.
- [Kiessling and Tamm, 2003] Kiessling, V. and Tamm, L. K. (2003). Measuring distances in supported bilayers by fluorescence interference-contrast microscopy: Polymer supports and SNARE proteins. *Biophys. J.*, 84(1):408–418.
- [Kim et al., 2001] Kim, F., Kwan, S., Akana, J., and Yang, P. (2001). Langmuir-Blodgett nanorod assembly. *J. Am. Chem. Soc.*, 123(18):4360–4361.
- [Kocabey et al., 2015] Kocabey, S., Kempter, S., List, J., Xing, Y., Bae, W., Schiffels, D., Shih, W. M., Simmel, F. C., and Liedl, T. (2015). Membrane-assisted growth of DNA origami nanostructure arrays. *ACS Nano*, 9(4):3530–3539.

- [Koenig et al., 1996] Koenig, B. W., Krueger, S., Orts, W. J., Majkrzak, C. F., Berk, N. F., Silverton, J. V., and Gawrisch, K. (1996). Neutron reflectivity and atomic force microscopy studies of a lipid bilayer in water adsorbed to the surface of a silicon single crystal. *Langmuir*, 12(5):1343–1350.
- [Kohman and Han, 2015] Kohman, R. E. and Han, X. (2015). Light sensitization of DNA nanostructures via incorporation of photo-cleavable spacers. *Chem. Commun.*, 51(26):5747–5750.
- [Krementsova et al., 2017] Krementsova, E. B., Furuta, K., Oiwa, K., Trybus, K. M., and Ali, M. Y. (2017). Small teams of myosin Vc motors coordinate their stepping for efficient cargo transport on actin bundles. *J. Biol. Chem.*, 292(26):10998–11008.
- [Krichevsky and Bonnet, 2002] Krichevsky, O. and Bonnet, G. (2002). Fluorescence correlation spectroscopy: the technique and its applications. *Rep. Prog. Phys.*, 65(2):251–297.
- [Kurokawa et al., 2018] Kurokawa, T., Kiyonaka, S., Nakata, E., Endo, M., Koyama, S., Mori, E., Tran, N. H., Dinh, H., Suzuki, Y., Hidaka, K., Kawata, M., Sato, C., Sugiyama, H., Morii, T., and Mori, Y. (2018). DNA origami scaffolds as templates for functional tetrameric Kir3 K⁺ channels. *Angew. Chem.*, 57(10):2586–2591.
- [Kusumi et al., 2012] Kusumi, A., Fujiwara, T. K., Chadda, R., Xie, M., Tsunoyama, T. A., Kalay, Z., Kasai, R. S., and Suzuki, K. G. (2012). Dynamic organizing principles of the plasma membrane that regulate signal transduction: Commemorating the fortieth anniversary of Singer and Nicolson’s fluid-mosaic model. *Annu. Rev. Cell Dev. Biol.*, 28(1):215–250.
- [Kuzuya et al., 2011] Kuzuya, A., Sakai, Y., Yamazaki, T., Xu, Y., and Komiyama, M. (2011). Nanomechanical DNA origami "single-molecule beacons" directly imaged by atomic force microscopy. *Nat. Commun.*, 2:449.
- [Kuzuya et al., 2014a] Kuzuya, A., Watanabe, R., Hashizume, M., Kaino, M., Minamida, S., Kameda, K., and Ohya, Y. (2014a). Precise structure control of three-state nanomechanical DNA origami devices. *Methods*, 67(2):250–255.
- [Kuzuya et al., 2014b] Kuzuya, A., Watanabe, R., Yamanaka, Y., Tamaki, T., Kaino, M., and Ohya, Y. (2014b). Nanomechanical DNA origami pH sensors. *Sensors*, 14(10):19329–19335.

BIBLIOGRAPHY

- [Kuzyk et al., 2014] Kuzyk, A., Schreiber, R., Zhang, H., Govorov, A. O., Liedl, T., and Liu, N. (2014). Reconfigurable 3D plasmonic metamolecules. *Nat. Mater.*, 13:862–866.
- [Kuzyk et al., 2016] Kuzyk, A., Yang, Y., Duan, X., Stoll, S., Govorov, A. O., Sugiyama, H., Endo, M., and Liu, N. (2016). A light-driven three-dimensional plasmonic nanosystem that translates molecular motion into reversible chiroptical function. *Nat. Commun.*, 7:10591.
- [Kwan et al., 2001] Kwan, S., Kim, F., Akana, J., and Yang, P. (2001). Synthesis and assembly of BaWO₄ nanorods. *Chem. Commun.*, (5):447–448.
- [Lagny and Bassereau, 2015] Lagny, T. J. and Bassereau, P. (2015). Bioinspired membrane-based systems for a physical approach of cell organization and dynamics: usefulness and limitations. *Interface Focus*, 5(4):20150038.
- [Lakowicz, 2006] Lakowicz, J. R. (2006). *Principles of Fluorescence Spectroscopy*. Springer US.
- [Langecker et al., 2012] Langecker, M., Arnaut, V., Martin, T. G., List, J., Renner, S., Mayer, M., Dietz, H., and Simmel, F. C. (2012). Synthetic lipid membrane channels formed by designed DNA nanostructures. *Science*, 338(6109):932–936.
- [Le et al., 2016] Le, J. V., Luo, Y., Darcy, M. A., Lucas, C. R., Goodwin, M. F., Poirier, M. G., and Castro, C. E. (2016). Probing nucleosome stability with a DNA origami nanocaliper. *ACS Nano*, 10(7):7073–7084.
- [Lehninger et al., 2005] Lehninger, A., Nelson, D., and Cox, M. (2005). *Lehninger principles of biochemistry*. WH Freeman.
- [Liedl et al., 2010] Liedl, T., Högberg, B., Tytell, J., Ingber, D. E., and Shih, W. M. (2010). Self-assembly of three-dimensional prestressed tensegrity structures from DNA. *Nat. Nanotechnol.*, 5:520–524.
- [Liedl and Simmel, 2005] Liedl, T. and Simmel, F. C. (2005). Switching the conformation of a DNA molecule with a chemical oscillator. *Nano Lett.*, 5(10):1894–1898.
- [Lingwood and Simons, 2010] Lingwood, D. and Simons, K. (2010). Lipid rafts as a membrane-organizing principle. *Science*, 327(5961):46–50.

- [Linko et al., 2015] Linko, V., Eerikäinen, M., and Kostiainen, M. A. (2015). A modular DNA origami-based enzyme cascade nanoreactor. *Chem. Commun.*, 51(25):5351–5354.
- [Lipowsky, 2013] Lipowsky, R. (2013). Spontaneous tubulation of membranes and vesicles reveals membrane tension generated by spontaneous curvature. *Faraday Discuss.*, 161:305–331.
- [Lis et al., 1981] Lis, L., Lis, W., Parsegian, V., and Rand, R. (1981). Adsorption of divalent cations to a variety of phosphatidylcholine bilayers. *Biochemistry*, 20(7):1771–1777.
- [List et al., 2014] List, J., Weber, M., and Simmel, F. C. (2014). Hydrophobic actuation of a DNA origami bilayer structure. *Angew. Chem.*, 53(16):4236–4239.
- [Liu et al., 2013] Liu, M., Fu, J., Hejesen, C., Yang, Y., Woodbury, N. W., Gothelf, K., Liu, Y., and Yan, H. (2013). A DNA tweezer-actuated enzyme nanoreactor. *Nat. Commun.*, 4:2127.
- [Macháň and Hof, 2010] Macháň, R. and Hof, M. (2010). Lipid diffusion in planar membranes investigated by fluorescence correlation spectroscopy. *Biochim. Biophys. Acta, Biomembr.*, 1798(7):1377–1391.
- [Madsen et al., 2010] Madsen, K. L., Bhatia, V. K., Gether, U., and Stamou, D. (2010). BAR domains, amphipathic helices and membrane-anchored proteins use the same mechanism to sense membrane curvature. *FEBS Lett.*, 584(9):1848–1855.
- [Magde et al., 1972] Magde, D., Elson, E., and Webb, W. W. (1972). Thermodynamic fluctuations in a reacting system—measurement by fluorescence correlation spectroscopy. *Phys. Rev. Lett.*, 29(11):705–708.
- [Magde et al., 1974] Magde, D., Elson, E. L., and W., W. W. (January 1974). Fluorescence correlation spectroscopy. II. An experimental realization. *Biopolymers*, 13(1):29–61.
- [Magde et al., 1978] Magde, D., Webb, W. W., and Elson, E. L. (February 1978). Fluorescence correlation spectroscopy. III. Uniform translation and laminar flow. *Biopolymers*, 17(2):361–376.
- [Mao et al., 1999] Mao, C., Sun, W., Shen, Z., and Seeman, N. C. (1999). A nanomechanical device based on the B–Z transition of DNA. *Nature*, 397:144–146.

- [Margolin, 2012] Margolin, W. (2012). The price of tags in protein localization studies. *J. Bacteriol.*, 194(23):6369–6371.
- [Marini et al., 2011] Marini, M., Piantanida, L., Musetti, R., Bek, A., Dong, M., Besenbacher, F., Lazzarino, M., and Firrao, G. (2011). A revertible, autonomous, self-assembled DNA-origami nanoactuator. *Nano Lett.*, 11(12):5449–5454.
- [Matek et al., 2015] Matek, C., Ouldrige, T. E., Doye, J. P. K., and Louis, A. A. (2015). Plectoneme tip bubbles: coupled denaturation and writhing in supercoiled DNA. *Sci. Rep.*, 5:7655.
- [Matek et al., 2012] Matek, C., Ouldrige, T. E., Levy, A., Doye, J. P. K., and Louis, A. A. (2012). DNA cruciform arms nucleate through a correlated but asynchronous cooperative mechanism. *J. Phys. Chem. B*, 116(38):11616–11625.
- [McIntosh et al., 2014] McIntosh, D. B., Duggan, G., Gouil, Q., and Saleh, O. A. (2014). Sequence-dependent elasticity and electrostatics of single-stranded DNA: Signatures of base-stacking. *Biophys. J.*, 106(3):659–666.
- [McLaughlin et al., 1978] McLaughlin, A., Grathwohl, C., and McLaughlin, S. (1978). The adsorption of divalent cations to phosphatidylcholine bilayer membranes. *Biochim. Biophys. Acta, Biomembr.*, 513(3):338–357.
- [McMahon and Gallop, 2005] McMahon, H. T. and Gallop, J. L. (2005). Membrane curvature and mechanisms of dynamic cell membrane remodelling. *Nature*, 438:590–596.
- [Mecke et al., 2003] Mecke, K. R., Charitat, T., and Graner, F. (2003). Fluctuating lipid bilayer in an arbitrary potential: Theory and experimental determination of bending rigidity. *Langmuir*, 19(6):2080–2087.
- [Miao et al., 1994] Miao, L., Seifert, U., Wortis, M., and Döbereiner, H. (1994). Budding transitions of fluid-bilayer vesicles: The effect of area-difference elasticity. *Phys. Rev. E Stat. Phys. Plasmas Fluids Relat. Interdiscip. Topics*, 49(6):5389–5407.
- [Michelman-Ribeiro et al., 2009] Michelman-Ribeiro, A., Mazza, D., Rosales, T., Stasevich, T. J., Boukari, H., Rishi, V., Vinson, C., Knutson, J. R., and McNally, J. G. (2009). Direct measurement of association and dissociation rates of DNA binding in live cells by fluorescence correlation spectroscopy. *Biophys. J.*, 97(1):337–346.

- [Minsky, 1957] Minsky, M. (1957). Microscopy apparatus. *US Patent# 3013467*.
- [Mosayebi et al., 2015] Mosayebi, M., Louis, A. A., Doye, J. P. K., and Ouldridge, T. E. (2015). Force-induced rupture of a DNA duplex: From fundamentals to force sensors. *ACS Nano*, 9(12):11993–12003.
- [Mouritsen and Bagatolli, 2015] Mouritsen, O. G. and Bagatolli, L. A. (2015). *Life - As a Matter of Fat: Lipids in a Membrane Biophysics Perspective*. Springer.
- [Müller and Anderson, 2002] Müller, D. J. and Anderson, K. (2002). Biomolecular imaging using atomic force microscopy. *Trends Biotechnol.*, 20(8):S45–S49.
- [Murphy et al., 2004] Murphy, M., Rasnik, I., Cheng, W., Lohman, T. M., and Ha, T. (2004). Probing single-stranded DNA conformational flexibility using fluorescence spectroscopy. *Biophys. J.*, 86(4):2530–2537.
- [Nicolson, 2014] Nicolson, G. L. (2014). The fluid-mosaic model of membrane structure: Still relevant to understanding the structure, function and dynamics of biological membranes after more than 40 years. *Biochim. Biophys. Acta, Biomembr.*, 1838(6):1451–1466.
- [Noy, 2007] Noy, A. (2007). *Handbook of Molecular Force Spectroscopy*. Springer Science & Business Media.
- [Nummelin et al., 2018] Nummelin, S., Kommeri, J., Kostiainen, M. A., and Linko, V. (2018). Evolution of structural DNA nanotechnology. *Adv. Mater.*, 30(24):1703721.
- [Ohmann et al., 2018] Ohmann, A., Li, C.-Y., Maffeo, C., Al Nahas, K., Baumann, K. N., Göpfrich, K., Yoo, J., Keyser, U. F., and Aksimentiev, A. (2018). A synthetic enzyme built from DNA flips 10^7 lipids per second in biological membranes. *Nat. Commun.*, 9(1):2426.
- [Olinger et al., 2016] Olinger, A. D., Spangler, E. J., Kumar, P. B. S., and Laradji, M. (2016). Membrane-mediated aggregation of anisotropically curved nanoparticles. *Faraday Discuss.*, 186(0):265–275.
- [Orponen, 2018] Orponen, P. (2018). Design methods for 3D wireframe DNA nanostructures. *Nat. Comput.*, 17(1):147–160.

BIBLIOGRAPHY

- [Ouldridge et al., 2011] Ouldridge, T. E., Louis, A. A., and Doye, J. P. K. (2011). Structural, mechanical, and thermodynamic properties of a coarse-grained DNA model. *J. Chem. Phys.*, 134(8):085101.
- [Pastré et al., 2003] Pastré, D., Piétrement, O., Fusil, S., Landousy, F., Jeusset, J., David, M.-O., Hamon, L., Le Cam, E., and Zozime, A. (2003). Adsorption of DNA to mica mediated by divalent counterions: A theoretical and experimental study. *Biophys. J.*, 85(4):2507–2518.
- [Pawlowski, 2010] Pawlowski, N. (2010). Dynamin self-assembly and the vesicle scission mechanism: how dynamin oligomers cleave the membrane neck of clathrin-coated pits during endocytosis. *BioEssays*, 32(12):1033–1039.
- [Perrault and Shih, 2014] Perrault, S. D. and Shih, W. M. (2014). Virus-inspired membrane encapsulation of DNA nanostructures to achieve *in vivo* stability. *ACS Nano*, 8(5):5132–5140.
- [Peters and Cherry, 1982] Peters, R. and Cherry, R. J. (1982). Lateral and rotational diffusion of bacteriorhodopsin in lipid bilayers: experimental test of the Saffman-Delbrück equations. *Proc. Natl. Acad. Sci.*, 79(14):4317–4321.
- [Petrov et al., 2006] Petrov, E. P., Ohrt, T., Winkler, R. G., and Schwille, P. (2006). Diffusion and segmental dynamics of double-stranded DNA. *Phys. Rev. Lett.*, 97(25):258101.
- [Petrov et al., 2012] Petrov, E. P., Petrosyan, R., and Schwille, P. (2012). Translational and rotational diffusion of micrometer-sized solid domains in lipid membranes. *Soft Matter*, 8(29):7552–7555.
- [Petrov and Schwille, 2008a] Petrov, E. P. and Schwille, P. (2008a). *State of the Art and Novel Trends in Fluorescence Correlation Spectroscopy*, pages 145–197. Springer Berlin Heidelberg, Berlin, Heidelberg.
- [Petrov and Schwille, 2008b] Petrov, E. P. and Schwille, P. (2008b). Translational diffusion in lipid membranes beyond the Saffman-Delbrück approximation. *Biophys. J.*, 94(5):L41–L43.
- [Petrova et al., 2017] Petrova, A. B., Herold, C., and Petrov, E. P. (2017). Conformations and membrane-driven self-organization of rodlike *fd*-virus particles on freestanding lipid membranes. *Soft Matter*, 13(39):7172–7187.

- [Phillips et al., 2012] Phillips, R., Kondev, J., Theriot, J., and Garcia, H. (2012). *Physical Biology of the Cell*. Garland Science.
- [Pisani et al., 2006] Pisani, M., Bruni, P., Caracciolo, G., Caminiti, R., and Francescangeli, O. (2006). Structure and phase behavior of self-assembled DPPC-DNA-metal cation complexes. *J. Phys. Chem. B*, 110(26):13203–13211.
- [Plumridge et al., 2017] Plumridge, A., Meisburger, S. P., Andresen, K., and Pollack, L. (2017). The impact of base stacking on the conformations and electrostatics of single-stranded DNA. *Nucleic Acids Res.*, 45(7):3932–3943.
- [Prinz and Hinshaw, 2009] Prinz, W. A. and Hinshaw, J. E. (2009). Membrane-bending proteins. *Crit. Rev. Biochem. Mol. Biol.*, 44(5):278–291.
- [Przybylo et al., 2006] Przybylo, M., Sýkora, J., Humpolíčková, J., Benda, A., Zan, A., and Hof, M. (2006). Lipid diffusion in giant unilamellar vesicles is more than 2 times faster than in supported phospholipid bilayers under identical conditions. *Langmuir*, 22(22):9096–9099.
- [Puchner and Gaub, 2009] Puchner, E. M. and Gaub, H. E. (2009). Force and function: probing proteins with AFM-based force spectroscopy. *Curr. Opin. Struct. Biol.*, 19(5):605–614.
- [Qualmann et al., 2011] Qualmann, B., Koch, D., and Kessels, M. M. (2011). Let’s go bananas: revisiting the endocytic BAR code. *EMBO J.*, 30(17):3501–3515.
- [Ramadurai et al., 2009] Ramadurai, S., Holt, A., Krasnikov, V., van den Bogaart, G., Killian, J. A., and Poolman, B. (2009). Lateral diffusion of membrane proteins. *J. Am. Chem. Soc.*, 131(35):12650–12656.
- [Ramakrishnan et al., 2013] Ramakrishnan, N., Sunil Kumar, P. B., and Ipsen, J. H. (2013). Membrane-mediated aggregation of curvature-inducing nematogens and membrane tubulation. *Biophys. J.*, 104(5):1018–1028.
- [Rigler et al., 1993] Rigler, R., Mets, Ü., Widengren, J., and Kask, P. (1993). Fluorescence correlation spectroscopy with high count rate and low background: analysis of translational diffusion. *Eur. Biophys. J.*, 22(3):169–175.

BIBLIOGRAPHY

- [Romano et al., 2013] Romano, F., Chakraborty, D., Doye, J. P. K., Ouldridge, T. E., and Louis, A. A. (2013). Coarse-grained simulations of DNA overstretching. *J. Chem. Phys.*, 138(8):085101.
- [Rothmund, 2006] Rothmund, P. W. K. (2006). Folding DNA to create nanoscale shapes and patterns. *Nature*, 440:297–302.
- [Roux et al., 2010] Roux, A., Koster, G., Lenz, M., Sorre, B., Manneville, J.-B., Nassoy, P., and Bassereau, P. (2010). Membrane curvature controls dynamin polymerization. *Proc. Natl. Acad. Sci.*, 107(9):4141–4146.
- [Russo et al., 2009] Russo, J., Tartaglia, P., and Sciortino, F. (2009). Reversible gels of patchy particles: role of the valence. *J. Chem. Phys.*, 131(1):014504.
- [Saffman, 1976] Saffman, P. G. (1976). Brownian motion in thin sheets of viscous fluid. *J. Fluid Mech.*, 73(4):593–602.
- [Saffman and Delbrück, 1975] Saffman, P. G. and Delbrück, M. (1975). Brownian motion in biological membranes. *Proc. Natl. Acad. Sci.*, 72(8):3111–3113.
- [Santos and Castanho, 2004] Santos, N. C. and Castanho, M. A. (2004). An overview of the biophysical applications of atomic force microscopy. *Biophys. Chem.*, 107(2):133–149.
- [Sato et al., 2018] Sato, Y., Endo, M., Morita, M., Takinoue, M., Sugiyama, H., Murata, S., Nomura, S.-I. M., and Suzuki, Y. (2018). Environment-dependent self-assembly of DNA origami lattices on phase-separated lipid membranes. *Adv. Mater. Interfaces*, 5:1800437.
- [Schindelin et al., 2015] Schindelin, J., Rueden, C. T., Hiner, M. C., and Eliceiri, K. W. (2015). The ImageJ ecosystem: an open platform for biomedical image analysis. *Mol. Reprod. Dev.*, 82(7-8):518–529.
- [Schmid and Frolov, 2011] Schmid, S. L. and Frolov, V. A. (2011). Dynamin: functional design of a membrane fission catalyst. *Annu. Rev. Cell Dev. Biol.*, 27:79–105.
- [Schreck et al., 2016] Schreck, J. S., Romano, F., Zimmer, M. H., Louis, A. A., and Doye, J. P. K. (2016). Characterizing DNA star-tile-based nanostructures using a coarse-grained model. *ACS Nano*, 10(4):4236–4247.

- [Schwille, 2011] Schwille, P. (2011). Bottom-up synthetic biology: engineering in a tinkerer’s world. *Science*, 333(6047):1252–1254.
- [Schwille and Diez, 2009] Schwille, P. and Diez, S. (2009). Synthetic biology of minimal systems. *Crit. Rev. Biochem. Mol. Biol.*, 44(4):223–242.
- [Schwille et al., 1999] Schwille, P., Korfach, J., and Webb, W. W. (1999). Fluorescence correlation spectroscopy with single-molecule sensitivity on cell and model membranes. *Cytometry*, 36(3):176–182.
- [Seeman, 1982] Seeman, N. C. (1982). Nucleic acid junctions and lattices. *J. Theor. Biol.*, 99(2):237–247.
- [Seifert et al., 2015] Seifert, A., Göpfrich, K., Burns, J. R., Fertig, N., Keyser, U. F., and Howorka, S. (2015). Bilayer-spanning DNA nanopores with voltage-switching between open and closed state. *ACS Nano*, 9(2):1117–1126.
- [Seifert and Lipowsky, 1995] Seifert, U. and Lipowsky, R. (1995). *Structure and Dynamics of Membranes: From Cells to Vesicles*, volume 1 of *Handbook of Biological Physics*, chapter Chapter 8 – Morphology of Vesicles, pages 403–463. Elsevier B.V.
- [Sharma et al., 2017] Sharma, R., Schreck, J. S., Romano, F., Louis, A. A., and Doye, J. P. K. (2017). Characterizing the motion of jointed DNA nanostructures using a coarse-grained model. *ACS Nano*, 11(12):12426–12435.
- [Simmel, 2012] Simmel, F. C. (2012). DNA-based assembly lines and nanofactories. *Curr. Opin. Biotechnol.*, 23(4):516–521.
- [Simons and Ikonen, 1997] Simons, K. and Ikonen, E. (1997). Functional rafts in cell membranes. *Nature*, 387(6633):569–572.
- [Simunovic et al., 2013a] Simunovic, M., Mim, C., Marlovits, T. C., Resch, G., Unger, V. M., and Voth, G. A. (2013a). Protein-mediated transformation of lipid vesicles into tubular networks. *Biophys. J.*, 105(3):711–719.
- [Simunovic et al., 2013b] Simunovic, M., Srivastava, A., and Voth, G. A. (2013b). Linear aggregation of proteins on the membrane as a prelude to membrane remodeling. *Proc. Natl. Acad. Sci.*, 110(51):20396–20401.

BIBLIOGRAPHY

- [Simunovic and Voth, 2015] Simunovic, M. and Voth, G. A. (2015). Membrane tension controls the assembly of curvature-generating proteins. *Nat. Commun.*, 6:7219.
- [Simunovic et al., 2015] Simunovic, M., Voth, G. A., Callan-Jones, A., and Bassereau, P. (2015). When physics takes over: BAR proteins and membrane curvature. *Trends Cell Biol.*, 25(12):780–792.
- [Singer and Nicolson, 1972] Singer, S. J. and Nicolson, G. L. (1972). The fluid mosaic model of the structure of cell membranes. *Science*, 175(4023):720–731.
- [Smith et al., 1996] Smith, S. B., Cui, Y., and Bustamante, C. (1996). Overstretching B-DNA: The elastic response of individual double-stranded and single-stranded DNA molecules. *Science*, 271(5250):795–799.
- [Stamov et al., 2015] Stamov, D. R., Stock, E., Franz, C. M., Jahnke, T., and Haschke, H. (2015). Imaging collagen type I fibrillogenesis with high spatiotemporal resolution. *Ultramicroscopy*, 149:86–94.
- [Strauss et al., 2018] Strauss, M. T., Schueder, F., Haas, D., Nickels, P. C., and Jungmann, R. (2018). Quantifying absolute addressability in DNA origami with molecular resolution. *Nat. Commun.*, 9(1):1600.
- [Sulc et al., 2012] Sulc, P., Romano, F., Ouldridge, T. E., Rovigatti, L., Doye, J. P. K., and Louis, A. A. (2012). Sequence-dependent thermodynamics of a coarse-grained DNA model. *J. Chem. Phys.*, 137(13):135101.
- [Sun et al., 2017] Sun, L., Gao, Y., Xu, Y., Chao, J., Liu, H., Wang, L., Li, D., and Fan, C. (2017). Real-time imaging of single-molecule enzyme cascade using a DNA origami raft. *J. Am. Chem. Soc.*, 139(48):17525–17532.
- [Sutherland, 1905] Sutherland, W. (1905). LXXV. A dynamical theory of diffusion for non-electrolytes and the molecular mass of albumin. *The London, Edinburgh, and Dublin Philosophical Magazine and Journal of Science*, 9(54):781–785.
- [Suzuki et al., 2015] Suzuki, Y., Endo, M., and Sugiyama, H. (2015). Lipid-bilayer-assisted two-dimensional self-assembly of DNA origami nanostructures. *Nat. Commun.*, 6:8052.
- [Suzuki et al., 2014] Suzuki, Y., Endo, M., Yang, Y., and Sugiyama, H. (2014). Dynamic assembly/disassembly processes of photoresponsive DNA origami nanostructures directly visualized on a lipid membrane surface. *J. Am. Chem. Soc.*, 136(5):1714–1717.

- [Swulius and Jensen, 2012] Swulius, M. T. and Jensen, G. J. (2012). The helical MreB cytoskeleton in *escherichia coli* MC1000/pLE7 is an artifact of the N-terminal yellow fluorescent protein tag. *J. Bacteriol.*, 194(23):6382–6386.
- [Szabat et al., 2015] Szabat, M., Pedzinski, T., Czapik, T., Kierzek, E., and Kierzek, R. (2015). Structural aspects of the antiparallel and parallel duplexes formed by DNA, 2'-O-methyl RNA and RNA oligonucleotides. *PLOS ONE*, 10(11):e0143354.
- [Tao et al., 2003] Tao, A., Kim, F., Hess, C., Goldberger, J., He, R., Sun, Y., Xia, Y., and Yang, P. (2003). Langmuir-Blodgett silver nanowire monolayers for molecular sensing using surface-enhanced Raman spectroscopy. *Nano Lett.*, 3(9):1229–1233.
- [Thormann et al., 2007] Thormann, E., Simonsen, A. C., Nielsen, L. K., and Mouritsen, O. G. (2007). Ligand–receptor interactions and membrane structure investigated by AFM and time-resolved fluorescence microscopy. *J. Mol. Recognit.*, 20(6):554–560.
- [Tinland et al., 1997] Tinland, B., Pluen, A., Sturm, J., and Weill, G. (1997). Persistence length of single-stranded DNA. *Macromolecules*, 30(19):5763–5765.
- [Torres and Levitus, 2007] Torres, T. and Levitus, M. (2007). Measuring conformational dynamics: A new FCS-FRET approach. *J. Phys. Chem. B*, 111(25):7392–7400.
- [Traub, 2015] Traub, L. M. (2015). F-BAR/EFC domain proteins: Some assembly required. *Dev. Cell*, 35(6):664–666.
- [Turek et al., 2018] Turek, V. A., Chikkaraddy, R., Cormier, S., Stockham, B., Ding, T., Keyser, U. F., and Baumberg, J. J. (2018). Thermo-responsive actuation of a DNA origami flexor. *Adv. Funct. Mater.*, 28(25):1706410.
- [Valeur and Berberan-Santos, 2012] Valeur, B. and Berberan-Santos, M. N. (2012). *Molecular Fluorescence: Principles and Applications*. John Wiley & Sons.
- [Viani et al., 2000] Viani, M. B., Pietrasanta, L. I., Thompson, J. B., Chand, A., Gebeshuber, I. C., Kindt, J. H., Richter, M., Hansma, H. G., and Hansma, P. K. (2000). Probing protein-protein interactions in real time. *Nat. Struct. Biol.*, 7(8):644–647.
- [Vink, 2009] Vink, R. L. C. (2009). The isotropic-to-nematic transition in a two-dimensional fluid of hard needles: a finite-size scaling study. *Eur. Phys. J. B*, 72(2):225–231.

BIBLIOGRAPHY

- [Vogel et al., 2017] Vogel, S. K., Greiss, F., Khmelinskaia, A., and Schwille, P. (2017). Control of lipid domain organization by a biomimetic contractile actomyosin cortex. *Elife*, 6.
- [Vogel et al., 2013] Vogel, S. K., Heinemann, F., Chwastek, G., and Schwille, P. (2013). The design of MACs (minimal actin cortices). *Cytoskeleton*, 70(11):706–717.
- [von Smoluchowski, 1906] von Smoluchowski, M. (1906). Zur kinetischen theorie der brownischen molekularbewegung und der suspensionen. *Ann. Phys.*, 326(14):756–780.
- [Wagenbauer et al., 2014] Wagenbauer, K. F., Wachauf, C. H., and Dietz, H. (2014). Quantifying quality in DNA self-assembly. *Nat. Commun.*, 5:3691.
- [Walsh and Menon, 2016] Walsh, L. and Menon, N. (2016). Ordering and dynamics of vibrated hard squares. *J. Stat. Mech. Theory Exp.*, (083302).
- [Weiß et al., 2013] Weiß, K., Neef, A., Van, Q., Kramer, S., Gregor, I., and Enderlein, J. (2013). Quantifying the diffusion of membrane proteins and peptides in black lipid membranes with 2-focus fluorescence correlation spectroscopy. *Biophys. J.*, 105(2):455–462.
- [Wen et al., 2012] Wen, X., Zhang, D., Chai, A., He, L., Ran, S., and Zhang, L. (2012). Self-assembly of nanorods on soft elastic shells. *Soft Matter*, 8(25):6706–6712.
- [Widengren et al., 1995] Widengren, J., Mets, U., and Rigler, R. (1995). Fluorescence correlation spectroscopy of triplet states in solution: a theoretical and experimental study. *J. Phys. Chem.*, 99(36):13368–13379.
- [Widengren and Schwille, 2000] Widengren, J. and Schwille, P. (2000). Characterization of photoinduced isomerization and back-isomerization of the cyanine dye Cy5 by fluorescence correlation spectroscopy. *J. Phys. Chem. A*, 104(27):6416–6428.
- [Widengren et al., 1999] Widengren, J., Terry, B., and Rigler, R. (1999). Protonation kinetics of GFP and FITC investigated by FCS – aspects of the use of fluorescent indicators for measuring pH. *Chem. Phys.*, 249(2):259–271.
- [Wilkinson et al., 1994] Wilkinson, F., McGarvey, D., and Olea, A. (1994). Excited triplet state interactions with molecular oxygen: Influence of charge transfer on the bimolecular quenching rate constants and the yields of singlet oxygen [$O_2^*(^1\Delta_2)$] for substituted naphthalenes in various solvents. *J. Phys. Chem.*, 98(14):3762–3769.

- [Williams and Carter, 1996] Williams, D. B. and Carter, C. B. (1996). The transmission electron microscope. In *Transmission electron microscopy*, pages 3–17. Springer.
- [Willner et al., 2017] Willner, E. M., Kamada, Y., Suzuki, Y., Emura, T., Hidaka, K., Dietz, H., Sugiyama, H., and Endo, M. (2017). Single-molecule observation of the photoregulated conformational dynamics of DNA origami nanoscissors. *Angew. Chem.*, 56(48):15324–15328.
- [Woo and Rothemund, 2011] Woo, S. and Rothemund, P. W. K. (2011). Programmable molecular recognition based on the geometry of DNA nanostructures. *Nat. Chem.*, 3:620–627.
- [Woo and Rothemund, 2014] Woo, S. and Rothemund, P. W. K. (2014). Self-assembly of two-dimensional DNA origami lattices using cation-controlled surface diffusion. *Nat. Commun.*, 5:4889.
- [Xu et al., 2016] Xu, W., Nathwani, B., Lin, C., Wang, J., Karatekin, E., Pincet, F., Shih, W., and Rothman, J. E. (2016). A programmable DNA origami platform to organize SNAREs for membrane fusion. *J. Am. Chem. Soc.*, 138(13):4439–4447.
- [Xu et al., 2013] Xu, W.-S., Li, Y.-W., Sun, Z.-Y., and An, L.-J. (2013). Hard ellipses: Equation of state, structure, and self-diffusion. *J. Chem. Phys.*, 139(2):024501.
- [Yang et al., 2016] Yang, Y., Wang, J., Shigematsu, H., Xu, W., Shih, W. M., Rothman, J. E., and Lin, C. (2016). Self-assembly of size-controlled liposomes on DNA nanotemplates. *Nat. Chem.*, 8:476–483.
- [Yoo et al., 2006] Yoo, P. J., Nam, K. T., Qi, J., Lee, S.-K., Park, J., Belcher, A. M., and Hammond, P. T. (2006). Spontaneous assembly of viruses on multilayered polymer surfaces. *Nat. Mater.*, 5(3):234–240.
- [Yue et al., 2013] Yue, T., Wang, X., Huang, F., and Zhang, X. (2013). An unusual pathway for the membrane wrapping of rodlike nanoparticles and the orientation- and membrane wrapping-dependent nanoparticle interaction. *Nanoscale*, 5(20):9888–9896.
- [Yurke et al., 2000] Yurke, B., Turberfield, A. J., Mills Jr, A. P., Simmel, F. C., and Neumann, J. L. (2000). A DNA-fuelled molecular machine made of DNA. *Nature*, 406:605–608.

BIBLIOGRAPHY

- [Zacharias and Sklenar, 1997] Zacharias, M. and Sklenar, H. (1997). Analysis of the stability of looped-out and stacked-in conformations of an adenine bulge in DNA using a continuum model for solvent and ions. *Biophys. J.*, 73(6):2990–3003.
- [Zadegan et al., 2017] Zadegan, R. M., Lindau, E. G., Klein, W. P., Green, C., Graugnard, E., Yurke, B., Kuang, W., and Hughes, W. L. (2017). Twisting of DNA origami from intercalators. *Sci. Rep.*, 7(1):7382.
- [Zadeh et al., 2011] Zadeh, J. N., Steenberg, C. D., Bois, J. S., Wolfe, B. R., Pierce, M. B., Khan, A. R., Dirks, R. M., and Pierce, N. A. (2011). NUPACK: Analysis and design of nucleic acid systems. *J. Comput. Chem.*, 32(1):170–173.
- [Zhang et al., 2015] Zhang, Y.-Y., Hua, Y.-F., and Deng, Z.-Y. (2015). Driven self-assembly of hard nanoplates on soft elastic shells. *Chin. Phys. B*, 24(118202).
- [Zhang et al., 2017] Zhang, Z., Yang, Y., Pincet, F., Llaguno, M. C., and Lin, C. (2017). Placing and shaping liposomes with reconfigurable DNA nanocages. *Nat. Chem.*, 9:653–659.
- [Zhao et al., 2011] Zhao, K., Bruinsma, R., and Mason, T. G. (2011). Entropic crystal-crystal transitions of Brownian squares. *Proc. Natl. Acad. Sci.*, 108(7):2684–2687.
- [Zhou et al., 2014] Zhou, L., Marras, A. E., Su, H.-J., and Castro, C. E. (2014). DNA origami compliant nanostructures with tunable mechanical properties. *ACS Nano*, 8(1):27–34.
- [Zieske et al., 2016] Zieske, K., Chwastek, G., and Schwille, P. (2016). Protein patterns and oscillations on lipid monolayers and in microdroplets. *Angew. Chem.*, 55(43):13455–13459.
- [Zimmerberg and McLaughlin, 2004] Zimmerberg, J. and McLaughlin, S. (2004). Membrane curvature: How BAR domains bend bilayers. *Curr. Biol.*, 14(6):R250–R252.
- [Zimmermann et al., 1986] Zimmermann, K., Hagedorn, H., Heuck, C. C., Hinrichsen, M., and Ludwig, H. (1986). The ionic properties of the filamentous bacteriophages Pfl and fd. *J. Biol. Chem.*, 261(4):1653–1655.
- [Zwang et al., 2010] Zwang, T. J., Fletcher, W. R., Lane, T. J., and Johal, M. S. (2010). Quantification of the layer of hydration of a supported lipid bilayer. *Langmuir*, 26(7):4598–4601.

A

APPENDIX TO II.1.4.2

The results discussed in this section are the outcomes of a close collaboration with the leading authors Sven Vogel and Ferdinand Greiss and have been published as:

Vogel, D. K., Greiss, F.*, Khmelinskaia, A., Schwille, P. (2017) Control of lipid domain organization by a biomimetic contractile actomyosin cortex. *eLife*, 6:e24350. doi: 10.7554/eLife.24350, *indicates equal contributions. The author of this thesis made all experiments on lipid monolayers in collaboration with S. Vogel. A reprint permission has been granted by the publisher.*



RESEARCH ADVANCE



Control of lipid domain organization by a biomimetic contractile actomyosin cortex

Sven Kenjiro Vogel^{1*†}, Ferdinand Greiss^{1,2,3†}, Alena Khmelinskaia^{1,3}, Petra Schwille^{1*}

¹Max-Planck Institute of Biochemistry, Martinsried, Germany; ²Systems Biophysics, Physics Department, Ludwig-Maximilians-University, Munich, Germany; ³Graduate School of Quantitative Biosciences, Ludwig-Maximilians-University, Munich, Germany

Abstract The cell membrane is a heterogeneously organized composite with lipid-protein micro-domains. The contractile actin cortex may govern the lateral organization of these domains in the cell membrane, yet the underlying mechanisms are not known. We recently reconstituted minimal actin cortices (MACs) (Vogel et al., 2013b) and here advanced our assay to investigate effects of rearranging actin filaments on the lateral membrane organization by introducing various phase-separated lipid mono- and bilayers to the MACs. The addition of actin filaments reorganized membrane domains. We found that the process reached a steady state where line tension and lateral crowding balanced. Moreover, the phase boundary allowed myosin driven actin filament rearrangements to actively move individual lipid domains, often accompanied by their shape change, fusion or splitting. Our findings illustrate how actin cortex remodeling in cells may control dynamic rearrangements of lipids and other molecules inside domains without directly binding to actin filaments.

DOI: [10.7554/eLife.24350.001](https://doi.org/10.7554/eLife.24350.001)

*For correspondence: svogel@biochem.mpg.de (SKV); schwille@biochem.mpg.de (PS)

†These authors contributed equally to this work

Competing interests: The authors declare that no competing interests exist.

Funding: See page 14

Received: 19 December 2016

Accepted: 29 April 2017

Published: 02 May 2017

Reviewing editor: Mohan K Balasubramanian, University of Warwick, United Kingdom

© Copyright Vogel et al. This article is distributed under the terms of the [Creative Commons Attribution License](https://creativecommons.org/licenses/by/4.0/), which permits unrestricted use and redistribution provided that the original author and source are credited.

Introduction

The spatiotemporal organization of lipids, proteins and other molecules at and within the cell membrane is pivotal for many fundamental cellular processes, such as signal transduction from the extracellular to the intracellular space (Groves and Kuriyan, 2010). Recent findings suggest that the cell membrane should be considered as a heterogeneous lipid protein layer with coexisting small micro domains and clusters of lipids and proteins that are assumed to dynamically form and reorganize in response to external and internal cues (Engelman, 2005; Simons and Gerl, 2010). Whether and how their spatiotemporal organization is actively regulated and maintained by the cell remains to be revealed. In vivo and in vitro studies suggest an important role of the eukaryotic actin cytoskeleton that interacts with the cell membrane via membrane-associated proteins (Heinemann et al., 2013; Köster et al., 2016; Murase et al., 2004; Sheetz et al., 1980). Actin structures were found to mediate the lateral organization of membrane proteins (Gudheti et al., 2013) and to modulate their diffusive behavior (Heinemann et al., 2013; Honigmann et al., 2014; Murase et al., 2004). Theoretical considerations have proposed a key role of the actin motor myosin for organizing and forming distinct protein and lipid micro-domains in cell membranes (Gowrishankar et al., 2012). However, direct experimental evidence for a control of lipid micro-domains by actomyosin rearrangements is still lacking.

In eukaryotic cells, the actin cortex is constantly rearranged by the motor protein myosin II and dozens of actin-binding proteins. Therefore, reducing the complexity of experimental conditions, e.g. reducing dimensionality or exploiting a minimal biomimetic system, and utilizing microscopic techniques with a high temporal resolution is beneficial for studying these processes. Phase-separated lipid bilayers with controlled lipid compositions are well-established test beds to mimic lipid

micro-domains in cell membranes and biological processes, e.g. the lateral organization of proteins that are otherwise difficult to observe in vivo. Ternary mixtures of lipids below their characteristic melting temperature (T_m) can phase separate into liquid disordered (L_d) and liquid ordered (L_o) domains. Liu and Fletcher used phase-separated giant unilamellar vesicles (GUVs) as a model system to study the influence of branched actin networks on the miscibility transition temperature (Liu and Fletcher, 2006). They reported that the formation of localized actin networks on PIP2-containing phase-separated GUVs could act as switch for the orientation of lipid domain growth sites.

However, the effects of an actin meshwork on individual lipid domains are technically difficult to study, due to the three-dimensional architecture of the GUVs. We therefore made use of a minimal biomimetic system of planar geometry that we recently developed (Vogel et al., 2013a, 2013b) and combined the minimal actin cortex (MAC) with supported phase-separated membranes and free-standing lipid monolayers. We then visualized and studied the effects of actin filament adhesion and myosin-driven rearrangements on the lateral organization of membrane domains with total internal reflection microscopy (TIRFM) and confocal spinning disk microscopy.

Results

Actin filament partitioning on phase-separated membranes

The effects of adhesion and myosin-induced contraction of an actin meshwork on the lateral organization of lipid domains was studied by combining phase-separated lipid membranes with our established assay featuring contractile MACs (Vogel, 2016; Vogel et al., 2013a, 2013b) (Figure 1A). For the adhesion assay, a ternary lipid mixture with DOPC, DPPC and Cholesterol in a 1:2:1 molar ratio was prepared (see Material and methods). Similar lipid compositions were described to form L_o and L_d phases in free-standing membranes up to 30°C (Veatch and Keller, 2003, 2005). The low miscibility transition temperature of the mixture avoids thermal degradation of proteins and allowed us to study the phase transition behavior in the presence of actin filaments. The fluorescent probe DiD (0.03 mol%) was used to label the L_d phases (García-Sáez et al., 2007). The density of biotinylated actin filaments was controlled by the concentration of biotinylated lipid DSPE-PEG(2000)-Biotin (see also [Vogel, 2016; Vogel et al., 2013b]). As observed with TIRF microscopy, the membrane separated into micrometer-sized L_o and L_d domains (Figure 1B–E) and homogenized at $\sim 37^\circ\text{C}$. The observed shift of 7°C in T_m compared with studies from Veatch and Keller (2003) agreed with our expectations considering the interaction of lipid molecules with the mica support (García-Sáez et al., 2007).

The adhesion of actin filaments via neutravidin to biotinylated DSPE provided a stable link between the MAC and the lipid bilayer over a wide range of temperatures. To validate the partitioning preference of all molecular components, the fluorescence signals of labeled neutravidin and actin filaments were acquired after domain formation when cooled below T_m (Figure 1B–E). We found that both neutravidin and actin filaments partitioned into the L_o phase (Figure 1B and C). We therefore concluded that the biotinylated lipid DSPE partitioned strongly to the L_o phase.

Actin filament crowding effects on supported phase-separated membranes

We prepared low (0.01 mol % DSPE-PEG(2000)-Biotin) and medium (0.1 mol % DSPE-PEG(2000)-Biotin, Figure 2B) dense MACs to investigate the effect of actin filament density on phase-separated membranes. To this end, the ternary lipid mixture was incubated with non-labeled neutravidin and placed on a temperature-controlled microscope objective. A fluorescence image was acquired as a reference before actin filaments were added (Figure 2A and B (left column)). A homogeneous membrane was produced by heating the microscope objective to 42°C (above T_m). Actin filaments were added to the membrane above T_m (Figure 2A and B (middle column)), and the sample was subsequently incubated for ~ 45 min at 42°C (Figure 2A). The membrane was completely covered by actin filaments after approximately 30 min (Figure 2A and B (middle column)). As final step, the membrane was slowly cooled down to 30°C without active cooling and the fluorescence signal was recorded after complete phase separation (Figure 2A and B (right column)). While the low-density MAC did not show any influence on membrane domain properties (data not shown), the medium-density MAC caused the formation of smaller domains (Figure 2B, right column). Both, actin filaments

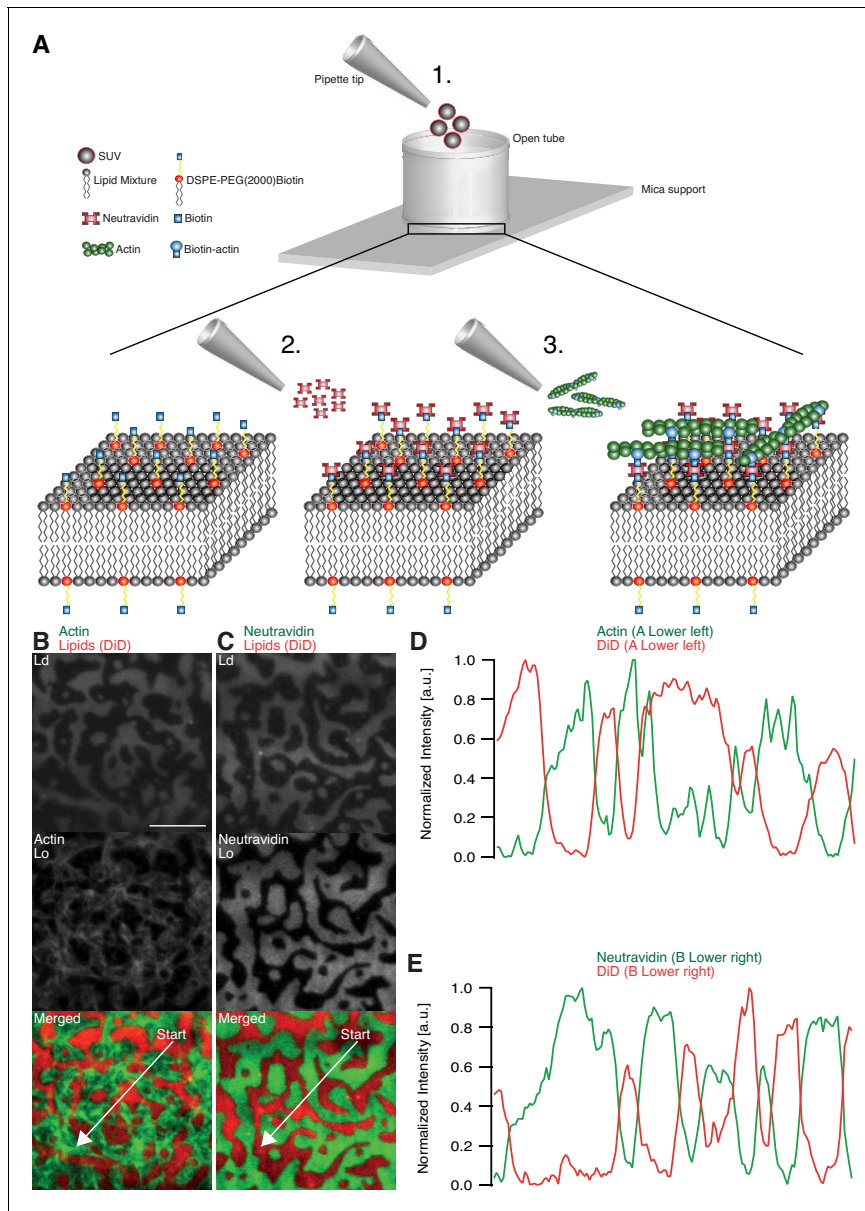


Figure 1. Minimal actin cortex on supported phase-separated lipid membranes. (A) Illustration depicting the preparation of the SLB and the coupling of actin filaments to the membrane (adapted from [Vogel et al., 2013a]). (B) Since DiD is known to partition specifically to the L_d phase (1:2:1 DOPC: DPPC:Cholesterol), the fluorescence signal of Alexa-488-phalloidin-labeled actin filaments showed that DSPE-PEG(2000)-Biotin partitioned into the L_o . Figure 1 continued on next page

Figure 1 continued

phase. (C) Likewise, Oregon-Green-labeled neutravidin colocalized with the L_0 phase. (D and E) Line profiles of the normalized fluorescence signal of the actin cortex, DiD and neutravidin as was measured along the superimposed arrows in (B) and (C). Scale bar, 10 μm .

DOI: 10.7554/eLife.24350.002

and DSPE-PEG(2000)-Biotin partitioned into the L_0 phase (Figure 2B and C), confirming our initial observations (Figure 1B–E). We conclude that actin filaments act as nucleation sites for domain formation and drive their lateral spatial distribution reproducing the observations reported by Honigmann et al. (2014).

To further investigate the relation between lateral membrane organization and the binding of actin filaments, we exposed high-density MACs containing a lipid mixture with 1.0 mol% biotinylated DSPE to different temperatures below T_m (Figure 2C–F). Fluorescently labeled actin filaments were added to the sample chamber at specified temperatures below T_m and imaged for ~30 min using TIRF microscopy (Figure 2C). Because of the strong binding affinity of neutravidin and biotin, we found that the change in fluorescence intensity of labeled actin filaments (which we used as a measure for actin filament binding) was independent of the applied temperature (Figure 2F). Hence, the adhesion process of actin filaments to the membrane was constant over the employed temperature range. The contour length (L) (Figure 2G) of membrane domains was extracted and tracked over time (Figure 2D). After ~1 min of actin filament addition, first domain deformations could be observed and the contour length was found to grow until a steady state at ~20 min was reached (Figure 2D). The final contour length increased with temperature (Figure 2E, final change in contour length: $L_{\text{Final}} = 188 \pm 4 \mu\text{m}$ and $\tau = 9.5 \pm 0.5 \text{ min}$ at 24°C, $L_{\text{Final}} = 314.0 \pm 1.5 \mu\text{m}$ and $\tau = 5.6 \pm 0.1 \text{ min}$ at 29°C, $L_{\text{Final}} = 706.3 \pm 2.5 \mu\text{m}$ and $\tau = 4.4 \pm 0.1 \text{ min}$ at 32°C). The line tension γ between L_0 and L_d domains is known to be a linear function of temperature with $\gamma \approx \gamma_0(T_C - T)/T_C$, where T_C is the critical temperature (Baumgart et al., 2003; Honerkamp-Smith et al., 2008; Veatch et al., 2008). With the temperature-independent actin filament binding and the boundary energy given by $E = \gamma L$ (Yang et al., 2016), where E is the boundary energy, the final contour length L should increase with

$$L = \frac{E}{\gamma_0} \frac{T_C}{T_C - T}. \quad (1)$$

The model describes the experimental data well (Figure 2E) and gives a length change (E/γ_0) of $86 \pm 9 \mu\text{m}$ at $T = 0^\circ\text{C}$ with $T_C = 37^\circ\text{C}$.

Actomyosin contraction governs lateral membrane domain organization

Aster shaped actomyosin clusters form in vivo (Luo et al., 2013; Munro et al., 2004; Verkhovskiy et al., 1997) and in vitro (Backouche et al., 2006; Köster et al., 2016; Murrell and Gardel, 2012; Soares e Silva et al., 2011; Vogel et al., 2013b) upon myosin's contractile activity. Synthetic myofilaments contract the MAC in the presence of ATP and, hence rearrange actin filaments to form stable actomyosin clusters (Figure 3A,C and G; Videos 1 and 5). For studying the effects of myofilament-induced actin rearrangements, we prepared two lipid mixtures for lipid mono- and bilayer experiments, namely DOPC, DPPC and Cholesterol in a 1:2:1 molar ratio and DOPC, PSM and Cholesterol in a 3:3:1 molar ratio containing 0.1 or 1 mol% DSPE-PEG(2000)-Biotin DSPE (see Material and methods).

We found that upon contraction, membrane domains deformed at the phase boundaries within minutes and resulted in various splitting and fusion events (Figure 3A,D,F and G; Videos 2–4 and 6). Domain shape changes, such as inward ingression, were observed and correlated with the movement of actomyosin clusters (Figure 3D; Videos 3 and 4). Actomyosin contraction against smaller L_d domains resulted in their net movement and occasionally led to splitting events of the domain (Figure 3D; Video 4), while the contraction for L_0 domains led to deformation and fusion with neighboring domains (Figure 3F; Video 6). For both mixtures, the area of the L_0 phase remained constant over the course of actomyosin contraction (Figure 3B and E, left panels). The number of L_d domains increased with time due to their splitting for the DOPC, DPPC, Cholesterol mixture (Figure 3B, right panel; Videos 2–4). The number of L_0 domains decreased in the DOPC, PSM, Cholesterol mixture due to their fusion and occasional disappearance during actomyosin contraction (Figure 3E (right

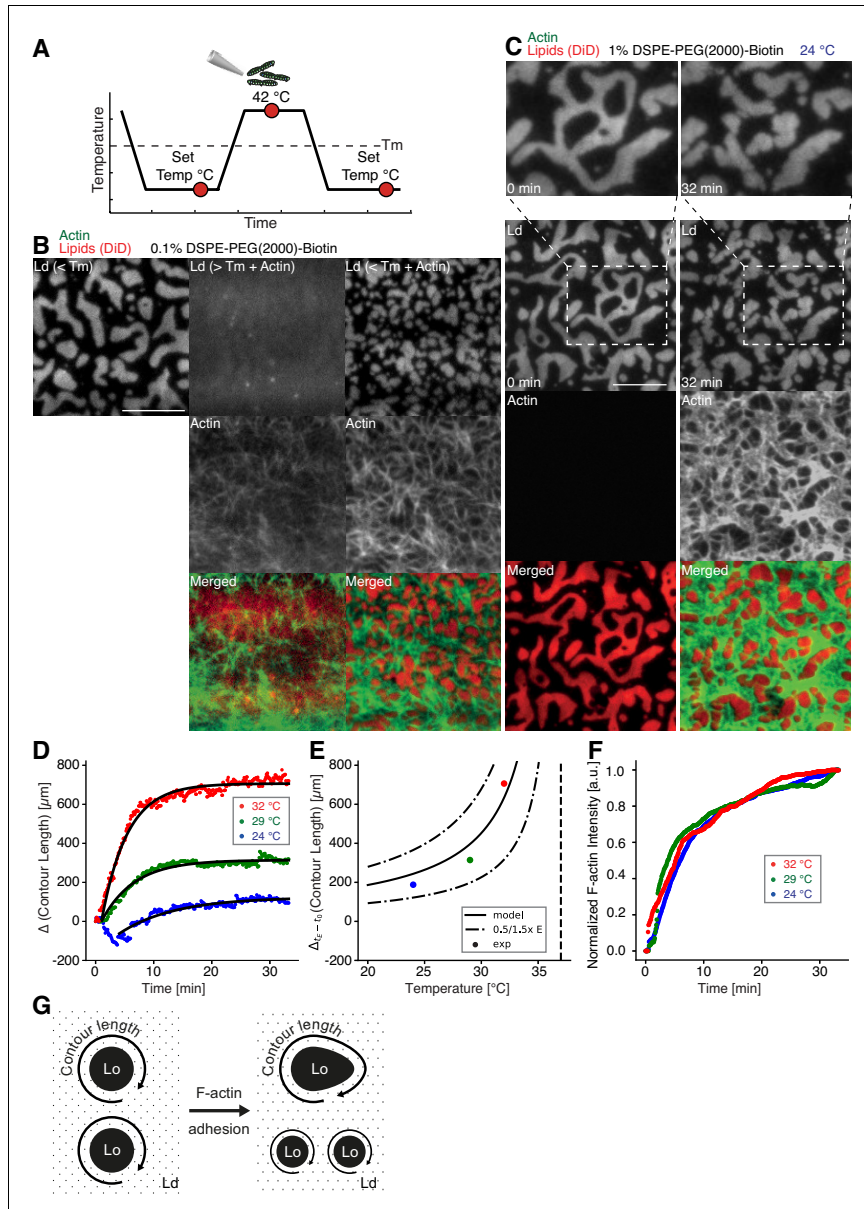


Figure 2. Impact of actin filaments on the lateral organization of phase-separated membranes. (A) Scheme of a phase separation experiment with and without MAC is shown with circles indicating time points when fluorescent images were acquired. (B) Size distribution of lipid domains changed in the presence of a MAC while undergoing phase separation. TIRF images of a medium-dense MAC with DiD-labeled L_d phase (1:2:1 DOPC:DPPC:Cholesterol) are shown below T_m (30°C) (left column), above T_m (42°C) in the presence of bound Alexa-488-phalloidin-labeled actin filaments (middle Figure 2 continued on next page

Figure 2 continued

column) and below T_m (30°C) in the presence of bound actin (right column). The final size of L_d domains decreased through the presence of actin filaments. (C) Change in contour length through the binding of actin filaments to the already phase-separated membrane at various temperatures below T_m . A high-density MAC with a DiD-labeled L_d phase before (0 min) and after the addition (32 min) of actin filaments at 24°C is shown. (D) Contour length of L_d domains upon F-actin adhesion with time and mono-exponential decay fits at 24°C (blue dots), 29°C (green dots) and 32°C (red dots). (Note that the observed local dip in contour length between 2 and 5 min at 24°C is because of a focal misalignment and blurring of the images after the addition of actin filaments). (E) Final change in contour length for the different temperatures. With a constant lateral pressure, the linearly decreasing line tension with temperature leads to an increase in final contour length according to Equation (1). Dashed vertical line indicates T_m of 37°C. (F) The binding kinetics of actin filaments was tracked with the normalized fluorescence signal over time at 24°C (blue dots), 29°C (green dots) and 32°C (red dots). (G) Illustrative sketch for the change in contour length before and after F-actin adhesion. Scale bars, 10 μm .

DOI: 10.7554/eLife.24350.003

panel) and G; Videos 6 and 7). A similar behavior in L_o domain disappearance has been observed by Köster *et al.* (2016). In contrast to their work, we did not observe a decrease of the total L_o phase domain area in neither of the lipid mixtures (Figure 3B and E, left panels). In summary, we showed active lateral reorganization of lipid domains for two different lipid mixtures, indicating the general validity of our experimental observations.

In order to mimic free-standing membranes without support-induced friction as in the SLBs but keeping the technical advantages of a planar geometry, we made use of a recently developed lipid monolayer system (Chwastek and Schwille, 2013) with an air-liquid interface (Figure 4A–D). Actin filaments were coupled to ternary phase-separated lipid monolayers similar to the situation in the supported lipid bilayer (SLB) system via biotinylated lipids (1 mol%) and the use of neutravidin. Contrary to the situation in the SLB system, actin filaments preferentially bind to the liquid extended (disordered) (L_e) phase where also the neutravidin anchor protein mainly partitioned to (Figure 4A–D). We observed this behavior for both lipid mixtures that were also used for the SLBs (see Material and methods). In low- and medium-dense monolayer MACs the liquid condensed (ordered) L_c domains acquire circular shapes and the actin filaments close to the phase boundaries align to their circular shape (Figure 4A). In the case of low and medium densities, we expect that the line tension energy dominates over the actin filament wetting energy at the phase boundary and hence the L_c can assume an unrestricted shape with aligned actin filaments. Similar effects have been observed using bacterial cytoskeleton proteins (Arumugam *et al.*, 2015). The addition of myosin filaments in the presence of ATP led to the contraction of the actin layer deforming and rearranging the L_c domains in both lipid mixtures similar to what we observed in the SLB systems (Figure 4B–D; Video 8). The shape changes included fusion and stretching of the L_c domains (Figure 4B–D; Video 8). Note that these ‘active’ deformation forces were only exerted in the presence of myosin filaments and ATP. Interestingly, the obtained lipid domain shapes seemed to be stabilized after the active contraction period, probably by the remaining actin filaments. Using the monolayer system also tells us that the frictional force caused by a solid support in SLBs does not play a significant role in the observed phenomena.

Discussion

As cells may need to quickly adapt the macro- and microscopic organization of lipid and protein aggregates within the cell membrane due to external or internal cues, we propose that actomyosin-driven reorganization of actin filaments may aid to quickly govern their lateral distribution. Recent evidence exists that the presence of an actin meshwork influences the lateral diffusion behavior of lipids and proteins in membranes *in vivo* (Murase *et al.*, 2004) and *in vitro* (Heinemann *et al.*, 2013) and that it impacts the behavior of phase-separated membranes (Honigsmann *et al.*, 2014; Liu and Fletcher, 2006). The important role of myosin is further supported by recent theoretical and *in vitro* studies (Gowrishankar *et al.*, 2012; Köster *et al.*, 2016). It is therefore tempting to speculate that cortical actomyosin contractility may be a generic model for eukaryotic organisms not only to control their mechanical stability and shape but also to quickly and actively control the lateral lipid and protein organization at the cell membrane.

In our MACs that were combined with ternary lipid mixtures, we found that binding of actin filaments to a homogeneous bilayer at temperatures above T_m -induced spatial alignment of L_o domains to actin-bound locations upon cooling below T_m (Figure 2). Here, actin filaments serve as

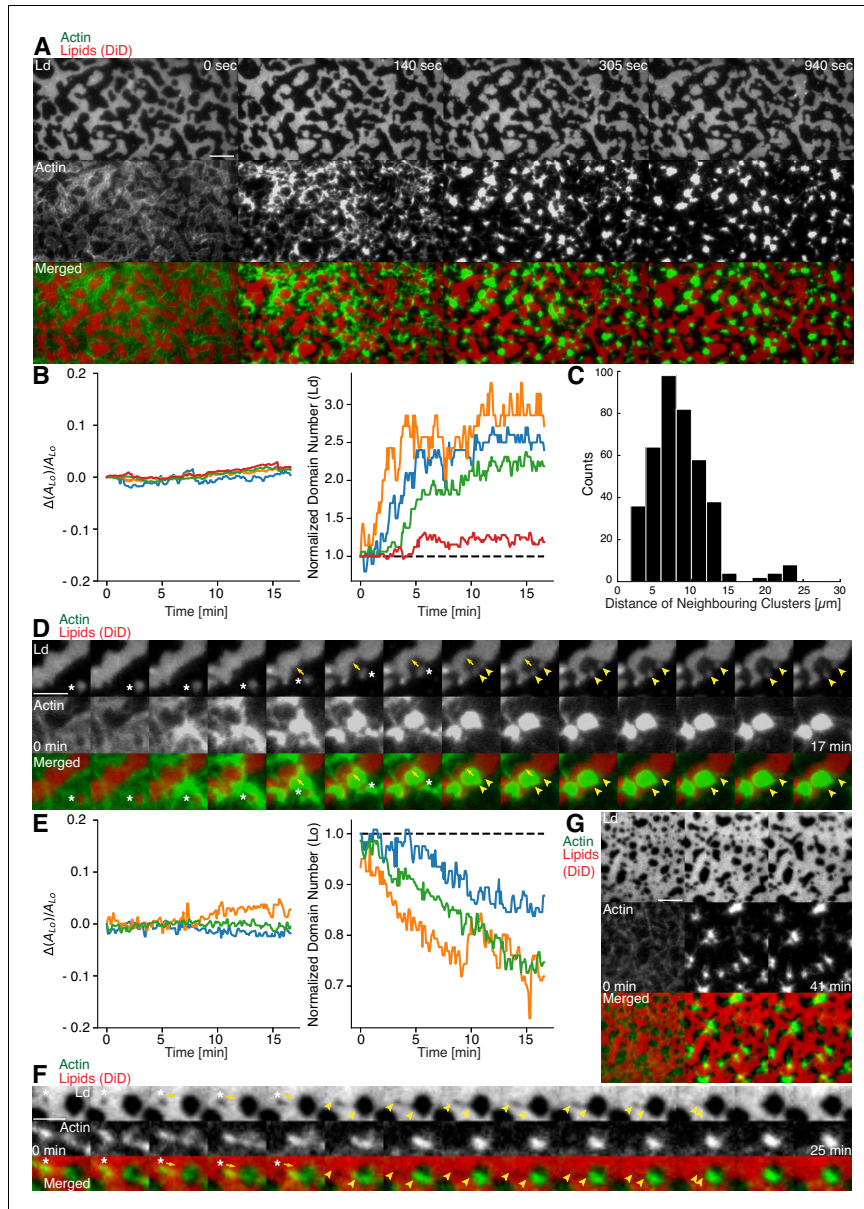


Figure 3. Actomyosin contraction governs lateral membrane organization for various lipid compositions. (A) TIRFM time-lapse images of a contracting MAC with Alexa-488-phalloidin labeled actin filaments and DiD-labeled L_d domains of a 1:2:1 DOPC:DPPC:Cholesterol mixture. Scale bar, 10 μ m. (B) For the 1:2:1 DOPC:DPPC:Cholesterol mixture the area of the L_o phase was found to remain constant while the number of L_o domains increased with time through splitting. (C) Distance to neighboring actomyosin clusters for the lipid composition of 1:2:1 DOPC:DPPC:Cholesterol. (D) Representative Figure 3 continued on next page

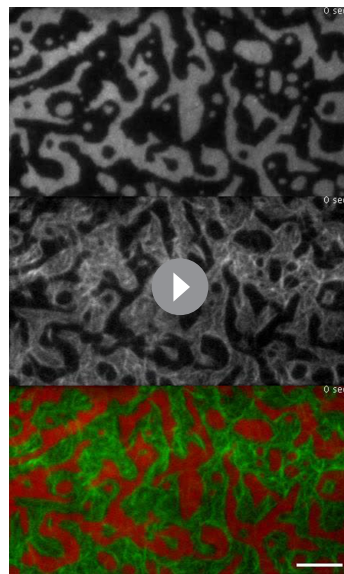
Figure 3 continued

example (1:2:1 DOPC:DPPC:Cholesterol mixture) showing movement (white asterisks) and deformation (inward ingestion, yellow arrows) of a phase boundary upon actomyosin contraction and its splitting into two separated domains (yellow arrowheads). Scale bar, 10 μm . (E) For a lipid composition of 3:3:1 DOPC:PSM:Cholesterol, the area of the L_o phase remained again constant and the number of L_o domains decreased. (F) Pulling of a L_o domain (white asterisk) for a lipid composition of 3:3:1 DOPC:PSM:Cholesterol by actomyosin led to fusion (yellow arrowheads) and relaxation into a larger neighboring domain. Scale bar, 2.5 μm . (G) Time-lapse montage of the actomyosin contraction on a 3:3:1 DOPC:PSM:Cholesterol phase-separated membrane. Small L_o domains are moved and fused to produce larger domains. Scale bar, 5 μm .

DOI: [10.7554/eLife.24350.004](https://doi.org/10.7554/eLife.24350.004)

nucleation sites for domain formation and drive their lateral spatial distribution. Already phase separated, we could show that membrane domains reorganized with the adhesion of actin filaments depending on line tension and actin filament density. We further give direct evidence that the

dynamic reorganization of actin filaments by myosin motors actively changes the macroscopic organization of membrane domains in our reconstituted phase-separated lipid bilayers and monolayers. We propose that the transition energy between the L_d and L_o phase (Baumgart et al., 2003; García-Sáez et al., 2007; Honerkamp-Smith et al., 2008) enabled the lipid anchored actin filaments to exert lateral forces on the phase boundaries leading to a macroscopic motion of lipid domains that eventually resulted in splitting, fusion or deformation of the lipid domains and in their overall change in number during and after the actomyosin contraction (Figure 3B and E, right panels; Videos 2–4, 6 and 8). In a model, we would first consider a biotinylated lipid that is dragged by an actomyosin filament (Figure 4E). The actomyosin filaments are unequally associated with the lipid phases (L_o and L_d) with different viscosities. The drag is counteracted by friction and, through the different viscosities, leads to domain deformation and rearrangement. Here, the force propagation would be independent of phase boundaries. As a second consideration, the



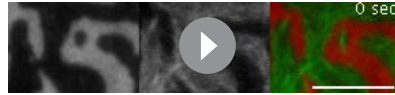
Video 1. Myosin-induced actin rearrangements in a minimal actin cortex (MAC) combined with a supported phase-separated lipid bilayer. MAC with a supported phase-separated membrane (1:2:1 DOPC:DPPC:Cholesterol) containing Alexa-488-phalloidin-labeled actin filaments (green) exhibits dynamic rearrangements of actin filaments after the addition of myofilaments in the presence of ATP and eventually forms actomyosin clusters. The phase-separated membrane containing DiD-labeled L_d domains (red) is shown in the upper channel. The middle channel shows Alexa-488-phalloidin-labeled actin filaments (green) that bind to the L_o domains. The lower channel shows the merge of both channels. TIRFM image sequence was acquired at 5 s. time intervals and contains 200 frames. The video is displayed at 15 frames per second (fps). Total time: 16.6 min. Scale bar, 10 μm . (Compressed JPG avi; 10.2 MB).

DOI: [10.7554/eLife.24350.005](https://doi.org/10.7554/eLife.24350.005)



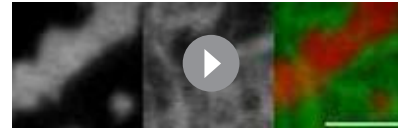
Video 2. Shape changes, rearrangements and fusion events of L_d domains during actomyosin contraction. The phase-separated membrane (1:2:1 DOPC:DPPC:Cholesterol) containing DiD labeled L_d domains (red) is shown in the left channel. The middle channel shows Alexa-488-phalloidin labeled actin filaments that bind to the L_o domains. The right channel shows the merge of both channels. TIRFM image sequence was acquired at 5 s. time intervals and contains 124 frames. The video is displayed at 15 frames per second (fps). Total time: 10.3 min. Scale bar, 10 μm . (Compressed JPG avi; 0.8 MB).

DOI: [10.7554/eLife.24350.006](https://doi.org/10.7554/eLife.24350.006)



Video 3. Splitting, shape changes and deformations of L_d domains during actomyosin contraction. The phase-separated membrane (1:2:1 DOPC:DPPC:Cholesterol) containing DiD labeled L_d domains (red) is shown in the left channel. The middle channel shows Alexa-488-phalloidin-labeled actin filaments that bind to the L_o domains. The right channel shows the merge of both channels. TIRFM image sequence was acquired at 5 s. time intervals and contains 200 frames. The video is displayed at 15 frames per second (fps). Total time: 16.6 min. Scale bar, 10 μ m. (Compressed JPG avi; 0.8 MB).

DOI: [10.7554/eLife.24350.007](https://doi.org/10.7554/eLife.24350.007)



Video 4. L_d domain movement, splitting and ingression during actomyosin contraction. The phase-separated membrane (1:2:1 DOPC:DPPC:Cholesterol) containing DiD-labeled L_d domains (red) is shown in the left channel. The middle channel shows Alexa-488-phalloidin-labeled actin filaments that bind to the L_o domains. The right channel shows the merge of both channels. TIRFM image sequence was acquired at 5 s. time intervals and contains 200 frames. The video is displayed at 15 frames per second (fps). Total time: 16.6 min. Scale bar, 5 μ m. Corresponds to **Figure 3D**. (Compressed JPG avi; 0.4 MB).

DOI: [10.7554/eLife.24350.008](https://doi.org/10.7554/eLife.24350.008)

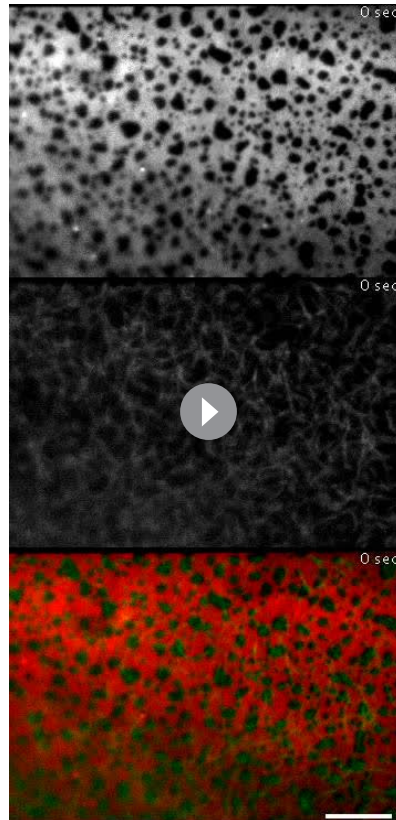
biotinylated lipid would need to overcome the transition barrier between phases while being dragged over a boundary (**Figure 4E**). Since our contraction experiments primarily showed that the boundaries deformed locally at actin filament sites and that actomyosin foci formed at the vicinity of phase boundaries, the high transition energy is favored as the dictating driving force for phase deformation. Furthermore, domain deformation was commonly found to happen when actin filaments were dragged over the L_d phase that impedes the free contraction process through the strong partitioning preference of DSPE-PEG(2000)-Biotin to the L_o phase.

With an estimated line tension of 1 pN for a 1:2:1 DOPC:DPPC:Cholesterol membrane (**Baumgart et al., 2003; Garca-Saez et al., 2007; Kuzmin et al., 2005; Veatch and Keller, 2005**) and a reported value of ~ 1.5 k $_B$ T for the transfer of DPPC between phases (**Veatch et al., 2004**), the energy for one DPPC molecule to transition is roughly sixfold higher than the energy that is needed to elongate the phase boundary by 1 nm. Further experiments should elaborate on the physical model since actomyosin contraction is clearly a non-equilibrium process and line tension itself was reported to depend on the applied lateral tension (**Akimov et al., 2007**). Together with our experimental findings, we can conclude that actively rearranging actin filaments will lead to an extensive deformation of membrane domains through the physical link with a small subset of membrane constituents. A plausible mechanism is therefore apparent that explains active lateral rearrangements of membrane components by actomyosin contractions without the need of binding directly to actin filaments.

Material and methods

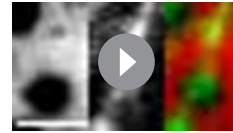
Actin labeling and polymerization

F-actin preparation was performed as described in **Vogel et al. (2013b)**. Briefly, a 39.6 μ M actin solution (Actin/Actin-Biotin ratio of 5:1) was prepared by mixing rabbit skeletal actin monomers (32 μ l, 2 mg/ml, Molecular Probes) with biotinylated rabbit actin monomers (1.6 μ l, 10 mg/ml, tebu-bio/Cytoskeleton Inc.). F-buffer (1 mM DTT, 1 mM ATP, 10 mM Tris-HCl (pH 7.4), 2 mM MgCl $_2$ and 50 mM KCl) was added to the mixture in order to start polymerization. Actin polymers were labeled and stabilized with Alexa Fluor 488 Phalloidin according to the manufacturer's protocol (Molecular Probes). Finally, the 2 μ M Alexa-488-Phalloidin-labeled biotinylated actin filament solution was stored at 4°C.



Video 5. Shape changes, rearrangements and fusion events of L_o domains during actomyosin contraction. The phase-separated and DiD labeled (red) membrane (3:3:1 DOPC:PSM:Cholesterol) containing L_o domains (dark) is shown in the upper channel. The middle channel shows Alexa-488-phalloidin-labeled actin filaments (green) that bind to the L_o domains. The lower channel shows the merge of both channels. TIRFM image sequence was acquired at 5 s. time intervals and contains 500 frames. The video is displayed at 15 frames per second (fps). Total time: 41.6 min. Scale bar, 10 μ m. (Compressed JPG avi; 28 MB).

DOI: [10.7554/eLife.24350.009](https://doi.org/10.7554/eLife.24350.009)



Video 6. Fusion event of a L_o domain during actomyosin contraction. A small L_o domain is stretched by actin filaments thereby pulling the domain toward a larger domain leading eventually to fusion of both L_o domains. The phase-separated and DiD-labeled (red) membrane (3:3:1 DOPC:PSM:Cholesterol) containing L_o domains (dark) is shown in the left channel. The middle channel shows Alexa-488-phalloidin-labeled actin filaments (green) that bind to the L_o domains. The right channel shows the merge of both channels. TIRFM image sequence was acquired at 5 s. time intervals and contains 337 frames. The video is displayed at 120 frames per second (fps). Total time: 28 min. Scale bar, 2.5 μ m. Corresponds to [Figure 3F](#). (Compressed JPG avi; 0.4 MB).

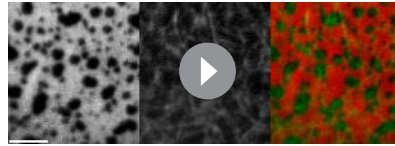
DOI: [10.7554/eLife.24350.010](https://doi.org/10.7554/eLife.24350.010)

MAC (minimal actin cortex) preparation

1,2-Dioleoyl-*sn*-glycero-3-phosphocholine (DOPC), 1,2-dipalmitoyl-*sn*-glycero-3-phosphocholine (DPPC), and cholesterol were added in a molar ratio of 1:2:1 or DOPC, N-palmitoyl-D-sphingomyelin (PSM), and Cholesterol in a molar ratio of 3:3:1 to a final lipid concentration of 5 mg/ml (Avanti Polar Lipids, Inc). The lipid bilayer was further supplemented with 0.03 mol% DiD (Molecular Probes, Eugene, OR) and 0.01, 0.1 or 1 mol% DSPE-PEG(2000)-Biotin (Avanti Polar Lipids, Inc.). The solution was dried under continuous nitrogen flux and then placed under vacuum for 1 hr to remove chloroform residuals. The pellet was rehydrated in SLB buffer (150 mM KCl, 25 mM Tris-HCl, pH 7.5) by vigorous vortexing and sonication.

20 μ l of clear lipid suspension, was then diluted in 130 μ l A-buffer (50 mM KCl, 2 mM $MgCl_2$, 1 mM DTT and 10 mM Tris-HCl, pH 7.5) and heated to 55°C. Meanwhile, freshly cleaved mica was fixated with immersion oil (Carl Zeiss, Jena, Germany) on a cover slip (22 \times 22 mm, #1.5, Menzel Gläser, Thermo Fisher) and covered with the center part of a cut 1.5 mL Eppendorf tube. The Eppendorf tube was glued with UV-sensitive glue (Norland Optical Adhesive 63,

Cranbury, USA). The chamber was filled with 75 μ l of small unilamellar vesicles and incubated at 55°C for 45 min with 1 mM $CaCl_2$. Non-fused vesicles were removed by washing the suspension with 2 ml warmed A-buffer and gentle pipetting. The chamber's temperature was slowly cooled. Next, 2 μ l of unlabeled or Oregon-Green-labeled neutravidin (1 mg/ml, Molecular Probes) diluted in 200 μ l



Video 7. Disappearance of small L_o domains during actomyosin contraction. Small L_o domains often vanish during actomyosin contractions. The phase-separated and DiD-labeled (red) membrane (3:3:1 DOPC:PSM:Cholesterol) containing L_o domains (dark) is shown in the left channel. The middle channel shows Alexa-488-phalloidin-labeled actin filaments (green) that bind to the L_o domains. The right channel shows the merge of both channels. TIRFM image sequence was acquired at 5 s. time intervals and contains 493 frames. The video is displayed at 120 frames per second (fps). Total time: 41 min. Scale bar, 5 μm . Corresponds to [Figure 3G](#). (Compressed JPG avi; 4.1 MB).

DOI: [10.7554/eLife.24350.011](https://doi.org/10.7554/eLife.24350.011)

A-buffer were added to the sample and incubated for 10 min. Finally, unbound proteins were removed by gently washing the solution with 2 ml A-buffer.

Phase separation with MAC

The phase-separated membrane was heated with an objective heater (Carl Zeiss, Jena, Germany) to the setpoint of 42°C and cooled down to 30°C, both with and without Alexa-488-Phalloidin-labeled biotinylated actin filaments. The area distribution of domains at equilibrium (45 min after 30°C was reached) was then compared between the different concentrations of DSPE-PEG(2000)-Biotin (0.1, 0.01 mol%).

Crowding-effect

The sample was placed on the TIRF microscope objective with attached objective heater and slowly warmed to the setpoint of 42°C. The lipid bilayer with 1.0% DSPE-PEG(2000)-Biotin was equilibrated at different temperatures below the melting point (~37°C for 1:2:1 DOPC:DPPC:Cholesterol). Of Alexa-488-Phalloidin-labeled biotinylated actin filaments, 20 μl were then carefully added to the chamber. Binding of actin filaments to the membrane was recorded by acquiring images in interleaved mode (488 nm and 640 nm) every 2.5 s, generating a time-lapse movie with a 5 s delay between subsequent images.

F-actin network contraction by myofilaments

After the addition of 20 μl Alexa-488-Phalloidin-labeled biotinylated actin filaments to the supported lipid bilayer at room temperature (~24°C), the mixture was incubated for approximately 45 min in order to ensure full binding of actin filaments to the membrane. Subsequently, residual actin was removed by gently exchanging the solution with 2 ml A-buffer. Once the properly assembled MAC was verified with TIRF microscopy, a solution of 20 μl myofilaments and 1 μl ATP (0.1 M) were added to start the compaction of actin filaments.

Images were acquired every 2.5 s in interleaved mode, which eliminated the cross talk between color channels of actin filaments and the phase-separated membrane.

TIRF microscopy

Fluorescent imaging of labeled proteins and membrane was carried out on a custom-built TIRF microscope. The setup was integrated into an Axiovert 200 microscope (Zeiss). The probe was illuminated and imaged through a Plan-Apochromat 100x/NA 1.46 oil immersion objective with a 488 nm and 630 nm laser. Images were acquired with an Andor Solis EMCCD camera (electron gain = 300, exposure time = 50 ms, frame interval = 2.5 or 5 s) in interleaved mode.

Data analysis

Image processing, analysis and data visualization were performed with Fiji and the scientific packages for Python. Multichannel beads were used to align double-color image stacks with the Fiji plugin Descriptor-based series registration. The contour length between the lipid domains was extracted by detecting edges (Canny edge detection; [[van der Walt et al., 2014](#)]) in single fluorescent images acquired from phase-separated membranes. The contour length over time was fitted to $L = L_{final} (1 - \exp(-1/\tau (t - t_0)))$ with $t_0 = 1$ min. The actomyosin clusters were detected using the Laplacian of Gaussian method (scikit-image [[van der Walt et al., 2014](#)]) and assigned to neighbors using the Delaunay triangulation and its method `vertex_neighbor_vertices`.

To detect the lipid domains, the fluorescence images were firstly corrected for an uneven background signal. Then, the DiD signal was classified with a local adaptive thresholding algorithm and

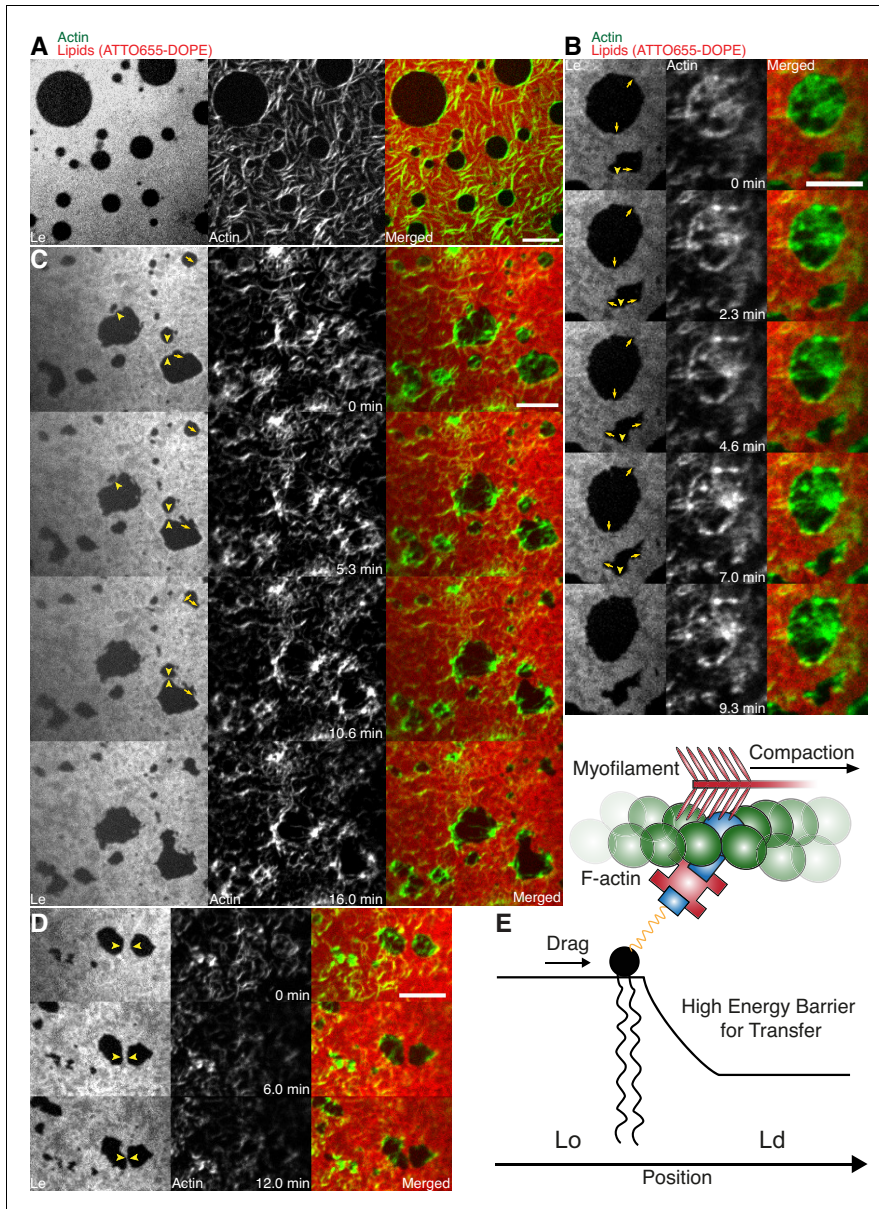


Figure 4. Lipid monolayer domain shape changes and fusion events induced by actomyosin contractions. (A) Confocal spinning disk microscope images of Alexa-488-phalloidin-labeled actin filaments coupled to a ATTO655-DOPE-labeled lipid monolayer (3:3:1 DOPC:PSM:Cholesterol) in the absence of myofilaments. Actin filaments close to the phase boundaries of lipid monolayer domains align to their circular shape. (B–D) Spinning Disk microscope time-lapse images of Alexa-488-phalloidin-labeled actin filaments coupled to ATTO655-DOPE-labeled lipid monolayers during myofilament contraction. *Figure 4 continued on next page*

Figure 4 continued

induced contractions of actin filaments. Actomyosin contractions lead to shape changes and fusion events (yellow arrows and arrowheads) of the lipid monolayer L_c domains. (E) Scheme of a microscopic model. Scale bars, 10 μm .

DOI: 10.7554/eLife.24350.012

the corresponding phase boundaries with the Canny edge detection algorithm. The binary image stacks were combined with the XOR operator and further refined using the morphological closing operation. Small holes were removed from the binary images. Small objects were detected with the Laplacian of Gaussian method and as a final step, combined with the binary images. The script was implemented in Python with the image processing package scikit-image.

MAC assembly on lipid monolayers

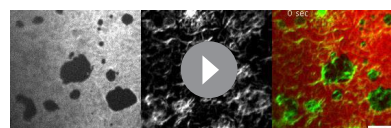
For the lipid monolayer assays, the same lipid mixtures and molar ratios were used as for the supported bilayers with 1 mol% of DSPE-PEG(2000)-Biotin. The lipids were mixed, dried under nitrogen flux for 15 min, subsequently put into vacuum for 30 min and dissolved in chloroform (total lipid concentration of 1 mg/ml). The mixtures were further diluted to a final lipid concentration of 0.1 mg/ml and labeled by addition of 0.1 mol% of ATTO655-DOPE (ATTO-TEC GmbH, Siegen, Germany). The total lipid concentration was confirmed by gravimetry.

To form a chamber (see *Scheme 1*), chamber spacers were cut from a 5-mm-thick sheet of PTFE by a laser cutter. The spacers were sonicated step-by-step in acetone, chloroform, isopropanol and ethanol (15 min each). Glass cover slips of 15 mm (Gerhard Menzel GmbH, Braunschweig, Germany) were fixed to the spacer by picodent twinsil 22 two component glue (picodent, Wipperfurth, Germany). The chambers were washed alternately with ethanol and water, air dried and air plasma-cleaned for 10 min in order to make the glass hydrophilic. The surface was then passivated by covering the glass surface with PLL-PEG(2000) (SuSos AG, Dübendorf, Switzerland) 0.5 mg/mL solution in PBS buffer and incubated for minimum half an hour. After thorough wash with water (5 times 200 μl) and reaction buffer (3 times 200 μl), the chambers were ready to use.

Lipid monolayers were formed by drop-wise deposition of the lipid mixture on the buffer-air interface (for further details, see also [Chwastek and Schwille, 2013]). A lipid mixture volume corresponding to a lipid surface density of 70 \AA^2 / molecule was deposited drop-wise on the surface of the buffer solution.

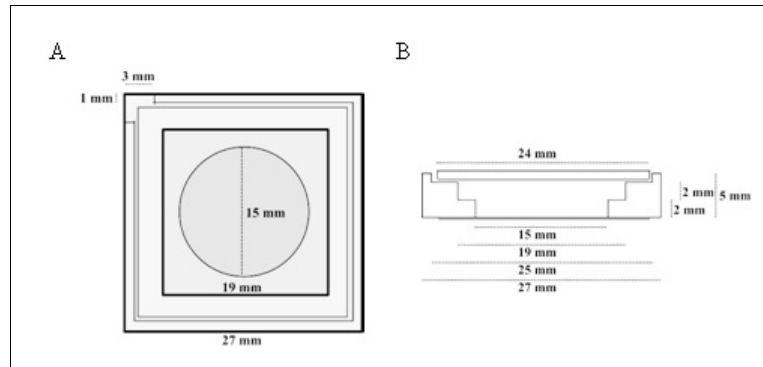
The samples were imaged using a Yokogawa scan head CSU10-X1 spinning disk system connected to a Nikon Eclipse Ti inverted microscope (Nikon, Japan) with an Andor Ixon Ultra 512 \times 512 EMCCD camera and a 3i solid state diode laser stack with 488 nm, 561 nm and 640 nm laser lines (3i133, Denver, Colorado USA). For simultaneous Alexa-488-phalloidin and ATTO655-DOPE excitation, the 488 nm and the 640 nm laser lines and an UPLanSApo 60x/1.20 Water UIS2 objective (Olympus, Japan) were used. The time interval between the recorded images was 20 s.

After confirming the formation of a phase-separated lipid monolayer by imaging, 100 μl of neutravidin solution (0.01 $\mu\text{g}/\mu\text{l}$) was added to the sample twice and was incubated for 5 min. Note that all protein solutions or other solutions are applied directly to the liquid subphase by dipping the pipette tip through the monolayer. Next, the subphase was washed five times with buffer (100 μl steps) to remove unbound neutravidin. Subsequently, 20 μl of Alexa-488-phalloidin-labeled actin filaments (2 μM) was added to the subphase and incubated for at least 60 min, since



Video 8. Shape changes and fusion events during actomyosin contraction of L_c domains in a MAC combined with a phase-separated lipid monolayer. Myofilaments in the presence of ATP led to the contraction of the actin layers and to shape changes and fusion events of the L_c domains. The phase-separated lipid monolayer (3:3:1 DOPC:PSM:Cholesterol) containing the ATTO655-DOPE-labeled L_c phase (red) is shown in the left channel. The middle channel shows Alexa-488-phalloidin-labeled actin filaments that bind to the L_c phase. The right channel shows the merge of both channels. Confocal Spinning Disk image sequence was acquired at 20 s. time intervals and contains 64 frames. The video is displayed at 15 frames per second (fps). Total time: 21 min. Scale bar, 10 μm . Corresponds to *Figure 4C*. (Compressed JPG avi; 1.7 MB).

DOI: 10.7554/eLife.24350.013



Scheme 1. Top (A) and lateral (B) schematic view of the PTFE chamber (adapted from [Chwastek and Schwille, 2013]).

DOI: 10.7554/eLife.24350.014

binding of actin filaments to the interface was assumed to occur relatively slowly. When the binding of the actin filaments was confirmed by imaging, the monolayer was thoroughly washed (7 to 10 steps of 100 μ l) with reaction buffer containing 1 μ M ATP and 100 μ l of myofilaments (0.3 μ M) containing 1 μ M ATP (enzymatically regenerated see above) was added to the subphase twice. The sample was sealed by a glass cover slide with grease to avoid subphase evaporation, allowing for long sample observation. The lipid monolayer MAC system started to contract after a few minutes of incubation, resulting in the formation of actomyosin clusters and deformation of the lipid domains.

Acknowledgements

We are grateful for the financial support by the Daimler und Benz foundation (Project Grant PSBioc8216), the Gottfried Wilhelm Leibniz-Program of the DFG (SCHW716/8-1), the support of the Graduate School of Quantitative Biosciences Munich and the MaxSynBio consortium, which is jointly funded by the Federal Ministry of Education and Research of Germany and the Max Planck Society.

Additional information

Funding

Funder	Grant reference number	Author
Daimler und Benz Stiftung	32-09/11	Sven Kenjiro Vogel
Max-Planck-Gesellschaft		Sven Kenjiro Vogel Ferdinand Greiss Alena Khmelinskaia Petra Schwille
Bundesministerium für Bildung und Forschung		Sven Kenjiro Vogel Petra Schwille
Deutsche Forschungsgemeinschaft	SCHW716/8-1	Sven Kenjiro Vogel Petra Schwille

The funders had no role in study design, data collection and interpretation, or the decision to submit the work for publication.

Author contributions

SKV, Conceptualization, Formal analysis, Supervision, Investigation, Writing—original draft; FG, Conceptualization, Formal analysis, Investigation, Writing—original draft; AK, Investigation, Writing—review and editing; PS, Funding acquisition, Writing—review and editing

Author ORCIDs

Sven Kenjiro Vogel,  <http://orcid.org/0000-0003-2540-5947>

Petra Schuille,  <http://orcid.org/0000-0002-6106-4847>

References

- Akimov SA, Kuzmin PI, Zimmerberg J, Cohen FS. 2007. Lateral tension increases the line tension between two domains in a lipid bilayer membrane. *Physical Review E* **75**:011919. doi: [10.1103/PhysRevE.75.011919](https://doi.org/10.1103/PhysRevE.75.011919)
- Arumugam S, Petrov EP, Schuille P. 2015. Cytoskeletal pinning controls phase separation in multicomponent lipid membranes. *Biophysical Journal* **108**:1104–1113. doi: [10.1016/j.bpj.2014.12.050](https://doi.org/10.1016/j.bpj.2014.12.050), PMID: 25762322
- Backouche F, Haviv L, Groswasser D, Bernheim-Groswasser A. 2006. Active gels: dynamics of patterning and self-organization. *Physical Biology* **3**:264–273. doi: [10.1088/1478-3975/3/4/004](https://doi.org/10.1088/1478-3975/3/4/004), PMID: 17200602
- Baumgart T, Hess ST, Webb WW. 2003. Imaging coexisting fluid domains in biomembrane models coupling curvature and line tension. *Nature* **425**:821–824. doi: [10.1038/nature02013](https://doi.org/10.1038/nature02013), PMID: 14574408
- Chwastek G, Schuille P. 2013. A monolayer assay tailored to investigate lipid-protein systems. *ChemPhysChem* **14**:1877–1881. doi: [10.1002/cphc.201300035](https://doi.org/10.1002/cphc.201300035), PMID: 23606346
- Engelman DM. 2005. Membranes are more mosaic than fluid. *Nature* **438**:578–580. doi: [10.1038/nature04394](https://doi.org/10.1038/nature04394), PMID: 16319876
- García-Sáez AJ, Chiantia S, Schuille P. 2007. Effect of line tension on the lateral organization of lipid membranes. *Journal of Biological Chemistry* **282**:33537–33544. doi: [10.1074/jbc.M706162200](https://doi.org/10.1074/jbc.M706162200), PMID: 17848582
- Gowrishankar K, Ghosh S, Saha S, C R, Mayor S, Rao M. 2012. Active remodeling of cortical actin regulates spatiotemporal organization of cell surface molecules. *Cell* **149**:1353–1367. doi: [10.1016/j.cell.2012.05.008](https://doi.org/10.1016/j.cell.2012.05.008), PMID: 22682254
- Groves JT, Kuriyan J. 2010. Molecular mechanisms in signal transduction at the membrane. *Nature Structural & Molecular Biology* **17**:659–665. doi: [10.1038/nsmb.1844](https://doi.org/10.1038/nsmb.1844), PMID: 20495561
- Gudheti MV, Curthoys NM, Gould TJ, Kim D, Gunewardene MS, Gabor KA, Gosse JA, Kim CH, Zimmerberg J, Hess ST. 2013. Actin mediates the nanoscale membrane organization of the clustered membrane protein influenza hemagglutinin. *Biophysical Journal* **104**:2182–2192. doi: [10.1016/j.bpj.2013.03.054](https://doi.org/10.1016/j.bpj.2013.03.054), PMID: 23708358
- Heinemann F, Vogel SK, Schuille P. 2013. Lateral membrane diffusion modulated by a minimal actin cortex. *Biophysical Journal* **104**:1465–1475. doi: [10.1016/j.bpj.2013.02.042](https://doi.org/10.1016/j.bpj.2013.02.042), PMID: 23561523
- Honerkamp-Smith AR, Cicuta P, Collins MD, Veatch SL, den Nijs M, Schick M, Keller SL. 2008. Line tensions, correlation lengths, and critical exponents in lipid membranes near critical points. *Biophysical Journal* **95**:236–246. doi: [10.1529/biophysj.107.128421](https://doi.org/10.1529/biophysj.107.128421), PMID: 18424504
- Honigsmann A, Sadeghi S, Keller J, Hell SW, Eggeling C, Vink R. 2014. A lipid bound actin meshwork organizes liquid phase separation in model membranes. *eLife* **3**:e01671. doi: [10.7554/eLife.01671](https://doi.org/10.7554/eLife.01671), PMID: 24642407
- Köster DV, Husain K, Iljazi E, Bhat A, Bieling P, Mullins RD, Rao M, Mayor S. 2016. Actomyosin dynamics drive local membrane component organization in an in vitro active composite layer. *PNAS* **113**:E1645–E1654. doi: [10.1073/pnas.1514030113](https://doi.org/10.1073/pnas.1514030113), PMID: 26929326
- Kuzmin PI, Akimov SA, Chizmadzhev YA, Zimmerberg J, Cohen FS. 2005. Line tension and interaction energies of membrane rafts calculated from lipid splay and tilt. *Biophysical Journal* **88**:1120–1133. doi: [10.1529/biophysj.104.048223](https://doi.org/10.1529/biophysj.104.048223), PMID: 15542550
- Liu AP, Fletcher DA. 2006. Actin polymerization serves as a membrane domain switch in model lipid bilayers. *Biophysical Journal* **91**:4064–4070. doi: [10.1529/biophysj.106.090852](https://doi.org/10.1529/biophysj.106.090852), PMID: 16963509
- Luo W, Yu CH, Lieu ZZ, Allard J, Mogilner A, Sheetz MP, Bershadsky AD. 2013. Analysis of the local organization and dynamics of cellular actin networks. *The Journal of Cell Biology* **202**:1057–1073. doi: [10.1083/jcb.201210123](https://doi.org/10.1083/jcb.201210123), PMID: 24081490
- Munro E, Nance J, Priess JR. 2004. Cortical flows powered by asymmetrical contraction transport PAR proteins to establish and maintain anterior-posterior polarity in the early *C. elegans* embryo. *Developmental Cell* **7**:413–424. doi: [10.1016/j.devcel.2004.08.001](https://doi.org/10.1016/j.devcel.2004.08.001), PMID: 15363415
- Murase K, Fujiwara T, Umemura Y, Suzuki K, Iino R, Yamashita H, Saito M, Murakoshi H, Ritchie K, Kusumi A. 2004. Ultrafine membrane compartments for molecular diffusion as revealed by single molecule techniques. *Biophysical Journal* **86**:4075–4093. doi: [10.1529/biophysj.103.035717](https://doi.org/10.1529/biophysj.103.035717), PMID: 15189902
- Murrell MP, Gardel ML. 2012. F-actin buckling coordinates contractility and severing in a biomimetic actomyosin cortex. *PNAS* **109**:20820–20825. doi: [10.1073/pnas.1214753109](https://doi.org/10.1073/pnas.1214753109), PMID: 23213249
- Sheetz MP, Schindler M, Koppel DE. 1980. Lateral mobility of integral membrane proteins is increased in spherocytic erythrocytes. *Nature* **285**:510–512. doi: [10.1038/285510a0](https://doi.org/10.1038/285510a0), PMID: 7402296
- Simons K, Gerl MJ. 2010. Revitalizing membrane rafts: new tools and insights. *Nature Reviews Molecular Cell Biology* **11**:688–699. doi: [10.1038/nrm2977](https://doi.org/10.1038/nrm2977), PMID: 20861879

- Soares e Silva M, Depken M, Stuhmann B, Korsten M, MacKintosh FC, Koenderink GH. 2011. Active multistage coarsening of actin networks driven by myosin motors. *PNAS* **108**:9408–9413. doi: [10.1073/pnas.1016616108](https://doi.org/10.1073/pnas.1016616108), PMID: [21593409](https://pubmed.ncbi.nlm.nih.gov/21593409/)
- van der Walt S, Schönberger JL, Nunez-Iglesias J, Boulogne F, Warner JD, Yager N, Gouillart E, Yu T, Scikit-image contributors. 2014. scikit-image: image processing in Python. *PeerJ* **2**:e453. doi: [10.7717/peerj.453](https://doi.org/10.7717/peerj.453), PMID: [25024921](https://pubmed.ncbi.nlm.nih.gov/25024921/)
- Veatch SL, Cicuta P, Sengupta P, Honerkamp-Smith A, Holowka D, Baird B. 2008. Critical fluctuations in plasma membrane vesicles. *ACS Chemical Biology* **3**:287–293. doi: [10.1021/cb800012x](https://doi.org/10.1021/cb800012x), PMID: [18484709](https://pubmed.ncbi.nlm.nih.gov/18484709/)
- Veatch SL, Keller SL. 2003. Separation of liquid phases in giant vesicles of ternary mixtures of phospholipids and cholesterol. *Biophysical Journal* **85**:3074–3083. doi: [10.1016/S0006-3495\(03\)74726-2](https://doi.org/10.1016/S0006-3495(03)74726-2), PMID: [14581208](https://pubmed.ncbi.nlm.nih.gov/14581208/)
- Veatch SL, Keller SL. 2005. Miscibility phase diagrams of giant vesicles containing sphingomyelin. *Physical Review Letters* **94**:148101. doi: [10.1103/PhysRevLett.94.148101](https://doi.org/10.1103/PhysRevLett.94.148101), PMID: [15904115](https://pubmed.ncbi.nlm.nih.gov/15904115/)
- Veatch SL, Polozov IV, Gawrisch K, Keller SL. 2004. Liquid domains in vesicles investigated by NMR and fluorescence microscopy. *Biophysical Journal* **86**:2910–2922. doi: [10.1016/S0006-3495\(04\)74342-8](https://doi.org/10.1016/S0006-3495(04)74342-8), PMID: [15111407](https://pubmed.ncbi.nlm.nih.gov/15111407/)
- Verkhovskiy AB, Svitkina TM, Borisy GG. 1997. Polarity sorting of actin filaments in cytochalasin-treated fibroblasts. *Journal of Cell Science* **110** (Pt **15**):1693–1704. PMID: [9264457](https://pubmed.ncbi.nlm.nih.gov/9264457/)
- Vogel SK, Heinemann F, Chwastek G, Schwille P. 2013a. The design of MACs (minimal actin cortices). *Cytoskeleton* **70**:706–717. doi: [10.1002/cm.21136](https://doi.org/10.1002/cm.21136), PMID: [24039068](https://pubmed.ncbi.nlm.nih.gov/24039068/)
- Vogel SK, Petrasek Z, Heinemann F, Schwille P. 2013b. Myosin motors fragment and compact membrane-bound actin filaments. *eLife* **2**:e00116. doi: [10.7554/eLife.00116](https://doi.org/10.7554/eLife.00116), PMID: [23326639](https://pubmed.ncbi.nlm.nih.gov/23326639/)
- Vogel SK. 2016. Reconstitution of a minimal actin cortex by coupling Actin Filaments to Reconstituted Membranes. *Methods in Molecular Biology* **1365**:213–223. doi: [10.1007/978-1-4939-3124-8_11](https://doi.org/10.1007/978-1-4939-3124-8_11), PMID: [26498787](https://pubmed.ncbi.nlm.nih.gov/26498787/)
- Yang ST, Kiessling V, Tamm LK. 2016. Line tension at lipid phase boundaries as driving force for HIV fusion peptide-mediated fusion. *Nature Communications* **7**:11401. doi: [10.1038/ncomms11401](https://doi.org/10.1038/ncomms11401), PMID: [27113279](https://pubmed.ncbi.nlm.nih.gov/27113279/)

B

APPENDIX TO III.1

These results have been published as supplementary information to III.1:

Khmelinskaia, A., Franquelim, H. G., Petrov, E. P., Schwille, P. (2016) Effect of anchor positioning on binding and diffusion of elongated 3D DNA nanostructures on lipid membranes. J. Phys. D Appl. Phys., 49: 194001. doi:10.1088/0022-3727/49/19/194001. A reprint permission has been granted by the publisher.

Supporting Information

Effect of anchor positioning on binding and diffusion of elongated 3D DNA nanostructures on lipid membranes

Alena Khmelinskaia, Henri G Franquelim*, Eugene P Petrov, Petra Schwille*

TABLE OF CONTENTS:

Figure S1

Figure S2

Figure S3

Figure S4

Figure S5

Figure S6

Table S1

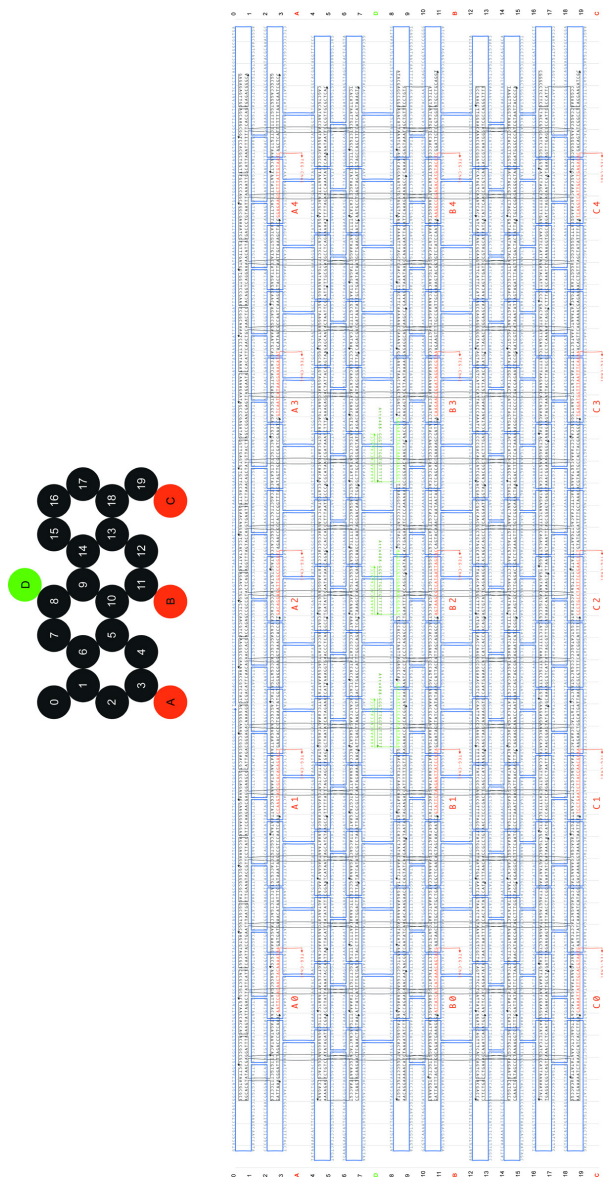


Figure S1. Design and oligonucleotide sequences of the elongated amphipathic 20-helix bundle DNA origami. The Atto488-modified and connector oligonucleotides needed for fluorescence detection are marked in green; the 15 possible positions with cholesteryl anchors for lipid membrane binding are marked in orange and labelled (A0-4, B0-4, C0-4); core staples are coloured in black; M13 p7249 scaffold is coloured in blue.

S1

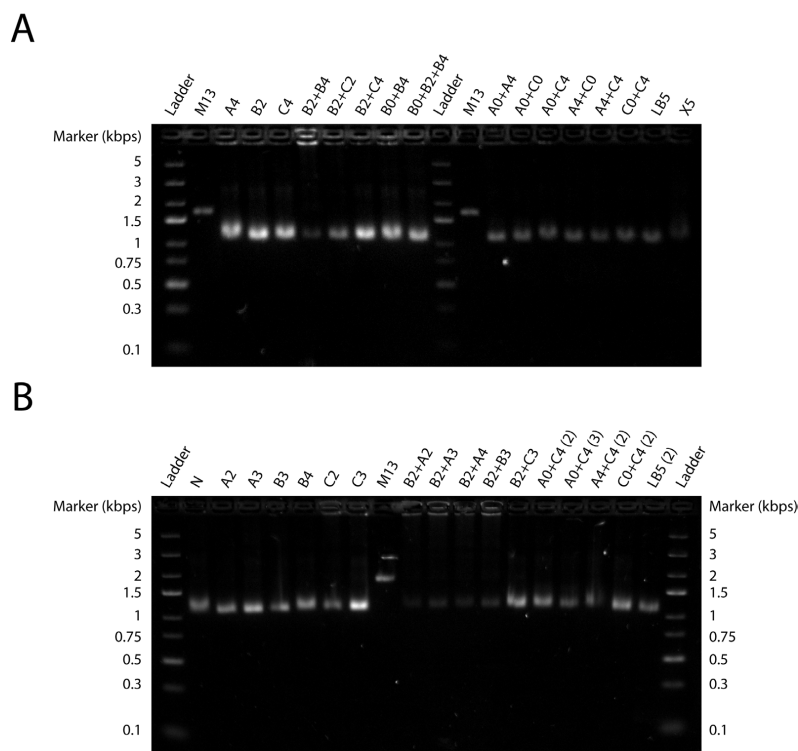


Figure S2. Agarose gel analysis of the folded and purified elongated 20-helix bundles DNA origami containing all the investigated combinations of positions with chol-TEG anchors. Different lanes in gels (A) and (B) correspond to the origami structures with chol-TEG anchors at defined positions, according to the naming. Special nomenclature was given to the lanes N (no anchor), LB5 (B0+B1+B2+B3+B4) and X5 (A0+A4+B2+C0+C4). Numbers in brackets correspond to new batches of the same samples. Lanes containing marker DNA ladder and M13 single-stranded p7249 scaffold were also included.

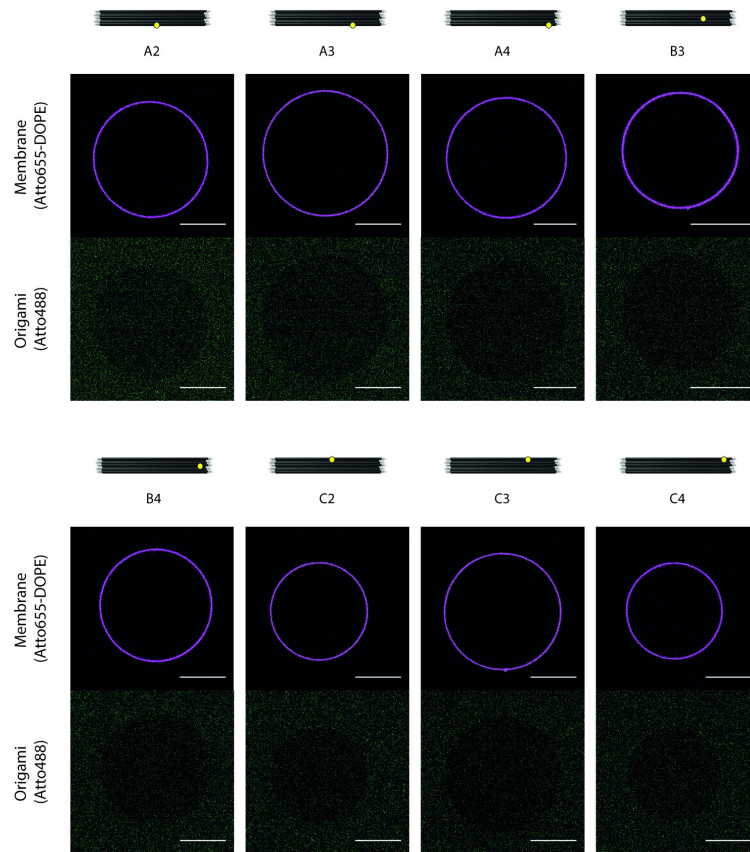


Figure S3. Membrane binding of the 20-helix bundle DNA origami structures with one chol-TEG anchor. Representative fluorescence e confocal images of DOPC giant unilamellar vesicles (GUVs) at the equatorial plane incubated with 1 nM DNA origami containing one chol-TEG anchor at positions A2, A3, A4, B3, B4, C2, C3 and C4. GUVs contained 0.005 mol% Atto655-DOPE (violet colour) for fluorescence detection; while each origami structure had 3× Atto488 dyes (green colour). Scale bar: 20 μm.

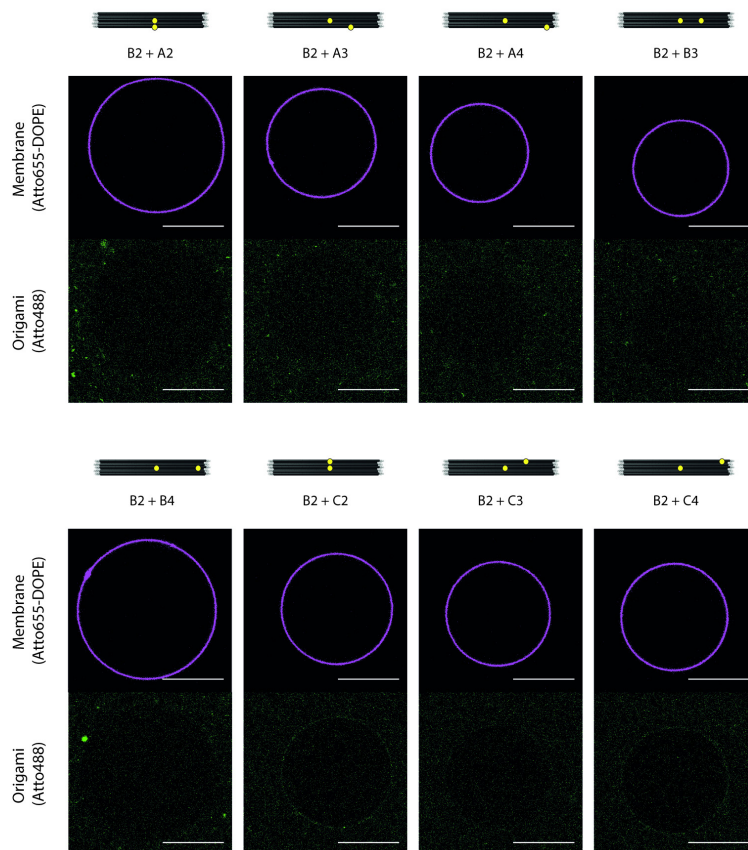


Figure S4. Membrane binding of the 20-helix bundle DNA origami structures with two chol-TEG anchors, one always fixed at the central B2 position. Representative fluorescence confocal images of DOPC GUVs at the equatorial plane incubated with 1 nM DNA origami containing one chol-TEG anchor at positions B2+A2, B2+A3, B2+A4, B2+B3, B2+B4, B2+C2, B2+C3 and B2+C4. GUVs contained 0.005 mol% Atto655-DOPE (violet colour) for fluorescence detection; while each origami structure had 3× Atto488 dyes (green colour). Scale bar: 20 μm .

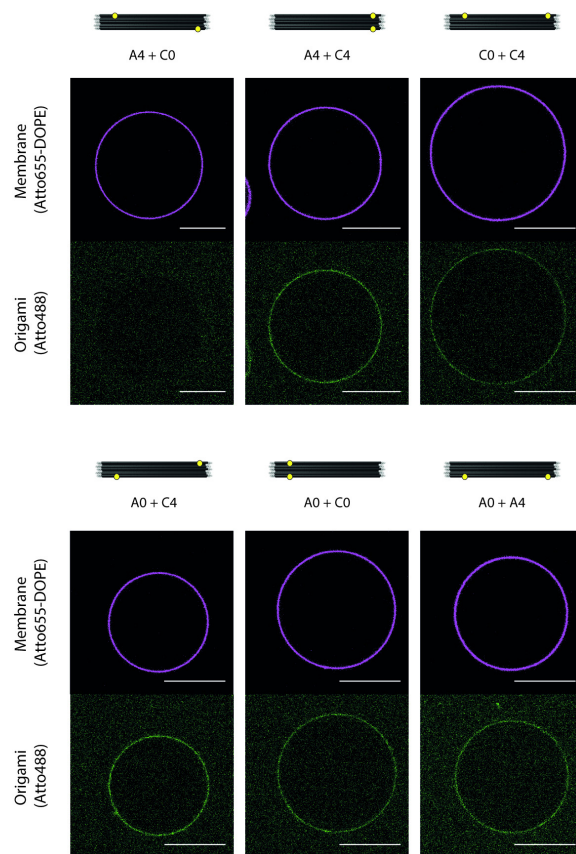


Figure S5. Membrane binding of the 20-helix bundle DNA origami structures with two chol-TEG anchors near the corners. Representative fluorescence confocal images of DOPC GUVs at the equatorial plane incubated with 1 nM DNA origami containing one chol-TEG anchor at positions A4+C0, A4+C4, C0+C4, A0+C4, A0+C0 and A0+A4. GUVs contained 0.005 mol% Atto655-DOPE (violet colour) for fluorescence detection; while each origami structure had 3× Atto488 dyes (green colour). Scale bar: 20 μm.

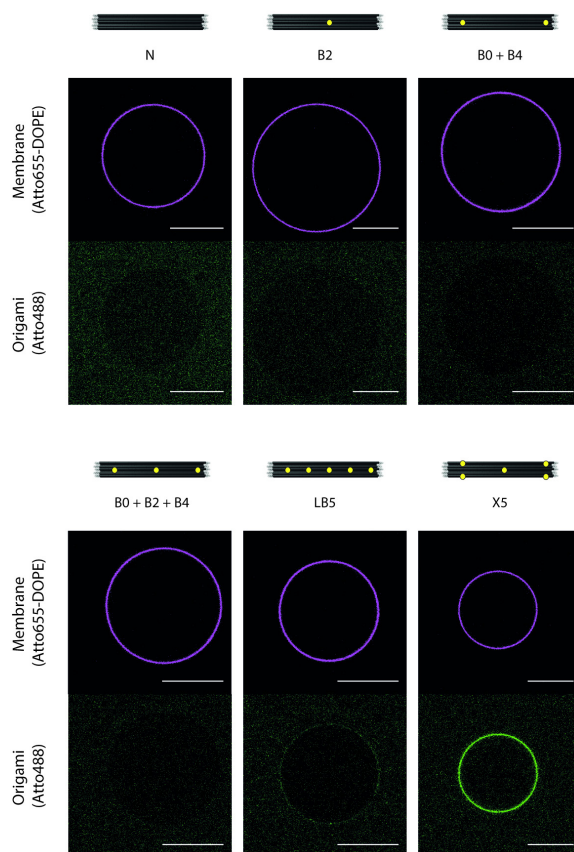


Figure S6. Membrane binding of the 20-helix bundle DNA origami structures with multiple combinations of chol-TEG anchor positioning. Representative fluorescence confocal images of DOPC GUVs at the equatorial plane incubated with 1 nM DNA origami containing no chol-TEG anchor (structure N), one chol-TEG anchor at the central B2 position, two (B0+B4), three (B0+B2+B4) or five (LB5: B0+B1+B2+B3+B4) chol-TEG anchors on helix B, and finally five chol-TEG anchors in a crossed conformation (X5: A0+A4+B2+C0+C4). GUVs contained 0.005 mol% Atto655-DOPE (violet colour) for fluorescence detection; while each origami structure had 3× Atto488 dyes (green colour). Scale bar: 20 μm .

Table S1. Relative diffusion coefficients of Atto655-DOPE in freestanding DOPC GUVs determined using FCS. Values correspond to the average diffusion calculated from measurements on n GUVs in the presence of membrane-bound DNA origami at $\rho > 0.2$, and were further normalized with respect to the diffusion coefficient of Atto655-DOPE obtained in the absence of origami ($\tau_D = 1.49 \pm 0.04$ ms, $n = 7$). Error values represent the standard error of the mean.

Membrane-bound origami	Lipid relative diffusion coefficient	Number of GUVs
A0 + C4	1.00 ± 0.04	7
A4 + C4	1.01 ± 0.04	5
C0 + C4	0.99 ± 0.12	5
X5	0.96 ± 0.05	4

C

APPENDIX TO III.2

These results have been published as supplementary information to III.2.

Khmelinskaia, A., Mücksch, J., Petrov, E. P., Franquelim, H. G., Schwille, P. (2018) Control of membrane binding and diffusion of cholesteryl-modified DNA origami nanostructures by DNA spacers. Langmuir: doi: 10.1021/acs.langmuir.8b01850. A reprint permission has been granted by the publisher.

Supporting Information

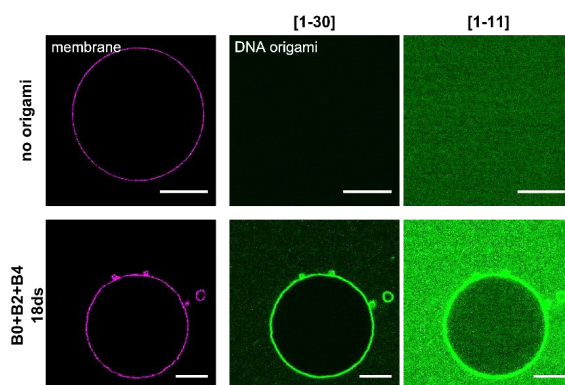
Control of membrane binding and diffusion of
cholesteryl-modified DNA origami nanostructures
by DNA spacers

Alena Khmelinskaia¹, Jonas Mücksch¹, Eugene P. Petrov^{1,2}, Henri G. Franquelin¹, Petra Schwille^{1}*

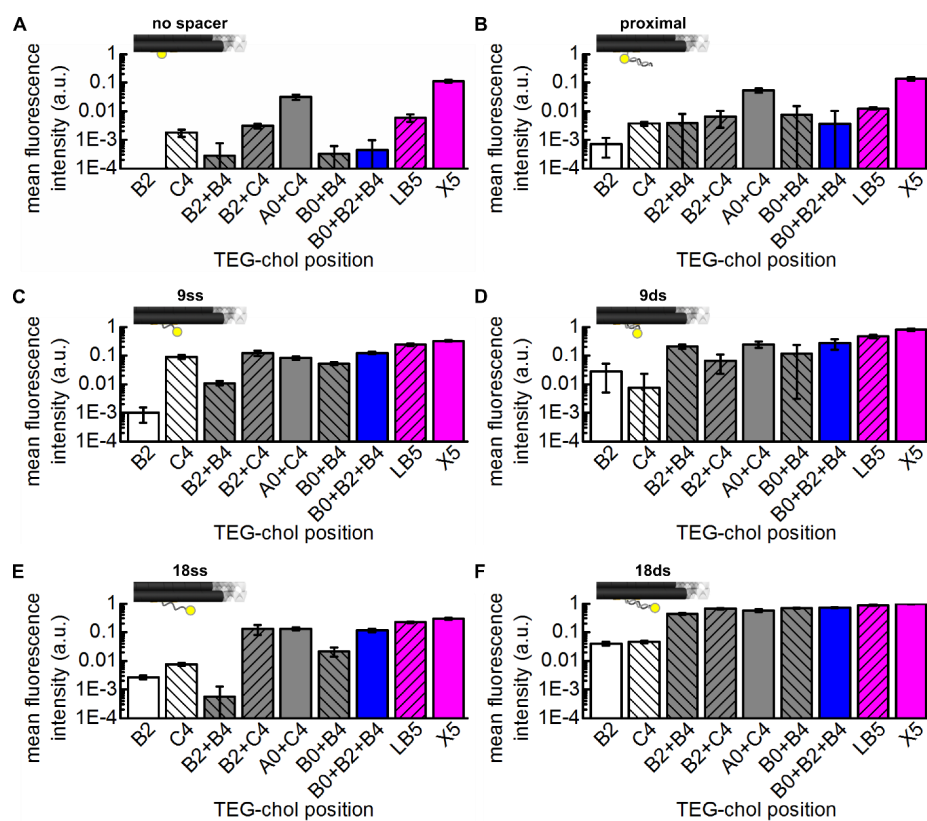
¹ Max Planck Institute of Biochemistry, Am Klopferspitz 18, 82152 Martinsried, Germany

² Faculty of Physics, Ludwig Maximilian University, Geschwister-Scholl-Platz 1, 80539 Munich, Germany



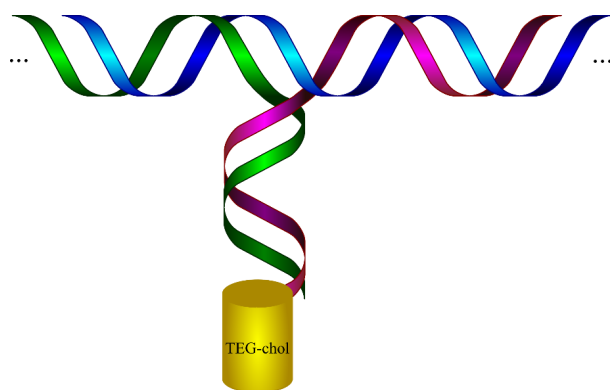


Supplementary Figure 1: DOPC GUVs are not permeable to DNA origami nanostructures. Atto655-DOPE labeled GUVs were incubated overnight without and with 24nM of B0+B2+B4 (18ds DNA spacer) DNA nanostructures labeled with three Alexa488 dyes. The DNA origami channel is displayed at two different ranges for comparison. A large fluorescence intensity difference between the outside and inside of the GUVs was observed, indicative of the GUV impermeability to DNA origami nanostructures. Indeed, the average signal measured by FCS inside of the GUV was similar to that of the background value in absence of DNA nanostructures (0.6 kHz and 0.2 kHz, respectively), while the signal in solution was much larger (5.6 kHz).

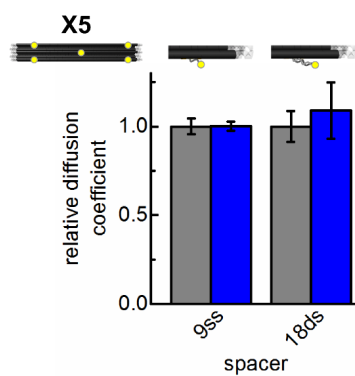


Supporting Figure 2. Mean fluorescence intensities of DNA nanostructures at the surface of DOPC GUVs for several combinations of TEG-chol anchors attached to the DNA nanostructures using distinct TEG-chol anchors: no spacer (A); 9 and 18 nucleotide-long extension of the directly inserted cholesteryl-modified oligonucleotide (9ss, C and 18ss, E, respectively); proximal positioning of the TEG-chol moieties upon hybridization of the modified DNA strand with the complementary 18 nucleotide-long extension (proximal, B); hybridization of the 9 nucleotide extended cholesteryl-modified nucleotides with the neighboring oligonucleotide extended with a complementary sequence (9ds, D); distal positioning of the TEG-chol anchor upon hybridization

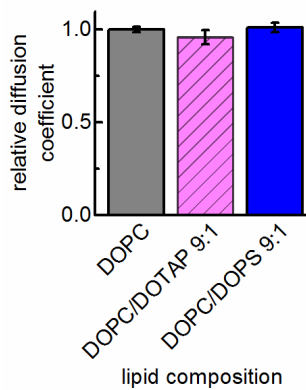
of the modified DNA strand with the complementary 18 nucleotide-long extension (18ds, F). Note that the intensity axis in the plots are in logarithmic scale and mean intensities were normalized in relation to X5 modified using 18bp dsDNA spacers. The plots with linear scale can be found in SA Figure 1. Error bars correspond to the standard deviation of typically 15-30 GUVs. The significance analysis of the data is summarized in SA Tables 1-3.



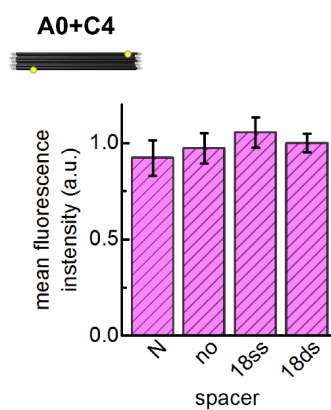
Supporting Figure 3. Schematic representation of the assembly-scheme of the 9ds TEG-chol anchor. The cholesteryl-modified oligonucleotide (magenta) at the location of interest (0-4 at helix A-C, Figure 1) hybridizes with the neighboring oligonucleotide (green), extended with the complementary sequence of 9 nucleotides. The blue strand corresponds to the scaffold strand (M13 nucleotide). The sequences used for the assembly are listed in the Supplementary Table 1.



Supporting Figure 4. Relative diffusion coefficient of TEG-chol-modified DNA nanostructures X5 using 9ss and 18ds DNA spacers. Two different membranes are compared: pure DOPC GUVs (grey) and containing 10 mol% DOPS (blue). Data sets were normalized to the diffusion coefficient of the nanostructure on DOPC GUVs. Error bars correspond to the standard deviation of 3-6 GUVs. The significance analysis of the data is summarized in SA Tables 10,11.



Supporting Figure 5. Relative diffusion coefficients of Atto655-DOPE in freestanding DOPC, DOPC/DOTAP 9:1 and DOPC/DOPS 9:1 GUVs determined using FCS. Values correspond to the average of 3 GUVs and were normalized with respect to the diffusion coefficient of Atto655-DOPE obtained in DOPC GUVs ($D = 12.4 \pm 0.2 \mu\text{m}^2/\text{s}$). Error values represent the standard error of the mean. The significance analysis of the data is summarized in SA Tables 12.



Supporting Figure 6. Mean fluorescence intensities at the membrane surface for A0 + C4 DNA nanostructures bound to DOPC/DOTAP 9:1 GUVs. DNA nanostructures modified using three different linkage strategies (no spacer, 18ss and 18ds DNA spacers) are compared. Bare DNA nanostructure N is shown for reference. All values are normalized to the fluorescence intensity of DNA nanostructures modified using 18ds spacers. Error bars correspond to the standard deviation of typically 30 GUVs. The significance analysis of the data is summarized in SA Tables 13,14.

Supporting Table 1. List of oligonucleotide sequences used as extensions or complementary to the extensions at locations A0-4, B0-4 and C0-4 in order to assemble each type of TEG-chol anchor (Figure 1).

Denomination	Extension/oligonucleotide sequence	TEG-chol modification	DNA spacer assembly
3'chol		3'	<u>no spacer</u>
9c (neighboring oligonucleotide)	AACCAGACC	no	<u>9ds</u> , when in combination with 3'chol(9) at the modification site
e18	GCTATGGGTGGTCTGGTT	no	<u>18ds</u> , when in combination with 5'chol(18) <u>proximal</u> , when in combination with 3'chol(18)d
3'chol(9)	GGTCTGGTT	3'	<u>9ss</u> <u>9ds</u> , in combination with 9c in the neighboring oligonucleotide
3'chol(18)s	GCTATGGGTGGTCTGGTT	3'	<u>18ss</u>
3'chol(18)d	AACCAGACCACCCATAGC	3'	<u>proximal</u> , when in combination with e18
5'chol(18)	AACCAGACCACCCATAGC	5'	<u>18ds</u> , when in combination with e18

D

APPENDIX TO III.3

These results have been published as supplementary information to III.3:

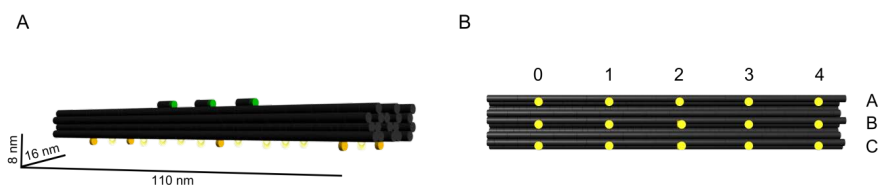
Khmelinskaia, A., Mücksch, J.*, Conci, F., Chwastek, G., Schwille, P. (2018) FCS analysis of protein mobility on lipid monolayers. Biophys. J., 114: 2444-2454. doi: 10.1016/j.bpj.2018.02.031, *indicates equal contributions. A reprint permission has been granted by the publisher.*

Biophysical Journal, Volume 114

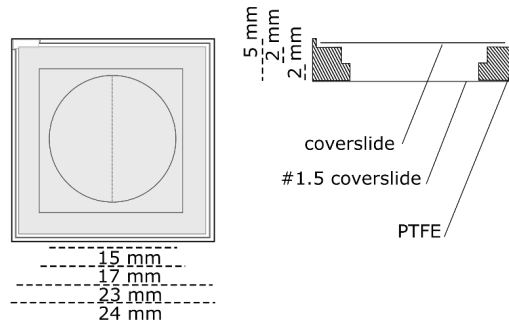
Supplemental Information

FCS Analysis of Protein Mobility on Lipid Monolayers

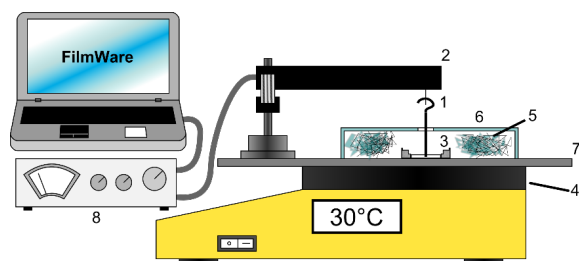
Alena Khmelinskaia, Jonas Mücksch, Franco Conci, Grzegorz Chwastek, and Petra Schwill



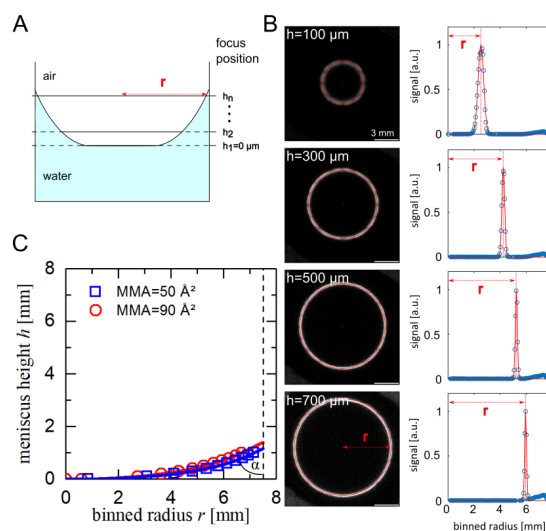
Supporting Figure S1: Schematic representation of the used flat 3D DNA nanostructure [Khmelinskaia et al. 2016]. A) 3D representation and predicted dimensions (8 nm × 16 nm × 110 nm) of the DNA origami nanostructures. The structures under investigation have three Atto488-modified oligonucleotides at the top facet for fluorescence detection and a maximum of five cholesteryl anchors at the bottom facet for membrane anchoring. B) Localization of the 15 possible sites (marked with pale circles) for the attachment of cholesterol (Chol)-modified oligonucleotides at the bottom facet of the DNA origami. Five positions (numbered 0–4) were spaced along three different helices of the origami (named A–C). For structure N, none of these positions were used. For structure X5, positions A0+A4+B2+C0+C4 were extended for the attachment of Chol-modified oligonucleotides (see Materials and Methods).



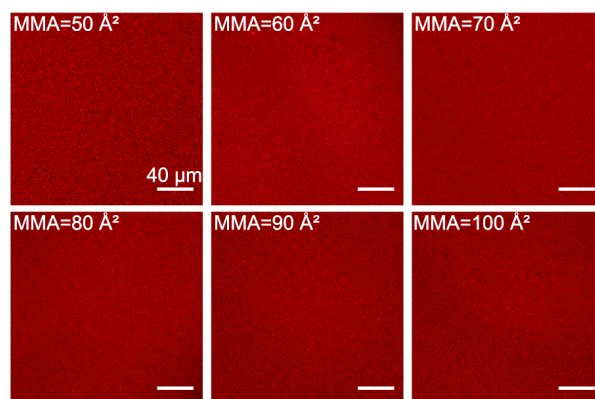
Supporting Figure S2: Miniaturized chamber schematics.



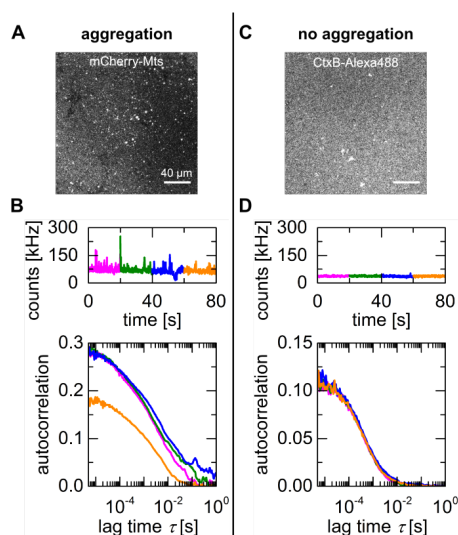
Supporting Figure S3: Schematic representation of surface pressure measurements in miniaturized chambers. A dyne probe (1) connected to a micro-balance (2) is calibrated in a miniaturized chamber (3) filled with aqueous buffer. To grant the probe access to the water surface, the miniaturized chamber is not sealed. The monolayers surface pressure is measured after chloroform evaporation upon lipid deposition at the air-water interface (see Materials and Methods, Figure 1A). When measuring at 30°C, the miniaturized chamber is placed on a heating plate (4). Aqueous subphase evaporation is minimized by surrounding the miniaturized chamber with paper tissue soaked in water (5). Additionally, the miniaturized chamber is physically isolated by an inverted petri dish (6) glued to the metal support (7). The probe can reach the water surface through a small hole in the petri dish. A Kybron interface (8) outputs the monolayers surface pressure and can be controlled by FilmWare software.



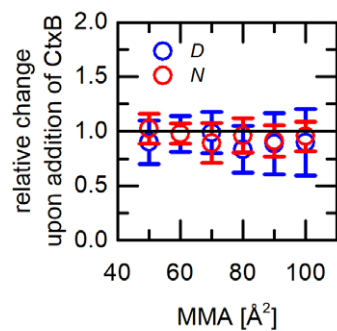
Supporting Figure S4: Estimation of the monolayer area. A) Schematic of the air-water interface, on which monolayers of defined MMA are deposited and are imaged with different nominal focus positions h . B) Confocal sections of the interface yield circles. The corresponding radii are determined by image processing. C) Resulting radial dependence of the interface position. The effective area is obtained by numerical integration of the determined profile. The dashed line corresponds to the physical radius of the miniaturized chamber $R=7.5$ mm. The meniscus area was measured on four independent monolayers of $90 \text{ \AA}^2/\text{molecule}$ on different days. The interface area was $(4\pm 1)\%$ larger than the area of the chamber, which is given as πR^2 . The corresponding contact angle α is estimated as $(72\pm 5)^\circ$. An MMA of 50 \AA^2 yields a similar meniscus shape.



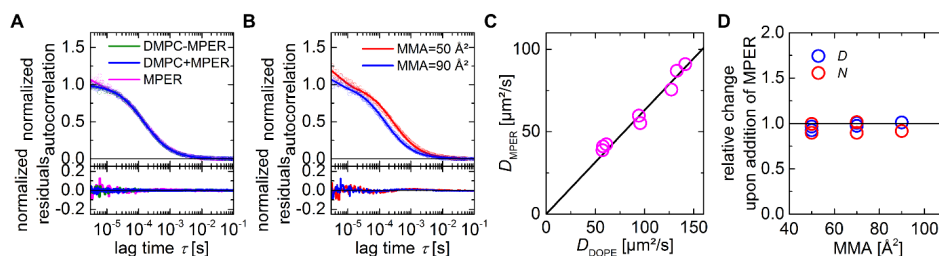
Supporting Figure S5: DMPC monolayers are homogeneous in the range from 50 to 100 Å²/molecule at 30°C. Confocal microscopy images of DMPC monolayers (0.01 mol% DOPE-Atto655) deposited in fixed-area miniaturized chambers at MMAs ranging from 50 to 100 Å²/molecule show homogeneous distributions. The scale bar corresponds to 40 μm.



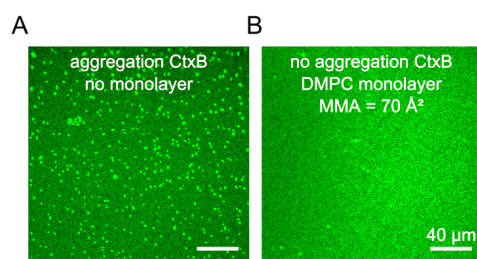
Supporting Figure S6: Homogeneously distributed molecules at the monolayer interface are critical for point FCS. A) Representative confocal fluorescence microscopy image of mCherry-MTS (chimeric fluorescent protein mCherry carrying the membrane targeting sequence (MTS) of the protein Min D from *Bacillus subtilis*) aggregation at the interface of a DMPC monolayer at 70 Å²/molecule. B) Corresponding fluorescence intensity traces (upper panel) and autocorrelation curves (lower panel) obtained by point FCS from the sample shown in A. The intensity traces show spikes originating from bright aggregates passing through the confocal volume, which manifest themselves in a large variation of autocorrelation curves and much slower decay times than expected for monomers. Notably, the sensitivity of FCS to aggregates renders it a suitable method to detect even small aggregates of only a few monomers. C) Representative confocal fluorescence microscopy image of the homogeneous binding of the model protein cholera toxin β (CtxB) labeled with Alexa488 to DMPC lipid monolayers at 70 Å²/molecule. D) The fluorescence intensity traces (upper panel) and autocorrelation curves (lower panel) obtained by point FCS from the samples shown in C are well reproducible.



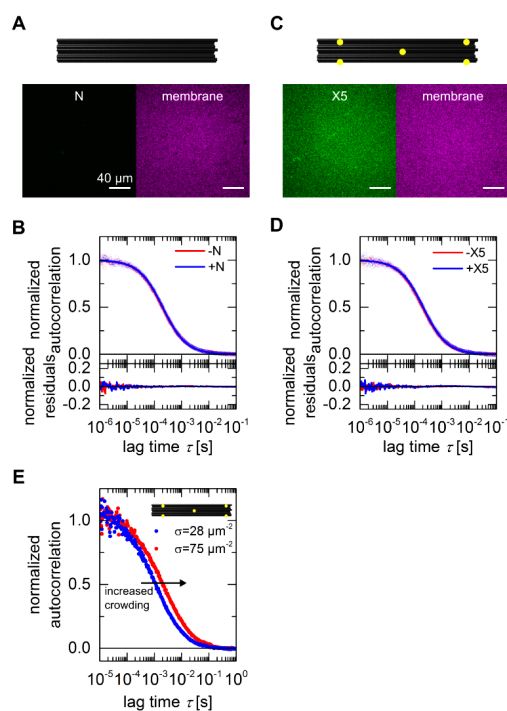
Supporting Figure S7: The addition of 10 nM CtxB to lipid monolayers does not change the monolayer properties. Relative change upon addition of CtxB of the number of particles N (red) and diffusion coefficient D (blue) obtained from autocorrelation functions for DMPC monolayers deposited at different MMAs in fixed-area chambers



Supporting Figure S8: Interaction of the membrane proximal external region (MPER) of the envelope glycoprotein gp41 of HIV-1 with DMPC lipid monolayers analyzed by point FCS. A) Autocorrelation curves obtained by point FCS for a DMPC monolayer at $70 \text{ \AA}^2/\text{molecule}$, before (green) and after (blue) addition of 10 nM MPER-Alexa488, and for the peptide MPER-Alexa488 (magenta). Fits with single component diffusion model and respective residuals are shown. B) Autocorrelation curves obtained for MPER-Alexa488 (10 nM) bound to DMPC monolayers at 90 (blue) and 50 (red) $\text{\AA}^2/\text{molecule}$. Fits with single diffusional component and respective residuals are shown. C) Lipid diffusion influence on MPER-Alexa488 diffusion in pure DMPC. The relation between the diffusion coefficients is linear (black line). D) Relative change upon addition of 10 nM MPER-Alexa488 of the number of particles N (red) and diffusion coefficient D (blue) obtained from autocorrelation functions for DMPC monolayers deposited at different MMAs in fixed-area chambers.



Supporting Figure S9: Lipids deposited at air-water interface can passivate the hydrophobic interface. A) Confocal microscopy image of CtxB (Alexa488) clusters at a clean air-water interface. B) Confocal microscopy image of homogeneously distributed CtxB (Alexa488) on a low density DMPC monolayer ($70 \text{ \AA}^2/\text{molecule}$). The scale bar corresponds to $40 \text{ }\mu\text{m}$.



Supporting Figure S10: Interaction of a flat 3D DNA nanostructure with DMPC lipid monolayers analyzed by point FCS. A,C) Confocal microscopy images of bare nanostructure N (500 pM) and nanostructure X5 modified with 5 cholesteryl anchors (200 pM), respectively, interacting with DMPC monolayers (0.01 mol% DOPE-ATTO655) at 70 $\text{\AA}^2/\text{molecule}$. B,D) Autocorrelation curves obtained by point FCS for a DMPC monolayer at 70 $\text{\AA}^2/\text{molecule}$, before (red) and after (blue) addition of nanostructure N (500 pM) and nanostructure X5 (200 pM). Fits with single diffusional component and respective residuals are shown. E) Autocorrelation curves obtained for nanostructure X5 with different densities σ on a DMPC monolayer at 70 $\text{\AA}^2/\text{molecule}$. The densities were estimated based on the amplitude of the autocorrelation function and the size of the confocal volume.

Supporting Table S1: Biomolecules tested on lipid monolayers. The binding of molecules to lipid monolayers through head-group specific interaction or the insertion of a hydrophobic moiety was tested by confocal microscopy. The protein distribution was considered homogeneous when the sample quality allowed for good FCS measurements. Otherwise, proteins that formed aggregates at the interface (here marked as X) were discarded.

Biomolecule	Nature of membrane binding	Lipid monolayer/air interface distribution
6xHis-mCherry	head-group	X
6xHis-mNeonGreen	head-group	X
(HIV) MPER	hydrophobic moiety	homogeneous
(<i>E. coli</i>) Mts (MreB)-mCherry	hydrophobic moiety	X
(<i>B. Subtilis</i>) mCherry-Mts (MinD)	hydrophobic moiety	X
(<i>E. coli</i>) mCherry-Mts (MinD)	hydrophobic moiety	X
(<i>E. coli</i>) mCherry-MinD	hydrophobic moiety	X
(<i>E. coli</i>) eGFP-MinD	hydrophobic moiety	X
(<i>E. coli</i>) MinD LD650	hydrophobic moiety	X
(<i>M. musculus</i>) 6xHis-VCA (NWASP) Alexa488	head-group	homogeneous
(<i>M. musculus</i>) 10xHis-VCA (NWASP) Alexa488	head-group	X
(<i>M. musculus</i>) miniNWASP-GFP	head-group	X
CtxB Alexa488	head-group	homogeneous
Origami Alexa488	hydrophobic moiety	homogeneous

Legend: X indicates considerable aggregation of the biomolecule at the lipid monolayers interface, hindering the performance of FCS measurements

Supporting Table S2: Dependence of the diffusion coefficient of DOPE-ATTO655 on the MMA of monolayers of different composition. The diffusion coefficient of DOPE-ATTO655 is linearly proportional to the MMA (Figure 2D): $D=m \times \text{MMA}+n$. The critical area a_c corresponds to the tightest packing of lipids in the monolayer and is estimated by extrapolation of the dependence of the diffusion coefficient vs. MMA to $D=0 \mu\text{m}^2/\text{s}$ (Figure 2D). The small content of G_{M1} used does not significantly alter the monolayer properties, as here illustrated by a_c .

Monolayer composition	$m \times 10^{-8}$ [1/s]	n [$\mu\text{m}^2/\text{s}$]	critical area a_c [$\text{\AA}^2/\text{molecule}$]
DMPC	1.5 \pm 0.1	-50.1 \pm 11.2	33.0 \pm 8.0
DMPC + 2 mol% G_{M1}	1.5 \pm 0.1	-45.8 \pm 10.0	31.4 \pm 7.4
DMPC + 5 mol% G_{M1}	1.2 \pm 0.1	-28.9 \pm 5.2	24.3 \pm 4.6

Supporting Table S3: Linear relation between the diffusion coefficients of lipids and CtxB and MPER. The diffusion coefficient of CtxB (Figure 3C) and MPER (Supporting Figure 11C) were linearly related to the lipid diffusion of DOPE-ATTO655 by a linear fit through the origin: $D_{\text{CtxB/MPER}} = m \times D_{\text{DOPE}}$. These results can be directly related to the MMA of DMPC through Supporting Table S2.

CtxB	<i>m</i>
DMPC	0.47±0.02
DMPC + 2 mol% G _{M1}	0.42±0.01
DMPC + 5 mol% G _{M1}	0.45±0.01

MPER	<i>m</i>
DMPC	0.63±0.01

E

APPENDIX TO IV

E Materials and Methods

E.1 DNA origami folding and purification

DNA origami nanostructures AR1, AR7 and AR22, consisting of a 52-, 20- and 12-helix bundle respectively, with hexagonal lattice based on the M13mp18 7429-nucleotide long scaffold plasmid (p7429), were designed using CaDNAno [Douglas et al., 2009b] (Figures IV.1 and E.1-E.3). High purity salt free (HPSF) purified staple oligonucleotides needed for origami folding were purchased from Eurofins MWG Operon (Ebersberg, Germany), and single-stranded M13mp18 scaffold DNA was supplied by Bayou Biolabs (Metairie, LA, USA). DNA origami nanostructures were folded and purified in FOB buffer containing 5 mM Tris-HCl, 1 mM EDTA, 20 mM MgCl₂, pH 8.0 as previously described (see III.1 and V.1).

E.2 Transmission electron microscopy (TEM)

To confirm the folding of the DNA origami nanostructures, negative-stain TEM imaging was performed on a CM120 BioTWIN (FEI/Philipds, Hillsboro, Oregon, USA) TEM , with a LaB6 filament operated at 120 kV. Images were recorded with a MegaView III camera (Soft Imaging System GmbH, Münster, Germany). Typically, 3 μ L of folded, purified and diluted (1/10 in FOB buffer) DNA origami nanostructures were adsorbed on glow-discharged formvar-supported carbon coated Cu300 grids (Plano GmbH, Wetzlar, Germany) and stained using a 2% aqueous uranyl formate solution containing 25 mM sodium hydroxide. Further image analysis was performed using the ImageJ software (<http://rsb.info.nih.gov/ij/>) [Schindelin et al., 2015].

E.3 Agarose gel electrophoresis

The folding quality of the DNA origami nanostructures AR1, AR7 and AR22 was investigated through agarose gel (Figure IV.1), as previously described (see III.1).

E.4 Supported lipid bilayer (SLB) preparation

1,2-distearoyl-*sn*-glycero-3-phosphocholine (DSPC), 1,2-dioleoyl-*sn*-glycero-3-phosphocholine (DOPC) and cholesterol (Chol) were purchased from Avanti Polar Lipids (Alabaster, AL, USA). Pure DSPC and phase separated DOPC/DSPC/Chol (2:2:1) [Feigenson, 2006] SLBs were obtained via fusion of small unilamellar vesicles (SUVs) deposited in FOB buffer on top of freshly cleaved mica, following the general protocol described elsewhere [Chiantia et al., 2005].

E.5 High speed atomic force microscopy (HSAFM)

Different volumes of solutions of purified DNA nanostructures were deposited on freshly cleaved mica or SLBs of defined composition (DSPC or DSPC/DOPC/Chol (2:2:1)). In FOB buffer, DNA nanostructures are completely immobilized on mica while freely diffusing on SLBs. To allow the diffusion of DNA nanostructures on mica, FOB buffer was doped with NaCl to reach 10:1 proportionality relatively to MgCl₂ [Aghebat Rafat et al., 2014, Woo and Rothmund, 2014], with a final buffer composition 5 mM Tris-HCl, 1 mM EDTA, 16 mM MgCl₂, 150 mM NaCl, pH 8.0. HSAFM in tapping mode was performed with the Nanowizard Ultra head, using USC-F0.3-k0.3 ultra-short cantilevers from Nanoworld (Neuchâtel, Switzerland) with typical stiffness of 0.3 N/m. The cantilever oscillation was tuned to a frequency of 100-150 kHz and the amplitude kept below 10 nm. Scan rate was set to 25-150 Hz. Images were acquired with a typical 256×256 pixel resolution. All measurements were performed at room temperature (20 °C). The force applied on the sample was minimized by continuously adjusting the set point and gain during imaging. Height, error, deflection and phase-shift signals were recorded and images were line-fitted as required. Data was analyzed using JPK data processing software Version 5.1.4 (JPK Instruments) and ImageJ (<http://rsb.info.nih.gov/ij/>) [Schindelin et al., 2015].

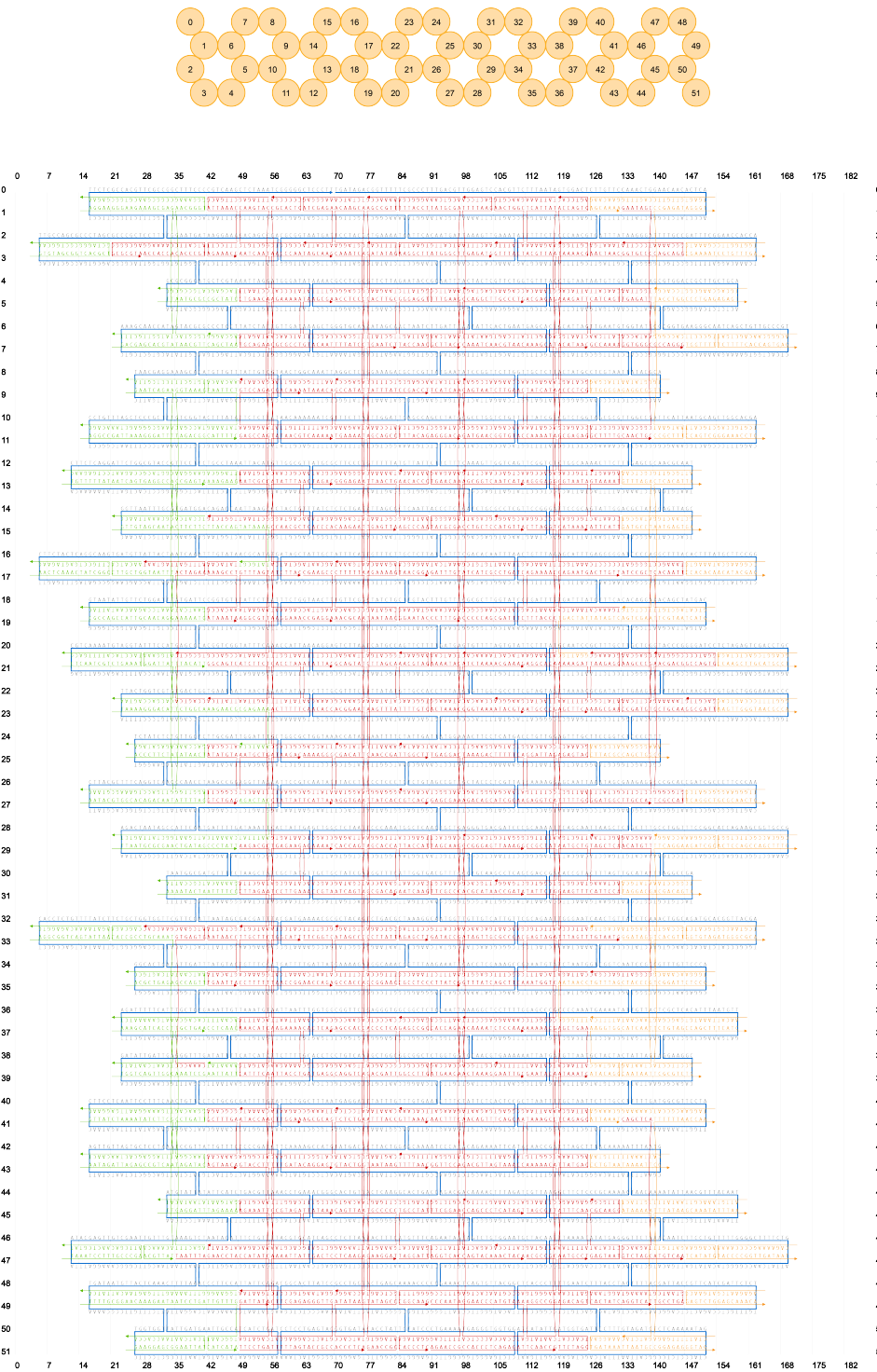


Figure E.1: Cadnano design and oligonucleotide sequences of the DNA origami structure AR1. The cross-section of the structure is shown above the Cadnano map. Lateral staples are coloured in green (left) and orange (right) while core staples are coloured in red; M13 p7249 scaffold is coloured in blue.

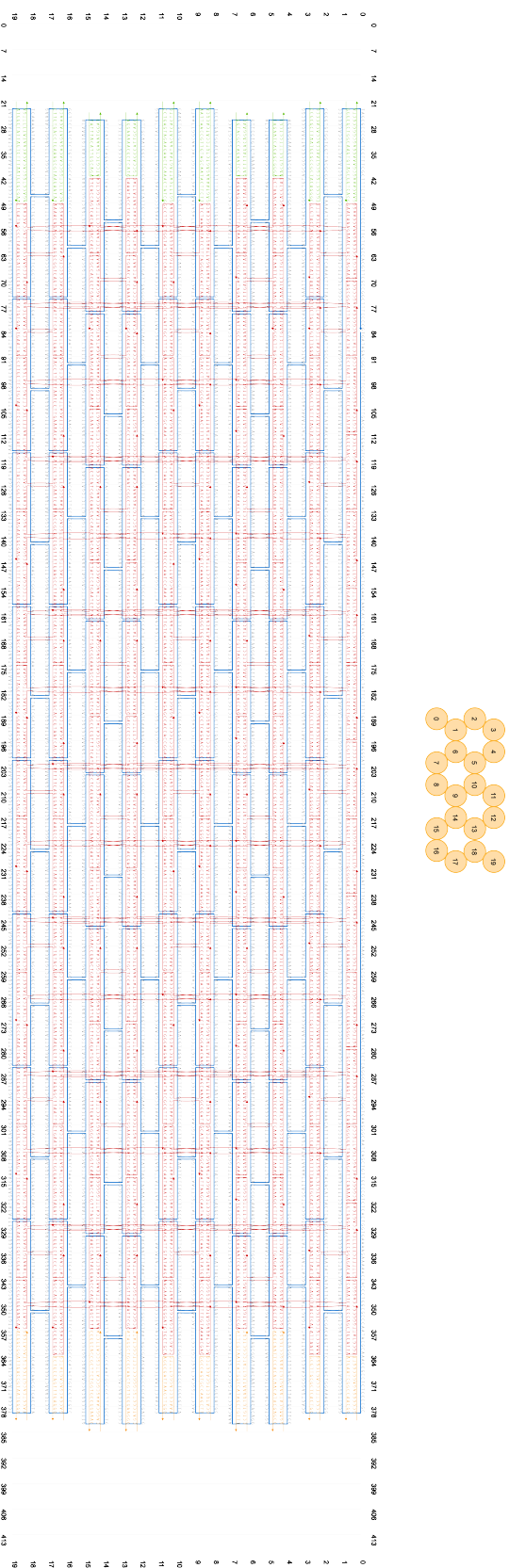


Figure E.2: Cadnano design and oligonucleotide sequences of the DNA origami structure AR7. The cross-section of the structure is shown above the Cadnano map. Lateral staples are coloured in green (left) and orange (right) while core staples are coloured in red; MI3 p7249 scaffold is coloured in blue.

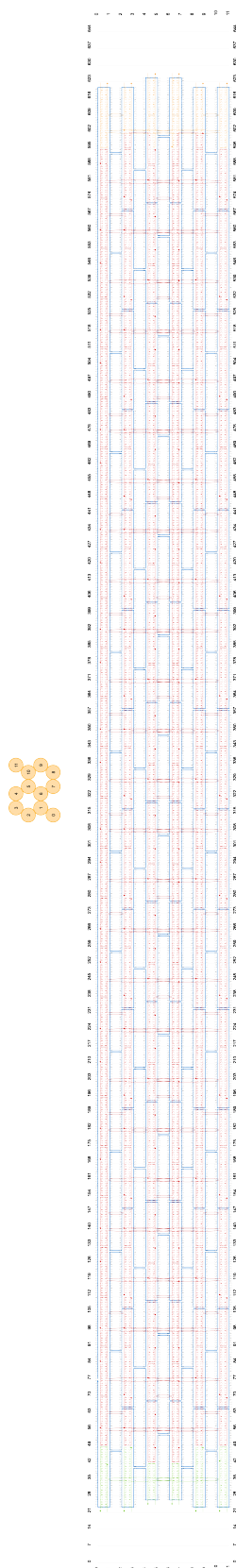


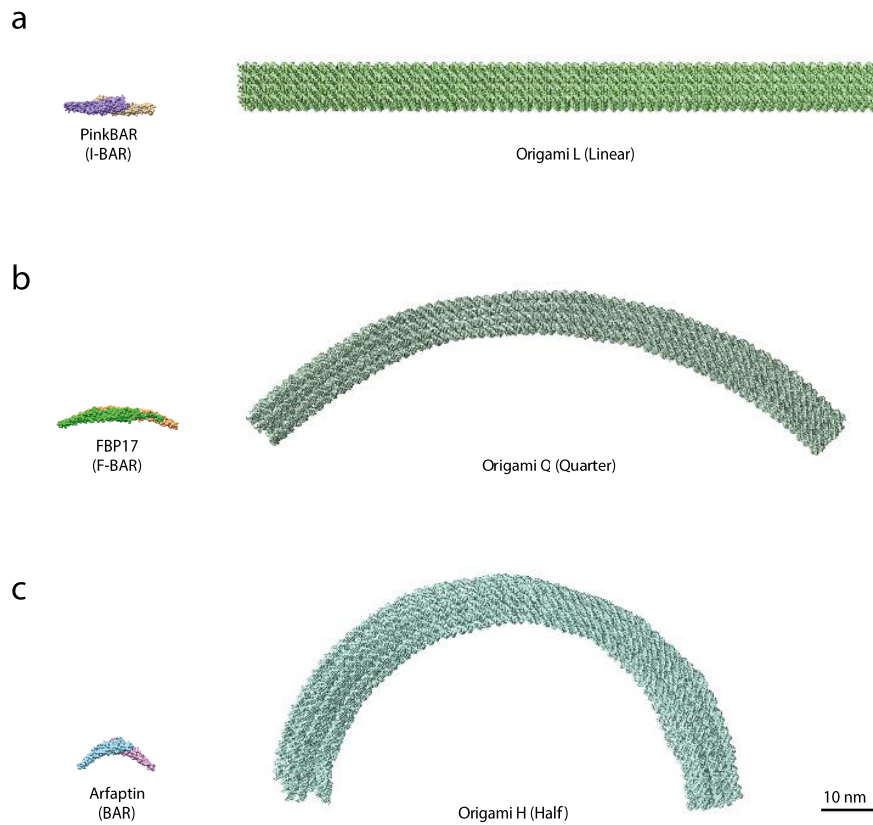
Figure E.3: Cadnano design and oligonucleotide sequences of the DNA origami structure AR22. The cross-section of the structure is shown above the Cadnano map. Lateral staples are coloured in green (left) and orange (right) while core staples are coloured in red; M13 p7249 scaffold is coloured in blue.

F

APPENDIX TO V.1

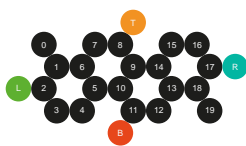
These results have been published as supplementary information to V.1:

Franquelim, H. G., Khmelinskaia, A., Sobczak, J.-P., Dietz, H., Schwille, P. (2018) Membrane sculpting by curved DNA origami scaffolds. Nat. Commun., 9: 811. doi: 10.1038/s41467-018-03198-9. A reprint permission has been granted by the publisher.

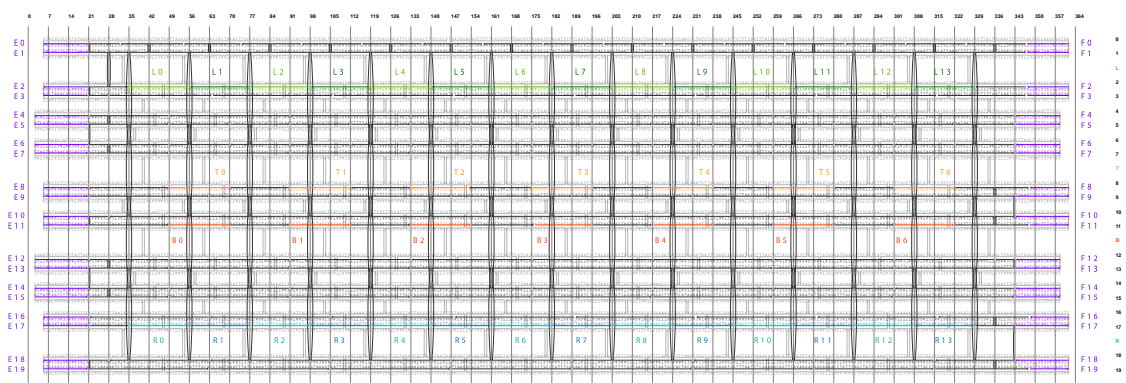


Supplementary Figure 1

Size comparison between BAR proteins and the designed BAR-mimicking DNA origami nanoscaffolds. (a) DNA origami L aims to mimic the shape of flat I-BAR domain proteins, such as PinkBAR; (b) origami Q aims to mimic the shape of moderately-curved F-BAR domain proteins, such as FBP17; and (c) origami H aims to mimic the shape of highly-curved BAR domain proteins, such as Arfaptin. When compared to BAR dimers, our DNA origami structures have at least a 5-fold increased length and 20-fold increased concave surface area. Scale bar: 10 nm.

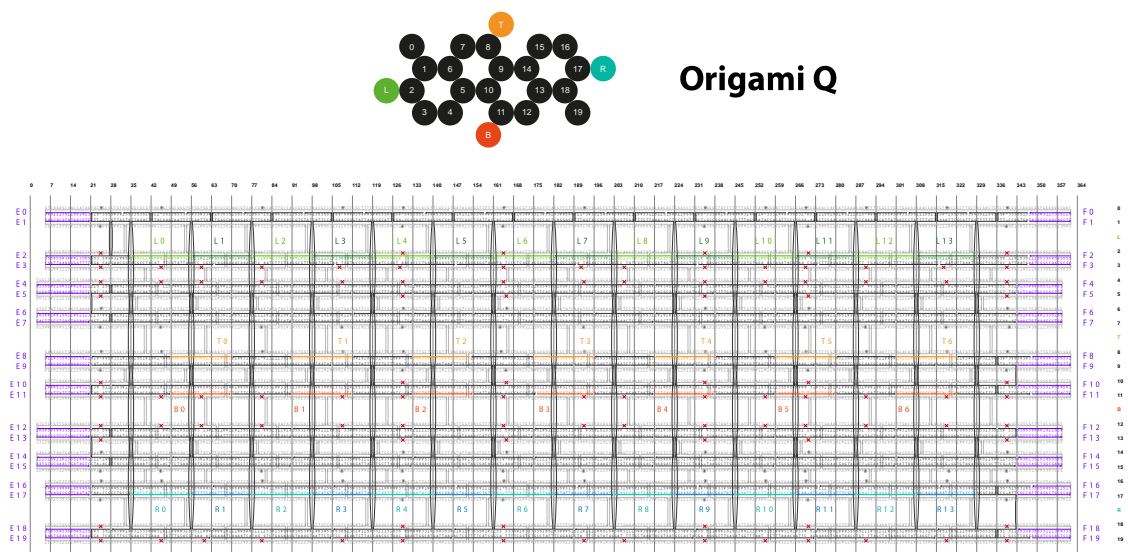


Origami L



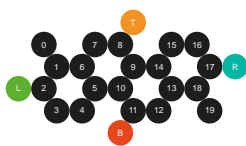
Supplementary Figure 2

Cadnano design and oligonucleotide sequences of the non-curved DNA origami structure L. Top positions T0-T7 are colored in gold, while bottom positions B0-B7 are colored in dark orange. Lateral positions L0-L13 and R0-R13 are colored in green and blue, respectively. Edge positions E0-E19 and F0-F19 are colored in purple. Core staples are colored in black; M13 p7249 scaffold is colored in grey. List of DNA staples can be found in Supplementary Table 1. Additional list of functional staples utilized can be found in appendix (see Supplementary Notes).

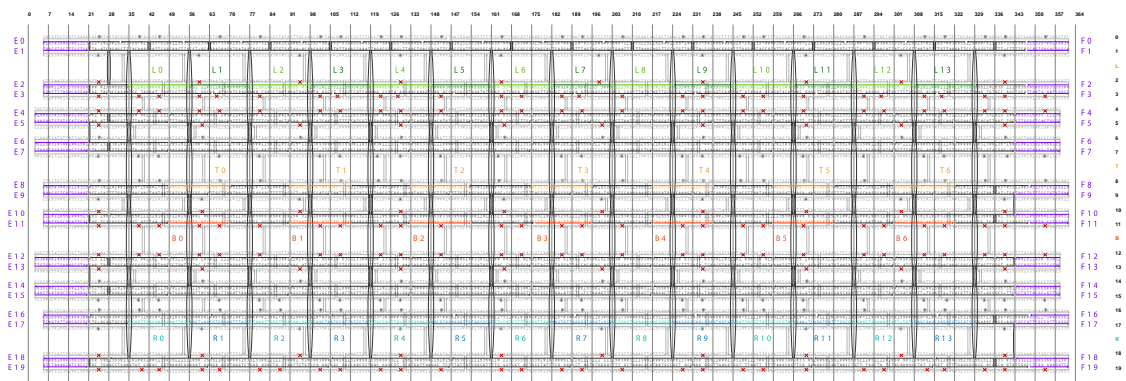


Supplementary Figure 3

Cadnano design and oligonucleotide sequences of the moderately-curved DNA origami structure Q. Top positions T0-T7 are colored in gold, while bottom positions B0-B7 are colored in dark orange. Lateral positions L0-L13 and R0-R13 are colored in green and blue, respectively. Edge positions E0-E19 and F0-F19 are colored in purple. Core staples are colored in black; M13 p7249 scaffold is colored in grey. List of DNA staples can be found in Supplementary Table 2. Additional list of functional staples utilized can be found in appendix (see Supplementary Notes).

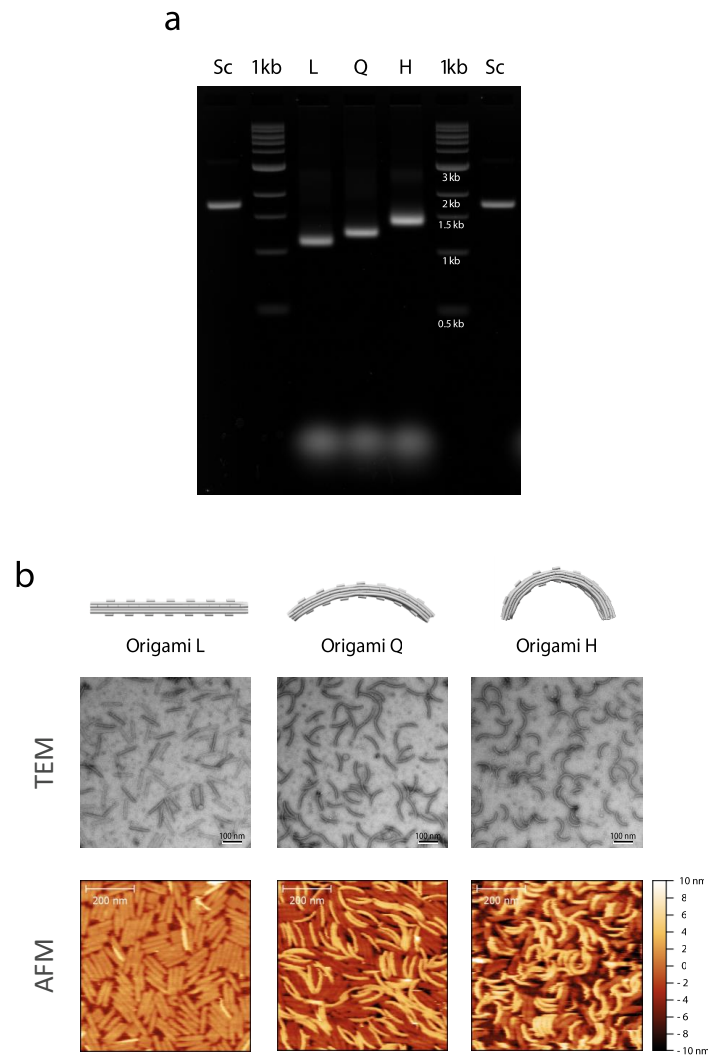


Origami H



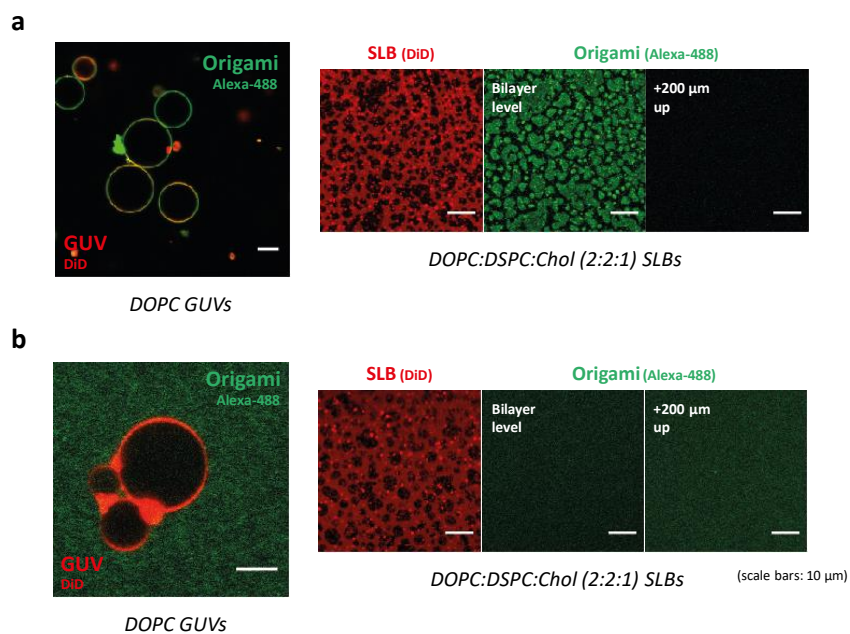
Supplementary Figure 4

Cadnano design and oligonucleotide sequences of the highly-curved DNA origami structure H. Top positions T0-T7 are colored in gold, while bottom positions B0-B7 are colored in dark orange. Lateral positions L0-L13 and R0-R13 are colored in green and blue, respectively. Edge positions E0-E19 and F0-F19 are colored in purple. Core staples are colored in black; M13 p7249 scaffold is colored in grey. List of DNA staples can be found in Supplementary Table 3. Additional list of functional staples utilized can be found in appendix (see Supplementary Notes).



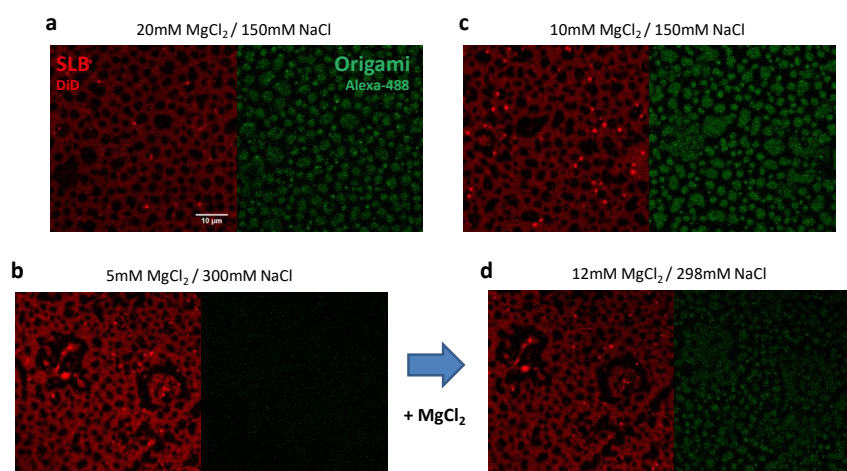
Supplementary Figure 5

Characterization of folded DNA origami nanoscaffolds. (a) Assembly of the folded bare origami structures L, Q, H was initially assessed via agarose gel (2%) electrophoresis analysis. Lanes containing marker DNA ladder (1kb) and M13 single-stranded p7249 scaffold (Sc) were also included. (b) Structure of folded bare origami L, Q and H was further validated using negative-stain transmission electron microscopy (TEM; scale bars: 100 nm) and atomic force microscopy (AFM; scale bars: 200nm).



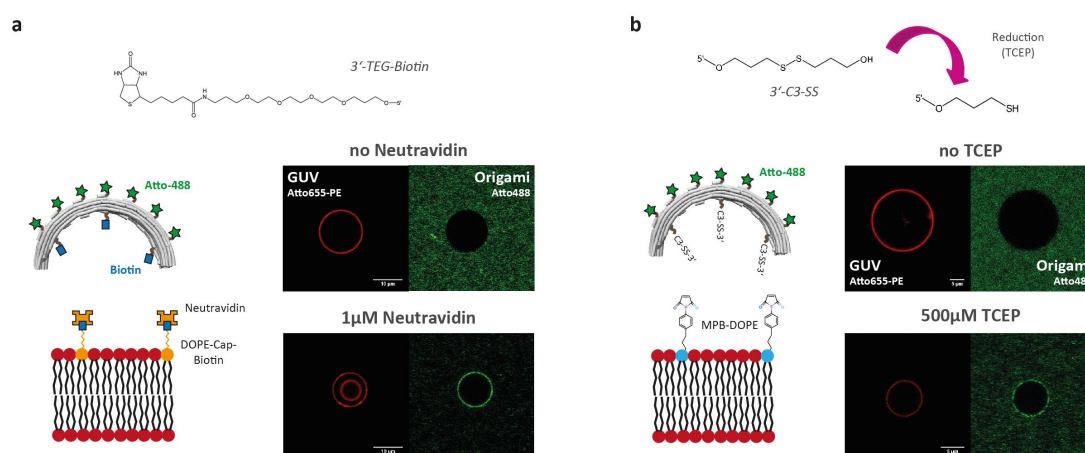
Supplementary Figure 6

Unspecific interaction of curved DNA origami with model lipid membranes, mediated by Mg^{2+} . Binding of bare origami H (labeled with Alexa488, green) to the surface of DOPC GUVs and DOPC:DSPC:Chol (2:2:1 mol ratio) supported lipid bilayers (SLBs) in a 5 mM Tris-HCl, 1 mM EDTA, pH 8.0 buffer containing (a) 20mM MgCl_2 and no NaCl or (b) a buffer with no MgCl_2 and 150mM NaCl. DOPC GUVs were electroformed in sucrose solutions iso-osmolar to the buffers utilized ((a) 70 mOsm kg^{-1} and (b) 300 mOsm kg^{-1}). For fluorescence detection, membranes were labeled with 0.1 % DiD (far-red fluorescent dye). As seen in panel (a), presence of a buffer containing 20 mM MgCl_2 and no NaCl led to extensive binding of DNA origami (labeled with green fluorescent dye Alexa488) to DOPC GUVs and to the liquid-ordered phase of DOPC:DSPC:Chol SLBs (dark regions). On the other hand as seen in panel (b), in the presence of a buffer containing no MgCl_2 and 150 mM NaCl, binding of DNA origami to the surface of membranes was not observed, as green fluorescence can be only found in solution and not at the membrane level. Scale bars: 10 μm .



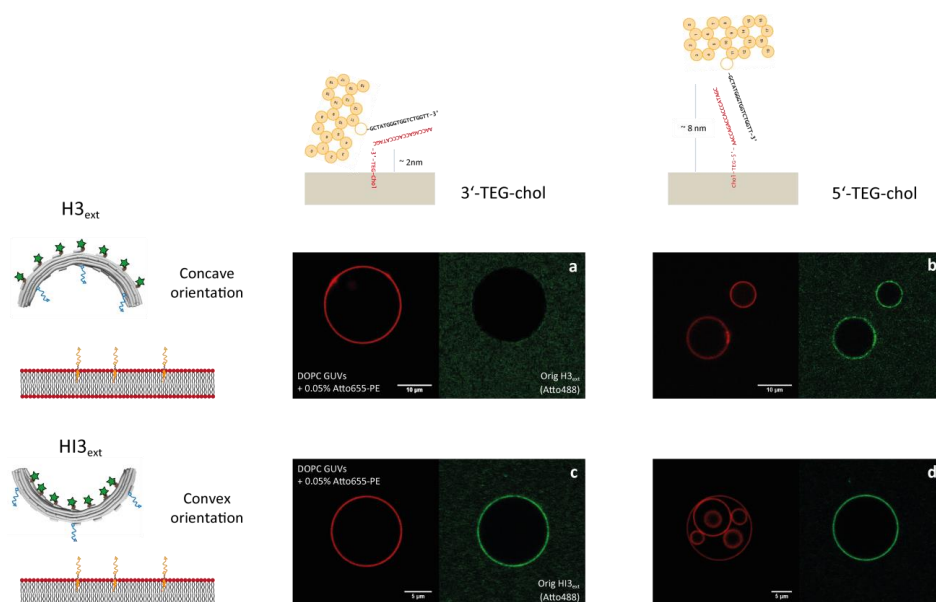
Supplementary Figure 7

Distinct amounts of MgCl₂ and NaCl in solution modulate the attachment of bare DNA origami to membranes. Varying amounts of MgCl₂ and NaCl in solution allowed (a-b) or prevented (c) unspecific attachment of bare DNA origami H (labeled with Alexa488, green) to lipid bilayers (DOPC:DSPC:Chol (2:2:1) SLBs; labeled with DiD, red). Upon addition of MgCl₂ to the lipid bilayer displayed in panel (c), binding of bare origami H to the membrane could be triggered (d). Scale bar: 10 μm.



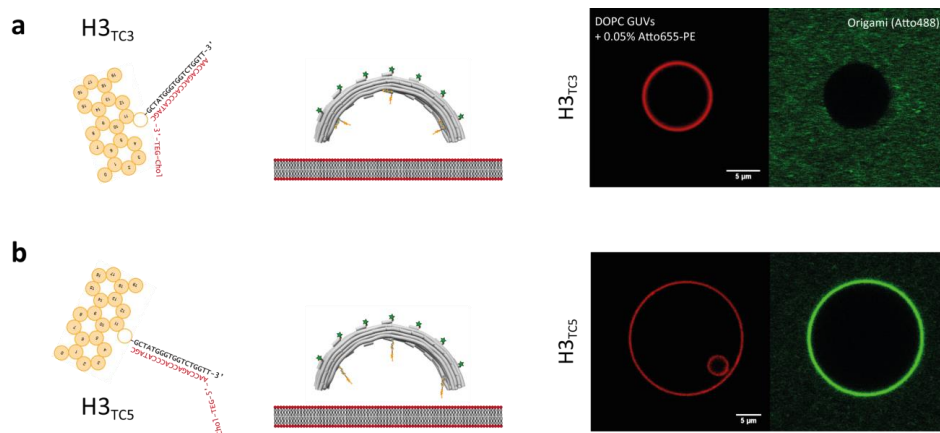
Supplementary Figure 8

Specific attachment of curved origami H to lipid membranes via (a) high affinity polyvalent neutravidin-biotin interaction and (b) covalent attachment. (a) DOPC GUVs containing 2 mol% of biotin-modified DOPE molecules (DOPE-Cap-Biotin) were incubated with DNA nanostructures H containing 3'-TEG-biotin functionalized oligonucleotide staples at origami positions B0, B3 and B6. Upon addition of neutravidin (1 μ M) and after less than 1h incubation, extensive binding of the curved nanostructure to the surface of GUVs was observed. (b) DOPC GUVs containing 10 mol% of maleimide-modified DOPE lipid molecules (MPB-DOPE) were incubated with DNA origami nanostructure H containing protected 3'-thiol-modified strands (3'-C3-SS at positions B0, B3 and B6). Upon addition of excess concentration of reducing agent (TCEP), which would cleave the protecting disulfide bonds, and after overnight incubation, the thiolated DNA origami nanostructure H was able to be crosslinked to GUVs, although not as efficiently as with the biotin-neutravidin strategy. For these experiments, GUVs were fluorescently-labeled with 0.05 mol% Atto655-DOPE (red) and the DNA origami nanostructures with Atto488-modified strands (green). Moreover, while for strategy (a) standard imaging buffer (5 mM Tris-HCl, 1 mM EDTA, 5 mM MgCl₂, 300 mM NaCl, pH 8.0) was utilized, in case of strategy (b) we utilized a 10 mM Hepes, 5 mM MgCl₂, 300 mM NaCl, pH 7.4 buffer, as the thiol-maleimide crosslinking requires a lower pH and a non-amine buffer. Scale bars: (a) 10 μ m; (b) 5 μ m.



Supplementary Figure 9

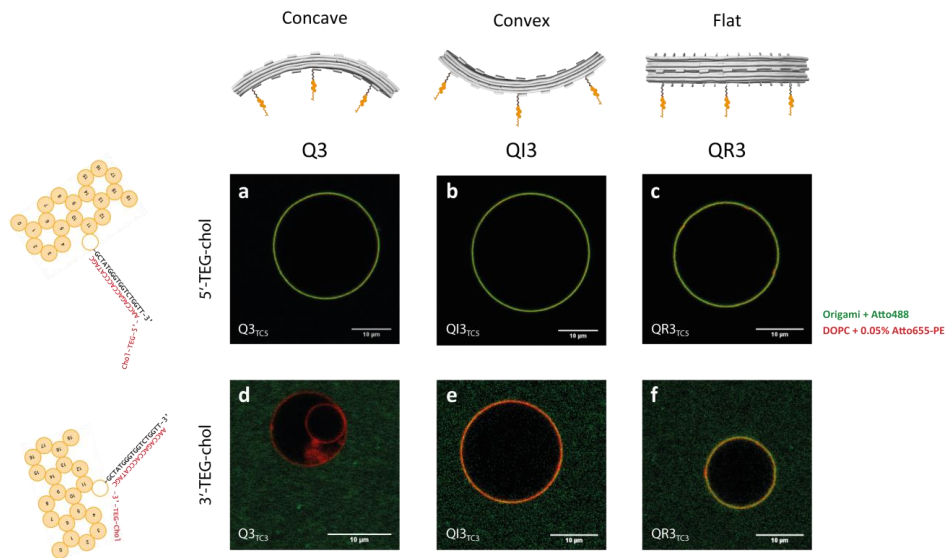
Side-specific attachment of origami H to GUVs through hybridization with TEG-chol modified oligonucleotides. Origami H nanostructures (labeled with Atto488, green) presenting 18 nucleotide-long single-stranded overhangs (**a-b**) on the concave surface – origami H3_{ext} (overhangs extending from the 3'-end of bottom positions B0, B3 and B6) or (**c-d**) on the convex surface – origami HI3_{ext} (overhangs extending from the 3'-end of top positions T0, T3 and T6), were added to DOPC GUVs (labeled with Atto655-DOPE, red) previously pre-incubated with 2 μM of 3'/5'-modified TEG-chol modified complementary oligonucleotide strands. **Panels (a,c):** when 3'-end TEG-chol functionalized oligonucleotides were used (proximal orientation), hybridization between the DNA overhangs on origami H and membrane-bound complementary strands will occur in tight proximity to lipid bilayer surface. Due to the bulkiness and curvature of this nanostructure, membrane attachment of structure H3_{ext} via its concave surface, will be hindered (**a**). On the other hand, significant binding of structure HI3_{ext} to membranes via its more accessible convex surface was still observed (**c**). **Panels (b,d):** when 5'-end TEG-chol functionalized oligonucleotides are used (distal orientation), hybridization between the DNA overhangs on origami H and membrane-bound complementary strands will be more accessible. Independently of the concave (H3_{ext}; **b**) or convex (HI3_{ext}; **d**) binding orientation, strong attachment of the curved origami H could be achieved. Scale bars: (**a, b**) 10 μm ; (**c, d**) 5 μm .



Supplementary Figure 10

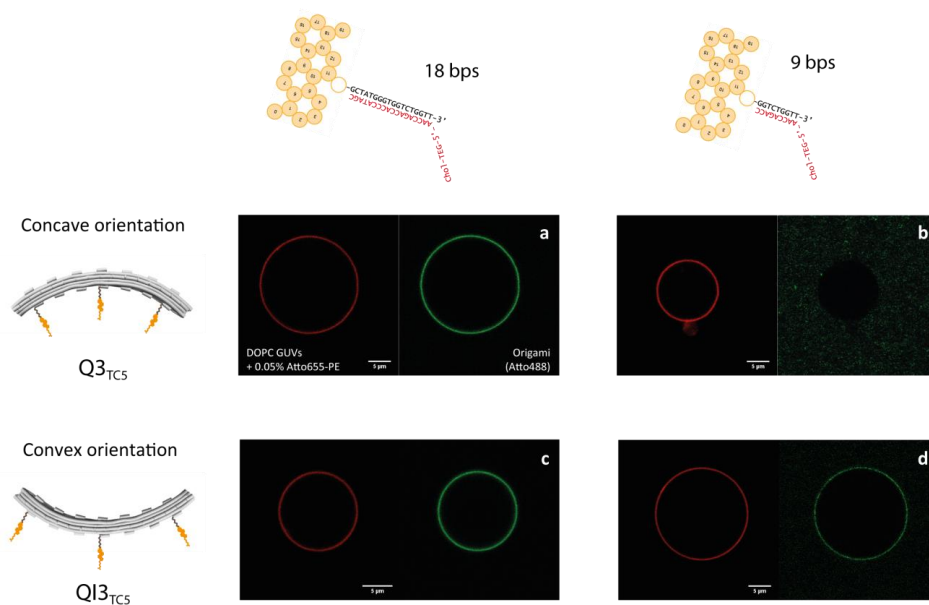
Attachment of origami H to GUVs through TEG-chol modified 18bps overhangs.

Nanostructures H (labeled with Atto488, green) displaying 3'/5'-TEG-chol modified 18 nucleotide-long DNA strands, now directly hybridized during origami folding with single-stranded overhangs at the bottom positions B0, B3 and B6, were used. **(a)** Proximal positioning of the three TEG-chol modifications on the concave surface (H3_{TC3}; TEG-Chol at 3'-end) resulted in virtually no attachment of origami H to DOPC GUVs (labeled with Atto655-DOPE, red), even after longer incubation times (i.e. overnight). **(b)** On the other hand, by placing the three TEG-Chol moieties at the distal end of the 18 bps overhangs (H3_{TC5}; TEG-Chol at 5'-end) strong membrane binding of origami H after 1h of incubation was observed. Hence, the increase of the linker length from ~2 nm (length of the TEG moiety) to ~8 nm (combined length of the TEG moiety and the 18 bps overhang) rendered the cholesteryl moieties on the curved and bulky origami H nanostructures less sterically hindered and more accessible for binding macroscopically flat lipid membranes, such as GUVs. Scale bars: 5 μm.



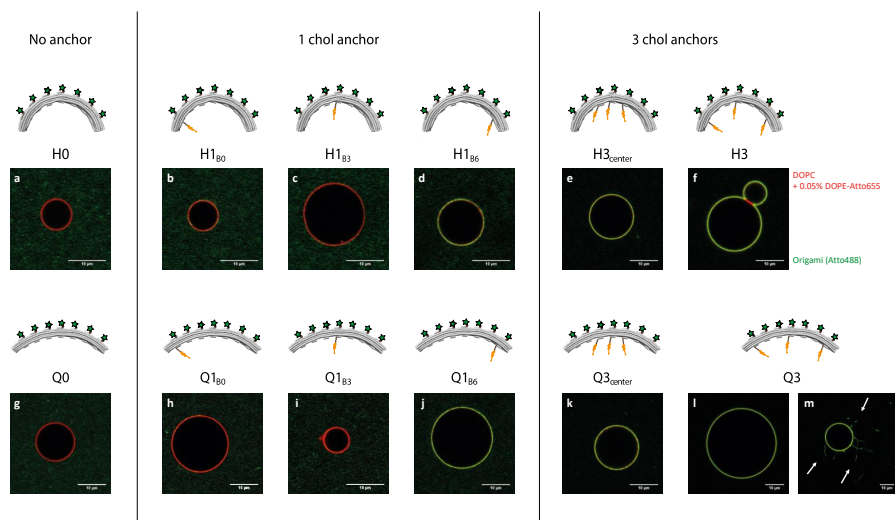
Supplementary Figure 11

Side-specific attachment of origami Q to GUVs through TEG-cholesterol modified 18bps overhangs. We further assessed binding to DOPC GUVs (labeled with Atto655-DOPE, red) of origami Q nanostructures (labeled with Atto488, green), previously functionalized with three TEG-cholesterol moieties at the distal 5' (TC5) and proximal 3' (TC3) ends of 18 bps overhangs at the concave (bottom positions B0, B3 and B6; origami Q3_{TCX}), convex (top positions T0, T3 and T6; origami QI3_{TCX}) or lateral non-curved (right positions R0, R6 and R12; origami QR3_{TCX}) origami surfaces. **(a-c):** Independently of the surface of the nanostructures carrying the modifications, distal positioning of the TEG-cholesterol moieties (TC5) resulted in strong binding of the DNA origami Q nanostructures to GUVs. **(d-f):** When the TEG-cholesterol moieties were positioned in close proximity to the DNA origami core (TC3), membrane binding of those nanostructures depended on which surface was carrying hydrophobic modifications. If the cholesterol groups are localized on the concave surface of origami Q (origami Q3_{TC3}, **(d)**), no significant binding to GUVs was reported. On the other hand, if the cholesterol groups were localized on the convex surface of origami Q (QI3_{TC3}, **(e)**) and mainly lateral surface with essentially zero curvature (QR3_{TC3}, **(f)**), significant (yet weaker) membrane binding was observed. Scale bars: 10 μm.



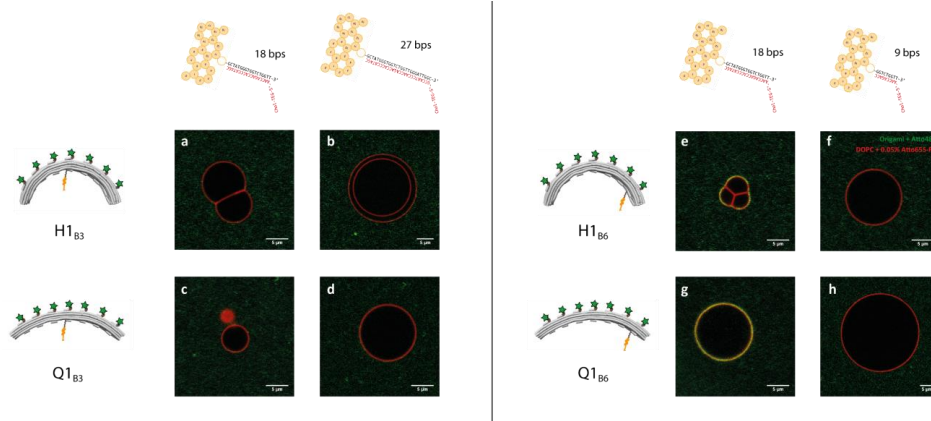
Supplementary Figure 12

Dependence on the length of the TEG-chol modified linkers/overhangs, for attaching origami Q to GUVs. Independently of the origami surface on which the distal 5'-TEG-chol moieties localized, for structure Q3_{TC5} (cholesteryl anchors at the concave facet of origami Q) and QI3_{TC5} (cholesteryl anchors at the convex facet of origami Q) with 18 bps overhangs (linker length ~8 nm), a strong attachment to lipid membranes was observed ((a) and (c), respectively). However, shortening those overhangs to 9 bps (linker length ~5 nm) resulted in a strong reduction of the binding of curved nanostructures Q to the GUVs. For such linker length, weak binding to lipid membranes was still observed for structure QI3_{TC5} with hydrophobic anchors at the convex origami facet (d); yet no membrane binding of structure Q3_{TC5} with anchors at the concave origami surface (b) was reported. Overall, placing the TEG-chol moieties at the distal end of 18 bps overhangs provided an appropriate linker length for overcoming steric hindrance during the attachment of our nanostructures to GUVs. Scale bars: 5 μm. Green fluorescence: origami labeled with Atto488; red fluorescence: membranes labeled with Atto655-DOPE.



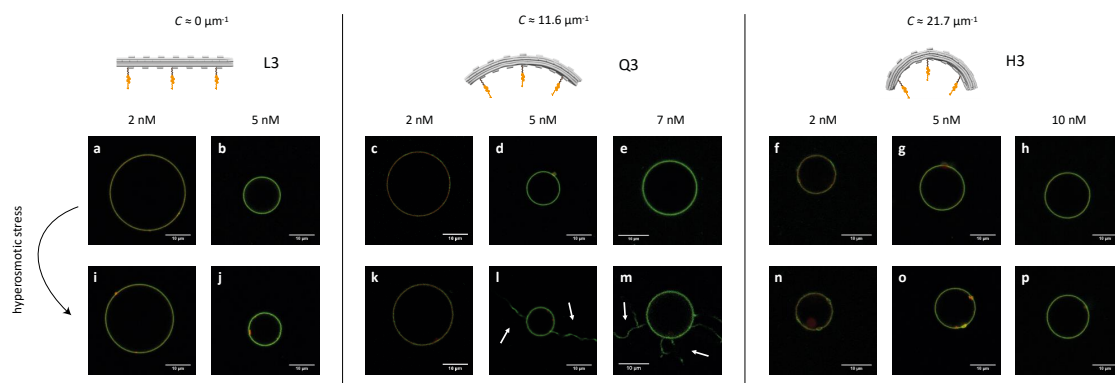
Supplementary Figure 13

Effect of the number and positioning of TC5 anchors on the binding of curved DNA origami nanostructures to freestanding lipid bilayers via their concave surface. TEG-chol moieties placed at the distal 5'-end of 18 bps overhangs (from here on called **TC5**) were used at the bottom concave origami positions. In the absence of TC5 anchors and using imaging buffer containing 5 mM MgCl₂ and 300 mM NaCl, bare origami structures H0 and Q0 did not attach to GUVs (**a**, **g**). Use of single TC5 anchors on structures H1 and Q1 did not promote efficient membrane binding of the nanostructures (**b**, **c**, **h**, **i**), unless the TC5 anchor was placed at the most accessible edge position B6 (**d**, **j**), indicating that steric hindrance clearly affected membrane binding. Strong binding to GUVs was however achieved upon incorporation of 3× TC5 anchors; independently of the anchors being localized at the central positions B2, B3 and B4 (H3_{center}, (**e**); Q3_{center}, (**k**)) or distributed across the concave facet at positions B0, B3 and B6 (H3, (**f**); Q3, (**l**)). Although membrane attachment did not greatly depend on the degree of curvature of our nanostructures, only in the presence of the moderately-curved structure Q3 a significant amount of GUVs (~ 18%) displayed tubular-like outwards deformations (arrows, (**m**)). Scale bars: 10 μm. Green fluorescence: origami labeled with Atto488; red fluorescence: membranes labeled with DOPE-Atto655.



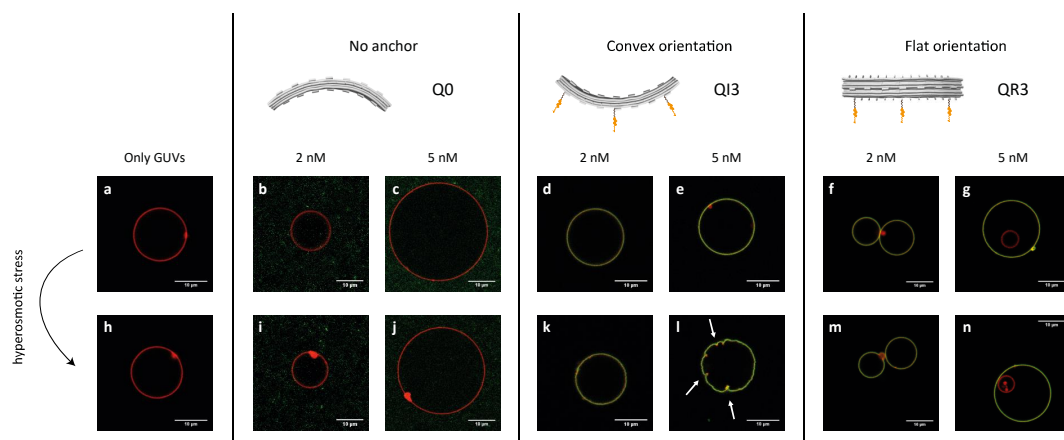
Supplementary Figure 14

Membrane binding of curved DNA nanostructures with single TC5 anchors is dependent on the linker/overhang length. The use of a longer linker/overhang (27 bps, instead of the typical 18 bps) did not improve membrane binding of nanostructures H1_{B3} and Q1_{B3} containing a single TC5 anchor at the central concave position B3 (**a-d**). On the other hand, shortening the linker/overhang from 18 to 9 bps for single TC5 anchors placed at the most accessible edge position B6, fully abolished the weak membrane binding observed for both DNA origami H1_{B6} and Q1_{B6} nanostructures (**e-h**). Scale bars: 5 μm . Green fluorescence: origami labeled with Atto488; red fluorescence: membranes labeled with Atto655-DOPE.



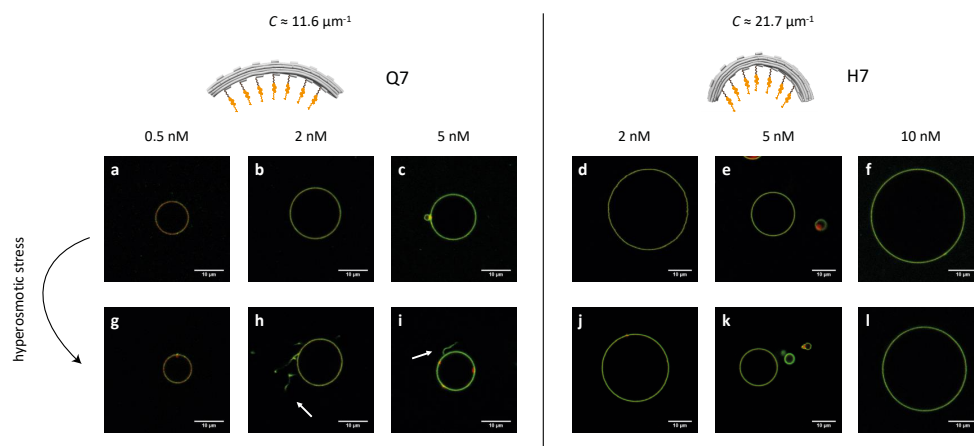
Supplementary Figure 15

Dependence on DNA origami bulk concentration and degree of curvature of DNA nanostructures with concave membrane-binding interface, for triggering membrane tubulation upon hyperosmotic stress. Structures L3, Q3 and H3 (possessing $3 \times$ TC5 anchors at positions B0, B3 and B6) bound to DOPC GUVs were imaged after at least 1h incubation period. Osmotic stress was achieved by increasing outer osmolarity in 10%. For origami structure Q3 (moderate curvature; **c-e, k-m**), triggering the generation of outwards positively-curved membrane tubules on GUVs upon hyperosmotic stress was dependent on the overall bulk concentration of origami utilized (at least 5 nM bulk concentration was required; deformations marked with arrows). On the other hand, origami structures L3 (no curvature; **a-b, i-j**) and H3 (strong curvature; **f-h, n-p**) were not able to significantly affect the shape of vesicles upon hyperosmotic stress. Note that even at increased bulk concentrations (10 nM), highly-curved origami H3 was not able to trigger significant membrane deformation on GUVs, e.g. tubulation (panels **h, p**). Scale bars: 10 μm . Green fluorescence: origami labeled with Atto488; red fluorescence: membranes labeled with DOPE-Atto655.



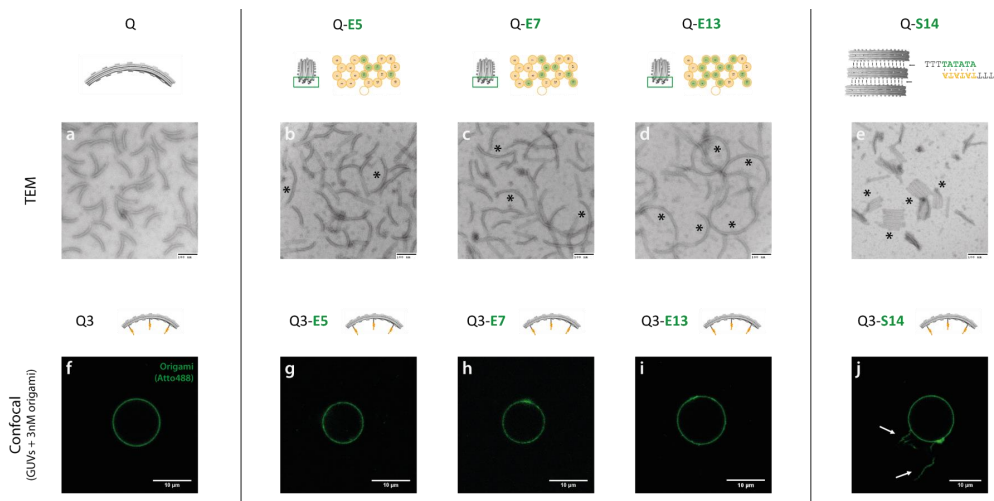
Supplementary Figure 16

Dependence on DNA origami bulk concentration and curvature of membrane anchoring origami facet, for triggering membrane deformations upon hyperosmotic stress with origami Q nanostructures. Data presented in this figure complements the previous data presented in Supplementary Fig. 15, being acquired under the same conditions. When compared with control vesicles in the absence of origami (**a**, **h**), no significant effect on vesicle shape was observed upon hyperosmotic stress when origami Q with no hydrophobic anchor (structure Q0) was present in solution, independently of the bulk concentration assayed (**b-c**, **i-j**). Regarding membrane-bound nanostructure Q variants with three TC5 anchors, for structure QR3 (displaying anchors at the non-curved origami lateral surface) no significant membrane deformations on GUVs were observed even at increased QR3 bulk concentrations (**f-g**, **m-n**). However, evagination/invagination-type of membranes deformations (marked with arrows) were observed for the membrane-bound convex QI3 structure (**d-e**, **k-l**). Similarly to what was reported for the concave Q3 structure (Supplementary Fig. 15), we also observed a dependence on the total bulk concentration of QI3 required for triggering deformations upon vesicle deflation; as shape changes only significantly happened at higher concentrations (5 nM). Scale bars: 10 μm . Green fluorescence: origami labeled with Atto488; red fluorescence: membranes labeled with DOPE-Atto655.



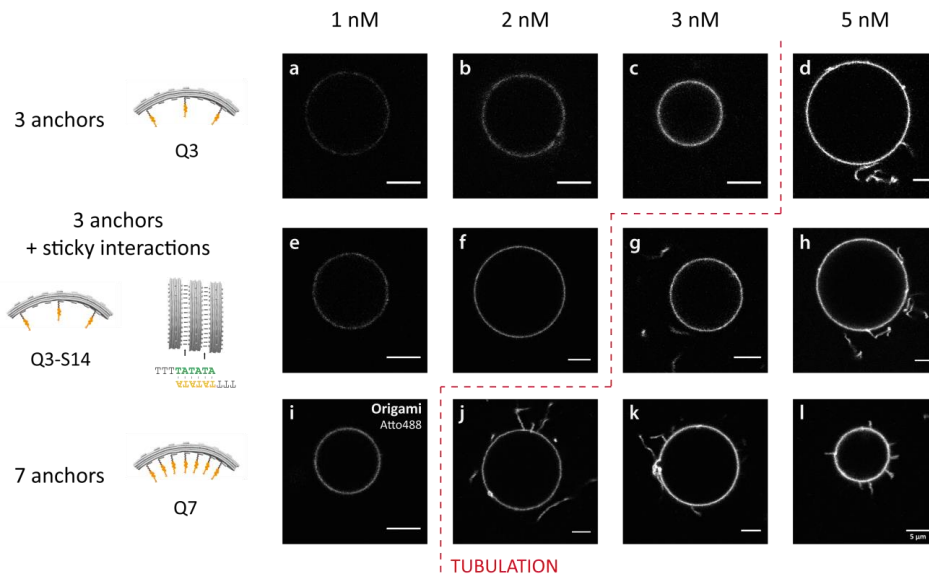
Supplementary Figure 17

Generation of membrane deformations upon hyperosmotic stress by concave nanostructures Q and H bearing increased number of TC5. Data presented in this figure complements previous data presented in Supplementary Fig. 15 and Supplementary Fig. 19, being acquired under the same conditions. The moderately-curved structure Q7 bearing 7× TC5 anchors required lower bulk concentrations for triggering membrane tubulation (marked with arrows) on GUVs (**a-c**, **g-i**), when compared with its counterpart bearing only 3× TC5 anchors (Supplementary Fig. 15c-e and k-m). For the highly curved DNA origami H7 bearing 7× TC5 anchors on their concave surface, on the other hand, despite the increase in the number of hydrophobic anchors resulting in a stronger membrane attachment, we were still not able to observe significant membrane deformations upon hyperosmotic stress (i.e. tubulation) on GUVs (**d-f**, **j-l**). Scale bars: 10 μm. Green fluorescence: origami labeled with Atto488; red fluorescence: membranes labeled with DOPE-Atto655.



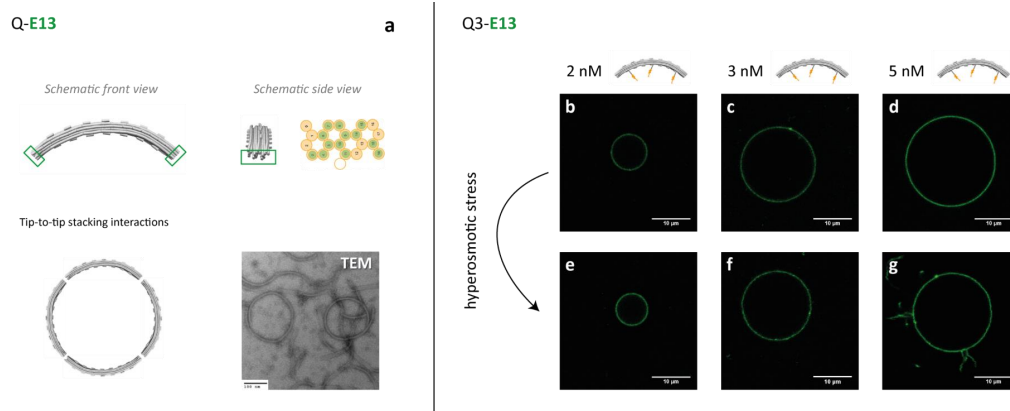
Supplementary Figure 18

Incorporation of polymerizing moieties and its effect on the ability of moderately-curved origami Q nanostructures to deform lipid vesicles. (a-e): Negative-stain TEM images of bare origami Q structure variants displaying different types and number of polymerizing moieties. Addition of polymerizing staples at the marked ends (in green; upper schemes) of monomeric structure Q (a) allowed for tip-to-tip blunt end stacking interactions (b-d). By varying the number of blunt ends from 5 to 7 and 13, it was possible to control the size of the resulting oligomers – dimers, trimers and even tetramers (marked as stars). Polymerization could also be triggered via lateral sticky interactions (e). Incorporation of 14 protrusions capable of hybridizing with their counterparts on each side of the origami Q, resulted in the formation of sheet like polymers of origami Q in solution (marked with asterisks). (f-j): Variants of structure Q3 (labeled with Atto488, green) with and without corresponding polymerizing moieties were pre-incubated at 3 nM with DOPC GUVs for at least 1h and generation of membrane tubulations was followed after hyperosmotic stress. Altogether, at such intermediate DNA origami bulk concentration, we could only report significant tubulation events (marked with arrows) on GUVs upon osmotic shock were for the membrane-bound variant Q3-S14 bearing lateral polymerization strands (j). Scale bars: (a-e) 100 nm; (f-j) 10 μ m.



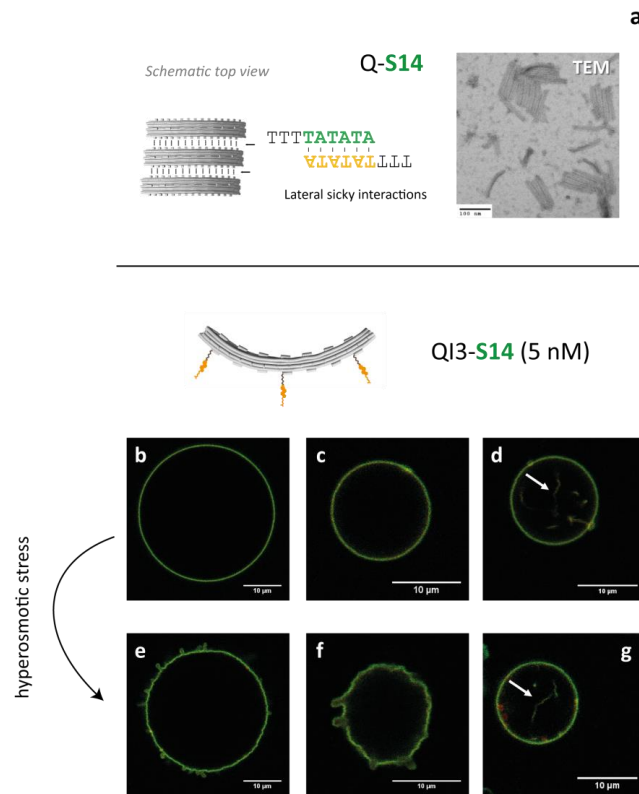
Supplementary Figure 19

Requirements for induction of membrane deformations by BAR-mimicking origami structure Q can be tuned via number of cholesteryl anchors or lateral polymerization. For structure Q3 (a-d), only at high bulk concentrations (5 nM) tubulation of almost all GUVs was triggered. For structure Q7 with additional cholesteryl anchors (i-j), the minimal bulk concentration required to trigger membrane tubulation was shifted to lower values (2 nM). Similarly for structure Q3-S14 displaying lateral sticky overhangs (e-h), lower total bulk concentration were necessary for triggering vesicle tubulation when compared to structure Q3 (a-d). Representative confocal images at the equatorial plane of GUVs incubated for at least 1 h with varying concentrations of Atto488-labeled DNA nanostructures are shown after hyperosmotic stress. The red dotted line indicates the concentration regime (total bulk concentration of origami Q) required for triggering membrane tubulation on freestanding lipid bilayers. Scale bars: 5 μm.



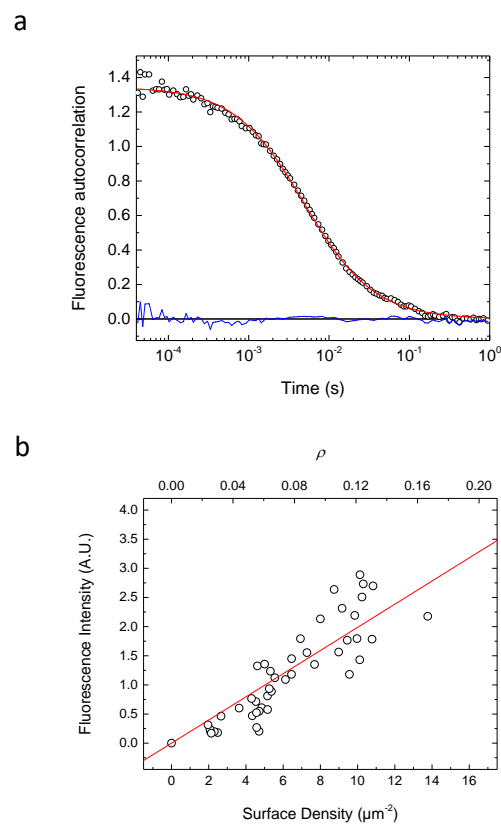
Supplementary Figure 20

Dependence on the total bulk concentration of linearly-polymerizing concave structure Q3-E13, for triggering membrane shape deformations upon hyperosmotic stress. Data presented in this figure was acquired under the same conditions as the one displayed in Supplementary Fig. 19 and Supplementary Fig. 15. (a) Schematic representations of the polymerization strategy based on tip-to-tip stacking interactions via 2×13 blunt ends, based on the polymers observed by negative-stain TEM with bare structure Q-E13. (b-g) Similar to what we observed for the monomeric membrane-bound structure Q3 (Supplementary Fig. 19 and Supplementary Fig. 15), membrane-bound structure Q3-E13 (labeled with Atto488, green) only triggered significant membrane deformations (i.e. tubulation) upon hyperosmotic stress at high bulk concentrations (5 nM). Scale bars: (a) 100 nm; (b-g) 10 μ m.



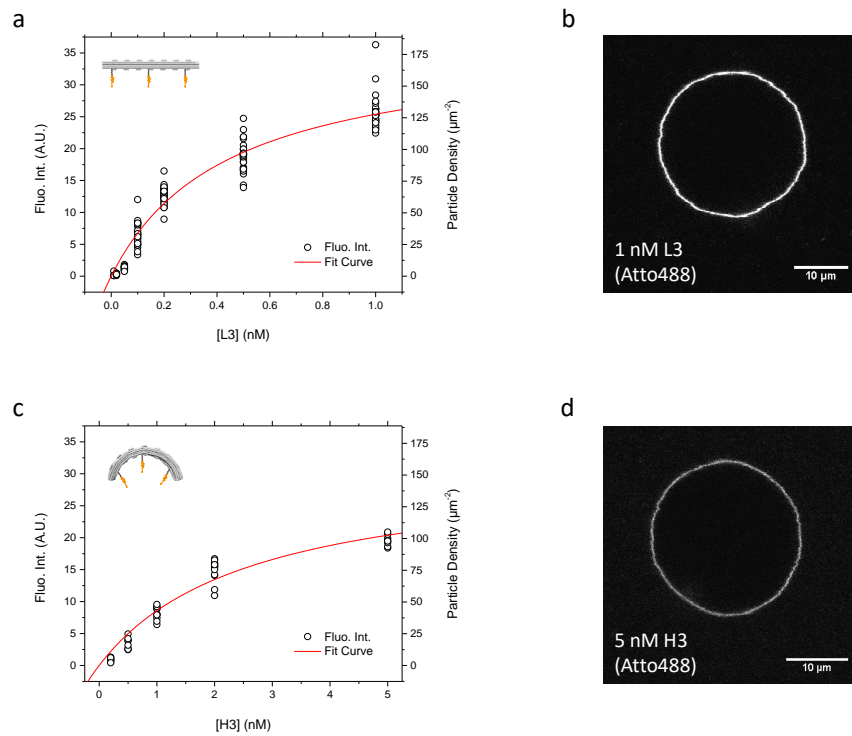
Supplementary Figure 21

GUV shape deformations triggered by membrane-bound convex variants of origami Q with lateral polymerization strands. Data presented in this figure complements previous data presented in Fig. 3 and Supplementary Fig. 16, being acquired under the same conditions. **(a)** Schematic representation of the formation of origami sheets by sticky interactions between neighboring origami structures displaying 2×14 lateral TATATA overhangs, based on the observations by negative-stain TEM imaging of origami Q-S14. **(b-g)** For vesicles incubated with high DNA origami bulk concentrations (i.e. 5 nM) of convex polymerizing structure Q13-S14, stable evagination-like deformations were reported upon hypersosmotic **(e, f)**. Additionally, a small percentage of vesicles (~15%) presented inwards tubules decorated with DNA origami (arrows), even in the absence of osmotic shock **(d, g)**. Scale bars: **(a)** 100 nm; **(b-g)** 10 μm . Green fluorescence: origami labeled with Atto488; red fluorescence: membranes labeled with DOPE-Atto655.



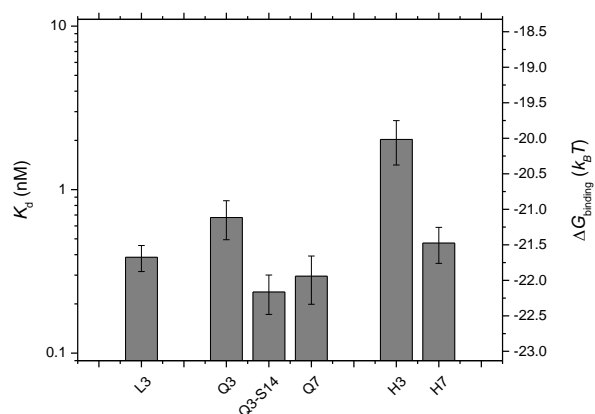
Supplementary Figure 22

Determination of DNA origami particle density at the surface of GUVs by point FCS and fluorescence intensity calibration. (a) Representative auto-correlation curve obtained for structure Q3 on the upper pole of a GUV at low ($\rho = 0.06$) surface densities. (b) Linear relationship (calibration curve in red) between fluorescence intensities (obtained via confocal microscopy) and surface densities (determined for $\rho < 0.2$, where the one-component two-dimensional diffusion model (equation 2) is valid) recovered for membrane-bound DNA origami on individual GUVs by FCS (open circles).



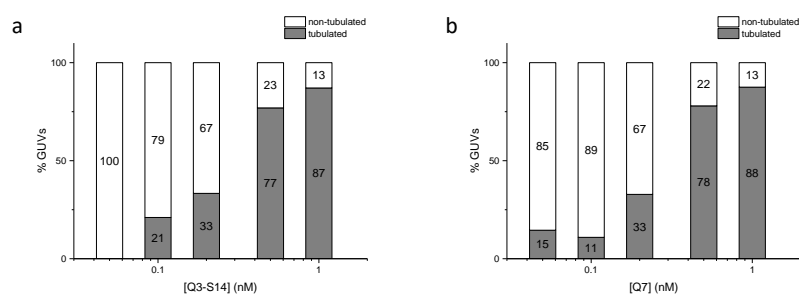
Supplementary Figure 23

Attachment of origami structures L3 and H3 to GUVs upon overnight incubation. (a, c) Representative membrane binding curves obtained using a Langmuir isotherm fit (equation 1) for the flat origami structure L3 (a) and the highly-curved origami structure H3 (c). Each data point corresponds to the fluorescence intensity at the membrane level of DNA origami structures (labeled with $3\times$ Atto-488 dyes) for single GUVs. (b, d) Shape variations observed for GUVs incubated overnight with structures L3 and H3. Even at high densities of membrane-bound DNA origami (≥ 100 particles per μm^2 , estimated from the fluorescence brightness via calibration curve of Supplementary Figure 22b), no tubulation events were observed for GUVs incubated with the flat structure L3 (b) or highly-curved structure H3 (d). Unlike the GUVs incubated with moderately-curved structure Q3 (Fig. 4c), GUVs with membrane-bound structures L3 and H3 displayed, at best, increased flaccid membrane deformations. Scale bars: 10 μm .



Supplementary Figure 24

Apparent dissociation constants (K_d) recovered from the analysis of membrane binding of different variants of curved DNA origami scaffolds. Affinity of various cholesteryl-modified BAR-mimicking DNA nanostructures to DOPC GUVs was determined after overnight incubation, from the analysis of the fluorescence intensity of membrane-bound DNA origami as a function of total bulk concentration. Representative binding curves obtained and respective Langmuir isotherm fits (equation 1) are depicted in Fig. 4a and Supplementary Fig. 23. Values correspond to the average K_d (\pm st. dev.): L3 ($n_{\text{total}} = 288$ GUVs; $n = 131$ -157 GUVs per fit, 2 repeats), Q3 ($n_{\text{total}} = 277$ GUVs; $n = 83$ -100 GUVs per fit, 3 repeats), Q3-S14 ($n_{\text{total}} = 84$ GUVs; $n = 36$ -48 GUVs per fit, 2 repeats), Q7 ($n_{\text{total}} = 117$ GUVs; $n = 53$ -64 GUVs per fit, 2 repeats), H3 ($n_{\text{total}} = 106$ GUVs; $n = 48$ -58 GUVs per fit, 2 repeats) and H7 ($n_{\text{total}} = 103$ GUVs; $n = 47$ -56 GUVs per fit, 2 repeats). $\Delta G_{\text{binding}}$ was calculated via $\Delta G = RT \ln K_d$.



Supplementary Figure 25

Efficiencies of vesicle tubulation for origami structure Q3-S14 bearing lateral polymerization overhangs and origami structure Q7 possessing additional cholesteryl anchors. Percentages of GUVs with (closed bars) and without (open bars) outwards tubules observed after overnight incubation at different total bulk concentrations of DNA origami structures Q3-S14 (**a**; $n_{\text{total}} = 118$ GUVs; $n = 13$ -31 GUVs per origami concentration) and Q7 (**b**; $n_{\text{total}} = 297$ GUVs; $n = 55$ -64 GUVs per origami concentration).

Supplementary Table 1
List of DNA staples - Origami L

Start	End	Sequence	Length	Type	Pos.
00[031]	03[027]	CCTAATGCGCCACGACGTTTCTCGGATAAA	32	#0_core	
00[053]	06[049]	CGTAACCACCACGAAGTATTAGACTTTAAAAAG	33	#0_core	
00[073]	06[070]	AGTGTAGCGGTTCAATTAACCTGAATAATTTCA	32	#0_core	
00[094]	06[091]	GCGGGCGCTAGTTTGAATACCGTTAGAAAA	32	#0_core	
00[115]	06[112]	GAAGGGAAGAAATTCGAAGAACGAGATCGTAG	32	#0_core	
00[136]	06[133]	CCGGCGAACGTCATTAGACGGGGAAGAGATA	32	#0_core	
00[157]	06[154]	AACCGTCTATCGGACATTCACAGATCACC	32	#0_core	
00[178]	06[175]	CTCCAAACGTCACACGAGCCGCGTAACAAAT	32	#0_core	
00[199]	06[196]	TCCACTATAAAGGTTTAGTACCAGATTTTCA	32	#0_core	
00[220]	06[217]	TGTTCCAGTTTCTTAAACGCTATTATATTC	32	#0_core	
00[241]	06[238]	GCCCGAGATAGACCGGAACGAGTTATGAACG	32	#0_core	
00[262]	06[259]	CCCTTATAAATCCACATTCACTGTCTATAAC	32	#0_core	
00[283]	06[280]	TGGTCCGAAAAACAGGTCAGGAAATTAGAGC	32	#0_core	
00[304]	06[301]	GCGGAAAATCCTGACCTGTAATTTTCATATA	32	#0_core	
00[325]	06[322]	CCACGCTGGTTGCATTAAATTTTTCTGGCC	32	#0_core	
00[346]	01[346]	GAGAGAGTTGCTGAGACGGGCA	22	#0_core	
02[034]	07[048]	TTGTGCTATAACGACGCAAAATAGAAGAACTCAAAGTAACTAGTAAC	42	#0_core	
02[346]	02[329]	GCGCCAGGGTGGTTTT	18	#0_core	
03[028]	03[063]	GGGATTTAGACCCGTCAAACAATTCGACAACTACA	36	#0_core	
03[064]	03[105]	AAATAAGATGATGAACAATAATTCGATAAAATAGCGCTCCA	42	#0_core	
03[106]	03[147]	ATCAAAACCAAGTACCGCACAGAGAGCTGAACCCCTGAAATA	42	#0_core	
03[148]	03[189]	TGGTGGGAGGGAAGGTAACCCCTTGACAGGAGGTTGGCC	42	#0_core	
03[190]	03[231]	CGGATCAGAACCGCCACCGGTTAGATAGTTGCGCCGATCG	42	#0_core	
03[232]	03[273]	AAATCGGTCAATCATAAGGAAAGATATACATAACGCCAATCA	42	#0_core	
03[274]	03[315]	AAGCGTACCTTTAATTGCAAAAGTACGGGAGAGCCCTTTATT	42	#0_core	
03[316]	03[346]	GTAATCAGCTCATTTTTTAAATGAATCGGCC	31	#0_core	
04[048]	10[028]	TTTTGAGAGAGGAAACGCTGCTGTCTTCTGCTCA	35	#0_core	
04[090]	04[049]	AACACTAGTAACATCAAGAAAAAAAAGTTCGTATTAATCC	42	#0_core	
04[132]	04[091]	GTAATTTTACTCATCGAACAACGAGAAAAATAAAGAATA	42	#0_core	
04[174]	04[133]	CGATTAGCCATTGACGGAATTAATTCGAAATCAGAGG	42	#0_core	
04[216]	04[175]	CCATCGTATCTCAGAACCCACCTTATAAGGCAGGTCAGA	42	#0_core	
04[258]	04[217]	GGCATGGTAGGAAACCGAACTGACCAATGTGCAATGACAAACA	42	#0_core	
04[300]	04[259]	GGTAGCATTCTCTTTGATAAGAGGTAGCTAAGGAATTACGA	42	#0_core	
04[342]	04[301]	CAGCTGCATAACCAATAGGAACGCCATTAATTTCAACGCAA	42	#0_core	
05[049]	05[048]	CGTTATTGGAGGAGCGAATTGAGGAAAGATATAGATTCGAA	42	#0_core	
05[070]	05[069]	TTACATTGATGTGAGCCTTTACATCGAAAAATCAATTA	42	#0_core	
05[091]	05[090]	TCATAATAAAAAAGCCATGCAAAATCAATTAATATTTTCGGAA	42	#0_core	
05[112]	05[111]	TTTTTATAAGCTTATCAGATAAGTCTGTAGCATGTAAGCCG	42	#0_core	
05[133]	05[132]	GCTAATAGAAATGAAAAATCCAAATAAGTTAGCAGCCTGAGC	42	#0_core	
05[154]	05[153]	AAAGGTGGCCAGTAGCAAGAAACGCAAAATCATAGAAATCATT	42	#0_core	
05[175]	05[174]	TGATATTAGTACCGTTACCACCGGAACCAACCTCAGGGCCT	42	#0_core	
05[196]	05[195]	CCACCACGATTTGTCGGGGTTTTGCTCCAATATAAGCAGAG	42	#0_core	
05[217]	05[216]	CGCATAAAATCGTCACTTTTTTACGTTCTTTAATGGCCCA	42	#0_core	
05[238]	05[237]	AAAGAGGTCTAATCTTATACCAAGCGCGCGATAAATCTTTG	42	#0_core	
05[259]	05[258]	GAGCAACAGTTTTGTCATGGGAAAGAAAAAATATTACAAGTAA	42	#0_core	
05[280]	05[279]	TTGCGGACATGCAACTTCAAAAGATTAACTAATTCGATTT	42	#0_core	
05[301]	05[300]	TTTTAGACAAGGGTGAATAATCATACAGGTGCTCAGAAAAAT	42	#0_core	
05[322]	05[321]	AATAATTTCAACCCCGCGTTGATAATACCAAAATATCAAA	42	#0_core	
06[048]	00[032]	TTTGAACTACTACAGGATTTAACCCGCGCG	31	#0_core	
06[069]	00[054]	TTTGATGCTTTGTTATTATTTCACGCTGCG	30	#0_core	
06[090]	00[074]	GCCTGTTCAAACTAATGGGGCGCTGGCA	31	#0_core	
06[111]	00[095]	GAATCTTTACGACTCTTATCAGCGAAAGGA	31	#0_core	
06[132]	00[116]	ACCCATGAAAAATCGGAAGCGGGCGAGAAAG	31	#0_core	
06[153]	00[137]	TCACCACAATCAAGCAAAGGACGGGGAAAG	31	#0_core	
06[174]	00[158]	AAATCACCCTTAATCAACCAAGGGCGAAA	31	#0_core	
06[195]	00[179]	GGGATAGGGTTGCAACTCAGGAGAACGTGGA	31	#0_core	
06[216]	00[200]	GGTCGAGGACCTCGTGAATTTGAAACAGAG	31	#0_core	

06[237]	00[221]	GTGTAATCGCCTGAGTACTTGGTTGAGTGT	31	#0_core
06[258]	00[242]	CCTCGACAACATAGAGGAATACAAAAGAATA	31	#0_core
06[279]	00[263]	TTAATCGCGTTTTAAACTCTCGGCAAAAT	31	#0_core
06[300]	00[284]	TTTTAAATAAAGGCAACATTATGTTGATGG	31	#0_core
06[321]	00[305]	TTCTGTATAAGCCAAAATTCGCCCAAGCA	31	#0_core
06[342]	00[326]	TCACATTAATTGCCTCACCAGAGCAAGCGGT	31	#0_core
07[021]	04[021]	CCTGAGTTAACCGTAAAAGAGCCAGAAT	28	#0_core
07[049]	07[090]	ATTATCATTGTTGATATTACCTTTTAAATGGACTTTTAG	42	#0_core
07[091]	07[132]	TATCATATGCGTCTAAATTACCGCGCCCAATAGAAAACAAGA	42	#0_core
07[133]	07[174]	ATTGAGTTAAGCTGTCGACTTGAGCCATTTGGGCAGACTCAT	42	#0_core
07[175]	07[216]	TAAAGCCAGAATCGAGAGCAAGCCCAATAGGAACAACTGAG	42	#0_core
07[217]	07[258]	GCTTCAGGAGGATATCCAGACCAGGCGCATAGGCGGATTAC	42	#0_core
07[259]	07[300]	CAGACGACGATAAATTGCTGAATATAATGCTGAAGCAATGC	42	#0_core
07[301]	07[342]	AATGCTGAGTAGATTGAGCCAGCTTTCATCACATAAAGTG	42	#0_core
08[048]	08[021]	ACTAGGAGCACTATCGGCCTTGTGGTA	28	#0_core
08[090]	08[070]	TACGAGAAAAACAGTACATA	21	#0_core
08[132]	08[112]	GCAACGTCACAAGCAAATCAG	21	#0_core
08[174]	08[153]	CTCCACCTAATTAGAGCCAGC	22	#0_core
08[216]	08[196]	TTAAGGCTCCCCATGTACCGT	21	#0_core
08[258]	08[238]	GCGAACTAACTGGCTGACCTT	21	#0_core
08[300]	08[280]	AGCAAAATTTAGCTCAACATG	21	#0_core
08[347]	11[347]	ATACGAGCCGGATCCTGTGATTCGTAATGCCTGCAGGT	38	#0_core
09[021]	15[048]	AACAGGAAAAACATAAGAATAATAGCCCTAAAAGTCGTTTG	42	#0_core
09[063]	09[062]	AACGGTCAATATCATAGAATCCTTGAGTCAGATATAAACAAT	42	#0_core
09[105]	09[104]	TAATAATAGAAGACGGAGGTTTTGAACAGAACGGCAGAAAAA	42	#0_core
09[147]	09[146]	ATAAGAAATCACCTTAGCAGCACCTCATACATGACCACGGA	42	#0_core
09[189]	09[188]	GATAACACTGAGAAAGTTAGCGTAACCCCTCAAGTCCAGGCG	42	#0_core
09[231]	09[230]	AACGGTCAAGAGTACATTCAGTGAATCACTCATCAAAGTAC	42	#0_core
09[273]	09[272]	GAAAGTTAAATAAGATTCTGCGAACGATAGTCAATGAAGCCC	42	#0_core
09[315]	09[314]	CAAAACGAGTAAATGTACGTTGGTGAACAGCGTAAAGCCC	42	#0_core
10[027]	11[048]	TGGAAATGATTATTACATTGGCAGATGAAAGGGA	35	#0_core
11[070]	11[090]	AATAACCTTGCTATGCTGAAC	21	#0_core
11[112]	11[132]	GTATTCTAAGAATTATCCCTA	21	#0_core
11[154]	11[175]	CATTACCATTAGCAGAGCCCA	22	#0_core
11[196]	11[216]	CAGTACAACTAATAATAACC	21	#0_core
11[238]	11[258]	CAAGAACCCGGATAGGACGTAA	21	#0_core
11[280]	11[300]	AGTACGGTGTCTATCCAATGA	21	#0_core
11[322]	05[342]	GGATTCTCCGTGGCATCATGCGCGGTTGCGCTCAC	35	#0_core
12[048]	18[028]	AGATGCAGTTTACCAGTACCCTGAAATATATTA	35	#0_core
12[090]	12[049]	AAATCGGTAATCTGTAATCGTCTACAGTTTCTGATTATC	42	#0_core
12[132]	12[091]	TTTTTTTATCGGAGGCGTTTTAGCGTTATGGCTTAATTGAG	42	#0_core
12[174]	12[133]	ATGATGAACCAAGCCGAAACGTCAGCAATTACCGAAGCCC	42	#0_core
12[216]	12[175]	ACGAGGCGACAACGCCGTAGCATTCTTAGACATGGCTTTTG	42	#0_core
12[258]	12[217]	AGTAAAGTCATTATTACCCAAATCACCCGACAGCATCGGA	42	#0_core
12[300]	12[259]	ATCAATAACGGAAGTTTATTCCATAAGCGAGAGGGGTAAT	42	#0_core
12[335]	12[301]	TTGGAACAACCGCGGATTTTCATAGTCAAATCAC	35	#0_core
13[049]	13[048]	AAATTCATGACTACCCTGAACTCAAAGCAAATCAAATGGC	42	#0_core
13[091]	13[090]	TTTAAACAGAAAAGTACTGAGAGACTACCCTATATCCATA	42	#0_core
13[133]	13[132]	AAGTAAGGCAATACCCTAACGAGCTCTGAGCCATAAAGAA	42	#0_core
13[175]	13[174]	AGTGACACGTTAATGCGGTATAGCCCTCATCACGACAGG	42	#0_core
13[217]	13[216]	CAACGGCCGTAATAAATACTTCAACAGTCAGGAATGGTAG	42	#0_core
13[259]	13[258]	TTAGACTAAATGCTTCTTAAATCATTGTTATACCAATGT	42	#0_core
13[301]	13[300]	TATTCAAAAACAAGGCATTTGGGGCGCCGTAGCATTATGA	42	#0_core
14[048]	14[049]	TGATTAGTTGGCGTCTAAAATATCTTACCAGAAAGATAATCC	42	#0_core
14[090]	14[091]	TAATTTTATATCTAGACAAGAAGCCAGTATCAACAATG	42	#0_core
14[132]	14[133]	ACAAAAATAAACCGGATTTTTTTTAAAGAAACCATAGCCGA	42	#0_core
14[174]	14[175]	TTTAAATCAAAGCCCTCAGAGCCGCTGAATTTAAATAAGT	42	#0_core
14[216]	14[217]	TGAGGCAACTAAATATCTCCAAAAAATGCGGGAACGAGGCTT	42	#0_core
14[258]	14[259]	AATACTGGCTCACTCGTTAATAAACGAGAGGAGGAGCGTCC	42	#0_core
14[300]	14[301]	GATAAAATAGTACAGCAAAGAAATAGATTCAAAGATCTAGCT	42	#0_core
14[342]	08[322]	TAAGTTGGGTAAAGAGCTTTAGACATTAAATGTG	35	#0_core
15[021]	12[021]	CGAACTGCGTGGCACTCTGAACGACCA	28	#0_core
15[049]	15[090]	GATTATACTCTTAAACAACATAGCGATAGCTTTGGGTAGGC	42	#0_core
15[091]	15[132]	AGAGGCATTTCAATGGCCTAAATCAAGATTAACAAGTTAC	42	#0_core

15[133]	15[174]	CAGAAGGAAACCAATAATCAGTAGCGACAGAATCATCGGGG	42	#0_core	
15[175]	15[216]	TCAGTGCCTTGAGACTGATCTAAAGTTTTGTCGGGAACTAA	42	#0_core	
15[217]	15[258]	AGACTTTTTCATAAAAAGGCTTGCCTGACGAGAACTGCGG	42	#0_core	
15[259]	15[300]	AATCGTCATAAATATTAGTAGATTTAGTTGACTACTATTAA	42	#0_core	
15[301]	15[342]	TGCCGGAGAGGGTAATAGATGGGCGCATCGTAATACGCCA	42	#0_core	
16[062]	16[021]	TTGAATAATGGAAAGGAATATCTCATCGCCATAAAAATACC	42	#0_core	
16[104]	16[063]	CTGAGCCAGTAATAAGCTTAGGTAGATTAAGACGCTGTGAGG	42	#0_core	
16[147]	16[105]	GAAGAGGAAACCAATAGCCAGTTGTTGCTATTTGCTTTCAG	43	#0_core	
16[189]	16[148]	TGAGTAACAGTGCCTGCATCTTTCAAGTTGCTTTCGTA	42	#0_core	
16[231]	16[190]	ACTGAGGAAAGTTTCCATATAGAAATCTTCCAGACGTTAGGC	42	#0_core	
16[273]	16[232]	GACTATTCAATGAATCCATTTAAGAAACACCGAAGCATAC	42	#0_core	
16[315]	16[274]	ATCTAGTATTTTTGAGTCAATCCATTAGATACATTTCCCT	42	#0_core	
16[347]	19[347]	CGGGCCTTCCGGCATTCCCGGAAACAGGAAGATCGC	38	#0_core	
17[021]	17[034]	TGAGGCGGTGAGTC	14	#0_core	
17[329]	16[316]	GCCATTCTACCGTGCATCTGCCGGTA	27	#0_core	
18[027]	19[062]	ACACCGCAATGAAAAATCTAAAGCATCACCTTGATCAAAATATTTGCA	49	#0_core	
18[062]	18[063]	AAATAAACAGAAATATAATTAATTTTCTCAATAGAACAG	42	#0_core	
18[104]	18[105]	AGACGACACCGCCTGTAACCTCCGACTTTACAATTTGTCC	42	#0_core	
18[146]	18[147]	TTATTACCAAAAAGGTGCCAATGAAACCCACGACTGTAACCTC	42	#0_core	
18[188]	18[189]	TTCTGAATGAGAAGGACACAGACGCCCTGAATTTTATTA	42	#0_core	
18[230]	18[231]	CCTAAAAACTTTGACACGTAACAAGCTGAATTGGGACCAA	42	#0_core	
18[272]	18[273]	ATAAATCGGGAAGCAATAACAGTTGATTAGGGTCAATTGACC	42	#0_core	
18[314]	18[315]	AGCAAACCCATGTCAAGACCGTAATGGGAAGGGGACGCTGG	42	#0_core	
19[063]	19[104]	CGTAATGAATTTATCAAAATCATAGGCGCAAAAAGGTAAGT	42	#0_core	
19[105]	19[146]	AATTCATCTGAACTTACCAACGCAAAAAGAACTGGCATGA	42	#0_core	
19[147]	19[188]	TTAAGGCGCGTTTTCATCGGCATTTCCCTGCCTATTTTCG	42	#0_core	
19[189]	19[230]	GAACCTGTATGGGATTTGCTAAACACGTAATGCCACTACG	42	#0_core	
19[231]	19[272]	AAGGCCTGAGATGGTTAATTTCAAAAACAGTTCAGAAAAC	42	#0_core	
19[273]	19[314]	GAGAAAACCTGTTAGCTATATTTTCTATCAGGTCATTGCCT	42	#0_core	
19[315]	12[336]	GAGAGACGACAGTATCGGCTCCAGGCAATCGCCAGGGTTTTGCCAAGC	49	#0_core	
11[049]	11[069]	ATTATCATATAAACAAGTATG	21	#1_bottom	B0
11[091]	11[111]	GCTCAACAGTAGCAACAATCG	21	#1_bottom	B1
11[133]	11[153]	GCAATAGCTATCCATATAAAC	21	#1_bottom	B2
11[176]	11[195]	GTAAGCGTCATGATTAGCAC	20	#1_bottom	B3
11[217]	11[237]	TCAGCAGCGAAAAGCGATTGA	21	#1_bottom	B4
11[259]	11[279]	AGAAGTTTTGCCGATTGCAAA	21	#1_bottom	B5
11[301]	11[321]	AAGGCCGGAGACATGTACTCT	21	#1_bottom	B6
08[069]	08[049]	AAATTGCCCGGAAACAAGAA	21	#2_top	T0
08[111]	08[091]	ATTCCCATCTATACAAAATCT	21	#2_top	T1
08[152]	08[133]	ATTTATTTCCAATAATAAGA	20	#2_top	T2
08[195]	08[175]	AAGTGCCGTGGAAGCGCAGT	21	#2_top	T3
08[237]	08[217]	CAAGATTTGTTAAAGCCGCT	21	#2_top	T4
08[279]	08[259]	TTACTTCAAAAACCAAAAATA	21	#2_top	T5
08[321]	08[301]	AGACAGGAAATGTGTAGGTAA	21	#2_top	T6
02[055]	02[035]	AATTTACAATAGATAATACAT	21	#3_left	L0
02[076]	02[056]	AAGCAAAAGCGCGACAGGGCG	21	#3_left	L1
02[097]	02[077]	CTACCGTGTATCTCTGACCT	21	#3_left	L2
02[118]	02[098]	ACGGTATAATAATCGGCTGT	21	#3_left	L3
02[139]	02[119]	AAGAATTAATAAACAATAAAA	21	#3_left	L4
02[160]	02[140]	CCCGATTGATTACCAAGCGCCA	21	#3_left	L5
02[181]	02[161]	CGGCCAGCATCAGAGCGGCCA	21	#3_left	L6
02[202]	02[182]	CGGCCACCCATAGGTGTATCA	21	#3_left	L7
02[223]	02[203]	CCTGATACCTCAGCTTGCTTT	21	#3_left	L8
02[244]	02[224]	ATGCGCAGACCGGACCTGCT	21	#3_left	L9
02[265]	02[245]	AAAATGCAAGTATCAGTTGAG	21	#3_left	L10
02[286]	02[266]	CATTAGAGAGAACCAGACCGG	21	#3_left	L11
02[307]	02[287]	TGACTTTTGAATCGTTGTAC	21	#3_left	L12
02[328]	02[308]	CTTGTTAAAACGTTAATATTT	21	#3_left	L13
17[035]	17[055]	AAACCTCAATCTTAGAACAA	21	#4_right	R0
17[056]	17[076]	TTGCGTAGATTAGAAGAGTT	21	#4_right	R1
17[077]	17[097]	TTTAACCTCCGGAGAATATCA	21	#4_right	R2
17[098]	17[118]	ATAAACACATGCCAGCTCC	21	#4_right	R3
17[119]	17[139]	AGAGCCTAATTTATAACGGAG	21	#4_right	R4
17[140]	17[160]	TATGTTAGCAAAAAGCGTCATT	21	#4_right	R5

17[161]	17[181]	ATTAGCGTTGCATAAACAAT	21	#4_right	R6
17[182]	17[202]	GAAAGTATTAAGAGTAAATTC	21	#4_right	R7
17[203]	17[223]	AGCGGAGTGAGATAAACGGAA	21	#4_right	R8
17[224]	17[244]	AGAGGCAAAGAAGTAGTAAA	21	#4_right	R9
17[245]	17[265]	TTACCTTATGCGCCCTCAAAA	21	#4_right	R10
17[266]	17[286]	ATCAGGTCTTTACGCAATCT	21	#4_right	R11
17[287]	17[307]	GAAAAGGTGGCAAGATCTAGA	21	#4_right	R12
17[308]	17[328]	GAATCGATGAACAGTTTGAGC	21	#4_right	R13
00[020]	00[005]	GCTACAGGGCGCGTAC	16	#5_ends	E0
00[361]	00[347]	TCACCGCTGGCCCT	15	#5_ends	F0
01[005]	01[020]	TATGGTTGCTTTGAGC	16	#5_ends	E1
01[347]	01[361]	ACAGCTGATTGCCCT	15	#5_ends	F1
02[020]	02[005]	TTAGAATCAGAGCGGG	16	#5_ends	E2
02[361]	02[347]	GCGGTTTGCCTATTG	15	#5_ends	F2
03[005]	03[020]	AGCTAAACAGGAGGCC	16	#5_ends	E3
03[347]	03[361]	AACGCGGGGGAGAG	15	#5_ends	F3
04[020]	04[002]	CCTGAGAAGTGTTTTATA	19	#5_ends	E4
04[358]	04[343]	GGGAAACCTGCTCGTG	16	#5_ends	F4
05[002]	05[020]	ATCAGTGAGGCCACCGAGT	19	#5_ends	E5
05[343]	05[358]	TGCCCGCTTCCAAGTC	16	#5_ends	F5
06[020]	06[002]	TGTAGCAATCTTCTTTGA	19	#5_ends	E6
06[358]	06[343]	TAATGAGTGAGCTAAC	16	#5_ends	F6
07[002]	07[020]	TTAGTAATAAACATCACTTG	19	#5_ends	E7
07[343]	07[358]	TAAAGCCTGGGGTGCC	16	#5_ends	F7
08[020]	08[005]	ATATCCAGAACAATAT	16	#5_ends	E8
08[361]	08[348]	CAATTCACACAAC	14	#5_ends	F8
09[005]	09[020]	TACCGCCAGCATTGC	16	#5_ends	E9
09[343]	09[361]	TGAAATTGTTATCCGCTCA	19	#5_ends	F9
10[020]	10[005]	ACCTACATTTTGACGC	16	#5_ends	E10
10[361]	10[343]	CCCCGGGTACCGAGCTCGA	19	#5_ends	F10
11[005]	11[020]	TCAATCGTCTGAAATG	16	#5_ends	E11
11[348]	11[361]	CGACTCTAGAGGAT	14	#5_ends	F11
12[020]	12[002]	GTAATAAAAGGGACATTCT	19	#5_ends	E12
12[358]	12[343]	TAAAACGACGGCCAGT	16	#5_ends	F12
13[002]	13[020]	GGCCAACAGAGATAGAACC	19	#5_ends	E13
13[343]	13[358]	CCCAGTCACGACGTTG	16	#5_ends	F13
14[020]	14[002]	CAGACAATATTTTGAATG	19	#5_ends	E14
14[358]	14[343]	TGTGCTGCAAGGCGAT	16	#5_ends	F14
15[002]	15[020]	GCTATTAGTCTTTAATGCG	19	#5_ends	E15
15[343]	15[358]	GCTGGCGAAAGGGGA	16	#5_ends	F15
16[020]	16[005]	GAACGAACCAACAGCA	16	#5_ends	E16
16[361]	16[348]	AAGGGCGATCGGTG	14	#5_ends	F16
17[005]	17[020]	GAAGATAAAACAGAGG	16	#5_ends	E17
17[343]	17[361]	AGGCTGCGCAACTGTTGGG	19	#5_ends	F17
18[020]	18[005]	CTGCAACAGTGCCAGC	16	#5_ends	E18
18[361]	18[343]	TCCGGCACCGCTTCTGGTG	19	#5_ends	F18
19[005]	19[020]	CTGAGAGCCAGCAGCA	16	#5_ends	E19
19[348]	19[361]	ACTCCAGCCAGCTT	14	#5_ends	F19

Supplementary Table 2
List of DNA staples - Origami Q

Start	End	Sequence	Length	Type	Pos.
00[031]	03[027]	ACAGGGCGCGTACTTTCTCGAGCGGAGACAG	32	#0_core	
00[053]	06[049]	CCCGCCGCGTTATTACAAACAATTTGAGTAAC	34	#0_core	
00[073]	06[070]	CGCTGCGCTACTGAGCAAAAGAGATTGTAA	32	#0_core	
00[094]	06[091]	GCGCTGGCAAGTACCGACCGTGTATGCCTGT	32	#0_core	
00[115]	06[112]	AGCGAAAGGAGCAGAACGGGTATTAAGGAATC	33	#0_core	
00[136]	06[133]	TGGCGAGAAAGGAGACGGGAGAATTAAGATAACC	34	#0_core	
00[157]	06[154]	AACCGTCTATCATTCAACCGATTACACCGTCA	32	#0_core	
00[178]	06[175]	ACTCCAACGTGAGCCCGCCGCACTAATAAAT	32	#0_core	
00[199]	06[196]	AGTCCACTATTATTTAGTACCCCGCATTTTCA	33	#0_core	
00[220]	06[217]	GTTGTTCCAGTTTCTTAAACAGTGTATAT	32	#0_core	
00[241]	06[238]	ATAGCCCGAGTACTTAGCCGGAACAGGACAGAT	34	#0_core	
00[262]	06[259]	AAATCCCTTATAAATACCACATTCCCAACACTA	33	#0_core	
00[283]	06[280]	GATGGTGGTTCACTCCAACAGGTGTGGATGGC	32	#0_core	
00[304]	06[301]	CCAGCAGGCGAACATTATGACCTTAGAACCTT	32	#0_core	
00[325]	06[322]	AAGCGGTCCACGAAAATTCGCATTGGAAATCCG	33	#0_core	
00[346]	01[346]	CTGGCCCTGAGATTTCACCACTGA	24	#0_core	
02[034]	07[048]	AGAATCAGTTAGTAGTGTAGTATCGGCCTTGGATTCAATTT	43	#0_core	
02[346]	02[329]	GCGTATTGGGCGCCAGG	17	#0_core	
03[028]	03[063]	GAACGGTACGCCTACATTCGTATTAATCCGCG	34	#0_core	
03[064]	03[105]	CAGAGAAAACAACATCAATCTTCTAAGCGTTAAATAAATA	41	#0_core	
03[106]	03[147]	ATCGTACCGCACTCATCGAATAACCCCTGAACAAAGGTT	40	#0_core	
03[148]	03[189]	TACCGGAAGGTAATATCCCTCAGCAGGAGTTGAGGCGGA	41	#0_core	
03[190]	03[231]	ATAGAACCGCCACCTATCGGTTCCGATAGTTGCGCCTGT	40	#0_core	
03[232]	03[273]	CGAAGACGGTCAATCATGTAGAAGCAGATACATAACGAG	39	#0_core	
03[274]	03[315]	CTTCAGAGAGTACCTTTGAGCATACTTTGCGGGAGAAATT	41	#0_core	
03[316]	03[346]	TAATGTTAAATCAGCTCGCTGCATTAATG	29	#0_core	
04[048]	10[028]	GTTAATAAAGAACTCTGAGAGCAAAATCTACATT	34	#0_core	
04[090]	04[049]	GAATCTTTCAGAAAAAAAATAAATCTTTGCCCGAAC	40	#0_core	
04[132]	04[091]	TGAGGAGAGAGAAACAAGCAAGCCGATCAGAATAAACACCG	40	#0_core	
04[174]	04[133]	TGGCCACCATGACGGAATTTATCATATGTCAGAGGTAAT	41	#0_core	
04[216]	04[175]	AACCATGTGAGAACCCACCTGCCAGGTGACAGCAT	40	#0_core	
04[258]	04[217]	TTACACAGAAGGGAAACCGAACTGAATTGGACAATGACAAC	40	#0_core	
04[300]	04[259]	ACGCACTCAAATGCTCCTTTGATATTGCCAAAAGGAA	40	#0_core	
04[342]	04[301]	TCGTGCCAATTTTTAACCAATAGAAATGCCCTTATTCA	40	#0_core	
05[049]	05[048]	TTTTAAAAATATCATCTATCTAAAATAATAATCAATAGTTAAT	42	#0_core	
05[070]	05[069]	TTAACAAACAGAAATAACATCGGGAGAAACGTGTACAATACAT	42	#0_core	
05[091]	05[090]	TACTAGAAAACGCTCAACCAATCGCAAGATTAGTTAAATAAT	42	#0_core	
05[112]	05[111]	ATTTTCAGACCGGTATGCTGCTGAACAAGAAGAACCAATTTTT	42	#0_core	
05[133]	05[132]	AAATACAAAAATAGCAAAATAAGAAACTCCTTTACACGCT	40	#0_core	
05[154]	05[153]	GGTGAATTGCGACCATACGCAAGACACGAAAATTCATAAA	42	#0_core	
05[175]	05[174]	ATTCACAACGTTCCAGCCGGAACCGCTAAGAGCCTTGAT	40	#0_core	
05[196]	05[195]	CCACCCTTTTCGTCAGTTTTCAGTAAAAGTATACAGAG	42	#0_core	
05[217]	05[216]	CACGCATCGGATCGTCAATTTTTTCAGCCCTTTAATCGCC	42	#0_core	
05[238]	05[237]	CTTGAAAAGAGTAATATTATACCAAGAACTGATAACCAA	40	#0_core	
05[259]	05[258]	ATAGTAAAGAGGCTTTAGCTGGGAAAGGATTTATGAGGC	42	#0_core	
05[280]	05[279]	GTCAATTTAAAAATATGTTGCATCAAAAGAGTTTAAAGAG	40	#0_core	
05[301]	05[300]	AAAAATTTGTTCAAAATCCAATAATCATTATAAAGCAGGAT	42	#0_core	
05[322]	05[321]	CCATCAATACGAGTAAATGTACCCCGTTTTATAAGCGAACG	42	#0_core	
06[048]	00[032]	ATTATAGAGCCGCTTAGACTATGCCCGCT	31	#0_core	
06[069]	00[054]	TTACCATACCAATTCAATTACACCAACACA	30	#0_core	
06[090]	00[074]	TAGTATATATTTCTTTGAAATGTAGCGGTCA	32	#0_core	
06[111]	00[095]	ATTACGCATGTAAACATTCAGGGCGCTAGG	31	#0_core	
06[132]	00[116]	CACAAAGTAGCAGCGTGCATTAAAGGGAAGAA	32	#0_core	
06[153]	00[137]	CCGACCAATAGAGAGGGCGACACGGCGAACG	31	#0_core	
06[174]	00[158]	CCTCACCCCTCTCCACCACAAAAGGGCGAAA	34	#0_core	
06[195]	00[179]	GGGATTTGATATCACAGGAGGAAGAACGTGG	31	#0_core	
06[216]	00[200]	TCGGTAAAGGAGTCAGGTGAATTGGAACAAG	31	#0_core	

06[237]	00[221]	GAACGGTCATGCCCCCATGTTAGGGTTGAGT	32	#0_core
06[258]	00[242]	TCATAGGAACAAGATTTAGGAATCAAAAAGA	31	#0_core
06[279]	00[263]	TTAGAAATATCGCGCGGAAGCAACGAAATCGGCA	34	#0_core
06[300]	00[284]	CATATTTAAGCAGCACCAAAAAATCCTGTTT	32	#0_core
06[321]	00[305]	GTCTGAAGATTGTATTTTGTCTGGTTGCC	31	#0_core
06[342]	00[326]	GCTAACTCAGTATTTTTCTGAGTTGCAGC	32	#0_core
07[021]	04[021]	ACTCAAACCAACTTCTCACAGTGT	28	#0_core
07[049]	07[090]	GCGGAACAAGATTGATTTTTTAATGGAAACAGTCAATCATA	43	#0_core
07[091]	07[132]	TGCGTTATACAACGACGCGCCCAATAGCAAGCAAAAAAATTGA	44	#0_core
07[133]	07[174]	GTTAAGCCCAATCAATTTGAGCCATTTGGGAATTACCGTTAAA	43	#0_core
07[175]	07[216]	GCCAGAATGGAAGGGAGCAAGCCCAATAGGAACCTCACGCTG	43	#0_core
07[217]	07[258]	AGGCTTGCAGGGTGTATGTACAGACCAGCGCATTAAACCCCTC	44	#0_core
07[259]	07[300]	GTTTACCAGACGATTACGCTTAATTGCTGAATATAAAAAATTTT	44	#0_core
07[301]	07[342]	AAATGCAATGCCAGGGCCTTCTGTAGCCAGCTCCGGAAGCAT	44	#0_core
08[048]	08[021]	GAACTAATATGGTAATATCCAGAACAATA	30	#0_core
08[090]	08[070]	ATACTTTTTACATAAATCAATA	22	#0_core
08[132]	08[112]	AACAAAAATGAATCAGATATAG	22	#0_core
08[174]	08[153]	GACCTCAGAAGAGCCAGCAAAAAT	23	#0_core
08[216]	08[196]	CTAAAAGGCCATGTACCGTA	21	#0_core
08[258]	08[238]	AAAAACGACAGGCTGGCTGAC	22	#0_core
08[300]	08[280]	AGAATTAGCATGCTGTAGCTCA	22	#0_core
08[347]	11[347]	CACACAACATACGATAGCTGTGAGCTCAGCTTGCATGC	38	#0_core
09[021]	15[048]	CATGGAAATACCTTTCACAGACTCGCCATTAATCAATATACT	44	#0_core
09[063]	09[062]	CGCCTTGTGAGTAACTTGAACACATAATATACCTACGGATT	42	#0_core
09[105]	09[104]	CCCATGGCTTATTTTTTGAAGCCTTCGCTGTTGATAATAT	42	#0_core
09[147]	09[146]	TTTATACCAGTACCAGCACCGTAATAAAGGAGGAATAAG	42	#0_core
09[189]	09[188]	AAGTGACTGAGTGAATGTTAGCGTAAAGAGAATAGCGGAT	42	#0_core
09[231]	09[230]	GTACAATCAAAAAGTCTCATTAGTAACTCTAAAACAAA	44	#0_core
09[273]	09[272]	AGCCCATGTTTTCAATTCCTCTCTATATAAGTAAGAGGA	44	#0_core
09[315]	09[314]	AAAGCATGTGAGATTGGGATAGGTCATCGTAAATCAATCAGA	42	#0_core
10[027]	11[048]	TTGACGAGATTCCAGCTCACAGGAAGTAT	32	#0_core
11[070]	11[090]	TGCTTCTGTAATGCAAAATC	20	#0_core
11[112]	11[132]	TAAGAACGCGAGCAATCCAT	20	#0_core
11[154]	11[175]	CCATTAGCAAGGCCACCAATA	21	#0_core
11[196]	11[216]	AGTACAACTAGAATAATAC	20	#0_core
11[238]	11[258]	TGACAAGAACCAGTTCAGGTG	20	#0_core
11[280]	11[300]	ACTAAAGTACGATTAACAGG	20	#0_core
11[322]	05[342]	ACCCGTGCGATTGAGAAATCGAAATTCGCTTGC	34	#0_core
12[048]	18[028]	CAATTGAGGACCAGTAATAAAGAATACATAACAG	34	#0_core
12[090]	12[049]	ATATTCTGAATCGTCGCTAATAATTGTACTCAGATGATGG	40	#0_core
12[132]	12[091]	AAGAATCCGCTTTTTCAGCAACCTCAATTTGAGAATCGCC	40	#0_core
12[174]	12[133]	TACAGCAGAGCCGAAACGTCACCAATATGAAGCCCTTTTT	41	#0_core
12[216]	12[175]	GAACGTTGCCAACGCTGTAGCATGATTGGCTTTTGATGA	40	#0_core
12[258]	12[217]	GGTAACCAGATATTCATTACCAAAACCAAGACAGCATCG	40	#0_core
12[300]	12[259]	ATCACTAGCGTGTCTGGAAGTTTCAAGCATTGCCAGAGGG	40	#0_core
12[335]	12[301]	GCCTCCGTGGGAACAACTGTCGGAGACAGTCAA	34	#0_core
13[049]	13[048]	AATATAAGTCAAAATATCAAAACCTCAGTAAGGAATTCATC	42	#0_core
13[091]	13[090]	ACGCCAAAACGACAAAGACTACCTTTTTGAGTAAATGTAACA	42	#0_core
13[133]	13[132]	TAAGCAGATCAAAAAGAGCGCTTTCCGAAATTTTAAAG	40	#0_core
13[175]	13[174]	TACTGGTTGATGCCCCATAGCCCTATCGGAACGAGTG	40	#0_core
13[217]	13[216]	AGCAACGAAGGGTAAACAACCTTCAACCAAGGAAAGGGT	42	#0_core
13[259]	13[258]	AAAATGTTATCAAAATGTCAACTTTAATCAATCATTATAGT	42	#0_core
13[301]	13[300]	ATATGATAGGATCTACATTTTCATTTGGGTATAGTAGCATCA	42	#0_core
14[048]	14[049]	TGGATCAGTTGAGGAGGAGCACTAACGCGGAATAGATTGTT	42	#0_core
14[090]	14[091]	GGCAGACTATATGAAACGAGAAAAAGCCAAATAATTTA	42	#0_core
14[132]	14[133]	AAGTTACAGCCATGTTTTGTTAACGTACAATGACGCCGAACA	44	#0_core
14[174]	14[175]	ACGGGAAAATCACAGTCAAGCCGCCCACTTACCCAAGTTTTA	44	#0_core
14[216]	14[217]	TTTGAACAACCTCAAAATCTCCAAAATTTGCGGCGCAGAGGC	42	#0_core
14[258]	14[259]	AGCGTAACTGGCAGTCTACGTTAATATAGCAGATAGTGGAT	42	#0_core
14[300]	14[301]	CTAGCTCTACTTGGGCAAGGCAAGGTAAGAAATAACCGTT	42	#0_core
14[342]	08[322]	GGCGATTAAAGTTGAAACATGCTGAGTTCATCAACATT	36	#0_core
15[021]	12[021]	CTAAAACAATATTTAGCGTAAAGGGA	28	#0_core
15[049]	15[090]	TCTGAATAATGGGATGAGCGATAGCTTAGATTAATATAAGGCA	43	#0_core
15[091]	15[132]	TTTTCGAGCCAGAAATCAAGATTAGTTGCTTAAACCAGAA	44	#0_core

15[133]	15[174]	GGAAACCAGGAATACCAGTAGCGACAGAATCAAATCGTCAG	43	#0_core	
15[175]	15[216]	TGCCTTGAGTAACTCACGATCTAAAGTTTTGTCAAGGGGACT	43	#0_core	
15[217]	15[258]	AAAGACTTTTTCTCAAGAATAAGGCTTGCCTGATAAGCCAATA	44	#0_core	
15[259]	15[300]	CTCGGGAATCGCTGAGCGAACGAGTAGATTTAGCAATTGATA	44	#0_core	
15[301]	15[342]	AATTAATGCCGGTAACTGTGGTGTAGATGGCGCTTCGCTATT	44	#0_core	
16[062]	16[021]	CAAAGGGTTAGAACTTTGGCAAAATACCGAACCAACCACGAGC	44	#0_core	
16[104]	16[063]	AGTAATAAGAGAATATTGGGTTAGACCTGAGAAAGGTAACGT	43	#0_core	
16[147]	16[105]	TACAACGCAATAAATACTACAAAATTTGCACCAGCTAATGC	45	#0_core	
16[189]	16[148]	ACTCAGTGCCTGATAATTTTCATGTTGCCCTTAGCGTAAAA	43	#0_core	
16[231]	16[190]	ACAATGAGGAAGTTTCCGAATAGAGTCTTCCAGACGTCTGAG	43	#0_core	
16[273]	16[232]	ACCATAAATATTATTGATGCGATTTCGAGAAACACCAGAAGAAT	45	#0_core	
16[315]	16[274]	ACGAGAGGGTAGCTATTGTGGCATTTTGACCATTAGATACTTT	43	#0_core	
16[347]	19[347]	GATCGGTGCGGGCGGCCATTTCTGGTCGGCCTCAGG	38	#0_core	
17[021]	17[034]	TAACACCGCCTGCCA	15	#0_core	
17[329]	16[316]	AGGCAAATCATCGTAACCTGCGCATGA	28	#0_core	
18[027]	19[062]	TGCCACGCATCACTTGTGAACCTCAAATATTTGCACGTAAAA	45	#0_core	
18[062]	18[063]	AAATGTCTCAGTAACAAATTTCCCTTAAAGAAATTTATAAG	42	#0_core	
18[104]	18[105]	CGACAATCATTAACCCGACTTCCGGAGTTATCCTGACGA	42	#0_core	
18[146]	18[147]	ACGCAGTATTGGCAACATGAAACCATCGTATAGCGCTTATT	42	#0_core	
18[188]	18[189]	TGAAACAAGGATAGTCCACAGACAGCAGTGAATTTTATTTC	42	#0_core	
18[230]	18[231]	CCAACTGCATCTTTGATCAACGTAACTGTAATTTGGCA	40	#0_core	
18[272]	18[273]	TGACCATTGTGAGTTCATATAACAGGCAATGGGAGAA	40	#0_core	
18[314]	18[315]	AGTCTGGACTAGCAGGCGGATTGACCAAAGTTGACTGAG	42	#0_core	
19[063]	19[104]	AGAAATCAAATCATAGTCTGGAAGGTAAGTAATCTG	41	#0_core	
19[105]	19[146]	TCCAGAATCTTCAACCGCTAACGAACCTGGCATGATTAAG	40	#0_core	
19[147]	19[188]	ACTCCTTTTATCGGCATTTTCGGTCTGCTATTTCCGGAAC	41	#0_core	
19[189]	19[230]	CTATTCTGTATGGGATTTGCTAAATACGTAATGCCACTA	40	#0_core	
19[231]	19[272]	CGAAGGGCTGAGATGGTTAATCTTTAAACAGTTCAG	39	#0_core	
19[273]	19[314]	AAAATCAATAACCTGTTAGCTATAAAGGCTATCAGGTCA	41	#0_core	
19[315]	12[336]	TTGCGGGGACGACGACAGTATGCCGAGTGGAACGCCAGGCCAGT	46	#0_core	
11[049]	11[069]	ATTCTGATTACTTTTACCT	20	#1_bottom	B0
11[091]	11[111]	AGTAGGGCTTAAAGATAATC	20	#1_bottom	B1
11[133]	11[153]	AGCTATCTTACCAAAGAATA	21	#1_bottom	B2
11[176]	11[195]	GCGTCATACATAGCGGGCC	19	#1_bottom	B3
11[217]	11[237]	CCTCAGCAGCACCAGCGCT	20	#1_bottom	B4
11[259]	11[279]	CAAAAGAAGTTAAGCGGACA	20	#1_bottom	B5
11[301]	11[321]	GTGAGAAAGCCCAATCATCA	20	#1_bottom	B6
08[069]	08[049]	TAGATTGCTAACCCAGAAAG	21	#2_top	T0
08[111]	08[091]	AACCTAATTTATCTTACCAGT	22	#2_top	T1
08[152]	08[133]	CTTTGTCAAATAAGAGCAAG	20	#2_top	T2
08[195]	08[175]	ACCCGTGAGAGCGCACTCTCT	22	#2_top	T3
08[237]	08[217]	CTCGGAGATTAGTTAAAGGCCG	22	#2_top	T4
08[279]	08[259]	ACGAAAGACCGATAAAAACCAA	22	#2_top	T5
08[321]	08[301]	AACCCAAAATGAGTAATGTGT	22	#2_top	T6
02[055]	02[035]	ATCGACAACGAGGATTAGA	21	#3_left	L0
02[076]	02[056]	ATAGATGATGGCAATTAATTC	21	#3_left	L1
02[097]	02[077]	TTGATAAATGACCTAAATTTA	21	#3_left	L2
02[118]	02[098]	GGAAACCAAGGCTGCTCTCC	21	#3_left	L3
02[139]	02[119]	AAAATGAACATAAAAACAG	20	#3_left	L4
02[160]	02[140]	GAGAGGGAGAGCGCAAAGAC	21	#3_left	L5
02[181]	02[161]	TAGCATTGAAGCCGCCACCA	20	#3_left	L6
02[202]	02[182]	TTACCTCAGGTGTATCACC	21	#3_left	L7
02[223]	02[203]	TGCTTGATATATCAGCTTGCT	21	#3_left	L8
02[244]	02[224]	TGGAGGCGCAATCCGCGCAC	20	#3_left	L9
02[265]	02[245]	GAACTAATAGATTATCAGT	21	#3_left	L10
02[286]	02[266]	TTCAGGATTAAGCGGAACCA	20	#3_left	L11
02[307]	02[287]	AATGTAATAAAGCTAAATCGG	21	#3_left	L12
02[328]	02[308]	GTAATTTTATTGTAACGTT	21	#3_left	L13
17[035]	17[055]	ATATCTGGTCAGACCATATAG	21	#4_right	R0
17[056]	17[076]	ATTTTCAGGTTTCAATAGTCC	21	#4_right	R1
17[077]	17[097]	TCCGGCTTAGGTAAGTACAC	21	#4_right	R2
17[098]	17[118]	AACATGTTCAAGTACAATTAG	21	#4_right	R3
17[119]	17[139]	CCTAATTGCCCAGGGAATACGT	22	#4_right	R4
17[140]	17[160]	TAGCAAACGTAGCAGACTGTT	21	#4_right	R5

17[161]	17[181]	AGCGTTTGCCATCACAGTTAAA	22	#4_right	R6
17[182]	17[202]	AGTATTAAGAGGTAGTAAATT	21	#4_right	R7
17[203]	17[223]	TCAGCGGAGTGAATTAACAAA	21	#4_right	R8
17[224]	17[244]	CGAAAGAGGCAAAACGAGTATG	22	#4_right	R9
17[245]	17[265]	TGAATTACCTTAATCCCCCAA	21	#4_right	R10
17[266]	17[286]	TCAAAAATCAGGTCATTTCCGG	22	#4_right	R11
17[287]	17[307]	CGAGCTGAAAAGTTTGAGACA	21	#4_right	R12
17[308]	17[328]	AACAAGAGAATCATCTGCCCC	21	#4_right	R13
00[020]	00[005]	CTATGGTTGCTTTGAC	16	#5_ends	E0
00[361]	00[347]	ATTGCCCTTCACCGC	15	#5_ends	F0
01[005]	01[020]	GAGCACGTATAACGTG	16	#5_ends	E1
01[347]	01[361]	GACGGCAACAGCTG	15	#5_ends	F1
02[020]	02[005]	GAGCTAAACAGGAGGC	16	#5_ends	E2
02[361]	02[347]	GGGGAGAGCGGTTT	15	#5_ends	F2
03[005]	03[020]	CGATTAAGGGATTTT	16	#5_ends	E3
03[347]	03[361]	AATCGGCCAACCGCC	15	#5_ends	F3
04[020]	04[002]	TTTATAATCAGTGAGGCCA	19	#5_ends	E4
04[358]	04[343]	CCAGTCGGGAAACCTG	16	#5_ends	F4
05[002]	05[020]	CCGAGTAAAAGAGTCTGTC	19	#5_ends	E5
05[343]	05[358]	GCTCACTGCCCGCTT	16	#5_ends	F5
06[020]	06[002]	CTTTGATTAGTAATAACAT	19	#5_ends	E6
06[358]	06[343]	GGTGCCTAATGAGTGA	16	#5_ends	F6
07[002]	07[020]	CACCTGCCTGAGTAGAAGA	19	#5_ends	E7
07[343]	07[358]	AAAGTGTAAGCCTGG	16	#5_ends	F7
08[020]	08[005]	TTACCGCCAGCCATTG	16	#5_ends	E8
08[361]	08[348]	TCCGCTCACAATTC	14	#5_ends	F8
09[005]	09[020]	CAACAGGAAAAACGCT	16	#5_ends	E9
09[343]	09[361]	TTCCTGTGTGAAATTGTTA	19	#5_ends	F9
10[020]	10[005]	CTCAATCGTCTGAAAT	16	#5_ends	E10
10[361]	10[343]	TAGAGGATCCCGGGTACC	19	#5_ends	F10
11[005]	11[020]	GGATTATTTACATTGG	16	#5_ends	E11
11[348]	11[361]	CTGCAGGTCGACTC	14	#5_ends	F11
12[020]	12[002]	CATTCTGGCCAACAGAGAT	19	#5_ends	E12
12[358]	12[343]	ACGTTGTAAAACGACG	16	#5_ends	F12
13[002]	13[020]	AGAACCCTTCTGACCTGAA	19	#5_ends	E13
13[343]	13[358]	GGTTTTCCCACTCAGC	16	#5_ends	F13
14[020]	14[002]	TGAATGGCTATTAGTCTTT	19	#5_ends	E14
14[358]	14[343]	GGGGATGTGCTGCAA	16	#5_ends	F14
15[002]	15[020]	AATGCGCGAACTGATAGCC	19	#5_ends	E15
15[343]	15[358]	ACGCCAGCTGGCGAAA	16	#5_ends	F15
16[020]	16[005]	AGAAGATAAAACAGAG	16	#5_ends	E16
16[361]	16[348]	CTGTTGGGAAGGCC	14	#5_ends	F16
17[005]	17[020]	GTGAGGCGGTCAAGTAT	16	#5_ends	E17
17[343]	17[361]	CGCATTCAAGGCTGCGCAA	19	#5_ends	F17
18[020]	18[005]	GCTGAGAGCCAGCAGC	16	#5_ends	E18
18[361]	18[343]	GCCAGCTTCCGGCACCCG	19	#5_ends	F18
19[005]	19[020]	AAATGAAAAATCTAAA	16	#5_ends	E19
19[348]	19[361]	AAGATCGCACTCCA	14	#5_ends	F19

Supplementary Table 3
List of DNA staples - Origami H

Start	End	Sequence	Length	Type	Pos.
00[031]	03[027]	GTACTATGGTTGTTAGAATCCTAAACCGGTAC	32	#0_core	
00[053]	06[049]	GCTTAATGCGCCGAATTCGACAACCTTATTACAT	34	#0_core	
00[073]	06[070]	CGTAACCACCACAAGAAGATGATAAATTACCT	33	#0_core	
00[094]	06[091]	CAAGTGTAGCGCGTGTGATAAATACAGTTTAGTA	34	#0_core	
00[115]	06[112]	AGGAGCGGGCGGTATTAACCAAAATTCATTAC	33	#0_core	
00[136]	06[133]	AGAAAGGAAGGGGAGAATTAACGACGCCACA	34	#0_core	
00[157]	06[154]	AACCGTCTATCACCATTGAGGGCACACCGAC	32	#0_core	
00[178]	06[175]	ACTCCAACGTCGCCGCCAGCACAAATAAA	32	#0_core	
00[199]	06[196]	GAGTCCACTATTGTTAGTACCCGGCGTCAITTTTC	35	#0_core	
00[220]	06[217]	GTGTTGTTCCACTTAAACAGCTTCCATATATT	32	#0_core	
00[241]	06[238]	AGAATAGCCCGATTAGCCGGAACGAGAGACAGAT	34	#0_core	
00[262]	06[259]	GGCAAAATCCCTATACCACTTACGACACTAT	33	#0_core	
00[283]	06[280]	GTTTGATGGTGTCCAACAGGTCTTGATGGCT	32	#0_core	
00[304]	06[301]	TGCCCCAGCAGAAACATTATGACCGTTTTTAGA	34	#0_core	
00[325]	06[322]	GCAGCAAGCGGTTTTGTTAAAATCCCAAAAAT	33	#0_core	
00[346]	01[346]	CACCGCTGGCCTTTTCTTTTCA	24	#0_core	
02[034]	07[048]	ACGGGAGAGAGCTCAATACTCTTGCTGTAATACCGTGAACA	44	#0_core	
02[346]	02[329]	GCGGTTTGCATTGGG	17	#0_core	
03[028]	03[063]	GCCAGAATCCTAGGATTAATCCTTTGCCGCGC	33	#0_core	
03[064]	03[105]	AATACATCAAGAAAACGACCTAATAAATAAGAATAAGCT	39	#0_core	
03[106]	03[147]	GTCACTCATCAGAACCATAAAGAACAAAGTCAGACCA	38	#0_core	
03[148]	03[189]	GCCGCTAAATATTGACGTGAGAGGGAGTTGAGGCACGG	39	#0_core	
03[190]	03[231]	AATAGAACCCTCCCGGTTTATATAGTTGCCCGCATCG	39	#0_core	
03[232]	03[273]	AAAACGGTCAATCATATAGAAAACAGATACATAACGAGC	38	#0_core	
03[274]	03[315]	TTCAGAGAGTACCTTTAAGAGCATACITTTGCCGGACAA	39	#0_core	
03[316]	03[346]	ATAATTTTGTAAATGTGCCAGCTGCA	28	#0_core	
04[048]	10[028]	TTTTTTGGAGAAAGTGTTAACCGTTGCCGCTC	33	#0_core	
04[090]	04[049]	ATAATTTCTAAAATTAATTACATTAGAGAACGTTATTA	39	#0_core	
04[132]	04[091]	CGCTATAAAAGCAAGCGTTTTTTCGACACCCGGAATC	38	#0_core	
04[174]	04[133]	TGGCACCCGAAATTTACCTTAAATTTAGGGTAATTGAG	39	#0_core	
04[216]	04[175]	ACCATTATCTCAGAACCCTCCAGCCGGTCAGACGAT	39	#0_core	
04[258]	04[217]	TACGCAAGAGGGAACCAACTGATGTGCAATGACAACA	38	#0_core	
04[300]	04[259]	TTCACTCATTTGCTCCTTTTGATATTCGCCAAAAGGAAT	39	#0_core	
04[342]	04[301]	AACCTGTCCAGCTCAATTTTAAATAAGGAAGCCTTTAT	38	#0_core	
05[049]	05[048]	TTTGAGTGGTATTCCTATATCTTTAGGAGTTAATACAAAAAG	42	#0_core	
05[070]	05[069]	ATTTCAATCGCTTGTGAAACAATAACAATCGCGCTAACCA	40	#0_core	
05[091]	05[090]	GAAAAAATCAGTAGCAAGACAAGAATTTTTCATCTACTA	40	#0_core	
05[112]	05[111]	CATCGTATTTCTAAGAAACAAGAAAAATAGCATCAATAATTTT	42	#0_core	
05[133]	05[132]	TCAGAGAAAAATAGCTGAAACGATTTTGGAGAGAGAAAAATA	40	#0_core	
05[154]	05[153]	ATTATCACTATTACCAAGACACCAGGACATATGGGGTGA	42	#0_core	
05[175]	05[174]	TATCACTATTCAGTGAACCGCTCCCGCCACCCCTTGA	40	#0_core	
05[196]	05[195]	GCCACCAACGTCACGTTTTTGCTCAGAATAAGTATTCAGA	40	#0_core	
05[217]	05[216]	ACGCATACGCGTCACTTTTTTACGTTGACTTAATTGCGCCC	42	#0_core	
05[238]	05[237]	CTTGAAAAAGTAATCTTATACCAAGCGAGATAAATCCAA	40	#0_core	
05[259]	05[258]	TAGTAAGGAGGCTTTTCGTTGGGAAGAAAGATTATTAAGGCA	42	#0_core	
05[280]	05[279]	TCATTTTATAATATGCTGCATCAAAAAAGTTTTAAAGAGG	40	#0_core	
05[301]	05[300]	AGGATACCGATTCAATCCAATAAATCTGAATAAAGACGCA	40	#0_core	
05[322]	05[321]	AGGAACCGAGTGAGCGATCATATGTACCAAGATTGTACCAAT	42	#0_core	
06[048]	00[032]	TTTGCCAAATAGAAAGTACAAACCTACAGGGCGC	32	#0_core	
06[069]	00[054]	TTTTTTACAAAACACCTGAGCAACCGCCGC	32	#0_core	
06[090]	00[074]	TCATATAGTTAAGATACCGAGCTCACGCTGCG	32	#0_core	
06[111]	00[095]	CGCGCAAAACCACTAGAACCGGTAGGGCGCTGG	32	#0_core	
06[132]	00[116]	AGAATTCCTTTACAATAGACGGAAGAAAGCGAA	33	#0_core	
06[153]	00[137]	TTGAGGAAAAATTTAACATCAAGAACCTGGCG	32	#0_core	
06[174]	00[158]	TCCTCCCTCAGAGTCCACCAGAAAAGGGCGAAA	34	#0_core	
06[195]	00[179]	AGGGAGTTGATAACTCAGGAGAAAAGAACGTGG	32	#0_core	
06[216]	00[200]	CGGTCGGAGCTCTGAATTTGTTGGAACAA	32	#0_core	

06[237]	00[221]	GAACGGATCGCCTCGATGTTACGATAGGTTGA	33	#0_core
06[258]	00[242]	CATAAGAACCAACAGTTTAGGATATAAATCAA	32	#0_core
06[279]	00[263]	TAGAGATATCGCGCAGAAGCAAAGTTCCGAAATC	34	#0_core
06[300]	00[284]	ACCCTATTAAAGCCGGTACCAAGCGAAAAATCCT	32	#0_core
06[321]	00[305]	AATTCACAGAAAAATAATATCCACGCTGGTT	32	#0_core
06[342]	00[326]	AGTGAGCTAACTCATAGGTTGGCTGAGAGATT	33	#0_core
07[021]	04[021]	CTATCGGCTCTTTGATCAAATTTATAA	28	#0_core
07[049]	07[090]	AAGAAAACCCACAAGAATGAAAACAGTACATAAAATTTGCGT	44	#0_core
07[091]	07[132]	TATACAAATCTTTGTACCAATAGCAAGCAAATCAGGCAGGAGTTA	46	#0_core
07[133]	07[174]	AGCCCAATAATAAATACCATTTGGGAATTAGAGCGCAATTAA	44	#0_core
07[175]	07[216]	AGCCAGAATGGAAGAGGTAGCAAGCCCAATAGGAACAAAAGCTGA	45	#0_core
07[217]	07[258]	GGCTTGACGGGATGATCTGTACAGACCAGGCGCATAAACGCCCTCG	46	#0_core
07[259]	07[300]	TTTACCAGACGACTCAACTTAATTGCTGAATATAACAAACATAT	44	#0_core
07[301]	07[342]	ATTTTAAATGCAAAAAAGCGTCTGGCTTCTGTAGTACGAGCCGG	46	#0_core
08[048]	08[021]	TTGATTAGAGTCCAGAACAAATATACGCCCA	31	#0_core
08[090]	08[070]	CACAAATATCAATATATGTGA	22	#0_core
08[132]	08[112]	TGTGAAAATAATATAGAAGGCTT	23	#0_core
08[174]	08[153]	AACAGAACCCAGCAAAATCACCA	23	#0_core
08[216]	08[196]	TTAGGCTCCCATGTACCGTAA	22	#0_core
08[258]	08[238]	ATAACGAATGGCTGGCTGACCT	23	#0_core
08[300]	08[280]	TGGAATTAGTGTGTAGTCAA	22	#0_core
08[347]	11[347]	CAATTCACACACACATGGTCAGGTTACGTGCCAAGCTT	38	#0_core
09[021]	15[048]	ACCTACATTTTGAACAATTTTTAAAAATACCGAATGAATGAATA	45	#0_core
09[063]	09[062]	TTGCTGAATAACCGAAACATAGCGGATGAACAGTTTCGCCTGA	44	#0_core
09[105]	09[104]	TAATCCGGTATGTAAGCCTTAAATCTTATCAATCCATCC	42	#0_core
09[147]	09[146]	TTTTGTAGCACCCCGTAATCAGTAGGTGGCAGAAATTTAT	42	#0_core
09[189]	09[188]	TAAGTCTGAGTTTAAATAGTTAGCTAACAAGAGAAAAGCGGA	44	#0_core
09[231]	09[230]	ACAACGATCAAGAATCTGCTCATTAGTCACTCATACACAAAGT	44	#0_core
09[273]	09[272]	GCCCGTGTTTAACTTCCCAATCTGTATTATAGGAAAAGAGGAA	44	#0_core
09[315]	09[314]	TCAGAAATTAATATACCGTAATGGGAGGTAATCATTTGATAA	42	#0_core
10[027]	11[048]	AATCGTCAGTCACACGACCATATCTAAAGA	31	#0_core
11[070]	11[090]	GTAATCGTCGCCAATCGGG	20	#0_core
11[112]	11[132]	GCGAGGCGTTTAAATAAAT	19	#0_core
11[154]	11[175]	AGCAAGGCCGGCCACCGAAG	20	#0_core
11[196]	11[216]	GTACAACTACTAATAATCT	20	#0_core
11[238]	11[258]	ACAAGAACCGGTACGGAGC	19	#0_core
11[280]	11[300]	CTAAAGTACGGATTAACAA	19	#0_core
11[322]	05[342]	TAACAAACCCGTACCGAGCTCCACATTATTGC	33	#0_core
12[048]	18[028]	CAATGTTAATAAAAAGGGACGTGGCACCTACGCT	33	#0_core
12[090]	12[049]	TAACAAAATCTTAAATTAATTTTTACATGGCAATTCAT	39	#0_core
12[132]	12[091]	AAAGATCTAGCGAACCTCCCGATAAGATCGCCATATT	38	#0_core
12[174]	12[133]	ATACGCCAAAACGTACCAATGAAAAAGCCTTTTTAAGA	39	#0_core
12[216]	12[175]	AACGACGAAAACGCTGTAGCATTGGATGGCTTTTGATG	39	#0_core
12[258]	12[217]	GTAACCAAGATATTCATACCCAACCCGACAGCATCGG	38	#0_core
12[300]	12[259]	GTATAGTGTCTGGAAGTTTCATGCAATGCCAGAGGGG	39	#0_core
12[335]	12[301]	GCCGGATTCTCCGTGGTAGCGCCGGAGACA	32	#0_core
13[049]	13[048]	CCTGATTTTTGCACTCAATCAATATAGGAGGAAGATAAT	42	#0_core
13[091]	13[090]	AACATGATGTAAGCTTTTTAACCTCTCTGTATGCACGCC	40	#0_core
13[133]	13[132]	CAGATAGAGAACTGGTTCCAGAGCCTTTATCCATAAG	40	#0_core
13[175]	13[174]	TGTAAGTATGCCCCGCCCTTATTAGACCAGAAGGAG	40	#0_core
13[217]	13[216]	GCAACGGAATAAAATAACTTTCAACAGTCCGGAATGGGGTA	42	#0_core
13[259]	13[258]	AAATGTTAACAATAAATGCAACTTTAATCAACATTATATAGTA	42	#0_core
13[301]	13[300]	CCATCATCAGAGATATTTTCAATTTGGTTATAGTGAATCA	40	#0_core
14[048]	14[049]	ACTTCAGGAATTAACAACATAAATCATCAATGGATTAT	42	#0_core
14[090]	14[091]	AGGCAGTAAATGGAAGAAAACCTTTTACGCTCAAATTTAGGCAG	44	#0_core
14[132]	14[133]	TACCAGTATTATTGTTAACGTCAAAAAATAGCTAACAAAGT	44	#0_core
14[174]	14[175]	TAACGTACCCGGACAGAGCCGCCACCTTTTACCCTAAGTTT	44	#0_core
14[216]	14[217]	TTGAGAATAAATCTTCCAAAAAAGCGGATAAAGAGGCT	42	#0_core
14[258]	14[259]	GCCTACTGGTAGCTACGTTAATAAAGCGAGATTCTGGATA	42	#0_core
14[300]	14[301]	ACCCTTACTAGAAAGGCAAGGCAAAATAGTTAAAGGGATATTCA	44	#0_core
14[342]	08[322]	TGCAAGGCGAATTATGCTAATCACCGCTTTCATCA	37	#0_core
15[021]	12[021]	ATCGCCATTTGAATGGAATACATTCTG	28	#0_core
15[049]	15[090]	ATGGAAGGGTTATACAAGCTTAGATTAAGACGCTGATATTTTCG	45	#0_core
15[091]	15[132]	AGCCAGTAATAAGCTGAAGATTAGTGTCTATTTGGCCAAAGGAA	46	#0_core

15[133]	15[174]	ACCGAGGAAACGCTAAAGCGACAGAATCAAGTTTGAAAAGGGTC	44	#0_core	
15[175]	15[216]	AGTGCCTTGAGTATCCTCGATCTAAAGTTTTGTCGTGAACGACTA	45	#0_core	
15[217]	15[258]	AAGACTTTTTATAAAAGAATAAGGCTTGCCCTGACAAGACAATAC	46	#0_core	
15[259]	15[300]	TGGGAATCGTCATGACCGAACGAGTAGATTTAGTCAATTCTAG	44	#0_core	
15[301]	15[342]	CTGATAAATTAATGAAC TAGGTACGTTGGTGTAGAGGCCCTCTTC	46	#0_core	
16[062]	16[021]	TAGAACCCTACCATCTCAACAGTCGAACCACCGAGAAGATAA	45	#0_core	
16[104]	16[063]	GCAGAAATAAAGTACCATATAACTAGAAGAGTCAATAGTGATGAA	46	#0_core	
16[147]	16[105]	ACAAATAAACGGAATAAATAACACACCCAGCTACAATTGAACGC	47	#0_core	
16[189]	16[148]	GACACAGTGCCCGTATAACATAATCCCTTTAGCGTCAGACACAT	44	#0_core	
16[231]	16[190]	ACTGAGGAAGTTTCCATTTAGAAAGCTTCCAGACGTTAGGCTGA	45	#0_core	
16[273]	16[232]	CCCTAAATATTCAATGAAGCGATTTTGAGAAACCCAGAACAATAC	46	#0_core	
16[315]	16[274]	GATGCCGGAGAGGGTAGCTGGCATTGGACCATTAGATACTTTA	44	#0_core	
16[347]	19[347]	AAGGGCGATCGGTAGGCAAAGCGACCCAGATATCGGC	38	#0_core	
17[021]	17[034]	CTGCAACAGTGCCGG	15	#0_core	
17[329]	16[316]	GGAAACCGCTGGGGCATCGTAACGAATC	29	#0_core	
18[027]	19[062]	GAGAGCTGCTGAACCTCAAATATCAAACCGTAAACAGAAATAA	44	#0_core	
18[062]	18[063]	GTAGATGATCCCTTTCCCTTAGAATCCCGTCAAATATTGC	40	#0_core	
18[104]	18[105]	AAACAACATAAGACTTGGGGAGGTTAGAATCTTACAAT	42	#0_core	
18[146]	18[147]	GTATGTTCCACATATAACCATCGATAGCAGCGTTTTTCACGCA	42	#0_core	
18[188]	18[189]	CTGAAACGTAGGATTACACAGACAGCTTTTTTCTTTATT	40	#0_core	
18[230]	18[231]	AACCTAACTCTTTGACATCAACGTAACCTTAAATGGCACC	40	#0_core	
18[272]	18[273]	GACCATTATCAGAATCCATATAACAGGAAATGGTAGAAT	40	#0_core	
18[314]	18[315]	CTGAGAGATGTAACAACAACCGCGGTGCTGCCAGATTGC	42	#0_core	
19[063]	19[104]	AGAACATAGGCTGAGAGACTACTAATCTGTCCAGAC	38	#0_core	
19[105]	19[146]	GACGACCAACGCTAACGAGCGCTCATGATTAAGACTCC	38	#0_core	
19[147]	19[188]	TTATTATCGGCATTTTCGGTCATAGCTGCTATTTCGGAA	39	#0_core	
19[189]	19[230]	CCTAGTATGGGATTTGCTAAACAGTAATGCCACTACG	39	#0_core	
19[231]	19[272]	AAGGGCTTGAGATGGTTAATTTTTAAACAGTTCAGA	38	#0_core	
19[273]	19[314]	AAACGCAATAACCTGTTAGCTATCTACAAGGCTATCA	39	#0_core	
19[315]	12[336]	GGTCTTTGAGGGGACGACGCTTCTGGATGTTGGGTAACACGACG	45	#0_core	
11[049]	11[069]	TTATCAGATGATCGGGACT	19	#1_bottom	B0
11[091]	11[111]	CTTAATTGAGATCCTGAAC	19	#1_bottom	B1
11[133]	11[153]	CTTACGGAAGCAAACGCATT	20	#1_bottom	B2
11[176]	11[195]	CGTCATACATTAGCGGCA	18	#1_bottom	B3
11[217]	11[237]	CAGCAGCGAAAAGCGATTG	19	#1_bottom	B4
11[259]	11[279]	AAAAGAAGTTTAGCGGATAA	20	#1_bottom	B5
11[301]	11[321]	AGGGTGAGAAAATGTCAAG	19	#1_bottom	B6
08[069]	08[049]	GTTTGAATACGAAGGAGCGGAA	22	#2_top	T0
08[111]	08[091]	ATTACGAGCAACCAAGTATAAGC	23	#2_top	T1
08[152]	08[133]	GCACAATCGAGCAAAGAACAA	21	#2_top	T2
08[195]	08[175]	CAGCCGTCGAAGCGCAGTCTCG	23	#2_top	T3
08[237]	08[217]	TCGAGATTTGTTAAAGGCCGCTT	23	#2_top	T4
08[279]	08[259]	CAAAAGACTGATAAAAACCAAA	22	#2_top	T5
08[321]	08[301]	ACAAAGCCCTGCTGAGTAATG	23	#2_top	T6
02[055]	02[035]	ATCGTATTATAGAAGTATTAG	21	#3_left	L0
02[076]	02[056]	GAGAAACAATATTCATTCA	20	#3_left	L1
02[097]	02[077]	TCAGGCGTATTTAATGGTTT	20	#3_left	L2
02[118]	02[098]	GCGTACCGCTTTCCTATCAT	21	#3_left	L3
02[139]	02[119]	GGACCCCTAACAGGGAAGC	20	#3_left	L4
02[160]	02[140]	ACAGGGAAGCAAAGACAAAAG	21	#3_left	L5
02[181]	02[161]	GTATTGACACCCGCCACAGA	20	#3_left	L6
02[202]	02[182]	GAACCCTCAGGTGATCACC	20	#3_left	L7
02[223]	02[203]	CTGATACCGCAGCTTGCTTTC	21	#3_left	L8
02[244]	02[224]	GAGGCGCAGTCCGCGACCTG	20	#3_left	L9
02[265]	02[245]	ACACTAATGGATTATCAGTT	21	#3_left	L10
02[286]	02[266]	GGAGGATTAAGCGAACCCAG	20	#3_left	L11
02[307]	02[287]	ACCTGTAATAAAGCTAAATC	20	#3_left	L12
02[328]	02[308]	CGGCATTAATTTAAATTGTAA	21	#3_left	L13
17[035]	17[055]	TCAGTTGGCAAAAAATATC	21	#4_right	R0
17[056]	17[076]	AGGTTAACGTCAGAATTTAGC	22	#4_right	R1
17[077]	17[097]	TTAGGTTGGTTGACAAAAGGT	22	#4_right	R2
17[098]	17[118]	TCAGCTAATGCATTATCCTAT	21	#4_right	R3
17[119]	17[139]	TTGCCAGTTACAACCCAAAACA	22	#4_right	R4
17[140]	17[160]	AACGTAGAAAATTGTAGCGCG	21	#4_right	R5

17[161]	17[181]	TTTGCCATCTTTACAGTTAGA	22	#4_right	R6
17[182]	17[202]	AAGTATTAAGAGTAAATGAACA	22	#4_right	R7
17[203]	17[223]	GCGGAGTGAGAAAAACGGGCG	21	#4_right	R8
17[224]	17[244]	AAAGAGGCAAAAGGAGTAGTGT	22	#4_right	R9
17[245]	17[265]	GAATTACCTTATCCCCCTAT	21	#4_right	R10
17[266]	17[286]	CAAAAATCAGGTCAITTCGCCG	22	#4_right	R11
17[287]	17[307]	CGAGCTGAAAAGTATTTTGTG	22	#4_right	R12
17[308]	17[328]	GAGCAACAAGACGTGCATCC	21	#4_right	R13
00[020]	00[005]	CTTTGACGAGCACGTA	16	#5_ends	E0
00[361]	00[347]	ACAGCTGATTGCCCTT	16	#5_ends	F0
01[005]	01[020]	TAACGTGCTTTCCTCG	16	#5_ends	E1
01[347]	01[361]	CCAGTGAGACGGGCA	15	#5_ends	F1
02[020]	02[005]	AGGAGGCCGATTAAG	16	#5_ends	E2
02[361]	02[347]	AACGCGGGGAGAG	15	#5_ends	F2
03[005]	03[020]	GGATTTAGACAGGAA	16	#5_ends	E3
03[347]	03[361]	TTAATGAATCGCC	14	#5_ends	F3
04[020]	04[002]	TCAGTGAGGCACCCGAGTA	19	#5_ends	E4
04[358]	04[343]	GCTTCCAGTCGGGA	15	#5_ends	F4
05[002]	05[020]	AAAGAGTCTGTCCATCACG	19	#5_ends	E5
05[343]	05[358]	GTTGCGCTCACTGCC	16	#5_ends	F5
06[020]	06[002]	TAGTAATAACATCACTTGC	19	#5_ends	E6
06[358]	06[343]	CCTGGGGTGCCTAATG	16	#5_ends	F6
07[002]	07[020]	CTGAGTAGAAGAACTCAAA	19	#5_ends	E7
07[343]	07[358]	AAGCATAAAGTGTAAG	17	#5_ends	F7
08[020]	08[005]	GCCATTGCAACAGGAA	16	#5_ends	E8
08[361]	08[348]	ATTGTTATCCGCTCA	15	#5_ends	F8
09[005]	09[020]	AAACGCTCATGGAAAT	16	#5_ends	E9
09[343]	09[361]	TAGCTGTTCTCTGTGTGAA	19	#5_ends	F9
10[020]	10[005]	CTGAAATGGATTATT	16	#5_ends	E10
10[361]	10[343]	TGGACTCTAGAGGATCCCC	19	#5_ends	F10
11[005]	11[020]	ACATTGGCAGATTCAC	16	#5_ends	E11
11[348]	11[361]	GCATGCCTGCAGG	13	#5_ends	F11
12[020]	12[002]	GCCAACAGAGATAGAACCC	19	#5_ends	E12
12[358]	12[343]	TCACGAGCTGTGAAA	15	#5_ends	F12
13[002]	13[020]	TTCTGACCTGAAAGCGTAA	19	#5_ends	E13
13[343]	13[358]	GCCAGGGTTTTCCAG	16	#5_ends	F13
14[020]	14[002]	CTATTAGTCTTTAATGCGC	19	#5_ends	E14
14[358]	14[343]	CGAAAGGGGGATGTGC	16	#5_ends	F14
15[002]	15[020]	GAAGTATAGCCCTAAAC	19	#5_ends	E15
15[343]	15[358]	GCTATTACGCCAGCTGG	17	#5_ends	F15
16[020]	16[005]	AACAGAGGTGAGGCGG	16	#5_ends	E16
16[361]	16[348]	TGCGCAACTGTTGGG	15	#5_ends	F16
17[005]	17[020]	TCAGTATTAACACCCG	16	#5_ends	E17
17[343]	17[361]	CGCCATTCGCCATTGAGGC	19	#5_ends	F17
18[020]	18[005]	CAGCAGCAAATGAAAA	16	#5_ends	E18
18[361]	18[343]	CACTCCAGCCAGCTTCCG	19	#5_ends	F18
19[005]	19[020]	ATCTAAAGCATCACCT	16	#5_ends	E19
19[348]	19[361]	CTCAGGAAGATCG	13	#5_ends	F19

Supplementary Notes – List of functional DNA staples

1. Functional staples for Origami H

Bottom positions

oligoname	Sequence	Description	Partner staples
B_00	TTATCAGATGATCGGGACT	unmodified staples	
B_01	CTTAATTGAGATCCTGAAC		
B_02	CTTACCAGCAAAACGCATT		
B_03	CGTCATACATTAGCGGCA		
B_04	CAGCAGCAAAAAGCGATTG		
B_05	AAAAGAAGTTTAGCGGATAA		
B_06	AGGGTGAGAAAATGTCAAG		
B18_00	TTATCAGATGATCGGGACT GCTATGGGTGGTCTGGTT	staples with extension for TEG-Chol(18)	<i>5'-Chol-TEG-AACCAGACCACCCATAGC</i>
B18_01	CTTAATTGAGATCCTGAAC GCTATGGGTGGTCTGGTT		
B18_02	CTTACCAGCAAAACGCATT GCTATGGGTGGTCTGGTT		
B18_03	CGTCATACATTAGCGGCA GCTATGGGTGGTCTGGTT		<i>AACCAGACCACCCATAGC-TEG-Chol-3'</i>
B18_04	CAGCAGCAAAAAGCGATT GCTATGGGTGGTCTGGTT		
B18_05	AAAAGAAGTTTAGCGGATA GCTATGGGTGGTCTGGTT		
B18_06	AGGGTGAGAAAATGTCA GCTATGGGTGGTCTGGTT		
B09_06	AGGGTGAGAAAATGTCA AGGCTCTGGTT	staples with extension for TEG-Chol(9)	<i>5'-Chol-TEG-AACCAGACC</i>
B27_03	CGTCATACATTAGCGGCA AGCTATGGGTGGTCTGGTTGGGATTGGC	staple with extension for TEG-Chol(27)	<i>5'-Chol-TEG-GCCAATCCCAACCAGACCACCCATAGC</i>
BD_00	TTATCAGATGATCGGGACT AAAAAACACCAAAACCC	staples with extension for Atto488 dye	<i>5'-Atto488-GGGTTGGTGTITTTT</i>
BD_01	CTTAATTGAGATCCTGAAC AAAAAACACCAAAACCC		
BD_02	CTTACCAGCAAAACGCATT AAAAAACACCAAAACCC		
BD_03	CGTCATACATTAGCGGCA AAAAAACACCAAAACCC		
BD_04	CAGCAGCAAAAAGCGATT AAAAAACACCAAAACCC		
BD_05	AAAAGAAGTTTAGCGGATA AAAAAACACCAAAACCC		
BD_06	AGGGTGAGAAAATGTCA AAAAAACACCAAAACCC		
B_00_Biot	TTATCAGATGATCGGGACT- TEG-Biotin-3'	biotinylated staples	
B_03_Biot	CGTCATACATTAGCGGCA- TEG-Biotin-3'		
B_06_Biot	AGGGTGAGAAAATGTCAAG- TEG-Biotin-3'		
B_00_Thio	TTATCAGATGATCGGGACT- C3-SS-3'	thiolated staples	
B_03_Thio	CGTCATACATTAGCGGCA- C3-SS-3'		
B_06_Thio	AGGGTGAGAAAATGTCAAG- C3-SS-3'		

Top positions

oligoname	Sequence	Description	Partner staples
T_00	GTTTGAATACGAAGGAGCGGAA	unmodified staples	
T_01	ATTACGAGCAACCGATATAAAG		
T_02	GCACAATCGAAGCAAGAAACAA		
T_03	CAGCCGTCGAAGCGCAGTCTCG		
T_04	TCGAGATTGTTAAAGGCGCTT		
T_05	CAAAAGACTGATAAAACCAA		
T_06	ACAAAGCCCTGCCTGAGTAATG		
TD_00	GTTTGAATACGAAGGAGCGGAA AAAAAACACCAAAACCC	staples with extension for At488 dye	5'-Atto488- GGGTTGGTGTITTTT
TD_01	ATTACGAGCAACCGATATAAAG AAAAAACACCAAAACCC		
TD_02	GCACAATCGAAGCAAGAAACAA AAAAAACACCAAAACCC		
TD_03	CAGCCGTCGAAGCGCAGTCTCG AAAAAACACCAAAACCC		
TD_04	TCGAGATTGTTAAAGGCGCTT AAAAAACACCAAAACCC		
TD_05	CAAAAGACTGATAAAACCAA AAAAAACACCAAAACCC		
TD_06	ACAAAGCCCTGCCTGAGTAATG AAAAAACACCAAAACCC		
T18_00	GTTTGAATACGAAGGAGCGGAA GCTATGGGTGGTCTGGTT	staples with extension for TEG-Chol(18)	5'-Chol-TEG- AACCAGACCACCCATAGC
T18_03	CAGCCGTCGAAGCGCAGTCTCG GCTATGGGTGGTCTGGTT		AACCAGACCACCCATAGC -TEG-Chol-3'
T18_06	ACAAAGCCCTGCCTGAGTAATG GCTATGGGTGGTCTGGTT		

Edge positions

oligoname	Sequence	Description	Partner staples
E_06	TAGTAAATACATCACTTGC AAAAAACACCAAAACCC	staples with extension for Al488 dye	5'-Alexa488- GGGTTGGTGTITTTT
E_13	CCCAAACACCAAAAAA CTGTGACCTGAAGCGTAA		TTTTTTGTGGTTGGG -Alexa488-3'
F_06	CCCAAACACCAAAAAA CTGGGGTGCCTAATG		
F_13	GCCAGGTTTTCCAG AAAAAACACCAAAACCC		

2. Functional staples for Origami Q

Bottom positions

oligoname	Sequence	Description	Partner staples
B_00	ATTCCTGATTACTTTTACCT	unmodified staples	
B_01	AGTAGGGCTTAAAGATAATC		
B_02	AGCTATCTTACAAAAGAATA		
B_03	GCGTCATACATAGCGGGCC		
B_04	CCTCAGCAGCGACCGGCT		
B_05	CAAAAGAAGTTAAGCGGACA		
B_06	GTGAAAAGGCCAATCATCA		
B18_00	ATTCCTGATTACTTTTACCT GCTATGGTGGTCTGGTT	staples with extension for TEG-Chol(18)	<i>5'-Chol-TEG-AACCAGACCCCATAGC</i> <i>AACCAGACCCCATAGC-TEG-Chol-3'</i>
B18_01	AGTAGGGCTTAAAGATAATC GCTATGGTGGTCTGGTT		
B18_02	AGCTATCTTACAAAAGAATA GCTATGGTGGTCTGGTT		
B18_03	GCGTCATACATAGCGGGCC GCTATGGTGGTCTGGTT		
B18_04	CCTCAGCAGCGACCGGCT GCTATGGTGGTCTGGTT		
B18_05	CAAAAGAAGTTAAGCGGACA GCTATGGTGGTCTGGTT		
B18_06	GTGAAAAGGCCAATCATCA GCTATGGTGGTCTGGTT		
B09_00	ATTCCTGATTACTTTTACCT GGTCTGGTT	staples with extension for TEG-Chol(9)	<i>5'-Chol-TEG-AACCAGACC</i>
B09_03	GCGTCATACATAGCGGGCC GGTCTGGTT		
B09_06	GTGAAAAGGCCAATCATCA GGTCTGGTT		
B27_03	GCGTCATACATAGCGGGCC GCTATGGTGGTCTGGTTGGGATTGGC	staple with extension for TEG-Chol(27)	<i>5'-Chol-TEG-GCCAATCCCAACCAGACCCCATAGC</i>
BD_00	ATTCCTGATTACTTTTACCT AAAAAACACCAACCC	staples with extension for Atto488 dye	<i>5'-Atto488-GGGTTGGTGTITTTT</i>
BD_01	AGTAGGGCTTAAAGATAATC AAAAAACACCAACCC		
BD_02	AGCTATCTTACAAAAGAATA AAAAAACACCAACCC		
BD_03	GCGTCATACATAGCGGGCC AAAAAACACCAACCC		
BD_04	CCTCAGCAGCGACCGGCT AAAAAACACCAACCC		
BD_05	CAAAAGAAGTTAAGCGGACA AAAAAACACCAACCC		
BD_06	GTGAAAAGGCCAATCATCA AAAAAACACCAACCC		

Top positions

oligoname	Sequence	Description	Partner staples
T_00	TAGATTGCTAACCCAGAG	unmodified staples	
T_01	AACCTAATTTATTCTTACAGT		
T_02	CTTTGTCAAATAAGAGCAAG		
T_03	ACCGTCGAGAGCGAGTCTCT		
T_04	CTCGGAGATTAGTTAAAGGCCG		
T_05	ACGAAAGACCGATAAAACCAA		
T_06	AACCCAAAATGAGTAATGTGT		
TD_00	TAGATTGCTAACCCAGAG AAAAAACCCAAACCC	staples with extension for At488 dye	<i>5'-Atto488-GGGTTGGTGTITTT</i>
TD_01	AACCTAATTTATTCTTACAGT AAAAAACCCAAACCC		
TD_02	CTTTGTCAAATAAGAGCAAG AAAAAACCCAAACCC		
TD_03	ACCGTCGAGAGCGAGTCTCT AAAAAACCCAAACCC		
TD_04	CTCGGAGATTAGTTAAAGGCCG AAAAAACCCAAACCC		
TD_05	ACGAAAGACCGATAAAACCAA AAAAAACCCAAACCC		
TD_06	AACCCAAAATGAGTAATGTGT AAAAAACCCAAACCC		
T18_00	TAGATTGCTAACCCAGAG GCTATGGGTGCTGGTT	staples with extension for TEG-Chol(18)	<i>5'-Chol-TEG-AACCAGACCCCATAGC</i> <i>AACCAGACCCCATAGC-TEG-Chol-3'</i>
T18_03	ACCGTCGAGAGCGAGTCTCT GCTATGGGTGCTGGTT		
T18_06	AACCCAAAATGAGTAATGTGT GCTATGGGTGCTGGTT		
T09_00	TAGATTGCTAACCCAGAG GGTCTGGTT	staples with extension for TEG-Chol(9)	<i>5'-Chol-TEG-AACCAGACC</i>
T09_03	ACCGTCGAGAGCGAGTCTCT GGTCTGGTT		
T09_06	AACCCAAAATGAGTAATGTGT GGTCTGGTT		

Lateral positions (left side)

oligoname	Sequence	Description	Partner staples
L_00	ATCGACAACCTGAGGATTTAGA	unmodified staples	
L_01	ATAGATGATGGCGAATTATTC		
L_02	TTGATAAATGACCTAAATTTA		
L_03	GGAAACCAAGGCTGCTTTCC		
L_04	AAAACCTGAACATAAAAACAG		
L_05	GAGAGGGAGAGCCCAAAGAC		
L_06	TAGCATTGAAGCCCAACCA		
L_07	TTACCTCAGGTGTATCACCG		
L_08	TGCTTGATATCAGCTTGCT		
L_09	TGGAGGCGCAATCCGCGACC		
L_10	GAAACTAATAGATTCATCAGT		
L_11	TTCAGGATTAAGCGAACCA		
L_12	AATGTAATAAAGCTAAATCGG		
L_13	GTAATTTTATTGTAACGTT		
LS_00	TATATATTT ATCGACAACCTGAGGATTTAGA	staples for lateral oligomerization	
LS_01	TATATATTT ATAGATGATGGCGAATTATTC		
LS_02	TATATATTT TGATAAATGACCTAAATTTA		
LS_03	TATATATTT GGAAACCAAGGCTGCTTTCC		
LS_04	TATATATTT AAAACCTGAACATAAAAACAG		
LS_05	TATATATTT GAGAGGGAGAGCCCAAAGAC		
LS_06	TATATATTT TAGCATTGAAGCCCAACCA		
LS_07	TATATATTT TTACCTCAGGTGTATCACCG		
LS_08	TATATATTT TGCTTGATATCAGCTTGCT		
LS_09	TATATATTT TGGAGGCGCAATCCGCGACC		
LS_10	TATATATTT GAAACTAATAGATTCATCAGT		
LS_11	TATATATTT TTCAGGATTAAGCGAACCA		
LS_12	TATATATTT AATGTAATAAAGCTAAATCGG		
LS_13	TATATATTT GTAATTTTATTGTAACGTT		

Lateral positions (right side)

oligoname	Sequence	Description	Partner staples
R_00	ATATCTGGTCAGACCATATAG	unmodified staples	
R_01	ATTTTCAGGTTTCAATAGTCC		
R_02	TCCGGCTTAGGTAAGTACAC		
R_03	AACATGTTCACTACAATTAG		
R_04	CCTAATTTGCCAGGGAATAGT		
R_05	TAGCAAACTAGCAGACTGTT		
R_06	AGCGTTTGCATCACAGTTAAA		
R_07	AGTATTAAGAGGTAGTAAATT		
R_08	TCAGCGAGTGAATTAACAA		
R_09	CGAAAGAGGCAAAACGAGTATG		
R_10	TGAATTACCTTAATCCCCAA		
R_11	TCAAAAATCAGGTCATTTCCGG		
R_12	CGAGCTGAAAAGTTTGAGACA		
R_13	AACAAGAAATCATCTGCCCC		
RS_00	TATATATTT ATATCTGGTCAGACCATATAG	staples for lateral oligomerization	
RS_01	TATATATTT ATTTTCAGGTTTCAATAGTCC		
RS_02	TATATATTT TCCGGCTTAGGTAAGTACAC		
RS_03	TATATATTT AACATGTTCACTACAATTAG		
RS_04	TATATATTT CCTAATTTGCCAGGGAATAGT		
RS_05	TATATATTT TAGCAAACTAGCAGACTGTT		
RS_06	TATATATTT AGCGTTTGCATCACAGTTAAA		
RS_07	TATATATTT AGTATTAAGAGGTAGTAAATT		
RS_08	TATATATTT TCAGCGAGTGAATTAACAA		
RS_09	TATATATTT CGAAAGAGGCAAAACGAGTATG		
RS_10	TATATATTT TGAATTACCTTAATCCCCAA		
RS_11	TATATATTT TCAAAAATCAGGTCATTTCCGG		
RS_12	TATATATTT CGAGCTGAAAAGTTTGAGACA		
RS_13	TATATATTT AACAAGAAATCATCTGCCCC		
R18_00	ATATCTGGTCAGACCATATAG GCTATGGGTGGTCTGGTT	staples with extension for TEG-Chol(18)	5'-Chol1-TEG-AACCAGACCACCCATAGC
R18_06	AGCGTTTGCATCACAGTTAAAG ACTATGGGTGGTCTGGTT		
R18_12	CGAGCTGAAAAGTTTGAGAC AGCTATGGGTGGTCTGGTT		

Edge positions

oligoname	Sequence	Description	Partner staples
E_08	TTACCGCCAGCCATTG	staples for tip-to-tip interactions: - Q-E5 structures (10 of 10) - Q-E7 structures (10 of 14) - Q-E13 structures (10 of 26)	
E_09	CAACAGGAAAAAGCT		
E_10	CTCAATCGCTGAAAT		
E_14	TGAATGGCTATTAGCTTT		
E_18	GCTGAGGCAGCAGC		
F_08	TCCGCTCACAAATC		
F_09	TTCCGTGTGAAATTGTTA		
F_10	TAGAGGATCCCGGGTACC		
F_14	GGGGATGTCTGCCAA		
F_18	GCCAGCTTCCGGCACCGC		
E_04	TTTATAATCAGTGAGGCCA	additional staples: - Q-E7 structures (4 of 14) - Q-E13 structures (4 of 26)	
E_19	AAATGAAAAATCTAAA		
F_04	CCAGTCGGAAACCTG		
F_19	AAGATCGCACTCCA		
E_03	CGATTAAAGGGATTTT	additional staples: - Q-E13 structures (12 of 26)	
E_05	CCGATATAAAGACTCTGTC		
E_06	CTTGATTAGTAATAACAT		
E_07	CACCTGCCAGTAGAAGA		
E_11	GGATTATTACATTGG		
E_15	AATCGCGCACTGATAGCC		
F_03	AATCGCGCAACGGCC		
F_05	GCTCACTGCCCGCTTT		
F_06	GGTGCTAATGAGTGA		
F_07	AAAGGTAAAGCTGG		
F_11	CTGAGGTGACTC		
F_15	ACGCCAGCTGGCGAAA		

3. Functional staples for Origami L

Bottom positions

oligoname	Sequence	Description	Partner staples
B_00	ATTATCATCATAAACAGTATG	unmodified staples	
B_01	GCTCAACAGTAGCAACAATCG		
B_02	GCAATAGCTATCCATATAAAC		
B_03	GTAAGCGTCATGATTAGCAC		
B_04	TCAGCAGCGAAAAGCGATTGA		
B_05	AGAAGTTTTGCCGATTGCAAA		
B_06	AAGCCGGAGACATGTACCTC		
B18_00	ATTATCATCATAAACAGTATG GCTATGGTGGTCTGGTT	staples with extension for TEG-Chol(18)	5'-Chol-TEG- AACCAGACCCCATAGC
B18_03	GTAAGCGTCATGATTAGCAC GCTATGGTGGTCTGGTT		
B18_06	AAGCCGGAGACATGTACCTC GCTATGGTGGTCTGGTT		

Top positions

oligoname	Sequence	Description	Partner staples
T_00	AAATTGCCCGGAACAAGAA	unmodified staples	
T_01	ATTCCCATCTATACAATTCT		
T_02	ATTATTTCCAATAATAGA		
T_03	AAGTCCCGTGGAAAGCGAGT		
T_04	CAAGATTTGTTAAAGCGCCT		
T_05	TTACTTCAAAAACCAAATA		
T_06	AGACAGGAATGTGTAGTAA		
TD_00	AAATTGCCCGGAACAAGAA AAAAAACCCAAACCC	staples with extension for At488 dye	5'-Atto488- GGGTTGGTGTITTT
TD_01	ATTCCCATCTATACAATTCT AAAAAACCCAAACCC		
TD_02	ATTATTTCCAATAATAGA AAAAAACCCAAACCC		
TD_03	AAGTCCCGTGGAAAGCGAGT AAAAAACCCAAACCC		
TD_04	CAAGATTTGTTAAAGCGCCT AAAAAACCCAAACCC		
TD_05	TTACTTCAAAAACCAAATA AAAAAACCCAAACCC		
TD_06	AGACAGGAATGTGTAGTAA AAAAAACCCAAACCC		

G

APPENDIX TO V.2

G Materials and Methods

G.1 DNA origami folding and purification

Dynamic DNA origami nanostructures consisting of a 22-helix bundle with hexagonal lattice based on the M13mp18 7429-nucleotide long scaffold plasmid (p7429), has been designed using CaDNAno [Douglas et al., 2009b] (Figures V.1 and G.1). All structures were constituted of one or more of three modules: basic module (N), short module (S) and long module (L). The list of sequences used for each module can be found in Supplementary Tables G.1 and G.2. Site specific toehold-mediated strand displacement was used to make the system dynamic. Protecting strands (P) contained 7/8 nucleotide overhangs (toeholds) on the 3'-end (Supplementary Tables G.1 and G.2), available for initiation of strand displacement upon addition of complementary removal strands (R).

High purity salt free (HPSF) purified staple oligonucleotides needed for origami folding were purchased from Eurofins MWG Operon (Ebersberg, Germany), and single-stranded M13mp18 scaffold DNA was supplied by Bayou Biolabs (Metairie, LA, USA). Long oligonucleotides (> 120 nucleotides) necessary to assemble DNA origami nanostructures containing the modules S and L were designed using the online application NUPACK (<http://www.nupack.org>) [Zadeh et al., 2011] and the IDT (Skokie, Illinois, USA) online tool OligoAnlalyzer 3.0 (<https://eu.idtdna.com/calc/analyzer>). These long oligos were purchased from Eurogentec (Seraing, Belgium). The 5'-Cy3 or Cy5-functionalized oligonucleotides were acquired from Eurofins, while the 5'-cholesterol modified with a tetraethylene glycol linker (chol-TEG)-functionalized oligonucleotides (all HPLC-purified) were purchased from Sigma-Aldrich (Taufkirchen, Germany). For DNA origami nanostructure modification with chol-TEG anchors, the respective bottom positions were extended with 18-nucleotide long sequence (GCTATGGGTGGTCTGGTT) complementary to the chol-TEG modified oligonucleotide. DNA origami nanostructures were folded, purified in FOB

buffer (5 mM Tris-HCl, 1 mM EDTA, 20 mM MgCl₂, pH 8.0) or imaging buffer (5 mM Tris-HCl, 1 mM EDTA, 5 mM MgCl₂, 300 mM NaCl, pH 8.0) and quantified as previously described (see III.1 and V.1).

G.2 oxDNA simulations

We ran molecular dynamic simulations (MD simulations) using oxDNA, a coarse-grained model whose basic unit is a rigid nucleotide that interacts with other nucleotides through stacking, hydrogen-bonding, excluded volume, electrostatic and backbone potentials [Ouldridge et al., 2011, Sulc et al., 2012]. An Andersen-like thermostat [Russo et al., 2009] ensured diffusive particle motion in the canonical ensemble. Simulations were performed on GPUs and required approximately 6×10^7 steps. Temperature was set to 23 °C and high salt concentration was used ($[\text{Na}^+] = 0.5 \text{ M}$), to resemble the experimental conditions.

Sequence was only incorporated into the single stranded region of the "closed" module L, where a hairpin is folded. Importantly, sequence did not significantly alter the angle distribution of the module N and the "flexible" module S.

To determine the angle of each DNA origami nanostructure, we consider two vectors \vec{A} and \vec{B} as shown in Figure G.2. A_{1x} , A_{1y} and A_{1z} denote the average of x, y and z component of coordinates for \vec{A} along the helices (0-21) (Figure V.1) defined by the centre of base-pair (bp) lying on the interface 1. Similarly, we have calculated the A_{2x} , A_{2y} and A_{2z} along the interface 2. \vec{A} is defined as $(A_{2x} - A_{1x})\hat{x} + (A_{2y} - A_{1y})\hat{y} + (A_{2z} - A_{1z})\hat{z}$. The same approach was used to define \vec{B} considering the centre of bp lying on interface 3 and 4. Using \vec{A} and \vec{B} , we defined the angle $\theta = \cos^{-1}(AB/|A||B|)$. We further defined the bend direction upward or downward using the vector \vec{C} and \vec{D} . The x component of \vec{C} is defined as $(A_{1x} + B_{4x})/2 - (A_{2x} + B_{3x})/2$. Similarly, y and z component of \vec{C} are obtained. \vec{D} is defined in same manner as \vec{C} considering the (8,13) and (10,11) along interface 5 and 6, correspondingly (Figure G.2B). If $C > 0$ the origami is bend in upward direction, if $C < 0$ the bend is in downward direction, according to the reference.

G.3 Transmission electron microscopy (TEM)

To confirm the folding of the DNA origami nanostructures, negative-stain TEM imaging was performed on a CM120 BioTWIN (FEI/Philips, Hillsboro, Oregon, USA) TEM, with a LaB6 filament operated at 120 kV. Images were recorded with a MegaView III camera (Soft Imaging System GmbH, Münster, Germany). Typically, 3 μ L of folded, purified and diluted (1/10 in FOB buffer) DNA origami nanostructures were adsorbed on glow-discharged formvar-supported carbon coated Cu300 grids (Plano GmbH, Wetzlar, Germany) and stained using a 2% aqueous uranyl formate solution containing 25 mM sodium hydroxide. To confirm the conformational switch upon strand displacement, samples were incubated with 100x excess of the respective removal strands (R) and imaged as described above. The bending angles were determined manually using ImageJ software (<http://rsb.info.nih.gov/ij/>) [Schindelin et al., 2015]. In short, the angle tool was used to measure the angle of individual structures (N = 200-500 particles) by choosing the edge and the centre positions of each structure. Bending angles were binned in ranges of 10° for display. Further image analysis was performed using the same software.

G.4 Agarose gel electrophoresis

The quality of DNA origami nanostructure folding was investigated through agarose gel electrophoresis (Figure V.4), as previously described (see III.1). Fluorescence analysis of agarose gels was used to verify the efficiency of the strand displacement mechanism. For this specific experiment, protecting strand (P) as well as n0(1-4) Cy5-modified at the 5'-end were incorporated into the DNA origami nanostructures. Additionally, a permanently bound Cy3-modified oligo was incorporated into the nanostructures. Individual samples were incubated overnight with $10\times$ excess of respective complementary removing strands (R). Samples were loaded in 2% agarose gel and electrophoresis was performed as always (see III.1). The gels were scanned with epi-illumination using Amersham 600 CCD Imager (GE Healthcare, Little Chalfont, UK) using a 460 nm or 630 nm LED light source for excitation of Cy3 or Cy5 fluorescence, respectively. After performing a background correction of the gel images, Atto488 and Cy5 fluorescence intensities within the bands of interest were integrated, and the normalized Cy5/Cy3 ratios were calculated (Figure V.4). As all structures possess a Cy3 label, this signal could be used as internal standard for

fluorescence intensity normalization. In the end, the gel was incubated with SYBR Safe for two hours for DNA staining and imaged as previously described (see III.1).

G.5 Giant unilamellar vesicle (GUV) preparation and confocal microscopy imaging

GUVs composed of 1,2-dioleoyl-*sn*-glycero-3-phosphocholine (DOPC) (Avanti Polar Lipids, Alabaster, AL, USA), containing additional 0.005 mol% Atto655-DOPE (AttoTEC GmbH, Siegen, Germany) were produced by electroformation [Angelova and Dimitrov, 1986] in polytetrafluoroethylene chambers with Pt electrodes 4 nm apart, as described previously (see III.1, III.2 and V.1). Importantly, the used aqueous sucrose solution was osmotically equilibrated to the imaging buffer (610 mOsm kg⁻¹). Experiments were carried out in 40 μ l 384-multiwell plates with 1.5 glass bottom (Sensoplate, Greiner Bio-One GmbH, Frickenhausen, Germany). Freshly plasma cleaned wells (10min) were passivated with PLL(20)-g[3.5]-PEG(2) (SuSoS AG, Dübendorf, Switzerland) by incubation with a 0.5 mg ml⁻¹ solution in Milli-Q water for at least 15min and consequently thoroughly washed with water and imaging buffer. 3 μ l of the GUV suspension (diluted 1:50 in 610 mOsm kg⁻¹ sucrose solution) were mixed with a 18 μ l DNA origami solution (5nM total concentration) diluted in imaging buffer, and samples were incubated at 4 °C overnight. Before measurement, the samples were equilibrated at the microscope objective ($T = 27.5 \pm 1.0^\circ\text{C}$) for at least 30 min.

Confocal imaging was performed on a commercial laser scanning microscope LSM 780 with a ConfoCor3 unit (Zeiss, Jena, Germany) using a water immersion objective (C-Apochromat, 40 \times /1.2W UV-VIS-IR, Zeiss, Jena, Germany). Samples were excited with the 488nm line of an Ar-ion-laser or with the 633nm line of a He-Ne laser (for Cy3 and Atto655 excitation, respectively). To avoid the effect of polarization selection in excitation of the GUVs, an achromatic $\lambda/4$ plate (Edmund Optics, Barrington, NJ, USA) was installed in the excitation beam path. Images were recorded at the equatorial planes of GUVs, with a 1 Airy unit pinhole, 512 \times 512 pixel resolution and a scan rate of 3.15 μ s per pixel. Further image analysis was performed using the ImageJ software (<http://rsb.info.nih.gov/ij/>) [Schindelin et al., 2015].

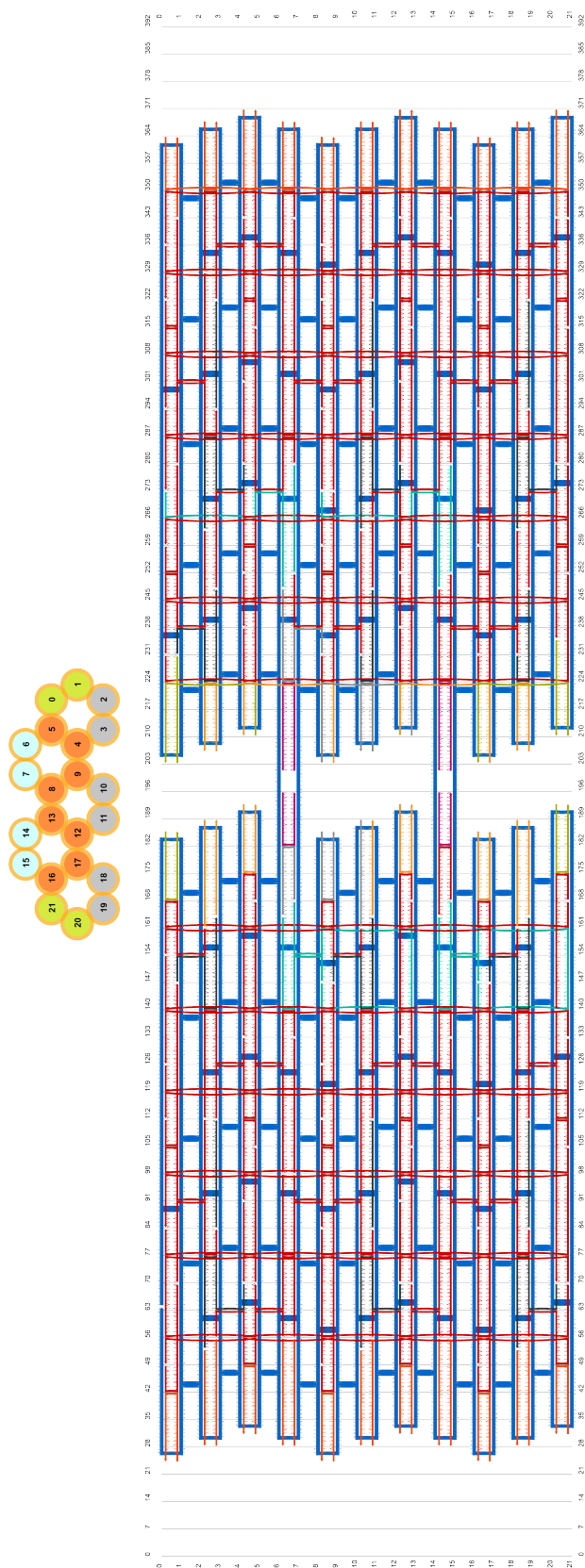


Figure G.1: Cadnano design and oligonucleotide sequences of the core DNA origami structure. The cross-section of the structure is shown above the Cadnano map. Lateral staples are coloured in dark orange, gap staples are highlighted in light orange while core staples are displayed in red; M13 p7249 scaffold is coloured in blue. Black staples correspond to bottom locations for modification with chol-TEG anchors while grey staples represent locations for fluorescent labelling with Cy3 or Cy5. Magenta staples correspond to locations for modification of the basic module (N); green and light blue staples are locations where staples for the short module (S) and long module (L) are attached.

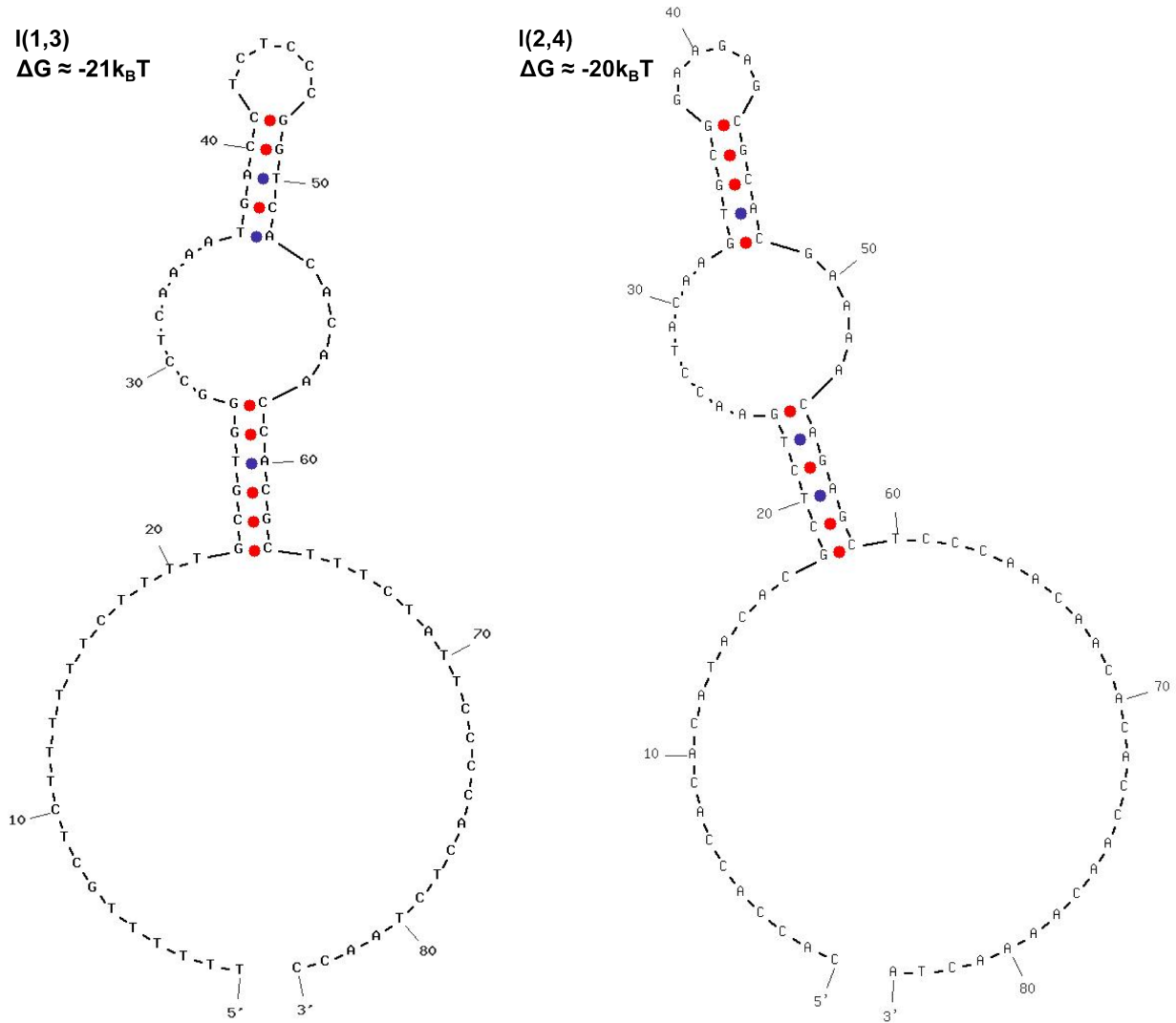


Figure G.2: Predicted hairpin folding in "closed" conformation of module L. Secondary structure and respective folding free-energy ΔG of strands I(1,3) (left) and I(2,4) (right) were predicted using the IDT (Skokie, Illinois, USA) online tool OligoAnalyzer 3.0 (<https://eu.idtdna.com/calc/analyzer>).

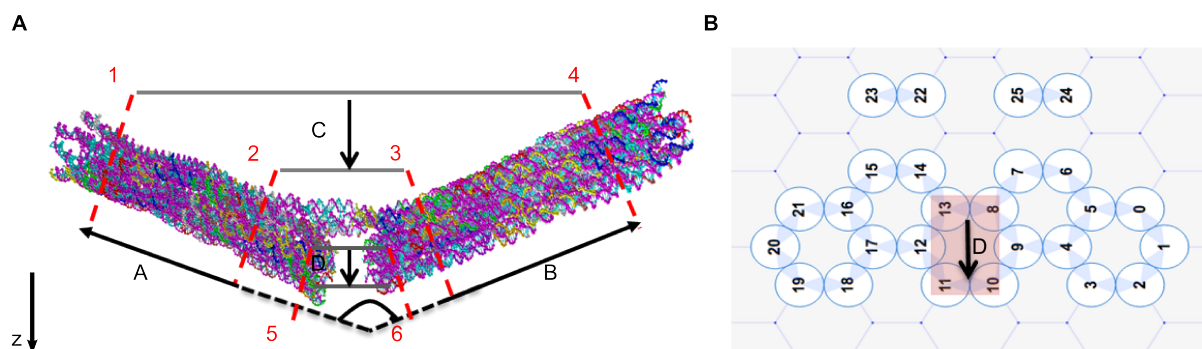


Figure G.3: Schematic representation of the vectors taken into account for bending angle determination. A) Angle θ is calculated from \vec{A} and \vec{B} , defined along the helices (0-21) (Figure V.1) by the centre of bp lying on the interface (1, 2) and (3, 4), respectively. The bend direction according to the reference (bottom-left corner) is defined using the vector \vec{C} , according to interfaces (1-4), and \vec{D} , according to the centre of bp lying on helices (8,13) and (10,11) over interface (5, 6). B) Cross-section view of the helices considered for definition of \vec{D} .

Table G.1: List of oligonucleotide sequences for assembly of each module and structure modification. Staples used to assemble different variants of the basic (N), short (S) and long (L) modules, and respective protecting strands (P). Toeholds for strand displacement are shown in bold. *Italic* is used to highlight the poly-thymine (T) region at the insertion point of the long strand of module L. Start and end position within the cadnano map (Supplementary Figure G.1) are indicated.

Staple	Start	End	Extension/oligonucleotide sequence	Module and modification
n5(1)	6[195]	7[195]	GATTAGGTCACCGTTTGGCCCTGAGTAATGTG	N ₅ (5 nucleotide (nt) gap)
n5(2)	7[201]	6[201]	AAAGATTCAAAAAGGGGTGAGAAAGGGGAACAAAACGGCGATTGACCGT	N ₅
n5(3)	14[195]	15[195]	AAGAAAGTTTTGGCCAGACGACGACAMTA	N ₅
n5(4)	15[201]	14[201]	ATGTTTCAGCTAATGCGAAGCAGACAAAACCAAAATAAGCGAGAGCGTTTT	N ₅
n0(1)	6[209]		ATTGACCAGATTCAAAAAGGGGTGAGAAAGGGGAACAAAACGGCGCAATCCGT	N ₀ (closed gap)
n0(2)	7[196]		TAGGTAAGTAATGGGATAGGTGACGTTGGCCTGAGTAATGTGAAC TACTAG	N ₀
n0(3)	14[209]		AGAGCGCTGTTCCAGCTAATGCAGAAACGAAACCAAAATAGCGGTGTGTA	N ₀
n0(4)	15[196]		AACGATTTTTGCAAAAAGAGTTTTCOCAGACGACATAAATCTCG	N ₀
s(1)	5[210]	1[230]	AACGTCGGATTCTCTAGGAAGCCCATCAAAAATAAFTTCTATAAAAAAATFCGATTAATCCGGCACC	S
s(2)	20[234]	16[203]	ATTTTATCGAATTTTTTAATFCGATTTTTTAATFCG TGCTACGA	S
Ps			AACGTCGGATTCTCTAGGAAGCCCATCAAAAATAAFTTCTATAAAAAAATFCGATTAATCCGGCACC	S _s
s(01)	5[210]	0[168]	GCCTTCTG	S _s
s(02)	1[168]	1[230]	GTA CTCCAGCCAGCTTAAATTTCTAT AAAAAAAAAAAAAAAAATCGATTAAATTCGGCCTTGTAAATCA	S _s
s(03)	20[234]	20[175]	AGGAATACCATGTAGAAAACCAATTAATTTCTATAAAAAAAAAAAAAAAAATCGATTAAAAACGCCAACATGTAAT	S _s
s(04)	21[175]	16[203]	AATCCGCATATTTAAACAATTTCTATATAAAAAAATAATCGATTAAACAATAATCCGGCTACCGCCTTTATCA	S _s
Ps*			ACAAAA	S _s
l(1)	0[272]	8[147]	ATTTTATAGAAATTTTTTAATFCG TACTACCA	S and S _s
l(2)	8[146]	7[279]	GGGAACGCTTACAAAAAATTTTCCAGAGCGCTAACCAAAATCAATTTTTTGGCTTTTTTCTTTTGGCG TTGGCCGCAAAATGACCTCTCCCGGTCCGACACACGCTTTCTATTTCCACCTTAACCAATTTT TTATGGCATCAATTTTATTTGGCGGAGCTGAAAATCTATAT	L
l(3)	8[272]	16[147]	TTTCATTTAGTTGATTTCCCAATTTCTGAACCAATAAAGGGAACCCCTCATATCAGCACC ACACATAACAGCTCTGTGAACCTTACAAGTGGGGAAGCGGCAACGCAAAAAACAGAGCTCCCAAGCAAC ACACGCAACAAAACCTAAGCCAAACGCTAACGAGCGTTTGAGCGCT	L
l(4)	16[146]	15[279]	CGACATTAACCTCCCCCAAGAACGGAGCGGCTGCGATTTTTTTTTTTGGCTTTTTTGGCGTGGG CGTGAATGAGCTCTGGGGTCAAGCAAGCAAGCGTTTCTATTTCCCGAGCTTAACGAATATCG CCATTTCCATATAAACAACGGGTGTGTGAAGTCCATATG CAACTAAATAAAGCCAAACGCTCAACAGTAAACAGATTTTAAITTCAGACACGACACACACATA CAGCGCTGTGAACCTAGAGTGGGAAGAGCGGCAACGAAACAGAGAGTCCCAACAACA CACCAACAACAACTAAAGGCGTTATCCGGTATTTCTGAACAAGT	L

Table G.2: List of oligonucleotide sequences for assembly of each module and structure modification – continuation. Staples used to assemble different variants of the basic (N), short (S) and long (L) modules, and respective protecting strands (P). Toeholds for strand displacement are shown in bold. *Italic* is used to highlight the poly- Γ region at the insertion point of the long strand of module L. Start and end position within the cadnano map (Supplementary Figure G.1) are indicated.

Staple	Start	End	Extension/oligonucleotide sequence	Module and modification
l_{4T} (1)	0[272]	8[147]	GGGAACCTTACAAAAAACCCTTCCAGAGCCCTACCAAAATCAA <i>TTTTTTTTTTTGGCTCTTTTTTTCTTTTGG</i> CGTGGCCCTCAAAATGACCTCTCCGGTCAACAAGCAGGCTTCTATTCGCCACTCTAACCAATTTT TATGGCATCAATTCATTGGCGAGCTGAAAATCTATAT	L_{4T} (additional 4 T for tension L_{4T})
l_{4T} (2)	8[146]	7[279]	TTTCAITTAGTTGATTCCCAATTCGAAACCATAAAGGGAACCCCTCATAT <i>TTTTTACCACCCACACAT</i> ACACGGCTTGAAACCTTACAAGTGGGAAGAGGGCAGCAAAAACAGAGCTCCCAACAACACACCAACAAA ACTAAGCCAAACGCTAACGAGGCTTTGAGGCT	L_{4T}
l_{4T} (3)	8[272]	16[147]	CCACATAACCTCCCCAAGAAGCGGAGGCTGGGATTTT <i>TTTTTTTTTTTGGCTCTTTTTTTCTT</i> TTGCGTGGGCTCAAAATGACCTCTCCGGTCAACAACCCACGCTTCTATTC CCCACCTTAACCAATATCGCCATTCATATAACAACCGGTCTGGGAGTCCATATG CAACTAATAAAGCCAAACGCTCAACAGTAAACAGATTGTTTTAATTCGA <i>TTTTTCAACCACACA</i> CATACAGGCTCTGAACCTACAAGTGGGAAGAGCGCACGAAAAACACAGAGCTCCCAACA	L_{4T}
l_{8T} (1)	0[272]	8[147]	ACACACCAAAAACCTAAGGGCTTATCCGGTATTCTGAACAAAAGT GGGAACCTTACAAAAAACCCTTCCAGAGCCCTACCAAAATCAA <i>TTTTTTTTTTTGG</i> TCTTTTTCTTTTGGGTGGCCCTCAAAATGACCTCTCCGGTCAACAACCCACGCTTCTAT	L_{8T} (additional 8 T for tension release) L_{8T}
l_{8T} (2)	8[146]	7[279]	TCCCACCTTAACC <i>TTAATTTTTTATGGCATCAATTCATTTGGCGGAGCTGAAAATCTATAT</i> TTTCAITTAGTTGATTCCCAATTCGAAACCATAAAGGGAACCCCTCATAT <i>TTTTTTTCAACCACCA</i> CACATACAGGCTTGAACCTACAAGTGGGAAGAGCGCAAGAAAAACAGAGCTCCCAACAACAC ACCAACAAAACCTA <i>TTAGCCAACGCTAACGAGCGTTTGAAGCGCT</i>	L_{8T}
l_{8T} (3)	8[272]	16[147]	CCACATAACCTCCCCAAGAAGCGGAGGCTGGGATTTT <i>TTTTTTTTTTTGGCTCTTTTTTTT</i> CTAATGCGTGGCCCTCAAAATGACCTCTCCGGTCAACAACCCACGCTTCTATTCGCCACT CTAACCTTAATATCGCCATTCATATAACAACGGTGTCTGGGAGTCCATATG	L_{8T}
l_{8T} (4)	16[146]	15[279]	CAACTAATAAAGCCAAACGCTCAACAGTAAACAGATTGTTTTAATTCGA <i>TTTTTTTCAACCACCA</i> CATACAGGCTTGAAACCTACAAGTGGGAAGAGCGCAAGAAAAACAGAGCTCCCAACA ACACACCAAAAACCTA <i>TTAGGGCTTATCCGGTATTCTGAACAAAAGT</i> TATGTGTGGTGTGAGGTGGGAAATAGAAAAGGCTGGTGTGTAGGTTTCAGAGCGTGT GCAACGTT ACGCAAAAAGAAAAAGCAAAAATTTGTTGGTGTGTTGGGAGCTCTGTTTTTCGTGGGCTC TTCCGCACTTACCGGGAGAGGTCATTTT GAGGCCCTGCTACGA	L_{8T} all L variations all L variations

PUBLICATIONS AND MANUSCRIPTS

Manuscripts 2, 5 and 6 compose chapter III. Manuscript 10 is based on chapter IV. Manuscript 4 composes V.1 and manuscript 11 is based on V.2. The sign * denotes equally-contributing authors and § denotes co-corresponding authors.

1. Alena Khmelinskaia*, Maitane Ibarguren*, Rodrigo F. M. de Almeida, David J. López, Vanda A. Paixão, Hasna Ahayayauch, Félix M. Goñi and Pablo Escriba (2014) Changes in membrane organization upon spontaneous insertion of 2-hydroxylated unsaturated fatty acids in the lipid bilayer. *Langmuir*, 30(18): 2117-2128.
2. Alena Khmelinskaia, Henri G. Franquelim§, Eugene P. Petrov, Petra Schwille§ (2016) Effect of anchor positioning on binding and diffusion of elongated 3D DNA nanostructures on lipid membranes. *Journal of Physics D: Applied Physics*, Special Issue on Molecular Movements in Biomembranes, 49:194001.
3. Sven Kenjiro Vogel*, Ferdinand Greiss*, Alena Khmelinskaia, Petra Schwille (2017) Control of lipid domain organization by a biomimetic contractile actomyosin cortex. bioRxiv, 096248. *eLife*, 6:e24350.
4. Henri G. Franquelim, Alena Khmelinskaia, Jean-Philippe J. Sobczak, Hendrik Dietz, Petra Schwille (2018) Membrane sculpting by curved DNA origami scaffolds. *Nature Communications*, 9 (1):811. F1000 Cell Biology recommended.
5. Alena Khmelinskaia*, Jonas Mücksch*, Franco Conci, Grzegorz Chwastek, Petra Schwille. (2018) FCS analysis of protein mobility on lipid monolayers. *Biophysical journal*, 114 (10):2444–2454.
6. Alena Khmelinskaia, Jonas Mücksch, Eugene P. Petrov, Henri G. Franquelim, Petra Schwille. Control of membrane binding and diffusion of cholesteryl-modified DNA origami nanostructures by DNA spacers. *Langmuir*, doi: 10.1021/acs.langmuir.8b01850.
7. Wooli Bae, Susanne Kempter, Alena Khmelinskaia, Maximilian T. Strauss, Petra Schwille, Ralf Jungmann, Tim Liedl. Stop-and-go super-resolution imaging of membrane-assisted DNA origami lattice assembly. (In revision)

8. Weixiang Ye, Sirin Celiksoy, Arpad Jakab, Ana Raso, Alena Khmelinskaia, Tamara Heermann, Seraphine V. Wegner, Germán Rivas, Petra Schwille, Rubén Ahijado-Guzmán and Carsten Sönnichsen. Plasmonic nanosensors show the axial location of the MinDE protein waves. (Submitted)
9. Alena Khmelinskaia, Joaquim M. T. Marquês, André E.P. Bastos, Catarina A. C. Antunes, Silvia Scolari, Gerson M. da S. Lobo, Rui Malhó, Andreas Herrmann, H. Susana Marinho, Rodrigo F. M. de Almeida. Liquid-ordered phase in mammalian and yeast membranes: a common feature behind fundamental differences. (Submitted)
10. Alena Khmelinskaia, Renukka Yaadav, Henri G. Franquelim, Eugene P. Petrov[§], Petra Schwille[§]. Self-organization of rodlike nanoparticles on supported lipid membranes. (In preparation)
11. Alena Khmelinskaia^{*}, Megan Engel^{*}, Garima Mishra, Jonathan Doye[§], Petra Schwille[§]. Integrating a conformational switch to achieve controllable membrane sculpting by DNA origami scaffolds. (In preparation)

ACKNOWLEDGEMENTS

These were four years of great challenges and adventures to which a number of people contributed, both professionally and emotionally. Thank you to...

Petra, for taking me in as a PhD student, for the endless freedom of mind, resources and experiences, from student exchanges to teaching, from conferences to collaborations.

Dieter Braun and Ralf Jungmann, for your scientific advise as part of my TAC and otherwise.

QBM, for the financial support and the amazing network of people (present and past) – Mara, Michael, Julia, Filiz, Markus, all the professors and students, specially the always active class of 2014 and the bits from 2013 that always join.

the SFB863 and all the people involved for the fun discussion.

CeNS for the unique experience that JNN is and all the people I got to meet, organizers and students.

the DNA node, for the open environment to share fresh and unbaked ideas with a beer and some food – Hendrik Dietz, for the collaboration and the always honest opinions, Tim and all the Liedl group, specially Wooly, Philipp, Mauricio and the tireless Susi, for the never-ending enthusiasm, fruitful discussions, tolerance of the "smelly bacteria" and for (to a certain degree) adopting me.

Megan and Garima, for accepting a challenge and transforming it into a productive collaboration, Jonathan Doye for not letting me give up.

Dina Grohmann and Herbert Tschochner for the TBP plasmids.

Carsten and the Sönnichsen lab, specially Weixiang and Ruben for the trust in a challenging collaboration.

my first students, Angela, Franco and Renukka, for the hard work and patience, for teaching me how to teach.

Henri, for sharing your experience and knowledge of scientific literature and wikipedia, for your special humour and support.

Eugene, for your sincere interest, deep insights and never-ending teaching that resulted in beautiful works and a friendship.

Jonas, for your dedication, brain, humour and hug, that not only made our work together fun but also made my days better.

Sven, for an efficient and fruitful collaboration.

Katharina, for the persistence and golden cloning hands.

Bea, for your example, exciting ideas and keeping the fridge refilled.

Blumi, for the correctness and the people skills.

Sigi, for keeping the GUV lab as a real temple, without you everything would be more difficult.

the habitants of the fun office, past and present, Sonal, Diego, Cate and Hiro, for making the working desk more than just that.

all other past and present Schwille lab members that from colleagues became friends, Grzesiek, Fabian, Franziska, Ilaria, Gosia, Kristina and Tamara, for the advice and support, scientific and emotional, for sharing a bite and a drink, for all the good times – a special note to Tamara and Jonas for the crash course on Latex and troubleshooting that enabled me to efficiently write this thesis, to them and Bea, Eugene and Kristina for proofreading the result.

all members of Schwille lab for making the lab be what it is.

the JuiceLovers and the ultimate frisbee crowd for giving me something more to do.

Anna for keeping my fingers moving and the music flowing.

the once from before that always stay, Marta, Joana, Flavia, Sara, Rodrigo e Tiago, for no matter how far, being always close.

the once from now, Jacob, Julie, Johanna, Erin, Charlène and Le Mu, for finding me and sticking around, independently of the ways of life.

my family, most of all mom Elena for the unconditional love and support, katze Marfa for the permanent company and cuddles, my dearest LT for the right words and warm hugs that lift me up even in the worst moments.

To all of you, an eternal thank you!